

AD-A254 162

AP02 8953.1-EL-CF

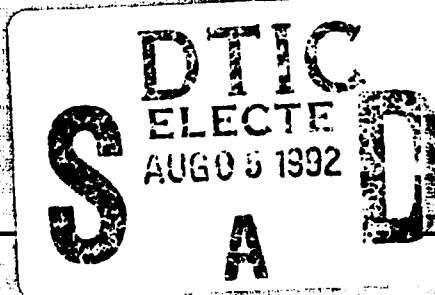


CONFERENCE PROCEEDINGS NO. 227

①

AMERICAN VACUUM SOCIETY SERIES 10

CONFERENCE PROCEEDINGS NO. 227
AMERICAN VACUUM SOCIETY SERIES 10
EDITOR: PAUL H. HOLLOWAY



ADVANCED PROCESSING AND CHARACTERIZATION TECHNOLOGIES

FABRICATION AND CHARACTERIZATION OF SEMICONDUCTOR
OPTOELECTRONIC DEVICES AND INTEGRATED CIRCUITS

CLEARWATER, FL 1991

EDITOR: PAUL H. HOLLOWAY

ADVANCED PROCESSING AND
CHARACTERIZATION TECHNOLOGIES
CLEARWATER, FL 1991

This document has been approved
for public release and sale; its
distribution is unlimited.

AIP

ADVANCED PROCESSING
AND CHARACTERIZATION
TECHNOLOGIES

| | | | | |
|---|---|--|--|--|
| REPORT DOCUMENTATION PAGE | | | Form Approved DMS No. 0104-0198 | |
| <small>1. AGENCY USE ONLY (Leave blank)</small> | | | | |
| 2. REPORT DATE Jul 92 | | 3. REPORT TYPE AND DATES COVERED Final 8 Apr 91-7 Apr 92 | | |
| 4. TITLE AND SUBTITLE Advanced Processing and Characterization Technologies | | | 5. FUNDING NUMBERS DAAL03-91-G-0142 | |
| 6. AUTHOR(S) Paul H. Holloway | | | | |
| 7. PERFORMING ORGANIZATION NAME(S) AND ADDRESS(ES) University of Florida Gainesville, FL 32611 | | | 8. PERFORMING ORGANIZATION REPORT NUMBER | |
| 9. SPONSORING / MONITORING AGENCY NAME(S) AND ADDRESS(ES) U. S. Army Research Office P. O. Box 12211 Research Triangle Park, NC 27709-2211 | | | 10. SPONSORING / MONITORING AGENCY REPORT NUMBER ARO 28953.1-EL-CF | |
| 11. SUPPLEMENTARY NOTES The view, opinions and/or findings contained in this report are those of the author(s) and should not be construed as an official Department of the Army position, policy, or decision, unless so designated by other documentation. | | | | |
| 12a. DISTRIBUTION / AVAILABILITY STATEMENT Approved for public release; distribution unlimited. | | | 12b. DISTRIBUTION CODE | |
| 13. ABSTRACT (Maximum 200 words) The conference consisted of papers on material growth techniques, processing and devices. | | | | |
| 14. SUBJECT TERMS Conference, Growth Techniques, Semiconductor Opto-electronic Devices, Integrated Circuits, Optoelectronic Systems | | | 15. NUMBER OF PAGES 223 | |
| | | | 16. PRICE CODE | |
| 17. SECURITY CLASSIFICATION OF REPORT UNCLASSIFIED | 18. SECURITY CLASSIFICATION OF THIS PAGE UNCLASSIFIED | 19. SECURITY CLASSIFICATION OF ABSTRACT UNCLASSIFIED | 20. LIMITATION OF ABSTRACT UL | |

CONFERENCE PROCEEDINGS NO. 227

AMERICAN VACUUM SOCIETY SERIES 10

SERIES EDITOR: GERALD LUCOVSKY
NORTH CAROLINA STATE UNIVERSITY

ADVANCED PROCESSING AND CHARACTERIZATION TECHNOLOGIES

FABRICATION AND CHARACTERIZATION OF SEMICONDUCTOR
OPTOELECTRONIC DEVICES AND INTEGRATED CIRCUITS

CLEARWATER, FL 1991

EDITOR:

J. H. HOLLOWAY
UNIVERSITY OF FLORIDA, GAINESVILLE

92-21100



92 8 34 1 0

AIP

American Institute of Physics

New York

Authorization to photocopy items for internal or personal use, beyond the free copying permitted under the 1978 U.S. Copyright Law (see statement below), is granted by the American Institute of Physics for users registered with the Copyright Clearance Center (CCC) Transactional Reporting Service, provided that the base fee of \$2.00 per copy is paid directly to CCC, 27 Congress St., Salem, MA 01970. For those organizations that have been granted a photocopy license by CCC, a separate system of payment has been arranged. The fee code for users of the Transactional Reporting Service is: 0094-243X/87 \$2.00.

© 1991 American Institute of Physics.

Individual readers of this volume and nonprofit libraries, acting for them, are permitted to make fair use of the material in it, such as copying an article for use in teaching or research. Permission is granted to quote from this volume in scientific work with the customary acknowledgment of the source. To reprint a figure, table, or other excerpt requires the consent of one of the original authors and notification to AIP. Republication or systematic or multiple reproduction of any material in this volume is permitted only under license from AIP. Address inquiries to Series Editor, AIP Conference Proceedings, AIP, 335 East 45th Street, New York, NY 10017-3483.

L.C. Catalog Card No. 91-55194
ISBN 0-88318-910-0
DOE CONF-9105134

Printed in the United States of America.

This book was put into production on 4 March 1991 and was published on 2 May 1991.

TABLE OF CONTENTS

| | <u>Page</u> |
|--|-------------|
| Preface | xi |
| I. GROWTH | |
| Techniques | |
| Chemical Beam Epitaxy for Opto-electronics and Electronics Applications | 2 |
| <i>W.T. Tsang</i> | |
| Doping Distributions in III-V Semiconductors | 5 |
| <i>E.F. Schubert</i> | |
| Incorporation of Arsenic in InP Layers and Heterointerfaces in GaInAs/InP Hetero-structures Grown by Low-pressure Metalorganic Vapor Phase Epitaxy | 9 |
| <i>M. Wada, K. Sakakibara and Y. Sekiguchi</i> | |
| In Situ Optical Characterization and Control of Epitaxial III-V Crystal Growth | 13 |
| <i>W.E. Quinn</i> | |
| Selective Growth | |
| Selective Epitaxial Growth of AlGaAs by MOCVD using Dialkylmetachloride | 17 |
| <i>K-I. Yamaguchi and K. Okamoto</i> | |
| Selective Growth of InP/GaInAs Heterostructures Using Metalorganic Molecular Beam Epitaxy | 21 |
| <i>Y.L. Wang, A. Feygenson, R.A. Hamm, D. Ritter, J.S. Weiner</i> | |
| <i>H. Temkin and M.B. Panish</i> | |
| In Situ Mass Spectrometric Analysis of the Mechanism of Selective-Area Epitaxy by MOMBE | 25 |
| <i>Y. Ohki and Y. Hiratani</i> | |
| Application of Migration-Enhanced Epitaxy to Novel Semiconductor Structures | 29 |
| <i>Y. Horikoshi, H. Yamaguchi, T. Sudersena, R.S. Ramesh and</i> | |
| <i>N. Kobayashi</i> | |
| II. CHARACTERIZATION | |
| Optical | |
| Photoluminescence Characterization of Compound Semiconductor Optoelectronic Materials | 34 |
| <i>G.E. Sillman, S.S. Bose and A.P. Curtis</i> | |
| Photoluminescence Mapping: New Technique to Characterize Materials and Structures for Fabrication of Photonic Devices | 38 |
| <i>M. Bugajski and Jacek Ornoch</i> | |

| | |
|--|----|
| Photoluminescence from InGaAs/InGaAsP Quantum Wires Fabricated by Ga Focused Ion Beam | 42 |
| <i>S.J. Yu, H. Asahi, J. Takizawa, S. Kim and S. Gonda</i> | |
| Infrared Characterization of Compound Semiconductors | 46 |
| <i>A. Deneuve, V. Zelezny, D. Tanner and P.H. Holloway</i> | |
| Optically Confirmed Two-Dimensional Confinement Effects in Ultra-Narrow InGaAs/InP Quantum Well Wires | 50 |
| <i>M. Notomi, M. Naganuma, H. Iwamura, T. Nishida, S. Nojima, M. Okamoto and T. Tamamura</i> | |
| Laser Scatterometry for Process Characterization | 54 |
| <i>S.M. Gaspar, K.C. Hickman, K.P. Bishop, S.S. Nagvi, J.R. McNeil, S. Wilson, Y.E. Strausser, R.A. Gottscho and A. Kornblit</i> | |

Electronic

| | |
|---|----|
| Study of Epitaxial Growth by UHV-SEM and RHEED-TRAXS | 56 |
| <i>S. Ino</i> | |
| Spectroscopy and Luminescence with STM on III-V Epitaxial Multilayers | 60 |
| <i>O. Albrektsen, S.F. Alvarado, H.P. Meier, Ph. Renaud and H.W.M. Salemink</i> | |
| Ga_{0.47}In_{0.53}As/InP Multiquantum Well Structures Observed by Scanning Tunneling Microscopy under Ultrahigh Vacuum | 64 |
| <i>T. Kato, F. Osaka, I. Tanaka and S. Ohkouchi</i> | |
| Characterization of Strained Heterostructures by Catholuminescence | 68 |
| <i>D. Bimberg, M. Grundmann and J. Christen</i> | |

III. PROCESSING

Quantum Sized Structures

| | |
|--|----|
| Formation of AlGaAs Quantum Wire-Like Structures on Vicinal (110) GaAs Substrates by Molecular Beam Epitaxy | 76 |
| <i>H. Nakashima, M. Sato, K. Maehashi, K. Kimura, H. Asahi, S. Hasegawa and K. Inoue</i> | |
| Fabrication of Arrays of High Quality Quantum Filaments by Deep UV Holography and MBE Growth on Channelled Substrates | 80 |
| <i>U. Marti, M. Proctor, R. Monnard, D. Martin, F.K. Reinhard, R. Widmer and H. Lehmann</i> | |
| Mesoscopic Size Fabrication Technology | 84 |
| <i>Y. Arakawa</i> | |
| Lateral Field Effect in Focused-Ion Beam Written In-Plane-Gated Systems | 88 |
| <i>A.D. Wieck, A. Fischer and K. Ploog</i> | |

Applications of Ion Beams and Etching

| | |
|--|-----|
| Focused-Ion-Beam Micromachining: A Fabrication Tool for Prototypal Semiconductor Lasers | 92 |
| <i>R.K. DeFrez</i> | |
| A Novel Vacuum Lithography with SiN_x Resist by Focused Ion Beam Exposure and Dry Etching Development | 96 |
| <i>S. Takahashi, M. Ohashi, S. Fukatsu, Y. Shiraki and R. Ito</i> | |
| ECR Plasma Etching of III-V Optoelectronic Devices | 100 |
| <i>S.J. Pearton</i> | |
| Influence of SiCl₄ Reactive Ion Etching on the Electrical Characteristics of GaAs | 104 |
| <i>D. Lootens, P. Clauws, P. Van Daele and P. Demeester</i> | |
| Electron-beam Writing System for Holographic Optical Elements | 108 |
| <i>Y. Hori, F. Sogawa and M. Kato</i> | |
| Micro Dry Etching Process for Vertical Cavity Surface Emitting Lasers | 112 |
| <i>A. Matsutani, F. Koyama and K. Iga</i> | |

Surfaces and Contacts

| | |
|--|-----|
| Sulfide Treatment on III-V Compound Surfaces | 116 |
| <i>Y. Nannichi</i> | |
| Sulfur Passivation of GaAs Surfaces | 118 |
| <i>Y. Wang and P.H. Holloway</i> | |
| Direct Observation of GaAs Surface Cleaning Process Under Hydrogen Radical Beam Irradiation | 122 |
| <i>H. Iwata and K. Asakawa</i> | |
| Near Surface Type Conversion of p-type, Single Crystal InP by Plasma Exposure | 126 |
| <i>X. Li, T.A. Gessert and T.J. Coutts</i> | |
| Advances in Controlling Electrical Contacts for Optoelectronics | 130 |
| <i>L.J. Brillson</i> | |
| Indium Ohmic Contacts to n-ZnSe | 134 |
| <i>Y.X. Wang and P.H. Holloway</i> | |

Diffusions and Large Areas

| | |
|---|-----|
| A New Method of Zn Diffusion into InP for Optical Device Fabrication | 138 |
| <i>M. Wada, K. Sakakibara and Y. Sekiguchi</i> | |
| Open Tube Double Diffusion for the Fabrication of Bipolar Transistor Waveguide Optical Switch | 142 |
| <i>D.K. Gautam, Y. Nakano and K. Tada</i> | |
| Full-Water Technology for Laser Fabrication and Testing | 146 |
| <i>D.J. Webb, M.K. Benedict, G.L. Bona, P. Buchmann, N. Cahoon, K. Darwyler, H.P. Dietrich, A. Moser, G. Sasso, H.K. Seitz, P. Vettiger, O. Voegeli and P. Wolf</i> | |

| | |
|-------------------------------------|-------------------------------------|
| Accession For | |
| NTIS CRA&I | <input checked="" type="checkbox"/> |
| DTIC TAB | <input type="checkbox"/> |
| Unannounced | <input type="checkbox"/> |
| Justification | |
| By | |
| Distribution / | |
| Availability Codes | |
| <input checked="" type="checkbox"/> | Avail and/or |

DTIC QUALITY INSPECTED 3

| | |
|--|-----|
| Fabrication Issues and Considerations for High Performance Grating-Surface-Emitting Semiconductor Lasers | 150 |
| <i>G.A. Evans, N.W. Carlson, J.M. Hammer, D.P. Bour, J.B. Kirk, S.K. Liew, H. Lee, W. Reichert, R.K. DeFreez, C.A. Wang, H.K. Choi, J.N. Walpole and J.K. Butler</i> | |
| Epitaxial Liftoff Technology for OEIC's | 154 |
| <i>E. Yablonovitch, W.K. Chan and A. Yi-Yan</i> | |

IV. DEVICES

Lasers

| | |
|--|-----|
| Submilliampere-threshold Multi-Quantum-Well AlGaAs Laser and Their Integration of More than 100 Lasers | 160 |
| <i>S. Hirata, H. Narui and Y. Mori</i> | |
| Fabrication of Low-Threshold InGaAs/GaAs Ridge Waveguide Lasers by Using In-Situ Monitored Reactive Ion Etching | 164 |
| <i>C.P. Chao, S.Y. Hu, P. Floyd, K-K. Law, J.L. Merz and A.C. Gossard</i> | |
| Fabrication of GaAlAs/GaAs Single Quantum Well Gain-Coupled Distributed Feedback Lasers | 168 |
| <i>Y. Luo, H.L. Cao, M. Dobashi, H. Hosomatsu, Y. Nakano and K. Tada</i> | |
| Effect of Window Diffusion Stripe Structure on Reduction of Temperature Rise at Laser Facet | 172 |
| <i>A. Shima, Y. Kokubo and M. Aiga</i> | |
| Differential Gain and Damping in High Speed 1.55μ Quantum Well Lasers | 176 |
| <i>M.C. Tatham, N.C. Fletcher, D.M. Cooper and L.D. Westbrook</i> | |
| Fabrication of GaInAs(P)/InP Quantum-Wire Structures for Lasers and Electro-Optical Devices | 180 |
| <i>S. Arai and Y. Suematsu</i> | |
| Polarization-Controlled Semiconductor Photonic Devices by Strained-Barrier Superlattice Structure | 184 |
| <i>M. Okamoto, K. Magari and Y. Itaya</i> | |

Integrated Structures

| | |
|---|-----|
| Fabrication and Characteristics of Tunable Twin-Guide DFB Lasers by All MOVPE | 188 |
| <i>M. Hamada, E. Yamamoto, K. Suda, S. Nogiwa and T. Oki</i> | |
| Buried Interconnect Structure for Symmetric SEEDs | 192 |
| <i>L.A. D'Asaro, L.M.F. Chirovsky, R.F. Kopf and S.J. Pearton</i> | |
| Tailoring of Electron and Hole Energies in Strained GaAsP/AlGaAs Quantum Wells using Fluorine Impurity Induced Layer Disordering | 195 |
| <i>U. Das, S. Davis, J-T. Hsu, R.V. Ramaswamy and F.A. Stevie</i> | |

Waveguides, Switches, and Modulators

| | |
|---|-----|
| Semiconductor Waveguide Switches and Modulators | 199 |
| <i>K. Tada</i> | |
| Properties of Waveguides, Routing Structures and Switches Fabricated by Impurity Induced Layer Disorder | 203 |
| <i>T.A. DeTemple</i> | |
| Room Temperature Stark-Ladder Transitions and Electro-Optic Bistability in GaAs/AlAs Superlattices with Different Miniband Widths | 206 |
| <i>K. Kawashima, K. Fujiwara, T. Yamamoto, M. Sigeta and K. Kobayashi</i> | |
| Very Low-Voltage MBE-Grown Asymmetric Fabry-Perot Reflection Modulator Based on Superlattice Wannier-Stark Localization | 210 |
| <i>K-K. Law, J.L. Merz and L.A. Coldren</i> | |
| Room Temperature Excitonic Transitions and Electro-Optical Bistability in Strained $\text{In}_{1-x}\text{Ga}_x\text{As}/\text{Al}_{0.15}\text{Ga}_{0.85}\text{As}$ Multiple Quantum Wells | 214 |
| <i>K. Kawashima, K. Fujiwara, K. Kobayashi and N. Sano</i> | |
| Ultrafast Measurements of Tunneling Dynamics in a GaAs/AlGaAs MQW Pin Optical Modulator | 218 |
| <i>C.B. Park, A. Miller, D.C. Hutchings and P. LiKamWa</i> | |

Preface

In our information-based, technologically sophisticated society, we are placing more and more demands on the ability to handle large volumes of information and rapid communications. As a result, optical and optoelectronic systems are now penetrating the market place. Examples of this include the fiber optics telephone lines with lower noise and clearer signals, optical storage of information and recall from CD players, infrared sensors and motion detectors for home security, remote controls for our televisions and VCR's, helium-neon lasers for reading bar codes at the supermarket check-out counters, and so forth. As these advances penetrate and establish themselves in the market place, there will be increasing demands to improve their performance even further, reduce their package size and power demands, and make them cheaper. For example, the helium-neon lasers for supermarket check-out are projected to be replaced by semiconductor diode lasers operating at the red wavelength of 670 nm. As a result there clearly is a future for the development and improvement of these technologies in semiconductor materials for performance and cost advantages.

To accelerate the development of technology for these improvements, it is necessary to facilitate the exchange of information about the current and improved practices leading to such devices and systems. Rapid improvement in compound semiconductors for optoelectronic applications is essential to this progress as they form the basis for making many of these devices possible. In order to facilitate this exchange, researchers at the University of Florida organized a topical conference in 1987 entitled **Compound Semiconductor Growth, Processing and Devices for the 1990's**. While there were (and still are) a large number of conferences addressing some aspects of the subject of semiconductor optoelectronics technology, the original organizers of the 1987 conference felt that no single conference of a topical size simultaneously brought together researchers in the three critical areas of material growth, processing and devices. This was particularly true with respect to bringing together an international collection of researchers in these somewhat technically disparate areas. The first conference was quite successful and we agreed with our Japanese colleagues that a continuation conference should be organized in 1989 in Japan. To facilitate technical exchange between the US, Japan and other countries interested in high technology subjects, we renamed the conference to its present title, **Advanced Processing and Characterization Technologies**, which gave us the opportunity to rotate the focus to topics other than compound semiconductors, if so desired. However the conference held October 4-6, 1989 in Tokyo, as well as the latest conference held May 8-10, 1991, in Clearwater Beach, Florida, both had the same focus, namely **Fabrication and Characterization of Semiconductor Optoelectronic Circuits**. We anticipate the next conference will be held in Japan in 1993, and the focus is yet to be determined. We also anticipate the continued support of the two sponsoring societies which were the American Vacuum Society and the Japan Society of Applied Physics. We certainly want to express our appreciation to these sponsoring societies, as well as the cosponsoring societies, which were the Lasers and Electro-Optics Society, Optical Society of America, Electrochemical Society of Japan, Institute of Electronics, Information and Communications Engineers, Institute of Electrical Engineers of Japan, and the Vacuum Society of Japan.

In the present conference, the Conference Co-Chairmen, Professor Ramu Ramaswamy of the University of Florida and Professor Kunio Tada of the University of Tokyo, put together an International Advisory Board which was truly international and of high quality. Dr. Thomas Paoli of Xerox-Palo Alto Research Center and his program committee worked extremely hard and put together an exceedingly good technical program, the summary of which constitutes this monograph. And finally a large number of scientists and engineers served on the Program Committee and Organizing Committee, putting in a lot of time and effort to make the meeting a success. I want to express my most sincere appreciation to all of these members listed below, for without their efforts, this meeting and these proceedings would not be possible.

Finally, we want to express our sincere appreciation to the Army Research Office and the Defense Advanced Research Project Agency. Without their support, the conference would not have been possible.

Paul H. Holloway
Organizing Committee Chair
Department of Materials Science and Engineering
University of Florida
Gainesville, Florida USA

CONFERENCE CHAIRMEN

Professor Ramu Ramaswamy, University of Florida, Chair
Professor Kunio Tada, University of Tokyo, Co-Chair

INTERNATIONAL ADVISORY BOARD

Alfred Cho, AT&T Bell Labs
Luis Figueroa, Boeing
Akira Kinbara, University of Tokyo
James Merz, University of California
at Santa Barbara
Takuo Sugano, University of Tokyo
Gus Witt, MIT
Hans Rupprecht, Fraunhofer Institut

Richard Eden, Giga Bit Logic
Izuo Hayashi, Optoelectronic Technology
Research Laboratory
Greg Olsen, Epitaxx Inc.
Yasuhara Suematsu, Tokyo Institute of
Technology
Cyril Hilsum, GEC Hurst Research Centre

PROGRAM COMMITTEE

Thomas Paoli, Xerox-PARC, Chair
Hisao Nakashima, Osaka University, Co-Chair
H.P.M.M. Abrosius, Phillips-Netherlands
Kiyoshi Asakawa, NEC
Richard de la Rue, University of Glasgow
Steve Forrest, University of Southern
California
Ken-ichi Iga, Tokyo Institute of Technology
Ozeki, Fujitsu
Franz Reinhart, Swiss Federal Institute
Wataru Susaki, Mitsubishi Electric
Jerry Woodall, IBM

Timothy Anderson, University of Florida
Jim Coleman, University of Illinois
Gary Evans, David Sarnoff Laboratory
Jim Harbison, Bellcore
Yoshiji Horikoshi, NTT
Yoshifumi Katayama, Optoelectronic Masashi
Technology Research Laboratory
Simon Ritchie, British Telecom
Henryk Temkin, AT&T Bell Labs
Jane Zucker, AT&T Bell Labs

ORGANIZING COMMITTEE

Paul Holloway, University of Florida, Chair
Shun-ichi Gonda, Osaka University, Co-Chair
Yasuhiko Arakawa, University of Tokyo
Alan Miller, University of Central Florida
P. N. Vaidyanathan, University of Florida

Hiroyoshi Matsumura, Hitachi
Lee Stefanakos, University of South Florida

I. GROWTH

Techniques

| | |
|---|----|
| Chemical Beam Epitaxy for Opto-electronics and Electronics Applications | 2 |
| <i>W.T. Tsang</i> | |
| Doping Distributions in III-V Semiconductors | 5 |
| <i>E.F. Schubert</i> | |
| Incorporation of Arsenic in InP Layers and Heterointerfaces in GaInAs/InP Hetero-structures Grown by Low-pressure Metalorganic Vapor Phase Epitaxy | 9 |
| <i>M. Wada, K. Sakakibara and Y. Sekiguchi</i> | |
| In Situ Optical Characterization and Control of Epitaxial III-V Crystal Growth | 13 |
| <i>W.E. Quinn</i> | |

Selective Growth

| | |
|--|----|
| Selective Epitaxial Growth of AlGaAs by MOCVD using Dialkylmetachloride | 17 |
| <i>K-I. Yamaguchi and K. Okamoto</i> | |
| Selective Growth of InP/GaInAs Heterostructures Using Metalorganic Molecular Beam Epitaxy | 21 |
| <i>Y.L. Wang, A. Feygenson, R.A. Hamm, D. Ritter, J.S. Weiner</i> | |
| <i>H. Temkin and M.B. Panish</i> | |
| In Situ Mass Spectrometric Analysis of the Mechanism of Selective-Area Epitaxy by MOMBE | 25 |
| <i>Y. Ohki and Y. Hiratani</i> | |
| Application of Migration-Enhanced Epitaxy to Novel Semiconductor Structures | 29 |
| <i>Y. Horikoshi, H. Yamaguchi, T. Sudersena, R.S. Ramesh and N. Kobayashi</i> | |

Chemical Beam Epitaxy for Opto-electronics and Electronics Applications

by

W. T. Tsang

AT&T Bell Laboratories
600 Mountain Avenue
Murray Hill, NJ 07974

Within the past few years, the progress in Chemical Beam Epitaxy (CBE) has been tremendous. It has attracted a great deal of interest from the MOCVD and MBE communities because it offers solutions to some of the most difficult problems encountered with each technique. The results thus far clearly demonstrated that high quality InGaAsP/InP materials and heterostructures can be routinely prepared by CBE.¹⁻³ With new metalorganic aluminum compounds such as triisobutylaluminum (TIBA), trimethylamine alane (TMN·AlH₃), and others, high quality AlGaAs with low residual carbon background has successfully been prepared. Both AlGaAs/GaAs and InGaAsP/InP electronic and photonic devices with the best state-of-the-art performance have been prepared. With the use of reflection high energy electron diffraction (RHEED), modulated beam mass spectrometry (MBMS) and other vacuum diagnostic techniques, very useful information has been obtained in understanding the metalorganic reaction chemistries on substrate surfaces. Such understandings are not only important for CBE, but also for MOCVD.

Since reference [1] already gives an extensive review on CBE, only a recent update is given here. 1.5 μm wavelength unstrained and strained-layer multi-quantum well (MQW) and graded-index separate confinement heterostructure (GRINSCH) InGaAs/InGaAsP single quantum well (SQW) injection lasers were successfully prepared by CBE.²⁻⁴ The strained-layer SCH 4QW lasers have threshold current densities, J_{th} , as low as 370 A/cm² and internal quantum efficiency of 90%. The GRINSCH SQW lasers have extremely low J_{th} of 170 A/cm², internal quantum efficiency of 83% and internal waveguide loss of 3.8 cm⁻¹. Such J_{th} for the first time breaks the barrier of 200 A/cm² in long wavelength lasers and approaches those values obtained in the more matured GaAs/AlGaAs QW lasers. More importantly, these QW laser wafers have thickness uniformity $< \pm 1\%$ and peak photoluminescence wavelength $< \pm 10$ nm (as good as ± 3 nm) across the entire 2 inch diameter wafer.² Such uniformity is important for low-cost laser fiber amplifier pump lasers, and for OEIC applications.

A monolithic p-i-n/HBT transimpedance photoreceiver circuit has also been fabricated from InP/InGaAs heterostructures grown by CBE.⁵ The OEIC, incorporating HBTs with f_T of 32 GHz and f_{max} of 28 GHz, had a bandwidth of 3.8 GHz with a mid-band transimpedance of 400 ohms. The photoreceiver was operated up to 5 Gb/s, at which bit rate a sensitivity of -18.8 dBm was measured at a wavelength of 1.5 μm . Taking into consideration the quantum efficiency η of the p-i-n photodetector, this

translates to a ηP value of -20.8 dBm, which is within 3.2 dB of the best hybrid results at this bit rate. The results demonstrate that the CBE growth technique is suitable for high performance HBT-based OEICs.

Selective area epitaxy and growth over patterned substrate using CBE were investigated.⁶ Truly selective area epitaxy with no deposition over the SiO_2 masks has been routinely obtained with excellent epilayer morphology. Uniform coverage was obtained for regrowth over etched mesas to form buried heterostructures. For growth over etched channels, very unique growth characteristics were obtained. Buried crescent stripes similar to those formed by liquid-phase epitaxy inside channels were also obtained by CBE. These growth characteristics demonstrated the unique capabilities of CBE. Planar buried heterostructure lasers⁷ with CBE-grown p-n InP current blocking layers have CW threshold current as low as 17 mA and power output up to 25 mW.

Recently, trimethylamine alane ($\text{TMN} \cdot \text{AlH}_3$) has been investigated^{8,9} as a potential metalorganic source for CBE. AlGaAs films with excellent structural and optical properties have been grown with this source. Photoluminescence intensities from AlGaAs grown by CBE at 500°C using $\text{TMN} \cdot \text{AlH}_3$ are comparable to those from material grown by metalorganic chemical vapor deposition at 675°C using trimethylaluminum (TMAI). Carbon and oxygen levels in CBE grown AlGaAs are drastically reduced in comparison to similar films grown with triethylaluminum (TEAl). Several groups⁸⁻¹⁰ have also prepared GaAs/AlGaAs HBT with carbon doped base. Chiu and co-workers⁹ demonstrate the entire structure of high quality AlGaAs/GaAs HBTs including a non-alloyed δ -doped ohmic contact and in situ Al metalization grown by chemical beam epitaxy using trimethylamine alane as the Al source. The graded $\text{Al}_x\text{Ga}_{1-x}\text{As}$ and uniform GaAs bases (both $\sim 1000\text{\AA}$ thick) are doped with carbon to high 10^{19} cm^{-3} using trimethyl-Ga.

A high performance GaAs p-MESFET using carbon as the p-dopant is also demonstrated for the first time. The channel and contact layers were grown by CBE.¹¹ The cap contact layer was highly doped with carbon ($5 \times 10^{20}\text{ cm}^{-3}$) in order to minimize the parasitic resistance in the FET structure. The sheet resistivity and transfer resistance of the contacts were 220 ohm/\square and 0.2 $\text{ohm}\cdot\text{mm}$ respectively. These are comparable to values achieved on n-type GaAs. The room temperature extrinsic transconductance and K-factor values were 50 mS/mm and 165 mS/V \cdot mm with 1 μm gate length and 3.5 μm source-to-drain spacings. These are the highest room temperature values ever demonstrated for p-GaAs MESFET. Carbon doping using TMGa in CBE will be a very powerful technique for preparing electronic circuits using MESFET and HBT. Carbon is an excellent dopant because it is highly electrically active, suffers no diffusion problem and can be incorporated in GaAs to concentrations as high as 10^{21} cm^{-3} .

The growth by CBE of other materials such as GaAs/Ga_{0.5}In_{0.5}P, II-VIs and Si are also under investigation. It is quite clear that CBE has a lot of unique capabilities to offer, tremendous progress has been made, and it should have a great potential of developing into a powerful epitaxial growth technique.

REFERENCES

- [1] For a review, see:
W. T. Tsang, *J. Crystal Growth* 95 (1989) 121;
W. T. Tsang, Chemical Beam Epitaxy, in: *VLSI Electronics Microstructure Science*, Vol. 21, Ed. N. G. Einspruch (Academic Press, New York, 1989) ch. 6, pp. 255-357; W. T. Tsang, *J. Crystal Growth*, 105 (1990) 1.
- [2] W. T. Tsang, M. C. Wu, T. Tanbun-Ek, R. A. Logan, S. N. G. Chu, and A. M. Sergent, *Appl. Phys. Lett.*, 57, 2065 (1990).
- [3] W. T. Tsang, M. C. Wu, L. Yang, Y. K. Chen, and A. M. Sergent, *Electronics Lett.*, 26, 2036 (1990).
- [4] W. T. Tsang, F. S. Choa, M. C. Wu, Y. K. Chen, A. M. Sergent, and P. F. Sciortino, Jr., "Very Low Threshold Single Quantum Well Graded-Index Separate Confinement Heterostructure (GRINSCH) InGaAs/InGaAsP Lasers Grown by CBE", submitted *Appl. Phys. Lett.*
- [5] S. Chandrasekhar, A. H. Gnauck, W. T. Tsang, F. S. Choa, and G. J. Qua, "A Monolithic 5 Gb/s p-i-n/HBT Integrated Photoreceiver Circuit Realized from Chemical Beam Epitaxial Material", submitted to *J. Photonic Technol. Lett.*
- [6] W. T. Tsang, L. Yang, M. C. Wu, and Y. K. Chen, *Electronics Letts.*, 27, 5 (1991).
- [7] M. Gailhanou, C. Labourie, J. L. Lievin, A. Perales, M. Lambert, F. Poingt, and D. Sigogne, *Appl. Phys. Lett.*, 58, 796 (1991).
- [8] C. R. Abernathy, A. S. Jordan, S. J. Pearton, and W. S. Hobson, "Growth of High Quality AlGaAs by MOMBE Using Trimethylamine Alane", to be published.
- [9] T. H. Chiu, T. Kuo, C. G. Fonstad, "Growth and Metalization of AlGaAs/GaAs Carbon-Doped HBTs Using Trimethylamine Alane by CBE", to be published.
- [10] A. Sandhu, T. Fujii, H. Ando, T. Takahashi, H. Ishikawa, N. Okamoto, and N. Yokoyama, "Gas Source MBE Growth of GaAs/AlGaAs HBT with a Carbon Doped Base Using Only Gaseous Sources", *Jpn. J. Appl. Physics Short Notes*, Vol. 30, No. 3, March 1991.
- [11] F. Ren, C. R. Abernathy, S. J. Pearton, "Novel Carbon-Doped p-Channel GaAs MESFET Grown by MOMBE", to be published.

Doping Distributions in III-V Semiconductors

E. F. Schubert

AT&T Bell Laboratories
Murray Hill, New Jersey 07974

I. Introduction

Doping distributions with spatially abrupt boundaries and high concentrations become increasingly important for compound semiconductor devices. A good understanding of the limitations of profiling techniques is required for such doping distributions. Two profiling techniques, capacitance-voltage (C-V) profiling and secondary ion mass spectrometry (SIMS), are used to study ultra-thin doping profiles and the limitations of the characterization techniques are analyzed.

II. The Capacitance-Voltage Technique in the Quantum regime

The C-V technique is a well-known method to characterize doping profiles in semiconductors. The resolution of the technique is given by the Debye and Thomas-Fermi screening length for non-degenerate and degenerate doping, respectively. In semiconductors with quantum confinement neither the Debye nor the Thomas-Fermi screening length limitations do apply. In quantum structures such as δ -doped structures and quantum well structures the carrier distribution is quantized and can not be described by classical screening lengths. It was recently shown that the resolution of the C-V technique, if applied to semiconductor quantum structures is limited to the spatial extent of the wave functions of the electron/hole system [1]. That is, the C-V profiles on semiconductor quantum structures is comparable in width with the wave functions.

Experimental C-V profiles p- and n-type δ -doped GaAs are shown in Fig. 1. The doping density of the p-type layers ($4 \times 10^{12} \text{ cm}^{-2}$) and n-type layers ($4.5 \times 10^{12} \text{ cm}^{-2}$) are comparable. The width of the C-V profiles at room temperature are 20 Å and 49 Å for p-type and n-type GaAs, respectively. Note that the profile width is significantly different for p-type and n-type material. The different profile widths are not due to a different width of the doping impurity distribution. The width of the actual doping distribution is <20 Å for both Be- and Si-doped GaAs, as concluded from SIMS measurements on the same samples [1].

The different width of the C-V profiles is due to the different spatial extent of the electron and hole wave functions. Heavy hole wave functions are spatially more confined than electron wave functions. The spatial width of the carrier wave function scales with the carrier mass according to $m^{-1/3}$ [1]. Using electron ($0.067 m_0$) and heavy hole masses ($0.45 m_0$) in GaAs, the profiles are expected to be different by a factor of $(m_e/m_{hh})^{-1/3} = 1.9$. The experimental ratio of the profile widths is $49 \text{ Å}/20 \text{ Å} = 2.4$ which is in reasonable agreement with the experimental value. Note that the C-V profiles on p- and n-type were expected to have the same widths on the basis of the classical Debye screening length limitation.

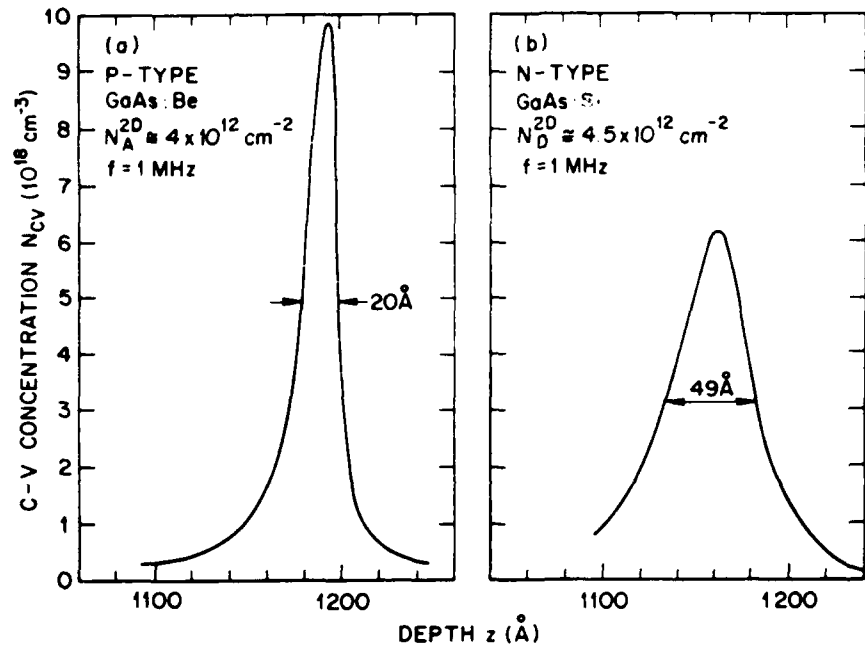


Fig. 1. Capacitance-Voltage profiles on (a) p-type and (b) n-type δ -doped GaAs. The Be and Si impurity density is 4×10^{12} and $4.5 \times 10^{12} \text{ cm}^{-2}$, respectively.

III. Resolution of Secondary Ion Mass Spectrometry

Secondary ion mass spectrometry (SIMS) is a well known structural technique to analyze impurity distributions in semiconductors. The increasing importance of spatially well defined doping profiles obtained during growth or by shallow ion implantation requires that the limitations of the SIMS technique are understood. In an effort to characterize the depth resolution of SIMS, δ -doped epitaxial layers were employed [2-5]. The purpose of these studies was twofold, i.e. (i) to optimize the measurement conditions (sputtering rate, sputtering angle, primary ion acceleration, etc.) and (ii) to determine the resolution under optimized measurement conditions.

The SIMS profile of a Be δ -doped GaAs film grown by molecular beam epitaxy is shown in Fig. 2. A narrow peak with a full width at half maximum of 29 \AA is measured at a depth of 200 \AA . The peak is the narrowest SIMS profile measured on a

III-V semiconductor. Even narrower peaks were obtained for isoelectronic monolayer doping, i.e. an AlAs monolayer embedded in GaAs [5].

The resolution of the SIMS technique is generally obtained by assuming that the shape of the profile is Gaussian. The symmetric Gaussian distribution is justified since the profile shown in Fig. 2 is symmetric. Provided that diffusion effects are negligible in the sample shown in Fig. 2, the profile shown is given by the resolution function of the technique. The resolution of the technique, Δz_R , is defined as twice the standard deviation of the Gaussian distribution, i.e., $\Delta z_R = 2\sigma_z$. Since the full width at half maximum is 2.36 times larger than the standard deviation of a Gaussian distribution, the resolution of our measurement under optimized conditions is $\Delta z_R = 25\text{\AA}$. The reproducibility of measurements with this resolution is good, i.e., spectra measured under identical conditions on the same sample have a width of $29\text{\AA} \pm 2\text{\AA}$.

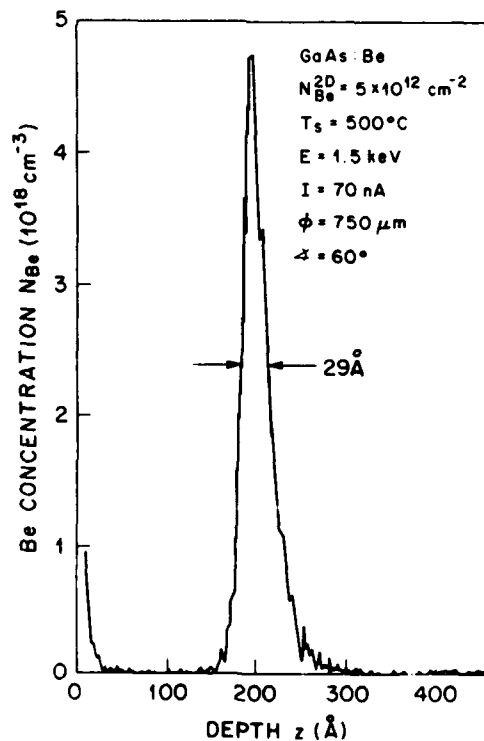


Fig. 2.

Secondary-ion mass spectrometry profile on epitaxial GaAs with a Be δ -doped layer 200Å below the surface. The following parameters are used for the MBE growth and the measurement: Growth temperature 500°C, primary-ion acceleration energy 1.5 keV, primary-ion current 70 nA, raster diameter 750μm, sputtering angle 60°.

If impurities diffused out of the δ -doped plane, the measured SIMS profiles broaden as well. Assuming that the impurity profiles are of Gaussian shape the measured width of the SIMS profile is given by

$$\Delta z_M^2 = \Delta z_D^2 + \Delta z_R^2, \quad (1)$$

where $\Delta z_D = 2\sigma_D$ is the width of the impurity profile after diffusion. The resolution $\Delta z_R = 25\text{\AA}$ and its reproducibility ($\pm 7\%$) are known. Therefore, we can determine the smallest impurity distribution width, i.e., diffusion length which can be determined by the technique. As an example we choose a diffusion length for impurities of $\Delta z_D/2 = \sigma_D = \sqrt{2D\tau} = 10\text{\AA}$ and obtain from Eq. (1) $\Delta z_M = 32\text{\AA}$ (FWHM = 38\AA) which represents a significant broadening of the profile as compared to the profile shown in Fig. 2. Thus, diffusion lengths of $\leq 10\text{\AA}$ can be clearly detected in our samples for the present optimized measurement conditions. This demonstrates that SIMS is presently the most sensitive structural method to determine impurity diffusion lengths in semiconductors.

IV. Conclusions

In conclusion, the fundamental limitations of the C-V and SIMS impurity distribution profiling techniques are analyzed. The resolution of the C-V technique is not limited by the Debye screening length in semiconductors with quantum confinement. Instead the resolution of the C-V technique is given by the spatial extent of the electron/hole wavefunction. Narrower C-V profiles are measured on p-type semiconductors due to the heavier mass of holes which results in spatially more confined wave functions. Profile width of a few tens of Angstroms are demonstrated. The SIMS technique has a resolution on the order of 20\AA for optimized measurement conditions, i.e. for low acceleration potential and shallow sputtering angle, low growth temperatures (500°C for GaAs), and for doping profiles in the proximity of the semiconductor surface.

- [1] E. F. Schubert, R. F. Kopf, J. M. Kuo, H. S. Luftman, and P. A. Garbinski, Appl. Phys. Lett. 57, 497 (1990).
- [2] R. B. Beall, J. B. Clegg, and J. J. Harris, Semicond. Sci. Technol. 3, 612 (1988).
- [3] A.-M. Lanzillotto, M. Santos, and M. Shayegan, Appl. Phys. Lett. 55, 1445 (1989).
- [4] E. F. Schubert, H. S. Luftman, R. F. Kopf, R. L. Headrick, and J. M. Kuo, Appl. Phys. Lett. 57, 1799 (1990).
- [5] H. S. Luftman, E. F. Schubert, and R. F. Kopf, to be published.

Incorporation of Arsenic in InP Layers and Heterointerfaces in GaInAs/InP Heterostructures Grown By Low-pressure Metalorganic Vapor Phase Epitaxy

Morio Wada, Katsutoshi Sakakibara and Yoichi Sekiguchi

Optical Measurement Technology Development Co., Ltd.

11-13 NAKA-CHO 2-CHOME MUSASHINO-SHI TOKYO, 180 JAPAN

1. Introduction

The growth of epilayers of III-V semiconductors by metalorganic vapor phase epitaxy (MOVPE) has made considerable advances in recent years, and the GaInAs/InP heterostructures have many applications in optoelectronic and high-speed devices. For a conventional MOVPE system with a single reactor, the same reactor is usually used for the growth of both InP and GaInAs layers. Most of the work has concentrated on the atomic roughness, disorder on the interface or thickness fluctuations with quantum wells (QWs), or fluctuation of gallium (Ga) composition x in $\text{Ga}_x\text{In}_{1-x}\text{As}$ for heterostructure growth¹⁻⁵. However, very little is known about the incorporation of arsenic (As) and Ga in InP layers, and the interfaces in the heterostructures, which exert the primary influence on the optical and electrical characteristics of heterostructure devices.

In this paper, we report on the investigation of compositional change in the InP layers in the thick GaInAs/InP double heterostructures and the structural imperfections at the well-to-barrier interfaces in the GaInAs/InP QWs grown by low-pressure MOVPE (LP-MOVPE).

2. Experimental procedures

The epilayers were grown on (100)InP substrates at 76Torr and 600-700°C in a conventional LP-MOVPE system with automatic pressure balancing and flow-balanced three-way valves for gas switching. The horizontal reactor chamber with a liner containing an RF-heated graphite susceptor is a cold-wall type. Triethylgallium (TEG), triethylindium (TEI), 20% arsine (AsH_3) and 40% phosphine (PH_3) in hydrogen are used as reactants.

To study the interfacial structure, multilayer single QW (SQW) structures consisting of 1-, 2.5-, 5-, 10- and 20-nm thick GaInAs wells, separated by 50-nm InP barriers were grown at 600°C, with and without growth interruptions at the well-to-barrier interfaces. The thicknesses of the wells were deduced from the steady-state growth rate and the satellite structures of the X-ray diffraction from the MQW structures, and were determined from secondary electron microscope images and in-depth profiles of secondary ion mass spectroscopy (SIMS). To study effects of As and Ga incorporation, the single heterostructure sample and the double heterostructure (DH) samples were prepared with various growth conditions and schedules previously described in detail⁶.

3. Results and Discussion

Figure 1 shows the 4.2-K PL spectra of the multilayer SQW samples grown without interruptions (QE41), and with interruptions, using PH_3 purge with a flow rate of 1slm for 2s (SW43) and for 30s (SW44) after the growth of the GaInAs wells. The full widths at half-maximum (FWHMs) of the PL spectra are

shown in Fig.2. Figure 3 is a plot of the energy shifts versus well thickness. The solid lines are calculations for optical transition energies, assuming that the interfacial layers are 0-3 monolayer (ML) thick InAs layers and are grown coherently. The calculations were carried out using finite square wells based on the Kronig-Penny model with a band offset of 40%. The increase and local variation of the InAs thickness at the well-to-barrier interfaces can explain the quantitative behavior of PL spectra for the QWs. The increase of the InAs thickness for thick GaInAs wells can lead to a large energy shift of ground-state energy on account of the effect of high confinement for heavy holes as shown in Fig.4.

For long growth time, the possible roles of As (and Ga) incorporation in InP layers must be taken into account. Figure 5 shows the in-depth SIMS profiles of the upper InP layer for two DH samples grown after the growth of 1.4- and 2.8- μm thick GaInAs layer at 600°C without growth interruptions. The As and Ga incorporation in the upper InP layers is apparent. Figure 6 shows X-ray rocking curves (XRCs) from the DH sample. Broadened peaks from the upper InP layer with the lattice mismatch ($\Delta a/a$) = $5-8 \times 10^{-4}$ were always observed. The lattice mismatches of the upper InP layers, obtained from XRC measurement, did not depend on those of the GaInAs layers within this range. By increasing the total flow rate, and with the high V/III ratio for the upper InP layer and the low V/III ratio for the GaInAs layer, the measured lattice mismatch decreased. The As and Ga incorporation in the upper InP layer obtained by SIMS analysis decreased with the increase in growth temperature and with the decrease in the GaInAs thickness. The measured lattice mismatches of the InP layers reasonably agree with the calculations with a kinematical step model using the As and Ga concentrations in the InP obtained by SIMS analysis^{6,7}. These results indicate that the observed incorporation is not attributed to compositional allowing or structural imperfection at the heterointerfaces owing to flow transients, but arises from the presence of residual As and Ga associated with both desorption and diffusion of their outgassing sources in the reactor.

The PL peak energies of the upper InP layers measured at 77K were lower than the PL energy of an InP homoepitaxial layer by 20-50meV and gradually increased with the increase in the thickness of the upper InP layers. This may be explained from the change in the energy band gap E_g of the InP layer caused by this incorporation. This incorporation also influences the characteristics of optical devices. Figure 7 shows the responsivities of PIN photodiodes with 0.1- and 0.7- μm thick InP cap layers fabricated by LP-MOVPE. The absorption edge of the thinner InP cap layer shifts to lower energy by 90-100meV. This value is very large in comparison with the optical band gap difference of 30-40meV between Zn-doped p⁺- and undoped InP.

4. Conclusion

We have investigated the properties of the InP layers grown sequentially after GaInAs growth by LP-MOVPE. It was found for the first time that the As

(and Ga) incorporation in InP occurred for an extended period during InP growth after the AsH₃ and TEG flows were stopped, resulting in the changes in the lattice parameter and band-gap energy of the InP layer. For QWs grown without interruptions, the interfacial layer caused by substituting of As atoms from phosphorus (P) at the well-to-barrier interfaces significantly changes the PL energy shifts.

References

1. T.Wang, K.L.Fry, A.Persson, E.H.Reihlen and G.B.Stringfellow: Appl. Phys. Lett. 54(1988)290.
2. D.Grutzmacher, K.Wolter, H.Jurgensen and P.Balk: Appl. Phys. Lett. 52 (1988) 872.
3. K.W.Carey, R.Hull, J.E.Fouquet, F.G.Kellert and G.R.Trott: Appl. Phys. Lett. 51(1987)910.
4. B.I.Miller, E.F.Schubert, U.Koren, A.Ourmazd, A.H.Dayem and R.J.Capik: Appl. Phys. Lett. 49(1986)1384.
5. M.Razeghi, Ph.Maurel, F.Omnes and J.Nagle: Appl. Phys. Lett. 51(1987) 2216.
6. M.Wada, M.Seko, K.Sakakibara and Y.Sekiguchi: Jpn. J. Appl. Phys. 29 (1990) 2342.
7. D.B.McWhan, M.Gurvitch, J.M.Rowell and L.R.Walker: J. Appl. Phys. 54 (1983) 3886.

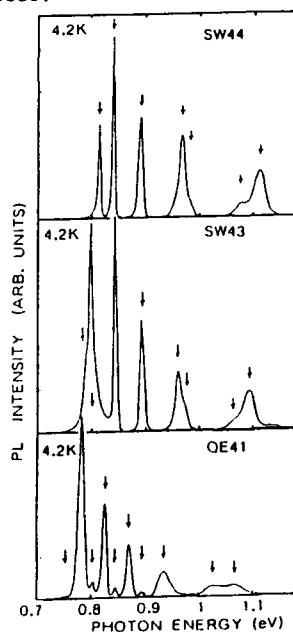


Fig.1 4.2-K PL spectra of QWs for. Arrows indicate the observed PL peak positions.

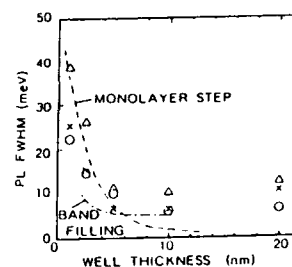


Fig.2 PL FWHM versus well thickness obtained from the spectra in Fig.1.

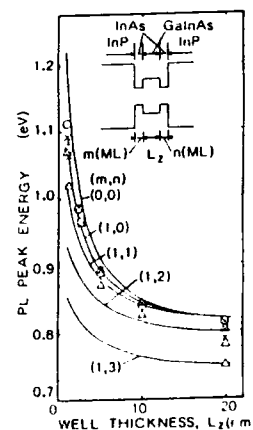


Fig.3 Plot of measured PL peak energies against well thickness (L_z) for samples QE41(Δ), SW43(x) and SW44(O). Solid lines represent PL energies calculated for Qws with and without InAs interfacial layers. The inset schematically illustrates the energy band of the QW structure used in the calculations.

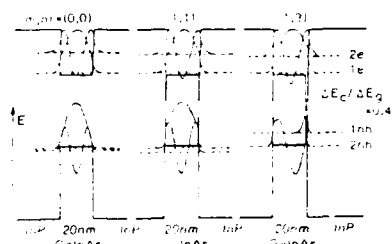


Fig. 4 Conduction- and valence-band potential profiles and confined quantum states for electron and heavy hole in the QW structure, consisting of a 20-nm GaInAs well and InAs interfacial layers. The letters m and n represent the numbers of InAs MLs at the barrier-to-well and well-to-barrier interface, respectively.

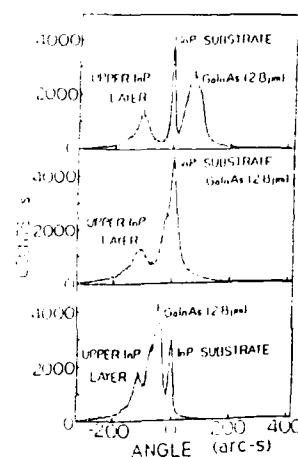


Fig. 6 XRCs for the DH samples measured at three locations spanning the 12-mm length along the gas flow direction. The lattice mismatches of the GaInAs layer and of the upper InP layer ranges from -6×10^{-4} to 4×10^{-4} and from 5×10^{-4} to 8×10^{-4} , respectively.

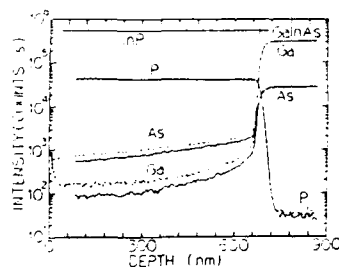


Fig. 5 In-depth SIMS profiles of Ga, As and P of the upper InP layers in the DH samples with (the dotted lines) a 2.8- and (solid lines) a 1.4-μm thick GaInAs layers.

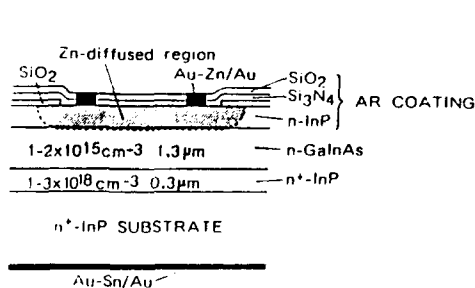
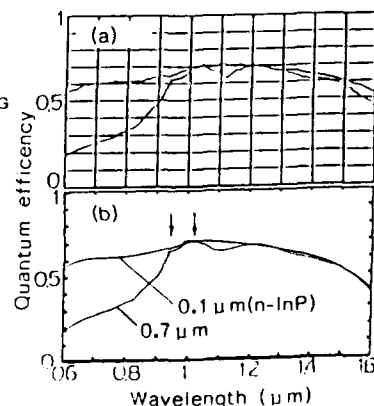


Fig. 7 Schematic drawing of the PIN photodiode and external spectral quantum efficiencies measured on a 380 μm-diam PIN photodiode (a), and calculated by solving the basic transport equations with considering the transmittance of an antireflective (AR) coating consist of SiO₂, Si₃N₄ and an n-InP upper layer (b). Arrows indicates the absorption edges of the upper InP layers used in the calculations.



IN SITU OPTICAL CHARACTERIZATION AND CONTROL OF EPITAXIAL III-V CRYSTAL GROWTH

W. E. Quinn

Bellcore
m/s 3Z-201
331 Newman Springs Rd.
Red Bank, NJ 07701-7040

Introduction

Device designers are placing new demands on crystal growers by requesting increasingly complex structures with more stringent constraints on composition, layer thickness and interface abruptness. Post growth analysis is no longer sufficient to meet these constraints and efforts are now underway to develop real time methods of monitoring and controlling crystal growth.

A number of diagnostic techniques are available for studying semiconductor surfaces during the growth process. Optical methods are preferred because they may be used at atmospheric pressure, in any transparent medium, and the photon flux is low so that the growth process is not disturbed. However, optical techniques have a limited spectral range, and low surface sensitivity. Fortunately, the 1.5 to 6 eV energy range of quartz-optics systems contains most of the bonding-antibonding transitions for materials used in the growth of III-V semiconductors. Recently, the surface sensitivity problem has been solved by techniques such as reflectance-difference spectroscopy (RDS)¹⁻³, which takes advantage of intrinsic symmetries to suppress the dominant bulk component of the optical signal. Classical probes such as spectroellipsometry (SE)⁴⁻⁸ which provide information over the penetration depth of light have advantages in growth control applications, where film thickness and compositions are obtained by integration over space.

In this paper we will briefly summarize our RDS characterization results and give a discussion of our SE based growth control system.

Reflectance-Difference Spectroscopy

Reflectance-difference spectroscopy is a normal incidence optical probe that takes advantage of symmetry to enhance the ordinarily weak contributions from the surface and to suppress the ordinarily dominant contributions from the bulk. The difference between normal-incidence reflectances for light polarized along the two principal optical axis in the plane of the surface is determined as a function of surface conditions and photon energy. In cubic materials the bulk contributions cancel in subtraction. Contributions from randomly oriented surface species also cancel, leaving only those contributions from species that are in registry (having reacted) with the underlying crystal lattice. Thus RDS is suited to provide information about surface chemistry.

Initial studies of (001) GaAs surfaces during MBE growth showed that RDS is sensitive to both structural and chemical information.⁹⁻¹² Figure 1 shows typical RHEED (top) and RD (bottom) responses for an As stabilized (2x4) to Ga stabilized (4x2) to As stabilized (2x4) (001) surface reconstruction generated by interrupting the As flux during the growth of GaAs at a rate of 1 GaAs monolayer per 4.6 s. As soon as the As flux is terminated, the RD signal begins to change nearly linearly in time and saturates when one monolayer of Ga has been accumulated. Recalling that RDS is sensitive only to surface species that have reacted with and are in registry with the surface, the RD signal implies that the excess Ga atoms are immediately forming Ga-Ga dimer bonds and that the 2.48 eV RD signal is following the chemistry of the growth surface. The 3.54 eV RD signal is similar to the RHEED signal shown above it. At this photon energy the RD signal and RHEED are determined by surface structure.

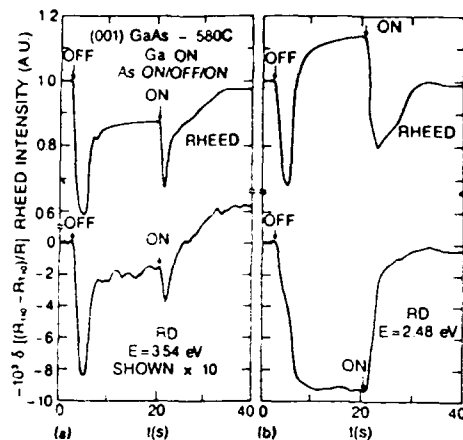


Fig. 1. Simultaneously measured RHEED and RD transients for a single As-to-Ga-to-As surface stabilization. RD photon energy (a) 3.54 eV and (b) 2.48 eV (after ref. 12).

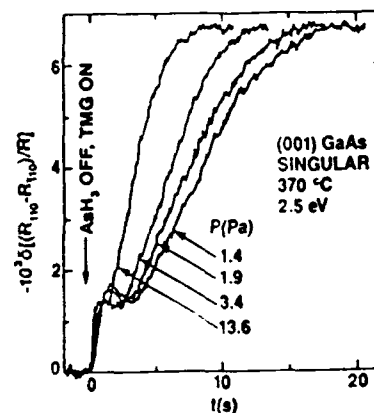


Fig. 2. Time dependence of RD signals at 2.5 eV for GaAs in an OMCVD reactor upon initiation of TMG exposure at $t=0$ (after ref. 14).

OMCVD results for the (001) GaAs-trimethylgallium-arsine system provided the first microscopic information about crystal growth by OMCVD.¹³⁻¹⁵ Figure 2 gives the 2.5 eV RD signal observed upon switching the gas composition in contact with an (001) GaAs substrate from H_2 containing AsH_3 to H_2 containing four different partial pressures of trimethylgallium (TMG), as indicated. The RD signal saturates at a common value regardless of the TMG pressure, which indicates a surface-site-specific mechanism that is arrested after the sites have been consumed. The time dependence is linear to about 80% coverage and exponential thereafter. The time, temperature and pressure dependences of the coverage show OMCVD growth to be kinetically limited by a combination of excluded volume chemisorption (at -26 kcal/mole) and subsequent irreversible decomposition (at 39 kcal/mole) of TMG at surface sites. Apparent activation energies will be a blend of these two values and range from a minimum of 13 kcal/mol near zero occupancy to a maximum of 39 kcal/mol at 100% occupancy.

Spectroellipsometry

Ellipsometry is a highly accurate method of measuring optical properties of a sample which are determined by composition and the number and thickness of layers, among others factors. Our experiments were performed in Organometallic-MBE chamber fitted with ellipsometry ports and Studna windows with an angle of incidence near 70° .

Using SE^{8,9} we obtain information on the near surface composition x of epitaxial $Al_x Ga_{1-x} As$ layers during growth from triethylaluminum (TEA), triethylgallium (TEG) and arsine and use this information to control the flux of TEA to the growth surface. The basic control principle can be understood by considering the dielectric response of bulk GaAs and optically thick layers of $Al_x Ga_{1-x} As$ with $x=0.095$, 0.14 and 0.36 as shown in Fig. 3. At 2.6 eV and $600^\circ C$, $\epsilon_2(x) = \epsilon_{2s} - 16.9x - 0.33x^2$, where $\epsilon_{2s} = \epsilon_2(0)$ is the dielectric function of GaAs measured at the beginning of each run. We use this expression to convert x to a target value ϵ_{2t} of ϵ_2 , then use the difference $(\epsilon_2 - \epsilon_{2t})$ to generate a correction to the voltage of the proportional valve metering the TEA into the chamber, thereby controlling x .

Figure 4 shows the trajectories (ϵ_2) vs (ϵ_1) with time as the running variable for two separate layers of $Al_x Ga_{1-x} As$ on GaAs. The dotted curve shows the trajectory when the control valve is set to a nominal value and not adjusted. The solid curve shows the trajectory when the control voltage to the TEA valve is set to

half the value required to reach the target value of x (and ϵ_{2f}). In both cases the trajectories start at the dielectric function of the substrate and converge to the limiting dielectric function of the film as the films

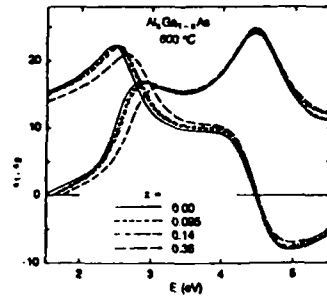


Fig. 3. Dielectric functions of $\text{Al}_x\text{Ga}_{1-x}\text{As}$ and GaAs for $x = 0.095, 0.14$ and 0.36 at 600°C (after ref. 7).

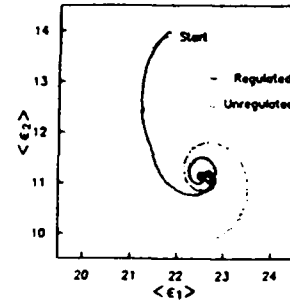


Fig. 4. Dotted line: control data for $\langle \epsilon_2 \rangle$ with TEA flow fixed throughout shown 20 min. of data. Solid line: closed loop control starting with TEA flow about half that required to react ϵ_{2f} (after ref. 8).

become optically thick. The performance of our system can be seen in Figs. 5, which show the final 40 minutes of the data from Fig. 4 on greatly expanded scales. For the regulated case, Fig 5(a) shows the convergence of the spiral to the target value of ϵ_{2f} to within the noise limit of the ellipsometer, an equivalent precision of ± 0.001 in x . The unregulated data show a drift of $\langle \epsilon_2 \rangle$ about the target value, indicating a drift in x of about 0.003 toward increasing Al content.

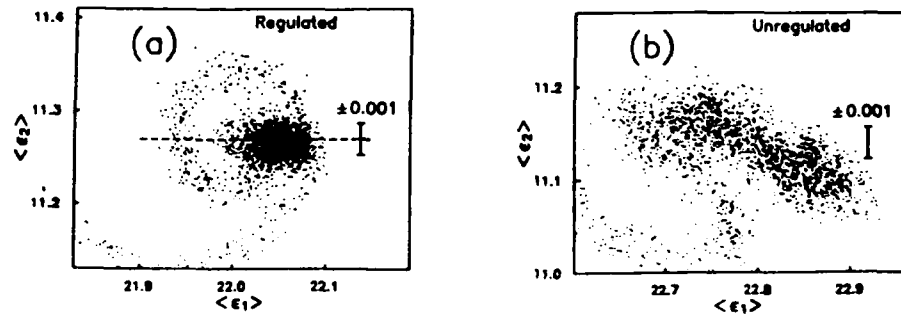


Fig. 5. 40 min. continuations of regulated (a) and unregulated (b) trajectories of Fig 4. (after ref. 8).

The above results demonstrate the feasibility of the control scheme; improvements are needed for practical applications. The precision to which we can maintain ϵ_2 exceeds the current accuracy of our system. We also need to implement a system that allows sample rotation (which will allow us to obtain RDS and SE simultaneously), and we need to develop multiwavelength capability to deal with a wider range of materials. Work in these areas is continuing.

I gratefully acknowledge the assistance of my collaborators, D. E. Aspnes, S. Gregory, J. P. Harbison, L. T. Florez, A. A. Studna, R. Bhat, E. Colas, M. A. Koza and V. G. Keramidas.

REFERENCES

1. D. E. Aspnes and A. A. Studna, Phys. Rev. Lett. **54**, 1956 (1985).
2. D. E. Aspnes and A. A. Studna, J. Vac. Sci. Technol. **A5**, 546, (1987).
3. D. E. Aspnes, J. Vac. Sci. Technol. **B3**, 1498 (1985).
4. T. Stehlin, M. Feller, P. Guyot-Sionnest and Y. R. Shen, Optics Lett. **13**, 389 (1988).
5. D. E. Aspnes in Optical Properties of Solids, New Developments, ed. B. O. Seraphin (North-Holland, Amsterdam, 1976), p799; Thin Solid Films **89**, 249 (1982).
6. J. B. Theeten, F. Hottier, and J. Hallis, J. Cryst. Growth **46**, 245 (1979); F. Hottier, J. Hallis and F. Simondet, J. Appl. Phys. **51**, 1599 (1980).
7. D. E. Aspnes, W. E. Quinn and S. Gregory, Appl. Phys. Lett. **56**, 2569 (1990).
8. D. E. Aspnes, W. E. Quinn and S. Gregory, Appl. Phys. Lett. **57**, 2707 (1990).
9. D. E. Aspnes, J. P. Harbison, A. A. Studna and L. T. Florez, Mat. Res. Soc. Symp. Proc. **91**, 57 (1987).
10. D. E. Aspnes, J. P. Harbison, A. A. Studna and L. T. Florez, Phys. Rev. Lett. **59**, 1687 (1987).
11. D. E. Aspnes, J. P. Harbison, A. A. Studna and L. T. Florez, J. Vac. Sci. Technol. **B6**, 740 (1988).
12. D. E. Aspnes, J. P. Harbison, A. A. Studna and L. T. Florez, J. Vac. Sci. Technol. **A6**, 1327 (1988).
13. E. Colas, D. E. Aspnes, R. Bhat, A. A. Studna, M. A. Koza and V. G. Keramidas, J. Cryst. Growth **94**, 613 (1989).
14. D. E. Aspnes, R. Bhat, E. Colas, L. T. Florez, J. P. Harbison, M. K. Kelly, V. G. Keramidas, M. A. Koza and A. A. Studna, Inst. Phys. Conf. Ser. **96** 283 (1988).
15. D. E. Aspnes, R. Bhat, E. Colas, V. G. Keramidas, M. A. Koza and A. A. Studna, J. Vac. Sci. Technol. **A7**, 711 (1989).

Selective Epitaxial Growth of AlGaAs by MOCVD Using Dialkylmetalchloride

Ko-ichi YAMAGUCHI and Kotaro OKAMOTO

University of Electro-Communications

1-5-1, Chofuga-oka, Chofu-shi, Tokyo 182, Japan

1. Introduction

Selective epitaxial growth by metalorganic chemical vapor deposition (MOCVD) is expected to be one of the important technologies to fabricate microstructures of semiconductor devices. Recently, selective epitaxial growth has been applied to fabricate quantum well wire's.¹⁾ In the fabrication of such a fine structure, good selectivity of deposition and excellent controllability of the ultrafine structure of epilayers is required. Many studies concerning to the selective epitaxial growth of III-V compound semiconductors by MOCVD have been reported.²⁾⁻¹⁰⁾ We investigated the selective epitaxial growth of GaAs and AlGaAs by atmospheric pressure (AP)-MOCVD using TMGa and TMAI.⁷⁾⁻⁹⁾ It was found that, in order to suppress the polycrystal deposition on masks, it is important to keep (1) substrate temperature high, (2) growth rate low, (3) mask width narrow, and (4) mask surface smooth (polycrystal deposition decreased on the mask surfaces treated by atom-beam irradiation⁶⁾). As a result, complete selective epitaxial growth of GaAs was achieved without polycrystal deposition on the SiO₂ mask when the width of the stripe mask was less than 150 μm .⁸⁾ However, the polycrystal deposition was always observed for the growth of epilayers containing aluminum species under AP conditions, and one method to suppress the polycrystal deposition was to carry out the selective epitaxial growth under low pressure (LP) condition.⁴⁾

Recently, some results concerning to the selective epitaxial growth of GaAs by using diethylgalliumchloride (DEGaCl) have been reported and the suppression of the

polycrystal deposition on masks has been much improved.⁵⁾ We have also investigated the selective epitaxial growth of AlGaAs by using DEGaCl and diethylaluminumchloride (DEAlCl), and high selectivity of the deposition has been attained even for the higher Al content under AP condition.⁹⁾ The improvement of the selectivity of deposition is explained by reevaporation enhancement (REE) effect. By REE, step-flow-mode growth is also carried out on the selective epilayers,¹⁰⁾ and an extremely thin epilayers obtained by the step-flow-mode growth can be applied to fabricate fine structures of quantum-size-effect devices.

In this article, the selectivity of deposition of GaAs and AlGaAs by using DEGaCl and DEAlCl will be described and the growth structures of the selective epilayers grown on vicinal surfaces will be also discussed.

2. Selective Epitaxial Growth of Al_xGa_{1-x}As by Using DEGaCl and DEAlCl

The surface morphologies of Al_xGa_{1-x}As selective epilayers and the polycrystal depositions are shown in Fig.1. The substrate temperature was 670°C for GaAs ($x=0$) and 730°C for AlGaAs ($x \neq 0$). The epitaxial growth rates were 0.023 $\mu\text{m}/\text{min}$ ((a)), 0.020 $\mu\text{m}/\text{min}$ ((b)), 0.017 $\mu\text{m}/\text{min}$ ((c)) and 0.016 $\mu\text{m}/\text{min}$ ((d)), respectively. In case of GaAs and Al_{0.18}Ga_{0.82}As, the polycrystal deposition on the SiO₂ masks was not observed completely. In case of high Al composition of 0.43 and 0.73, a slight deposition of the polycrystals was observed on the SiO₂ masks, but the selectivity of deposition becomes high

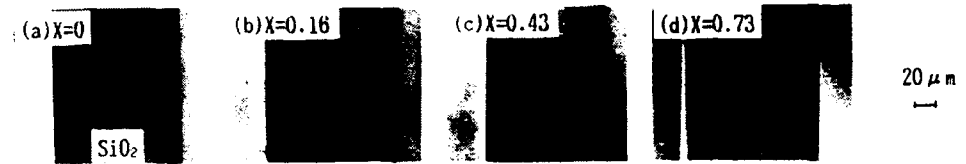


Fig.1. Photomicrographs of selective AlGaAs epilayers and polycrystals depositing on SiO₂ masks.

drastically in comparison with the selective epitaxial growth by using TMGa and TMAI. The high selectivity was caused by the REE effect due to GaCl and AlCl species on the mask surfaces.

Figure 2 shows the SEM photographs of selectively grown epilayers of GaAs ((a)) and Al_{0.16}Ga_{0.84}As ((b)). The GaAs epilayers were flat and ridge growth was never observed. On the other hand, in case of the selective epitaxial growth of AlGaAs, the ridge growth occurs and the undulation was observed on the side surfaces. These results suggest that the surface residence time of AlCl species is longer than that of GaCl species.

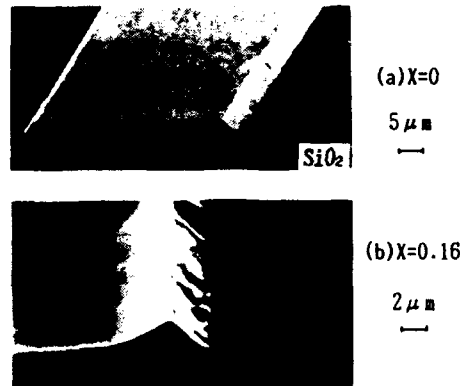


Fig.2. SEM photographs of selective AlGaAs epilayers.

3. Selective Epitaxial Growth on Vicinal Surfaces

The REE effect due to GaCl and AlCl species is also expected to occur on the epilayer surfaces. Therefore, REE effect suppresses

not only deposition of polycrystals on masks but also occurrence of two-dimensional (2D) nucleations on terrace areas of an epilayer, and, as a result, step-propagation mode is enhanced. In this section, the selective epitaxial growth of GaAs by using DEGaCl was carried out on the (100) vicinal surfaces.

Figure 3 shows the photographs of the two typical surface morphologies of GaAs epilayers selectively grown on circularly patterned window areas. The substrates are (100) misoriented in [010] direction and the nominal misorientation angle is 2°. The substrate temperature and the growth rate were 590°C and 0.055 μm/min ((a)), and 730°C and 0.019 μm/min ((b)), respectively. In case of the growth condition (a), the ridge growth extends mainly in [011] and [01̄1] directions from the mask edges (type I). However, in case of the growth condition (b), the extension of the ridge growth in the <011> direction is not clearly observed, and extremely flat surfaces indicated by arrow L₂ appear in the [010] off-angle direction (type II). The morphology of type II is easier to appear for higher substrate temperature and lower growth rate. The transition temperature from type I mode to type II mode decreased with increase in the amount of the off angle.⁽¹⁰⁾ Therefore, it is considered that the appearance of the surface morphology of type II is due to the occurrence of the step-flow mode.

Next, figure 4 shows the relationships between the transition temperature from type I mode to type II mode and the Al composition. The epitaxial growth rate was always kept at 0.088 ± 0.008 μm/min. The transition tempe-

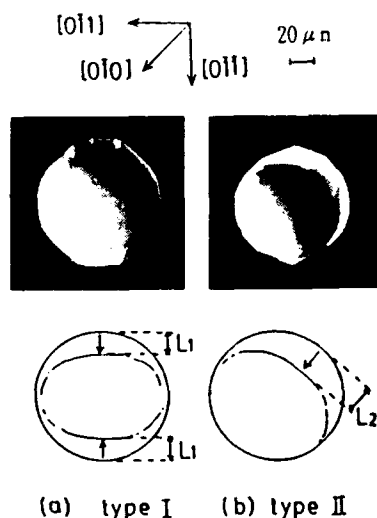


Fig.3. Photomicrographs of selective GaAs epilayers.

rate increases with increasing the Al composition. Although aluminum species are easier to bring about 2D nucleation on the terrace area than Ga species, in case of dialkylmetalchloride sources, the surface morphologies of type II were observed in a wide range of the growth conditions.

Figure 5 shows the photomicrographs of the surface view and (011) cross-sectional view of GaAs selective epilayers grown under the condition of the step-flow mode mentioned above. The off angle of the substrates is 2° in [011] direction, and the edges of the stripe shaped mask are aligned along [011] direction. The extremely flat surfaces are observed extending in the off-angle direction ([011]) from a mask edge. The inclination angle between the flat surface of the epilayer and the substrate surface is about 2° , and the flat surface is identified as an exactly (100)-oriented plane. Followings become apparent from the above results. First, the terraces extend in the downstream direction (Fig.5(c)). Second, as the terrace length becomes longer, 2D nucleation is apt

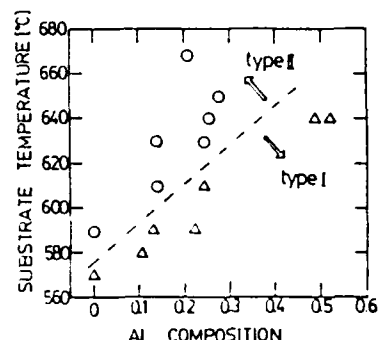


Fig.4. Al composition dependences of growth mode of selective AlGaAs epilayers.

to occur on the terrace because the surface concentration of the reactant species in the central part of the extended terrace overcomes a critical value for 2D nucleation (Fig.5(d)). That is, when the length of the terrace starting from the 2D nucleus exceeds a critical value, 2D nucleation begins to occur on the new terrace and, hereafter, the repetition continues and the selective

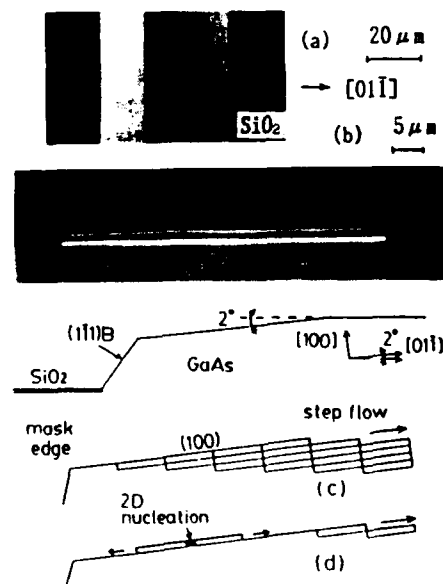


Fig.5. Photomicrographs of over view (a) and cross-sectional view (b) of selective GaAs epilayers, and schematic diagrams of step propagation ((c),(d))

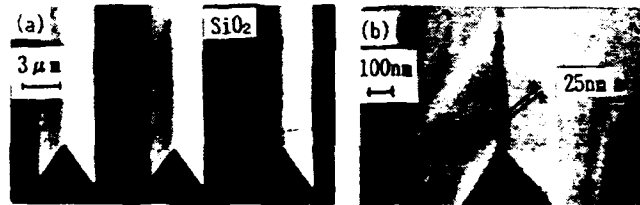


Fig.6.
SEM photomicrographs of selective GaAs epilayers grown on 4 μ m-width grating patterned substrate.
(a) $\times 3000$, (b) $\times 50000$

epilayer departing from the upstream edge extends in the downstream direction.

4. Selective Epitaxial Growth

of Fine Structures

By using dialkylmetalchloride, not only the polycrystal deposition on the masks but also 2D nucleation on the terrace can be suppressed effectively. So that, this growth technique can be applied to prepare fine structures such as the quantum well wire's.

Figure 6 shows the SEM photographs of selective epilayers grown on the stripe-mask patterned substrates (the stripes are aligned along $\langle 011 \rangle$). The substrate temperature and the epitaxial growth rate on the unmasked substrates was 730°C and 0.0071 μ m/min, respectively. It is well known that $\{111\}$ B facets appear on the both side surfaces of stripe shaped epilayers. However,

both of $\{111\}$ B facets do never cross at the top of the triangle-shaped epilayer for sufficiently long growth time (Fig.6(b)). The width of the remaining flat top area was about 25 nm. The dependence of the width of the top flat surfaces on the growth time is shown in Fig.7, and the width becomes almost constant after the growth time goes over 100 min.

5. Conclusion

We investigated the selective epitaxy of AlGaAs by AP-MOCVD using DEGaCl and DEAlCl. and high selectivity of deposition was obtained even at a high Al composition. The reactant species were easily to reevaporate not only on the mask surfaces but also on the terrace surfaces. So that, the step-flow-mode growth could occur dominantly without occurrence of 2D nucleations on the terraces. This growth technique is available to fabricate the fine structures of AlGaAs/GaAs devices.

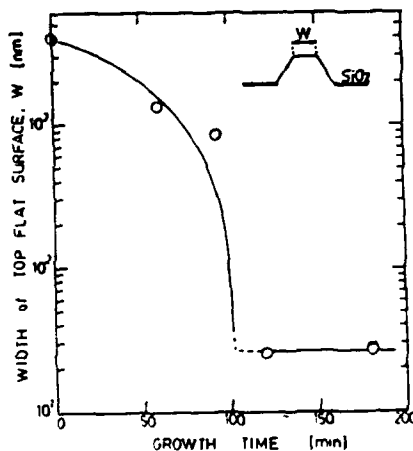


Fig.7. Relationships between growth time and width of top flat surface.

References

- 1) T. Fukui and S. Ando : *Electro. Lett.* 25 (1989) 410.
- 2) R. Azoulay, M. Bouadma, J. C. Bouley and L. Dugrand : *J. Cryst. Growth* 55 (1981) 229.
- 3) N. Oishi and K. Kuroiwa : *J. Electrochem. Soc.* 132 (1985) 1209.
- 4) K. Nason, S. Takagishi and N. Mori : *Jpn. J. Appl. Phys.* 25 (1986) L10.
- 5) T. F. Kuech, M. A. Tinchler and R. Potemski : *Appl. Phys. Lett.* 54 (1989) 910.
- 6) Y. D. Galeuchet, P. Roentzen and V. Graf : *J. Appl. Phys.* 68 (1990) 580.
- 7) K. Yamaguchi, K. Okamoto and T. Imai : *Jpn. J. Appl. Phys.* 24 (1985) 1868.
- 8) K. Yamaguchi and K. Okamoto : *Jpn. J. Appl. Phys.* 28 (1989) L1489.
- 9) K. Yamaguchi and K. Okamoto : *Jpn. J. Appl. Phys.* 29 (1990) 1408.
- 10) K. Yamaguchi and K. Okamoto : *Jpn. J. Appl. Phys.* 30 (1991) L231.

**Selective Growth of InP/GaInAs Heterostructures
Using Metalorganic Molecular Beam Epitaxy**

Y. L. Wang, A. Feygenson, R. A. Hamm, D. Ritter,
J. S. Weiner, H. Temkin, and M. B. Panish

AT&T Bell Laboratories
Murray Hill, New Jersey 07974

SUMMARY

Selective area growth is used in the fabrication of Si epitaxial devices such as bipolar transistors. This growth technique facilitates the preparation of very complex self-aligned and buried transistor structures. Selective growth has been investigated in the III-V materials, without, however, any significant results pertaining to the optical or electrical quality of the material grown, or device results.

In this work, we investigate selective growth of InP and GaInAs on SiO₂-masked InP substrates using metalorganic molecular beam epitaxy (MOMBE). Group III and V elements are derived from triethylgallium and trimethylindium, and AsH₃ and PH₃ respectively. Excellent selectivity is achieved in the temperature range from 510 to 540 °C.

Dielectric masks (4000 Å thick SiO₂) are deposited on either n type or Fe-doped semi-insulating (100) InP wafers by plasma enhanced chemical vapor deposition at 300 °C. Patterns of rectangles and stripes with varying widths are defined by standard photolithography. After removing the photoresist with acetone, the substrates are cleaned

in low power oxygen plasma. We find that thorough removal of organic residue from the substrate is essential for achieving high selectivity. In order to achieve high quality growth of materials within the openings, the substrates are further cleaned by a novel process designed for removing a thin layer of foreign substance from InP surface. This consists of an exposure to 200 eV Ar ($1 \times 10^{16} \text{ cm}^{-2}$) beam followed by Cl_2 (3×10^{-4} Torr) etching at 200 °C. This process has been shown to prepare a high quality, damage free surface for high quality epitaxial growth [1].

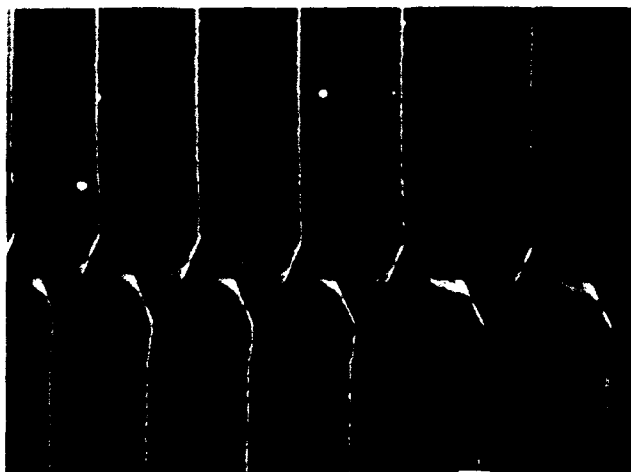


Fig. 1. SEM micrograph of selectively grown InP/GaInAs/InP (150 Å/2500 Å/5000 Å) stripes. Scale bar is 1 μm .

The morphology of the epitaxial layer inside the window is excellent (Fig. 1), however, the growth rate at the window edge is faster than at the center, and the epitaxial layer has different faceting depending on the window orientation with respect to the crystal axis. GaInAs grown into stripes wider than 5 μm shows high cathodoluminescence efficiency at room temperature. The cathodoluminescence spectra (Fig. 2) at 25 °K exhibit

both a red shift and reduced intensity as the stripe width decreases from $13\text{ }\mu\text{m}$ to $1.9\text{ }\mu\text{m}$. The former indicates an increase in the In to Ga ratio, and the latter is the result from the increasing fractional volume of edge materials.

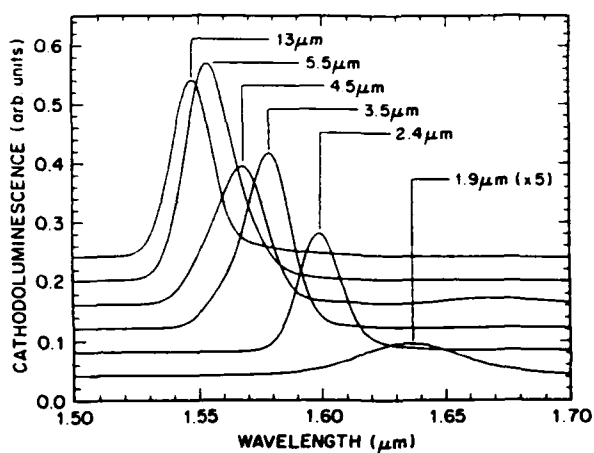


Fig. 2. Cathodoluminescence spectra (25 °K) from stripes of various width. Same structure as shown in Fig. 1.

Selectively grown GaInAs/InP p-n junctions exhibit excellent electrical characteristics ($n < 1.2$) after removal of about $1\text{-}2\text{ }\mu\text{m}$ of the window edge material (Fig. 3). This result together with the observed high cathodoluminescence indicates that the selectively grown materials, excluding the edges, are comparable in quality to the materials grown on broad area. Preliminary results from heterostructure bipolar transistors prepared by such techniques show excellent emitter characteristics and current gains similar to conventionally grown devices. The possibility of using such techniques for the fabrication of buried heterostructure laser will be discussed.

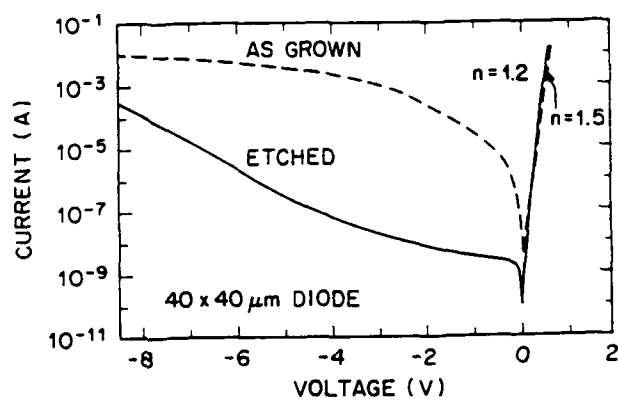


Fig. 3. I-V characteristics of selectively grown GaInAs/InP p-n junctions before and after removal of the window edge materials.

Reference

1. Y. L. Wang, H. Temkin, L. R. Harriott, R. A. Hamm, and J. S. Weiner, Appl. Phys. Lett., 57 (1990) 1672.

In Situ Mass Spectrometric Analysis of the Mechanism of Selective-Area Epitaxy by MOMBE

Y. Ohki and Y. Hiratani

Optoelectronics Technology Research Laboratory
5-5 Tohkodai, Tsukuba, Ibaraki 300-26, JAPAN

Introduction

To understand the growth mechanism of metal-organic molecular beam epitaxy (MOMBE), an analysis of the chemical species involved in the growth reaction was made by in situ mass spectrometry.¹⁻⁴⁾ We have reported that the decomposition of metal-organics (MO's) is largely affected by the surface material.^{3,4)} Hence, it is expected that selective-area epitaxy can be carried out by utilizing the difference between the reaction characteristics on a bare semiconductor surface and those on a masked surface.

In this paper we report on the results of mass spectrometric measurements of the species desorbed from various substrates under MOMBE growth conditions. Preliminary results for a novel in situ selective-area epitaxy of GaAs using a thin oxide layer of GaAs as a mask is also presented.⁵⁾

Apparatus

Figure 1 shows a schematic illustration of the MOMBE system used in this experiment. This system comprises three chambers: a sample introduction chamber, a main chamber and a quadrupole mass spectrometer (QMS) analyzer chamber. The introduction chamber is used for wafer loading. An oxygen gas line and an argon-ion (Ar^+) gun are also attached to the chamber for the oxidation of the GaAs surface and for patterning the oxide, respectively. The main chamber has nozzles for MO's and a K-cell for an arsenic source, and is used for both initial surface cleaning and the epitaxial growth of GaAs. The QMS analyzer chamber has a liquid-nitrogen cooled sampling aperture and shroud assembly. By using this cold

sampling aperture, the QMS analyzer detects mainly species desorbed from the substrate surface.

Results and Discussion

(1) Analysis of the desorbed species

The species desorbed or reflected from the substrate surface when TMG was exposed to the substrate were measured as a function of the substrate temperature. A quartz wafer and a (100) semi-insulating GaAs wafer, both 5 cm in diameter, were used as substrates. Figure 2 shows the detected signal intensity of Ga^+ ions desorbed from a quartz substrate (open circles) and that from GaAs (closed circles) versus the substrate temperature. The Ga^+ signal from the GaAs surface dropped above 350 °C, indicating that thermal decomposition of TMG took place on the surface, and that the resulting Ga atoms were incorporated in the epitaxial layer. On the other hand, the Ga^+ signal from quartz showed a gradual decrease, which was caused by a decrease in the ionization probability in the QMS due to an increase in the velocity of reflected TMG molecules with substrate temperature. It is thus concluded that TMG does not decompose on a quartz surface.

These results can explain the reported characteristics of selective-area epitaxy by either MOMBE,⁶⁾ or very low-pressure (<1 Torr) metal-organic vapor phase epitaxy:⁷⁾ the absence of both edge growth (abnormally high growth rate at the pattern edge) and polycrystalline deposition on the mask surface. Since the incident TMG was reflected from the quartz surface without decomposition, there was no chance to form polycrystalline deposition on the mask surface. Edge growth, which is caused by a migration of Ga-species on the mask surface to the growth region, was also absent.

(2) Selective-area epitaxy using GaAs oxide mask

We have proposed a novel in situ selective-area epitaxy technique using a thin oxidized layer of GaAs as a mask material (GaAs oxide mask).⁵⁾ Figure 3 shows the intensity of the Ga^+ signal versus the substrate temperature when TEG was exposed to

the GaAs wafers, both with and without a thin surface oxidized layer. The Ga^+ signal from a bare GaAs surface (closed circles) showed a steep decrease above 300 °C due to the decomposition of TEG. However, the signal from the oxidized surface (open circles) showed a gradual decrease similar to the case of TMG exposed to SiO_2 , indicating that TEG was reflected from the surface without decomposition. Selective-area epitaxy is, therefore, possible in the temperature range from 350 to 450 °C using a GaAs oxide mask. The upper limit was determined by the stability of GaAs oxide.

The selective-area epitaxy of GaAs has been carried out with the following steps: (1) cleaning of the GaAs surface at 650 °C under As_4 flux, (2) oxidization of the surface in pure oxygen ambience of 10 Torr under light from a halogen lamp, (3) patterning of the oxide layer by Ar^+ sputtering through a shadowing mask or electron-beam induced Cl_2 etching,⁸⁾ and (4) MOCBE growth of GaAs. Figure 4 shows a Nomarski microphotograph of the as-grown surface. The rounded rectangular regions are the selectively grown layer. No polycrystalline deposition can be observed on the mask surface. Furthermore, the GaAs oxide mask can be removed by heating the substrate up to 600 °C under As_4 flux, and overgrowth of the epitaxial layer is possible on the entire surface.

This technique has enabled us to construct an in situ selective-area epitaxy process in which every wafer process, such as mask formation, mask patterning, and epitaxial growth, can be done in an ultra-high vacuum system without exposure to air or other contaminants.

Summary

Mass spectrometry was applied in order to study the decomposition of MO's on the surfaces of GaAs, quartz, and GaAs oxide. Decomposition took place on the GaAs surface above 350 and 300 °C for TMG and TEG, respectively, and on GaAs oxide above 590 °C where the GaAs oxide evaporated. No decomposition was observed up to 700 °C on the SiO_2 surface. Incident TMG molecules are reflected from the surface of SiO_2 or GaAs oxide. By using a GaAs oxide mask, a novel in situ selective-area epitaxy technique has

been demonstrated.

References

1. E.M.Gibson et al.: J.Crystal Growth 105 (1990) 81.
2. T.Martin and C.W.Whitehouse: J. Crystal Growth 105 (1990) 57.
3. Y.Ohki et al.: Japan. J. Appl. Phys. 28 (1989) L 1486.
4. Y.Ohki and Y.Hiratani: J. Crystal Growth 105 (1990) 77.
5. Y.Hiraatani and Y.Ohki: Japan. J. Appl. Phys. 29 (1990) L1360.
6. E.Tokumitsu et al.: J. Appl. Phys. 55 (1984) 3163.
7. K.Kamon et al.: J. Crystal Growth 73 (1985) 73.
8. M.Taneya et al.: Japan. J. Appl. Phys. 28 (1989) L515.

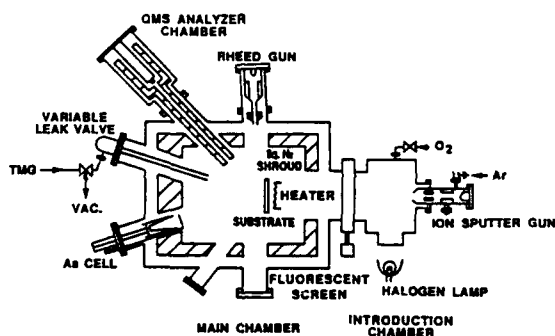


Fig. 1 Schematic illustration of the MOMBE system used in this study.

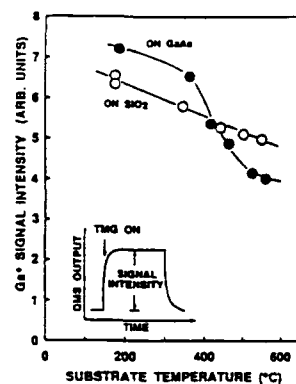


Fig. 2 Substrate temperature dependence of the Ga^+ signal from GaAs (closed circles) and from SiO_2 (open circles).

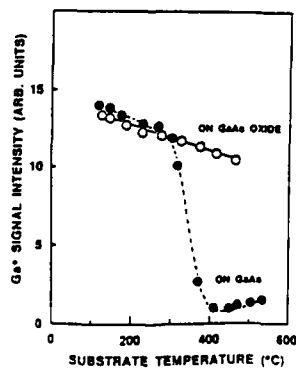


Fig. 3 Substrate temperature dependence of the Ga^+ signal from GaAs (closed circles) and from GaAs oxide (open circles).

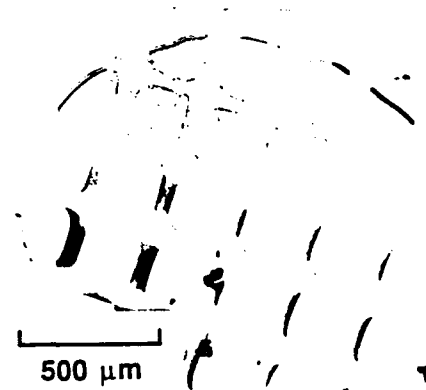


Fig. 4 Nomarski microphotograph of as-grown surface: the rounded square patterns are the selectively grown region.

Application of migration-enhanced epitaxy to novel semiconductor structures

Y.Horikoshi, H.Yamaguchi, T.Sudersena.Rao,
S.Ramesh and N.Kobayashi

NTT Basic Research Laboratories
Musashino-shi, Tokyo 180 Japan

1. Introduction

Enhanced surface migration is essential to the growth of high quality epitaxial layers. In the growth of III-V compound semiconductors, surface migration is effectively enhanced by supplying group III atoms to the growing surface in the absence of group V atoms or molecules. In this situation, the lifetime of isolated group III atoms, which are quite mobile on the growing surface, is greatly increased resulting in these atoms migrating a large distance during growth. Migration-enhanced epitaxy (MEE) is based on this characteristic[1]. MEE has proved useful for growing flat heterojunctions and for lowering the epitaxial growth temperature of III-V compound semiconductors. This paper describes the principle of MEE and its application to the growth of novel semiconductor structures such as GaAs/AlAs horizontal superlattices, ZnSe/GaAs superlattices, and $(\text{GaAs})_{1-x}(\text{Si}_2)_x/\text{GaAs}$ superlattices.

2. Principle of migration-enhanced epitaxy

In MBE and MOVPE the growth of GaAs, for example, is performed by a simultaneous deposition of the constituent atoms and molecules under As-stable conditions. In this situation, the growing surface is covered with a large number of GaAs islands because the Ga atoms deposited on the growing surface react with As to form small islands. These small islands are not very mobile along the surface because of the stable chemical bonds between GaAs molecules in the islands and As atoms in the underlying As plane.

Even in this situation, however, there exists an equilibrium density of isolated Ga atoms on the growing surface. These isolated Ga atoms are quite mobile and easily migrate to find more stable sites. Let D_s be the diffusion coefficient of isolated Ga atoms on GaAs (001) surfaces, and τ be the average lifetime of isolated Ga atoms before

reacting with As. When Ga atoms are deposited on the surface with steps and kinks, the motion of the isolated Ga atoms depends strongly upon the magnitude of $(D_s\tau)^{-1}$ relative to N_{sk} , where N_{sk} represents the effective adsorption site density for migrating isolated Ga atoms provided by steps and kinks.

All the deposited Ga atoms will be adsorbed at the steps or kinks and incorporated into the crystal without creating additional islands when $N_{sk} > (2 D_s\tau)^{-1}$. Thus, step-flow growth takes place, maintaining a good surface flatness. When $N_{sk} < (2 D_s\tau)^{-1}$, however, most of the isolated Ga atoms cannot arrive at the steps or kinks within their lifetime, but tend to form small islands by reacting with As. Thus, two dimensional nucleation growth dominates in this case. The above discussion implies that a large migration distance of isolated Ga atoms, rather than migration velocity, is essential to step-flow growth. When Ga atoms are deposited on surfaces with small N_{sk} values, step-flow growth still dominates if $D_s\tau$ is increased. However, artificial enhancement of D_s is very difficult, unless an excess energy is added to the surface, because D_s is an inherent characteristic determined by the surface structure and chemical nature of surface adatoms. However, τ is the average lifetime of isolated Ga atoms before reacting with As to form GaAs islands, and so it is rather easily modulated in MEE, in that Ga atoms are deposited separately from As₄. Thus, migration distance is easily enhanced and controlled in MEE[2].

3. Growth of novel semiconductor structures

3.1 Horizontal superlattices

The stepflow growth plays a major role in growing horizontal superlattices on the vicinal surface[3]. The RHEED study during the growth of GaAs by MEE on vicinal (001) GaAs surfaces revealed that the stepflow growth dominated over the two dimensional nucleation growth due to the enhanced migration of surface adatoms. Therefore, MEE is suitable for growing horizontal superlattices. We have successfully grown the GaAs/AlAs horizontal superlattices by optimizing the MEE conditions[4].

3.2 ZnSe/GaAs superlattices

ZnSe/GaAs superlattices are quite attractive because of their enormous potentialities in both electrical and optical applications. Selective doping to GaAs layers in ZnSe/GaAs superlattices may open the way to control the electrical transport characteristics of large

bandgap materials, since GaAs can be doped quite heavily for both n- and p-type impurities. In addition, a large optical nonlinear effect is expected in ZnSe/GaAs superlattices because of the greater stability of excitons formed in the GaAs well of the structure as compared with that in the GaAs well of the AlGaAs/GaAs superlattices.

However, while a large number of studies have been reported on the ZnSe-on-GaAs heterostructures, it is difficult to form the GaAs-on-ZnSe heterostructure by MBE and metalorganic chemical vapor deposition techniques. This difficulty is primarily due to the large difference in optimal growth temperatures of ZnSe ($\sim 250^\circ\text{C}$) and GaAs ($\geq 550^\circ\text{C}$). The optimal temperature mismatch was solved by applying MEE for lowering the growth temperature of GaAs to 250°C . The problem of the low sticking coefficient of As on ZnSe surface was circumvented by As_4 deposition at very low temperatures[5]. Thus, a ZnSe/GaAs with quite high optical quality were grown.

The interface and the crystal quality of the superlattices as well as the period thickness were determined using double-crystal x-ray diffraction and TEM. A double-crystal x-ray rocking curve for ZnSe/GaAs superlattice of a 40 nm period in the vicinity of the (004) GaAs Bragg angle showed sharp satellite peaks (~ 100 arcsec), which indicates the high crystalline and interfacial quality of the superlattice. Since the ZnSe layers are thin they would be expected to be fully strained pseudomorphic with the GaAs. The period thickness of superlattices calculated from the angular spacing of the superlattice satellite peaks is in agreement with the average period obtained from TEM measurements.

3.3 $(\text{GaAs})_{1-x}(\text{Si}_2)_x/\text{GaAs}$ superlattice

The band gaps of $(\text{GaAs})_{1-x}(\text{Si}_2)_x$ alloy system can be tailored between 1.43 eV(GaAs) and 1.1 eV(Si), and the corresponding interband transition changes from direct to indirect (Γ -L). In fact, a simple extrapolation of the Γ , L and X bands of GaAs and Si based on Vegards rule shows that with increasing Si content the bandgap of $(\text{GaAs})_{1-x}(\text{Si}_2)_x$ may increase by as much as 0.35 eV, before the direct to indirect crossover occurs. Early work[6] on the preparation of $(\text{GaAs})_{1-x}(\text{Si}_2)_x$ alloy has been based on the sputtering techniques, and there is no report till date on the growth of this alloy layer using epitaxial growth process like MBE.

$(\text{GaAs})_{1-x}(\text{Si}_2)_x$ layers with various x values of $0 < x \leq 0.25$ were grown in the temperature range of 500°C – 620°C by MEE on (001) GaAs substrate. Structural and compositional analysis of the as grown $(\text{GaAs})_{1-x}(\text{Si}_2)_x$ layers indicated single crystal zincblende structure with no evidence of phase separation throughout the compositional

range $0 < x < 0.25$. The lattice constant of the alloys was found to decrease linearly with increasing Si content from 0.56543 nm at $x=0$ to 0.5601 nm at $x=0.25$.

The $(\text{GaAs})_{1-x}(\text{Si}_2)_x/\text{GaAs}$ superlattices were grown using various x values. The structures were examined by double-crystal x-ray diffraction and TEM. The x-ray diffraction linewidth of the main superlattice peak for $(\text{GaAs})_{0.8}(\text{Si}_2)_{0.2}/\text{GaAs}$ superlattice with a 32 nm period was only 74 arcsec, indicating high crystalline quality of the superlattice structure[7].

4. Conclusion

Applying migration-enhanced epitaxy, novel semiconductor structures such as GaAs/AlAs horizontal superlattices, ZnSe/GaAs superlattices and $(\text{GaAs})_{1-x}(\text{Si}_2)_x/\text{GaAs}$ superlattices have been successfully grown on (001) GaAs. Characterizations by double-crystal x-ray diffraction and transmission electron microscopy showed that these superlattices have an excellent crystalline quality.

References

- [1] Y. Horikoshi, M. Kawashima, and H. Yamaguchi, Japan. J. Appl. Phys. 25 (1986) L868.
- [2] Y. Horikoshi, H. Yamaguchi, F. Briones, and M. Kawashima, J. Crystal Growth 105 (1990) 326.
- [3] P. M. Petroff, A. C. Gossard, and W. Wiegmann, Appl. Phys. Lett. 45 (1984) 620.
- [4] H. Yamaguchi, and Y. Horikoshi, Japan. J. Appl. Phys. 28 (1989) L1456.
- [5] N. Kobayashi, and Y. Horikoshi, Japan. J. Appl. Phys. 28 (1989) L1880.
- [6] D. H. Mei, Y. W. Kim, D. Lubben, I. M. Robertson and J. E. Greene: Appl. Phys. Lett. 55 (1989) 2649.
- [7] T. Sudersena Rao, K. Nozawa and Y. Horikoshi, Japan. J. Appl. Phys; (to be published).

II. CHARACTERIZATION

Optical

| | |
|--|----|
| Photoluminescence Characterization of Compound Semiconductor Optoelectronic Materials | 34 |
| <i>G.E. Stillman, S.S. Bose and A.P. Curtis</i> | |
| Photoluminescence Mapping: New Technique to Characterize Materials and Structures for Fabrication of Photonic Devices | 38 |
| <i>M. Bugajski and Jacek Ornoch</i> | |
| Photoluminescence from InGaAs/InGaAsP Quantum Wires Fabricated by Ga Focused Ion Beam | 42 |
| <i>S.J. Yu, H. Asahi, J. Takizawa, S. Kim and S. Gonda</i> | |
| Infrared Characterization of Compound Semiconductors | 46 |
| <i>A. Deneuve, V. Zelezny, D. Tanner and P.H. Holloway</i> | |
| Optically Confirmed Two-Dimensional Confinement Effects in Ultra-Narrow InGaAs/InP Quantum Well Wires | 50 |
| <i>M. Notomi, M. Nagamura, H. Iwamura, T. Nishida, S. Nojima, M. Okamoto and T. Tamamura</i> | |
| Laser Scatterometry for Process Characterization | 54 |
| <i>S.M. Gaspar, K.C. Hickman, K.P. Bishop, S.S. Naqvi, J.R. McNeil, S. Wilson, Y.E. Strausser, R.A. Gottscho and A. Kornblit</i> | |

Electronic

| | |
|---|----|
| Study of Epitaxial Growth by UHV-SEM and RHEED-TRAXS | 56 |
| <i>S. Ino</i> | |
| Spectroscopy and Luminescence with STM on III-V Epitaxial Multilayers | 60 |
| <i>O. Albrektsen, S.F. Alvarado, H.P. Meier, Ph. Renaud and H.W.M. Salemink</i> | |
| Ga_{0.47}In_{0.53}As/InP Multiquantum Well Structures Observed by Scanning Tunneling Microscopy under Ultrahigh Vacuum | 64 |
| <i>T. Kato, F. Osuka, I. Tanaka and S. Ohkouchi</i> | |
| Characterization of Strained Heterostructures by Catholuminescence | 68 |
| <i>D. Bimberg, M. Grundmann and J. Christen</i> | |

Photoluminescence Characterization of Compound Semiconductor Optoelectronic Materials

G.E. Stillman, S.S. Bose, and A.P. Curtis
 Center for Compound Semiconductor Microelectronics
 Department of Electrical and Computer Engineering
 University of Illinois at Urbana-Champaign, Urbana, IL 61801

For many optoelectronic applications of compound semiconductors, low defect concentration and either high-purity or low carrier concentration epitaxial layers are required. In order to be able to achieve these conditions reproducibly, it is important to have reliable high-purity sources appropriate for the desired epitaxial growth technique, and to be able to optimize the growth parameters for minimum non-radiative defects or deep levels. Because electrically active defects and impurities with concentrations in the part per billion (ppb) range can influence the performance of the devices of interest, the usual techniques are not useful. Mass spectrographic or x-ray techniques are not sensitive enough for identification of the residual impurities in high-purity epitaxial layers. The optical technique of photoluminescence (PL), can be used to identify the residual electrically active acceptor impurity species in these epitaxial layers as well as to detect optically active defects and to generally evaluate the quality of the material.¹ In this paper we review the photoluminescence technique for characterization of GaAs and InP, and give examples of the information that can be obtained by this technique.

A schematic diagram typical of the apparatus used for low temperature and variable temperature PL is shown in Fig. 1. Significant features of this arrangement include the provisions for: (1) varying the incident power over a wide range; (2) collecting a significant fraction of the photoluminescence emission while excluding the radiation from the exciting laser; and (3) mounting the sample in a strain-free manner while providing the capability of maintaining the sample temperature constant at a fixed value in the range from about 1.7 K up to about 20 K.

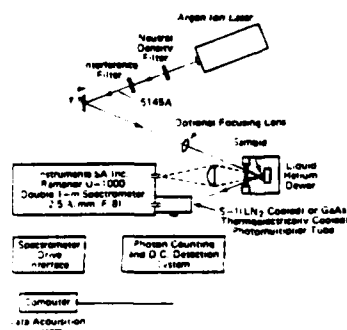


Figure 1: Schematic diagram of experimental apparatus used for low temperature photoluminescence measurements

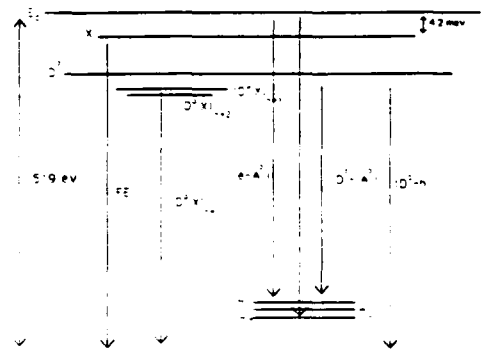


Figure 2: Band Diagram for Low Temperature Recombination Processes in GaAs

Figure 2 gives an energy band diagram showing the transitions observed in near band-edge photoluminescence (PL). Figures 3 and 4 show the near band-edge photoluminescence (PL) spectra of exciton recombination in n-type high purity MOCVD-grown GaAs and InP. These figures represent the typical high resolution spectra observed in high purity epitaxial layers at 1.7 K and low excitation. The spectra contain peaks due to recombination of free excitons (FE), excitons bound to neutral donors (D^0, X)_{n=1} (leaving donor in the ground state in the final state), excitons bound to ionized donors (D^+, X), and excitons bound to neutral acceptors (A^0, X). Generally, the exciton spectra are dominated by donor bound exciton peaks in n-type materials and by acceptor bound exciton peaks in p-type materials. The multiple lines in (D^0, X)_{n=1} result from the different (non-rigid) rotational levels of the (D^0, X) complex in the initial state. The doublet (rarely triplet) in the acceptor bound exciton transitions (A^0, X) arises from the coupling of two holes and one electron in the complex (A^0, X). The (A^0, X) peaks occur at different energies for different acceptors. The peak labeled (D^0, h), which is not excitonic in nature, is the free hole-to-neutral donor transition. This peak occurs at almost the same energy as (D^+, X) in GaAs; but in InP these transitions are well resolved. "Two-electron" replicas of (D^0, X) denoted by (D^0, X)_{n=2} (leaving donor in the 1st excited state in the final state) are also observed. The bound exciton peaks are sharp because the excitons which bind to the impurity have no kinetic energy associated with them. The linewidths of the bound exciton peaks are usually a good indication of the purity of the epitaxial layers of GaAs and InP. The narrowest linewidth of the strong (D^0, X)_{n=1} peak in GaAs and InP, measured in our laboratory, are ~ 0.11 meV and ~ 0.04 meV respectively.

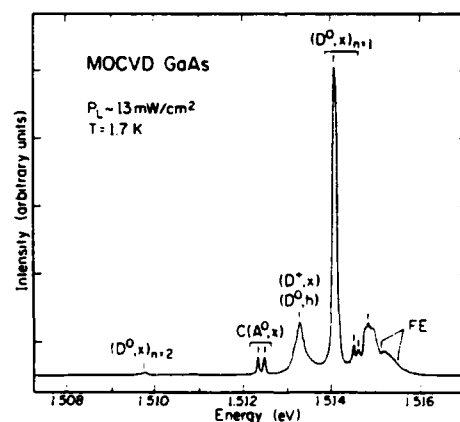


Figure 3: Excitonic Spectrum of High Purity MOCVD n-GaAs at Low Temperature

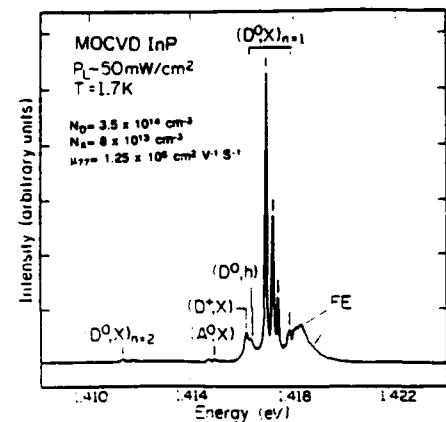


Figure 4: Excitonic Spectrum of High Purity MOCVD n-InP at Low Temperature

Figure 5 shows typical spectra of conduction band/donor-to-acceptor transitions in n-type high purity GaAs grown by MOCVD. The top spectrum is recorded at 1.7 K and low excitation. C and Zn are identified as the only acceptor impurity species in this sample from donor-to-acceptor (D^0-A^0) transitions. Since the donors in GaAs and InP have nearly equal binding energies and the acceptors have different binding energies, the (D^0-A^0) transitions can be used to identify the acceptor impurity species. The bottom spectrum is recorded at ~ 12 K, and contains three peaks, namely cond. band-to-acceptor ($e-A^0$) transitions for C-acceptors, (D^0-A^0) transitions for Zn acceptors and a mixture of $C(D^0-A^0)/Zn(e-A^0)$. As the temperature of the sample increases, donors begin to ionize and the ($e-A^0$) peak broadens and increases in intensity relative to the (D^0-A^0) peak. In certain situations like this example, the acceptor binding energies are such that the (D^0-A^0) and ($e-A^0$) peaks for two different acceptors can overlap. In those cases, the behavior of these peaks with different temperatures can be used to identify the transitions. Moreover, variable excitation intensities can also be used to identify these transitions. With increasing excitation, the (D^0-A^0) peak grows and saturates (at high enough excitation), and shifts to higher energy, while the ($e-A^0$) peak intensity increase monotonically with excitation. The top spectrum can also be used to estimate the relative concentrations of C and Zn acceptors. Since the (D^0-A^0) peaks for both C and Zn acceptors have similar linewidths, their peak intensities can be taken as a measure of the relative concentrations of those impurities. These relative concentrations along with the Hall-effect measurements can yield the absolute concentrations of the acceptor impurity species present.

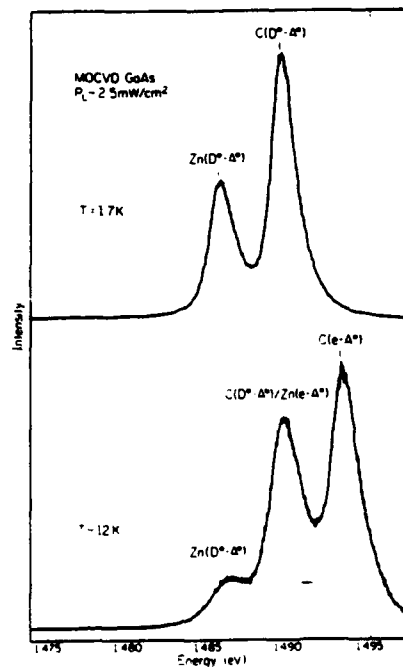


Figure 5: Band/Donor - Acceptor Spectra of High Purity MOCVD n-GaAs at Low Temperature

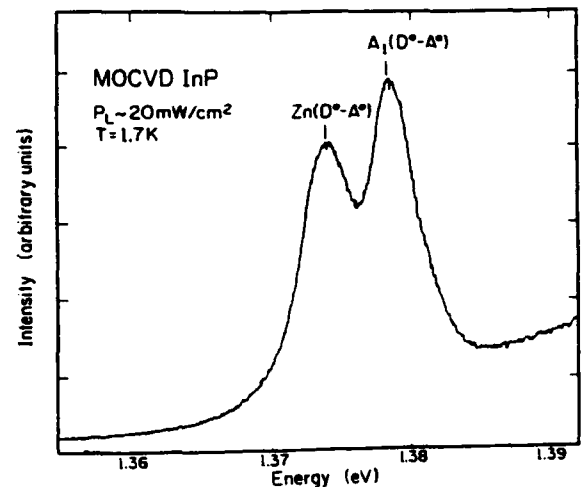


Figure 6: Band/Donor - Acceptor Spectrum of High Purity MOCVD n-InP at Low Temperature

Figure 6 shows a typical spectrum of $(D^0-A^0)/(e-A^0)$ transitions in n-type high purity MOCVD-grown InP at 1.7 K and low excitation. Again, Zn and A_1 (an unknown impurity species) are identified as the dominant acceptors in this InP sample. The A_1 acceptor is commonly observed in epitaxial InP, and the most likely candidate for this acceptor is Mg. Also, C is not typically incorporated as a residual acceptor in epitaxial InP. The LO and TO phonon replicas of free excitons occur at the same energies as $C(D^0-A^0)$ and $C(e-A^0)$ peaks at liquid helium temperatures. Therefore, care must be exercised to identify these transitions from the variable excitation and variable temperature PL measurements.

REFERENCE

1. B.J. Skromme, S.S. Bose, B. Lee, T.S. Low, T.R. Lepkowski, R.Y. DeJule, and G.E. Stillman, "Characterization of high-purity Si-doped molecular beam epitaxial GaAs," *J. Appl. Phys.* **58**, pp. 4685-4702 (1985).

PHOTOLUMINESCENCE MAPPING: NEW TECHNIQUE TO CHARACTERIZE MATERIALS AND STRUCTURES FOR FABRICATION OF PHOTONIC DEVICES

Maciej Bugajski, Jacek Ornoch
Institute of Electron Technology
Al.Lotnikow 32/46, 02 668 Warsaw, Poland

Abstract

Since the fabrication of photonic devices is a complex and expensive process it is highly desirable to characterize both starting material and device structures after each step of technological process. The ideal candidate which meets the production and research criteria is photoluminescence mapping technique. In this paper we describe apparatus for measuring photoluminescence over the entire wafer and discuss a number of applications of this technique.

Introduction

There are many reasons why optical spectroscopy is especially appropriate for characterizing semiconductors, not the last of which is the non-contact and non-destructive nature of this technique. Capable of being fully automated photoluminescence spectroscopy also yields a variety of data unmatched by other methods.

The information available via photoluminescence analysis includes impurity levels in a sample and the distribution of dopants or defects over the surface of the wafer. These data are basic to establishing optimum growth parameters and judging whether specified parameters are being maintained. With the increased use of growth techniques such as molecular beam epitaxy (MBE) and metallorganic vapor phase epitaxy (MO VPE) photoluminescence has been used extensively for measuring the quality of both the semiconductor substrates and epitaxial layers. Quality control of GaAs and InP substrates is crucial for efficient yield and acceptable performance of optoelectronic devices such as laser diodes or photodetectors. Using photoluminescence mapping technique on the fabrication line can greatly improve their operation and provide continuous monitoring of the technological process.

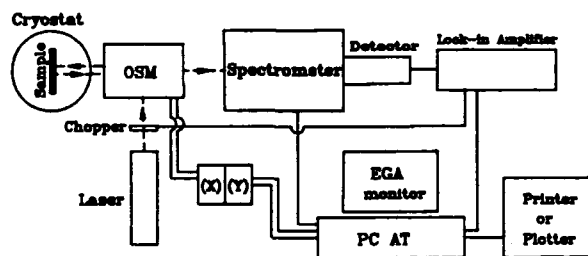
Photoluminescence process

Photoluminescence is the optical radiation emitted by a crystal resulting from excitation to a nonequilibrium state by irradiation with light. The major contribution to the photoluminescence signal comes from the near-surface region. Consequently majority of the photoluminescence experiments are arranged to examine the light emitted from the irradiated side of the sample. That means only the one side of the sample needs to be polished which is usually the case for commercially available substrates. The room temperature photoluminescence consists of one peak which can be ascribed to band-to-band radiative recombination. The peak wavelength gives information about material composition; the peak intensity is a measure of the ratio of radiative to nonradiative

transitions due to defects or deep levels associated with impurities and consequently is the measure of material quality. At low temperatures besides the direct transitions between conduction and valence band a number of well resolved lines due to the transitions via excitonic states and through intermediate states such as donors and acceptors can be observed. That immediately allows for studying by photoluminescence mapping not only the distribution of deep non-radiative states but also the distribution of various impurities and contaminants present in the crystal. This is usually done by tuning spectrometer to the specific wavelength referring to the transition in question and recording photoluminescence intensity distribution.

Photoluminescence mapping system PMS 100

Photoluminescence mapping system developed in our laboratory is shown in Fig.1. It includes: optical scanning module (OSM), power drivers for stepping motors, 8255 digital input/output card for stepping motors control, 12 bit 60 μ s analog/digital converter card for data acquisition and PC AT computer with hard disk and EGA



Simplified block diagram of Photoluminescence Mapping System - PMS 100

Fig.1

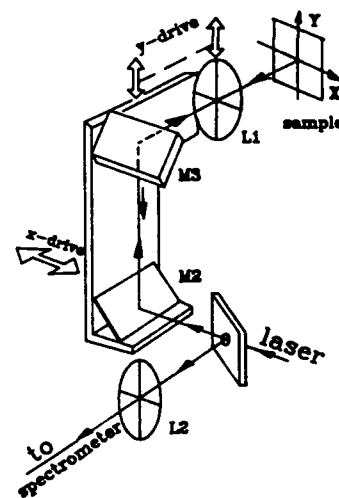


Fig.2

OSM - Optical Scanning Module

monitor. The rest of the system is a conventional photoluminescence equipment. We use argon laser, grating monochromator and photomultiplier or cooled germanium detector. The system is equipped with large window liquid helium cryostat allowing for mapping of 2 inch wafers. The main part of the photoluminescence mapping system is the optical scanning module shown in details in Fig.2. We have followed the design of Yokogawa et al [1]. The radiation emitted by the sample retraces the laser's path on its way to the spectrometer. Displacing the upper mirror and the focusing lens vertically results in a vertical scan of a wafer. Similarly, displacing the whole assembly horizontally results in a horizontal scan. The optical scanning module combined with

appropriate software controlling its movement allows the user to map the entire wafer for photoluminescence intensity completely automatically. Menu-driven software developed for PL mapping system assures the interactive operation, data averaging and smoothing and a possibility of displaying data in different modes, i.e., color map, contour plot, pseudo three dimensional plot. Positioning accuracy of the scanner is better than $1\mu\text{m}$ and the minimum step is $5\mu\text{m}$. The size of the map can be varied (typically it is 100×100 points). The hard copy of the results can be obtained on a dot-matrix graphic printer with different colors represented by different shades of gray.

Experimental results

To test the validity of PL mapping technique the large number of both monocrystalline and epitaxial samples were studied. PL mapping is applicable for monitoring fabrication process of photonic devices since it can detect and localize spatially modifications of the material at each step during the production process. The ability to measure PL maps of the entire wafers allows the use of the method to characterize performance of the epitaxial reactors, e.g., to optimize gas flow design in MO VPE reactor. Here we will show only a few typical applications of the method demonstrating its great potential for research and production control in the area of photonic devices.

(a) semi-insulating LEC GaAs

Maps of PL intensity (see Fig.3) have been found to correlate closely to cellular structure of dislocations revealed by chemical etching. Analysis of the spectra (Fig.4) taken at different distances to cell walls show that distribution of carbon in bulk crystals is uniform and contrary to previously published data, there is no recognizable gettering of this impurity on dislocations [2]. It seems likely, therefore, that PL contrast in SI-GaAs is mostly related to the variations in the effective lifetime brought about by segregation of defects on dislocations forming cellular structure. In indium doped material growth striations have been observed by PL mapping but again no indium segregation has been found on dislocations [3].

(b) conducting-Bridgman grown GaAs:Si

Inhomogeneities in PL intensity (see Fig.5) have been found to result from inhomogeneous doping level and degree of compensation. The source of those inhomogeneities is the nonuniform temperature distribution during crystal growth and changes of the shape of the crystallization front along the ingot [4].

(c) MO VPE grown GaAs

On the microscale (see Fig.6) PL maps of the epitaxial layers show uncorrelated fluctuations of PL intensity mainly related to the surface recombination nonuniformities. On the macroscale a systematic variations of PL intensity due to thickness nonuniformity are observed.

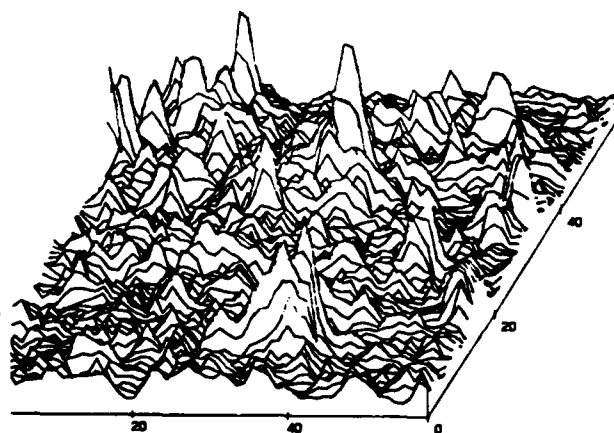
- [1] M.Yokogawa et al, Jap.J.Appl.Phys. 23 (1984) 648
- [2] M.Bugajski, P.Edelman, J.Ornoch, Acta Phys.Pol. A77 (1990) 347
- [3] M.Skowronski, M.Bugajski, DRIP-II, Monterey 1987, p.241
- [4] P.Edelman, J.Ornoch, W.Lewandowski, Crystal Propert.& Prepar., vol.19/20, Trans.Tech.Pbl., Switzerland (1989) p.91



Fig.3

500 μm

2D map of photoluminescence in undoped semi-insulating GaAs ($\lambda=8200\text{\AA}$, $T=10\text{K}$). Note the cellular dislocation network with characteristic dimensions of the order of a few hundreds micrometers.



GaAs Epi layer $3\times 5\text{ mm}$, $T = 77\text{K}$, $\langle a, a \rangle$ line

Fig.6

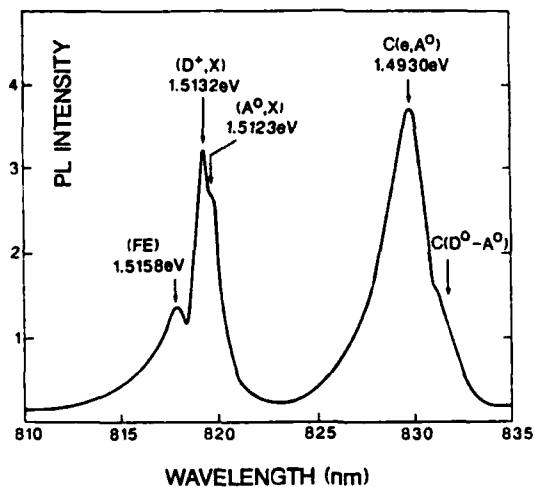


Fig.4

PL spectrum of GaAs Czochralski (LSC) sample ($T=10\text{K}$)
(Note exciton transitions around $\lambda = 8200\text{\AA}$ and carbon acceptor related transitions around $\lambda = 8300\text{\AA}$)



Fig.5

PL intensity maps for Bridgman grown GaAs:Si ($T=300\text{K}$)
Band-to-band transitions at $\lambda = 8700\text{\AA}$

Photoluminescence from InGaAs/InGaAsP
Quantum Wires Fabricated by Ga Focused Ion Beam

S.J. Yu, H. Asahi, J. Takizawa, S. Kim and S. Gonda

Osaka University, The Institute of Scientific and Industrial Research
8-1, Mihogaoka, Ibaraki, Osaka 567, Japan

1. Introduction

Low dimensional structures such as quantum wires and boxes are one of the interesting subjects. Up to date, various microstructures have been fabricated and characterized by various methods. Focused ion beam (FIB) is one of the useful methods because this method makes it possible to modify, deposit and etch various materials in desired pattern.

In this paper, we report fabrication of InGaAs/InGaAsP quantum wires by Ga FIB. The properties of quantum wires were investigated by photoluminescence(PL) method.

2. Fabrication of wire structures

Figure 1 shows schematic view of fabrication procedure of quantum wires. At first, InP buffer layer, $\text{In}_{0.53}\text{Ga}_{0.47}\text{As}$ reference layer and InP/InGaAs(50Å)/InP superlattices (single quantum well, SQW) were grown on (100)InP substrate by MOMBE. Secondly, InP/InGaAs/InP layers are etched to mesas of $100\mu\text{m}\times 100\mu\text{m}$ using photolithography. Thirdly, Ga FIB was irradiated in lines onto the top plane of the mesas. The energy of ion beam is 100kV. The ion implanted line width is 100nm and the lateral period T is changed from 238nm to 400nm. The annealing was performed using Si_3N_4 coating in N_2 atmosphere at 650–670°C for 60min. From the experiment of Ga broad beam implantation, it was confirmed that alloying of InGaAs/InP superlattice takes place in such a way that alloyed $\text{In}_{1-x}\text{Ga}_x\text{As}_y\text{P}_{1-y}$ has the composition of alloy lattice matched to InP and has smaller compositions x and y at higher dose.¹⁾ Although in FIB implantation with higher ion current density somewhat different behaviors (in defect formation, implanted ion profile, etc.) may be seen from those of broad beam implantation, alloying of InGaAs/InP

materials is expected in the FIB implanted region.

3. Photoluminescence from wire structures

PL spectra from the wire structures fabricated by FIB implantation were shown in Fig.2, together with the spectra of unimplanted as-grown samples. FIB implantation was carried out at doses of 1×10^{13} and $1 \times 10^{14} \text{ cm}^{-2}$ and subsequent anneal was made at 670°C . PL measurements were carried out at 30K using the excitation of 514.5-line of an Ar⁺ ion laser. The excitation power was 0.3~1mw and the beam diameter was $10 \mu\text{m}$. In Fig.2, the peaks around 1560.4nm and 1587.9nm are from the reference InGaAs bulk layer of 2000 \AA in thickness and the peak at 1478.6 nm is from the SQW (50 \AA). The PL peaks show considerable blue shifts from SQW peak of 37meV and 10meV in 1×10^{14} and $1 \times 10^{13} \text{ cm}^{-2}$ dose sample, respectively. The larger blue shift at higher dose is mainly due to the larger lateral straggling of implanted ions. The $1 \times 10^{14} \text{ cm}^{-2}$ implanted sample shows stronger PL intensity than the $1 \times 10^{13} \text{ cm}^{-2}$ sample. This stronger intensity at higher dose is mainly attributed to the higher InGaAsP barriers in the alloyed regions. The formation of higher barrier at higher dose is consistent with our previous experiment in which $\text{In}_{1-x}\text{Ga}_x\text{As}_y\text{P}_{1-y}$ alloy has smaller compositions x,y at higher dose.

Photoluminescence spectra from the sample (lateral period=400 and 263nm, dose= $1 \times 10^{14} \text{ cm}^{-2}$, annealing at 670°C) are shown in Fig.3, along with those of as-grown SQW and reference InGaAs layer. The peaks from the wire structures show considerable blue shift with decreasing lateral period. The intensity is about 1/100 and 1/200 for T=400nm and 263nm, respectively.

Figure 4 shows the luminescence energy shift of fabricated wire structures as a function of lateral period. Smallness of the shift at lower annealing temperature may be attributed to the insufficient formation of InGaAsP barriers. The broken line in Fig.4 is the result in which quantum levels are calculated in the case of rectangular potential well. The solid line shows calculated results in which the deviation from the rectangular barrier potential due to the broadening of alloyed region is taken into account. That is, the lateral straggling length for constituent atoms by Ga

FIB implantation (100kV, $1 \times 10^{14} \text{cm}^{-2}$) was estimated from the LSS theory and the dose dependence of the interdiffusion length. Quantum levels in this potential well were obtained by calculating the levels in each part of the well divided into 200 parts and taking the level of the maximum in number as the energy level.

Thus, the shift as a function of lateral period can be explained semi-quantitatively by taking account of lateral straggling of implanted ions. This indicates that alloyed regions formed by Ga FIB implantation works as lateral potential barriers for electrons and holes in InGaAs single quantum well.

Summary

Fabrication of InGaAs/InP quantum wires was tried by Ga FIB implantation. From the PL measurement of the samples, it is confirmed that alloyed regions formed by implantation work as lateral potential barriers for electrons and holes in InGaAs single quantum well.

Acknowledgement

The authors would like to thank Y.kawaguchi, Y.Hirayama and M. Ikeda of NTT Laboratories for MOMBE growth, FIB implantation and Si_3N_4 film deposition, respectively. Thanks are also due to H.Kubo and C.Hamaguchi of Osaka University for micro-beam photoluminescence measurements. This work was supported in part by Grant-in-Aid for Scientific Research on Priority Area, "Electron Wave Interference Effects in Mesoscopic Structures" from the Ministry of Education, Science and Culture.

References

- 1) The related paper is ; Soon Jae Yu, Hajime Asahi, Hitoshi Sumida, Shuichi Emura and Shun-ichi Gonda and Hisao Tanoue, Inst. Phys. Conf. Ser. No 106 (Int. Symp. GaAs and Related Compounds 1989)

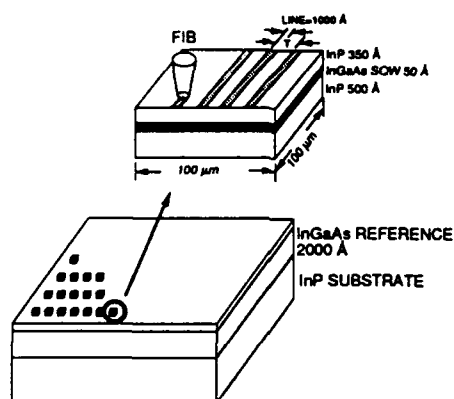


Fig.1 Fabrication process of InGaAs/InP Quantum Wires.

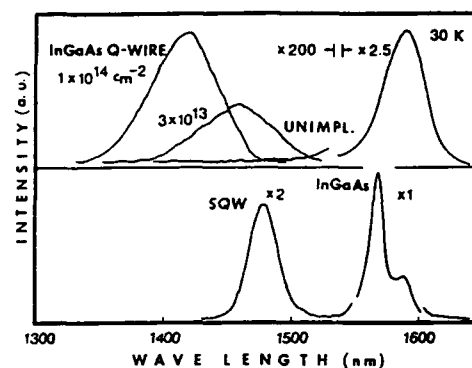


Fig.2 Photoluminescence spectra at 30K from wire structures fabricated at doses of 1×10^{13} and $1 \times 10^{14} \text{ cm}^{-2}$, as-grown layer and InGaAs reference layer.

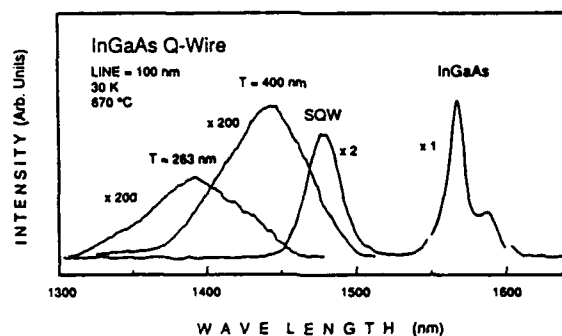


Fig.3 Photoluminescence spectra at 30K from wire structures with $T=263\text{nm}$ and 400nm , as-grown layer and InGaAs reference layer.

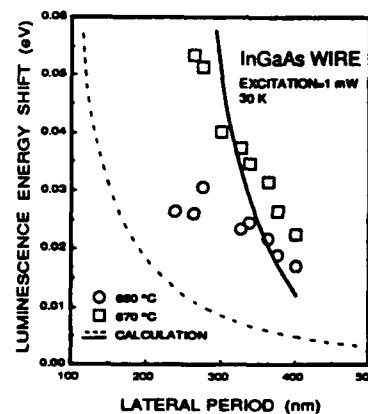


Fig.4 Luminescence energy shift of quantum wires annealed at 650°C and 670°C as a function of lateral period.

INFRARED CHARACTERIZATION OF COMPOUND SEMICONDUCTORS

A. Deneuville, Laboratoire d'Etudes des Propriétés Electroniques des Solides, BP 166 X 38042 Grenoble, France; and Department of Material Sciences and Engineering, University of Florida, Gainesville, FL 32 611, USA

The determination of the carrier concentration N and mobility μ from plasmon - phonon coupling through far infrared reflection measurements is shown in particular for n type ZnSe / undoped ZnSe / Semi insulating GaAs.

As the band gaps of semiconductors are increasing, there are more and more problems to achieve large doping levels and good ohmic contacts to measure the carrier concentrations N and mobilities μ by Hall effect. On the other hand, as the devices structures contain more and more layers, in situ control at each processing step becomes more and more necessary. A solution of both problems might be contactless determination of N and μ from infrared (IR) reflectivity. In the following, we give the physical and analytical bases of such determinations, and show examples of derivation of "optical" N and μ on bulk GaAs and thin films of ZnSe.

For semiconductors exhibiting some ionicity, as compound semiconductors, there is at low wavenumber a coupling between the LO(Γ) phonon mode and the plasmon via the electric field⁽¹⁾. The resulting modes (Raman active) exhibit both plasmon like and phonon like characteristics. They induce a large optical absorption in the far infrared, which allows for bulk substrates⁽²⁾ and thin films⁽³⁾ the determination of both N and μ from reflection or transmission measurements, in the $10^{16} < N < 10^{19} \text{ cm}^{-3}$ and $200 < \mu < 600 \text{ cm}^2 \text{ V}^{-1} \text{ s}^{-1}$ ranges⁽³⁾ for ZnSe heteroepitaxial thin films.

However, for compound semiconductors, the selection rules also allow in IR the first order TO(Γ) mode (wave number W_{TO}), which gives the main contribution to the ground complex dielectric constant K of the undoped material. In the simpler approximation of an harmonic oscillator, the two phonons contributions are neglected and K is written⁽⁴⁾ as the 2 first terms of equ.1, where K_0 and K_∞ are the DC and the optical dielectric constant respectively, and γ_p is the damping coefficient for the harmonic oscillator.

For doped semiconductors, the plasmon phonon coupling introduces an additional term⁽⁴⁾ and K is written

$$K = K_\infty + \frac{W_{TO}^2 (K_0 - K_\infty)}{W_{TO}^2 - W^2 + i \gamma_p W} + \frac{K_\infty W_p^2}{W(W - i \gamma_e)} \quad (1)$$

where W_p is the plasmon frequency, and γ_e its damping coefficient. The carrier concentration N and the mobility μ can be extracted from W_p and γ_e respectively through the relations (m^* effective mass, c light speed)

$$W_p^2 = \frac{Nq^2}{4\pi c^2 K_\infty m^*} \quad (2) \quad \gamma_e = \frac{q}{2\pi c m^* \mu} \quad (3)$$

W_p and γ_e can be derived from n and k (or α) the real and imaginary parts of the refractive index respectively (α absorption coefficient related to

k through $\alpha = 4\pi kW$. n and k can be calculated from the real (K_1) and the imaginary (K_2) parts of the dielectric constant⁽⁴⁾ $K = K_1 - iK_2$ through

$$n = \frac{((K_1^2 + K_2^2)^{1/2} + K_1)^{1/2}}{2^{1/2}} \quad (4) \quad k = \frac{((K_1^2 + K_2^2)^{1/2} - K_1)^{1/2}}{2^{1/2}} \quad (5)$$

n and α can be extracted from optical measurements on the structure. The expressions of the transmission T and reflection R can be determined analytically or computed versus n, k and α , but in general, n, k, α cannot be calculated analytically or computed from T and R, and we are looking for fits of T and R versus W with the best values of W_p and γ_c through equ. 1 to 5.

The derivation of N and μ can only be done for the top layer, and requires the knowledge of all the optical characteristics of the underlying layers, and of the wavenumber W_{TO} and of the damping coefficient γ_p of the harmonic oscillator (equ. 1) of the top doped layer we look at.

The analytical expressions of T and R are simple and classical when only an absorbing substrate (optically "thick" layer) is studied

$$T = \frac{(1-R_{01})^2 \exp(-\alpha_1 d_1)}{1-R_{01}^2 \exp(-2\alpha_1 d_1)} \quad R_{01} = R_{10} = \frac{(n_1-1)^2 + k_1^2}{(n_1+1)^2 + k_1^2} \quad (6)$$

where the substrate (optical medium 1) has n_1 and k_1 as real and imaginary parts respectively for its refractive index, a thickness d_1 and is in the air (optical medium 0).

Those corresponding to several absorbing films (optically "thin" layers") stacked on a substrate are calculated and discussed elsewhere⁽³⁾. They are rapidly larger and larger as the number of the films is increasing, in particular because the phase shift introduced by the crossing of each film ϕ_i and interface Φ_{ij} has to be taken into account. For instance for a film (medium 3) on another film (medium 2) deposited on a substrate (medium 1) and measured in air, the reflectivity R_{03} at the air - film interface can be written

$$R_{03} = R_c + \frac{T_c^2 \exp(-\alpha_1 d_1) R_{01}}{1-R_{01} R_c' \exp(-2\alpha_1 d_1)} \quad (7) \quad \text{with } T_c = \frac{A}{D}; \quad R_c = \frac{B}{D}; \quad R_c' = \frac{C}{D} \quad \text{and}$$

$$A = \frac{n_1(n_3^2+k_3^2)(n_2^2+k_2^2)(1-R_{03})(1-R_{23})(1-R_{12}) \exp(-\alpha_2 d_2 - \alpha_3 d_3)}{n_3(n_3 n_2 + k_3 k_2)(n_2 n_1 + k_2 k_1)}$$

$$B = R_{03} + R_{23} \exp(-2\alpha_3 d_3) + R_{12} \exp(-2\alpha_3 d_3 - 2\alpha_2 d_2) + R_{03} R_{23} R_{12} \exp(-2\alpha_2 d_2) + 2\sqrt{R_{03} R_{23}} \exp(-\alpha_3 d_3) \cos(\Phi_{32} + 2\Phi_3 - \Phi_{03}) + 2\sqrt{R_{03} R_{12}} \exp(-\alpha_3 d_3 - \alpha_2 d_2) \cos(\Phi_{21} + 2\Phi_3 + 2\Phi_2 - \Phi_{03}) + 2R_{03} \sqrt{R_{23} R_{12}} \exp(-\alpha_2 d_2) \cos(\Phi_{32} + \Phi_{21} + 2\Phi_2) + 2R_{23} \sqrt{R_{03} R_{12}} \exp(-\alpha_3 d_3 - \alpha_2 d_2) \cos(2\Phi_3 - \Phi_{03} - \Phi_{21} - 2\Phi_2) + 2R_{12} \sqrt{R_{03} R_{23}} \exp(-\alpha_3 d_3 - 2\alpha_2 d_2) \cos(2\Phi_3 - \Phi_{03} - \Phi_{32}) + 2\sqrt{R_{23} R_{12}} \exp(-2\alpha_3 d_3 - \alpha_2 d_2) \cos(\Phi_{32} - \Phi_{21} - 2\Phi_2).$$

$$C = R_{12} + R_{23} \exp(-2\alpha_2 d_2) + R_{03} \exp(-2\alpha_3 d_3 - 2\alpha_2 d_2) + R_{03} R_{23} R_{12} \exp(-2\alpha_3 d_3) + 2\sqrt{R_{23} R_{12}} \exp(-\alpha_2 d_2) \cos(\Phi_{32} + 2\Phi_2 - \Phi_{21}) + 2\sqrt{R_{03} R_{12}} \exp(-\alpha_3 d_3 - \alpha_2 d_2) \cos(\Phi_{03} + 2\Phi_3 + 2\Phi_2 - \Phi_{21}) + 2R_{12} \sqrt{R_{03} R_{23}} \exp(-\alpha_3 d_3) \cos(\Phi_{03} + \Phi_{32} + 2\Phi_3) + 2R_{23} \sqrt{R_{03} R_{12}} \exp(-\alpha_3 d_3 - \alpha_2 d_2) \cos(\Phi_{03} + 2\Phi_3 - 2\Phi_2 + \Phi_{21}) + 2R_{03} \sqrt{R_{23} R_{12}} \exp(-2\alpha_3 d_3 - \alpha_2 d_2) \cos(\Phi_{32} - 2\Phi_2 + \Phi_{21}) + 2\sqrt{R_{03} R_{23}} \exp(-\alpha_3 d_3 - 2\alpha_2 d_2) \cos(\Phi_{03} + 2\Phi_3 - \Phi_{32}).$$

$$D = 1 + R_{03} R_{23} \exp(-2\alpha_3 d_3) + R_{23} R_{12} \exp(-2\alpha_2 d_2) + R_{03} R_{12} \exp(-2\alpha_3 d_3 - 2\alpha_2 d_2) + 2\sqrt{R_{03} R_{12}} \exp(-\alpha_3 d_3 - \alpha_2 d_2) \cos(\Phi_{03} + \Phi_{21} + 2\Phi_3 + 2\Phi_2) + 2R_{23} \sqrt{R_{03} R_{12}} \exp(-\alpha_3 d_3 - \alpha_2 d_2) \cos(\Phi_{03} + 2\Phi_3 - \Phi_{21} - 2\Phi_2) + 2R_{03} \sqrt{R_{23} R_{12}} \exp(-2\alpha_3 d_3 - \alpha_2 d_2) \cos(\Phi_{32} - \Phi_{21} - 2\Phi_2) + 2R_{12} \sqrt{R_{03} R_{23}} \exp(-\alpha_3 d_3 - 2\alpha_2 d_2) \cos(\Phi_{32} - \Phi_{03} - 2\Phi_3) + 2\sqrt{R_{03} R_{23}} \exp(-\alpha_3 d_3) \cos(\Phi_{03} + \Phi_{32} + 2\Phi_3) + 2\sqrt{R_{23} R_{12}} \exp(-\alpha_2 d_2) \cos(\Phi_{32} + \Phi_{21} + 2\Phi_2).$$

$$\text{with } R_{ij} = \frac{(n_i - n_j)^2 + (k_i - k_j)^2}{(n_i + n_j)^2 + (k_i + k_j)^2}; \quad \text{tg } \Phi_{ij} = \frac{2(k_j n_i - k_i n_j)}{(n_j^2 + k_j^2) - (n_i^2 + k_i^2)}; \quad \Phi_i = 2\pi n_i W d_i$$

As a first example, we give on Fig. 1A after Holm et al⁽²⁾, the experimental points and their fit (solid line) by the equ. 6 for the reflectivity of an isolated thick substrate of GaAs with three n type high doping levels. Table I shows the very good agreement between the electronic (Hall effect) and the optical determination of the carrier concentration and mobility.

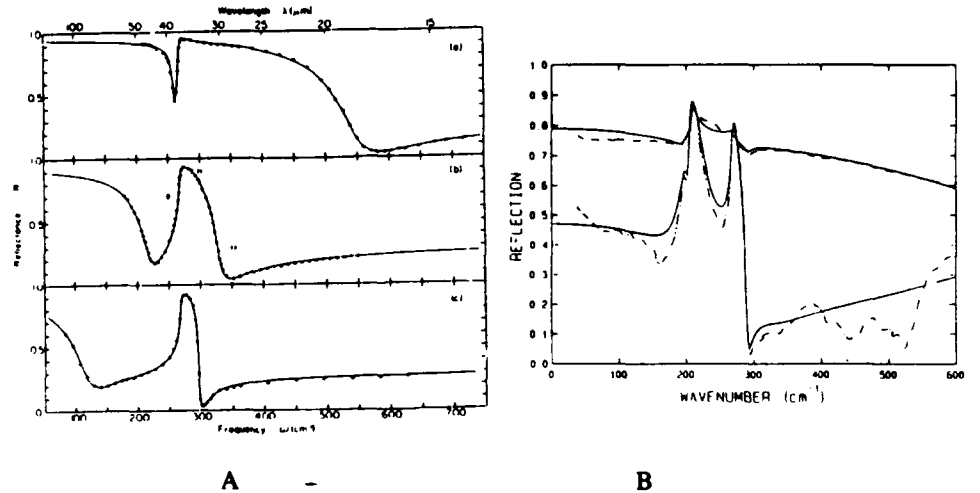


Fig. 1 : Reflection versus wavenumber for n-type doped semiconductors
A/ GaAs substrates, (.) experimental points, (—) fit, after Ref. 2 ; B/ Doped ZnSe film/ undoped ZnSe film/ SI GaAs substrate, (---) experiment, (—) fit.
See the samples characteristics on table I.

Table I : Comparison of the concentration N and mobility μ of carriers from electrical and optical measurements.

| sample | $N_{\text{opt}}(10^{16}\text{cm}^{-3})$ | $N_{\text{el}}(10^{16}\text{cm}^{-3})$ | $\mu_{\text{opt}}(\text{cm}^2 \text{V}^{-1}\text{s}^{-1})$ | $\mu_{\text{el}}(\text{cm}^2 \text{V}^{-1}\text{s}^{-1})$ |
|-----------|---|--|--|---|
| GaAs (a) | 270 | 280 | 1950 | 2360 |
| GaAs (b) | 70 | 83 | 2500 | 2750 |
| GaAs (c) | 16 | 20 | 2520 | 2900 |
| ZnSe top | 940 | 800 | 183 | 207 |
| ZnSe Bot. | 19 | 3 | 275 | 415 |

As a second example, we give on Fig. 1B, the experimental curve (broken line) and its fit through equ. 1 to 7, for high and low doping levels of n-type ZnSe films on an undoped ZnSe buffer film on GaAs semi insulating (SI) substrate, with $W_{\text{TO}} = 206 \text{ cm}^{-1}$ and $\gamma_e = 4.5 \text{ cm}^{-1}$. The fit is very good for $N = 9 \times 10^{18} \text{ cm}^{-3}$, but less good for $N = 3 \times 10^{16} \text{ cm}^{-3}$, in particular for the fine structures at low W . They originate from two phonons absorption in GaAs which induces significant structures at low doping levels, and which is not taken into account in the harmonic models used here. Quite generally, the transmission curves are much more sensitive at doping level $< 5 \times 10^{17} \text{ cm}^{-3}$, and better fits can be obtained using transmission measurements where the main contributions of the substrate and undoped ZnSe two phonons effects can be cancelled⁽³⁾. The values deduced for N and μ are compared to those deduced from Hall effect in Table I. The agreement is good for $9 \times 10^{18} \text{ cm}^{-3}$, but poor for $3 \times 10^{16} \text{ cm}^{-3}$. At low N , systematic differences with N_{el} and μ_{el} are also found from transmission, with close N_{opt} from R and T, but μ_{opt} lower and higher respectively than μ_{el} . These differences originate from slightly different physical species measured in optical and electrical measurements and are discussed in another paper⁽³⁾.

In conclusion, contactless IR reflectivity can be used to determine the carrier concentration N and mobility μ of thin films, or bulk semiconductors, with good agreement between optical and electrical N and μ for $N > 5 \times 10^{17} \text{ cm}^{-3}$. The lower range is discussed elsewhere⁽³⁾.

The author thanks Dr. Holloway, Tanner and Park of the University of Florida for helpfull discussions. This work was supported by DARPA grant MDA 972 88 5 1006.

REFERENCES

- 1/ I. Yokota, J. Phys. Soc. Jpn. **16** 2075 (1961); B. B. Varga, Phys. Rev. **137A** 1896 (1965); K. S. Singwi and M. P. Tosi, Phys. Rev. **147** 658 (1966).
- 2/ R. T. Holm, J. W. Gibson and E. D. Palik, J. Appl. Phys. **48** 212 (1977).
- 3/ A. Deneuve, G. Lindauer, D. B. Tanner, R. M. Park and P. H. Holloway, Appl. Phys. Lett. **57** 2458 (1990); A. Deneuve, D. B. Tanner and P. H. Holloway, Phys. Rev. **43** 15 March 91; A. Deneuve, V. Zeleny, D. B. Tanner, R. M. Park and P. H. Holloway, submitted for publication; A. Deneuve, V. Zeleny, D. B. Tanner and P. H. Holloway, submitted for publication.
- 4/ e. g. J. S. Blakemore, J. Appl. Phys. **53** R123 (1982).

Optically Confirmed Two-Dimensional Confinement Effects in Ultra-Narrow InGaAs/InP Quantum Well Wires

M. Notomi, M. Naganuma, H. Iwamura, T. Nishida
S. Nojima, M. Okamoto and T. Tamamura

NTT Opto-electronics Laboratories,
3-1 Morinosato-Wakamiya, Atsugi, Kanagawa 243-01, Japan

1. Introduction

Multi-dimensional hetero-structures, such as quantum well wires (QWWs), have been theoretically predicted to have numerous attractive aspects, which lead workers to many attempts at fabricating them.¹⁾⁻⁵⁾ Although several quantum confinement effects have been confirmed for conventional quantum well films (QWFs), for example, blue shifts of photoluminescence (PL) energy or observation of newly appeared quantized levels, there are almost no systematic data on QWWs. The reason for this is two fold. First of all, it is extremely difficult to fabricate optically-active QWWs which are small enough to exhibit lateral confinement effects and even if this difficulty is overcome, we are then forced with the task of systematically varying QWW size so as to examine these effects.

To eliminate these problems, we have adopted a fabrication procedure that combines EB lithography and reverse-mesa wet chemical etching (RMWE)⁵⁾. This process enables us to obtain optically-active ultra-narrow InGaAs/InP wires as narrow as 10 nm, as a result of the reverse-mesa profile and the damage-reducing property of RMWE. Furthermore lateral sizes of wires are easily controlled systematically by EB exposure conditions. Owing to this combination's superior characteristics, we confirmed, for the first time, an apparent blue shift of the PL wavelengths which varied consistently with the lateral dimension of the QWWs and observed several higher quantized levels including newly appeared lateral quantized levels in the PL measurements. We also performed a theoretical calculation of the quantized levels in QWWs and its result coincided with the above characteristics of PL peaks, which showed that they are caused by the lateral confinement effects. In addition to that, the observation of higher levels in the PL measurement suggests that the change in the density-of-state spectrum due to the one-dimensional nature of QWWs strongly affects the carrier relaxation process.

2. Fabrication Procedure

A schematic diagram outlining the fabrication process of the QWWs is shown in Fig.1. First, single QWF structure with a 3-nm InGaAs cap layer on

its top was grown by gas-source molecular beam epitaxy. Then a resist pattern was formed by EB lithography with an acceleration voltage of 50 keV. The EB resist used here was ϕ -MAC⁶) and a 150-nm pitch line-and-space pattern was written in the (110) direction.

Next, the 3-nm InGaAs thin layer was selectively etched by $\text{H}_2\text{SO}_4/\text{H}_2\text{O}_2/\text{H}_2\text{O}$. During this process side-etching is negligible because the etching depth is extremely small. After removing the resist, the InP layer was etched anisotropically into a reverse-mesa shape by $\text{HCl}/\text{H}_2\text{O}$ with no undercutting because the patterned InGaAs thin layer was used as an etching mask. Then QWWs were formed after etching of the SQW layer by $\text{H}_2\text{SO}_4/\text{H}_2\text{O}_2/\text{H}_2\text{O}$. Finally etched wires were embedded in InP by metalorganic vapor phase epitaxy.

Figure 2 shows cross-sectional views of an etched wire before embedding in InP (a) and of buried QWWs (c). It is clearly seen that RMWE was performed successfully even in these micro-structures. The lateral size of QWWs in this figure is about 10 nm. To our knowledge, these are the smallest wires fabricated by the lithography process ever reported.

3. Optical measurements

We examined the optical properties of buried QWWs by low-temperature photoluminescence measurements. In contrast to the dry-etched wires, the wet-etched ultra-narrow wires of the present case were not *optically dead* and we could investigate the PL properties of wires as narrow as 10 nm. Figure 2 shows the PL spectrum of 10-nm wide wires, 20-nm wide wires and unpatterned QWF. In this figure, it is apparently shown that the PL wavelengths are shifted as the lateral size of wires decreases, which is consistent with the blue shift due to the lateral quantum confinement effect in QWWs as mentioned before. In addition, a peculiar shoulder structure was seen in the spectrum of 20-nm wires at a wavelength of about 50 nm shorter than the main peak. This shoulder-shape structure was observed in every 20-50 nm wide wires and it also shifted to a shorter wavelength as the wire width decreased. As the main peak is thought to be the 11H transition, we assigned this shoulder structure to 12H, which is the first subband that appeared as a result of the lateral quantization.

Figure 4 exhibits the energy shift of the PL main peak (solid circle) and of the shoulder structure (open circle) versus wire width. These were scaled from the PL peak of the reference SQW. The shifts of both structures increase with decreasing wire width, which is expected from the lateral confinement effect.

In order to clarify the lateral confinement effect, we calculated the energy levels in InGaAs/InP. We assumed rectangular QWWs confined by a finite potential. The solid line and the broken line in Fig.4 show the calculated energy shift of the 11H transition and the 12H transition for the InGaAs/InP QWW of 5-nm vertical width, respectively. It can be clearly seen that there is a fairly good agreement between the theoretical curves and the experimental data, which verifies that the dependence of the shift is caused by the lateral confinement. This

is the first systematic result that evidently shows that the PL wavelengths of the ground level and the subband level are dependent on wire width and its dependency agrees with the theoretical expectation.

Besides these structures, we observed other peaks in the PL measurement. Figure 5 shows the PL spectrum of 25-nm wide wires. In this figure two remarkable peaks were observed in the higher energy region. These high energy peaks appeared only in 25-30 nm wide wires. We assigned these to the 11L and 12L transitions. Furthermore, we performed PL measurements of QWW samples whose vertical width was 12 nm. In these thicker samples, we observed 11L and 21H transition for the wires narrower than 30 nm. Because 11L and 21H are excited levels that appear as a result of the vertical quantization, they must exist even in QWFs. These assignments are consistent with the PLE measurement of the QWF. For QWF structures, the excited levels are unobservable in the conventional CW PL measurement. These facts indicate that the PL of QWWs is quite different from that of QWFs. One possibility for this is that change in the density-of-state spectrum due to two-dimensional quantization - it becomes spiky in QWWs - might affect the relaxation process of the excited carriers or might affect the band-filling process. A more detailed mechanism is under investigation.

4. Conclusion

We fabricated optically-active ultra-narrow InGaAs/InP QWWs between 10-80nm wide utilizing EB lithography and reverse-mesa wet etching and successfully obtained photoluminescence in all these wires. As a result, we have observed, for the first time, systematically varying blue-shifted features in both the ground level and the subband level in the PL spectrum, which coincide well with our calculation. Furthermore, we found that, in contrast to QWFs, several higher levels were observable by PL measurements in QWWs, which suggests that a change in the density of state plays a significant role in the luminescence process of QWWs.

References

- 1) H.Temkin, G.J.Dolan, M.B.Panish and S.N.G.Chu, Appl.Phys.Lett. **50**, 413 (1987)
- 2) M.Tsuchiya, J.M.Gains, R.H.Yan, R.J.Simes, P.O.Holtz, L.A.Coldren and P.M.Petroff, Phys.Rev.Lett. **62**, 466 (1989)
- 3) T.Fukui and H.Saito, Appl.Phys.Lett. **50**, 824 (1987)
- 4) B.E.Maile, A.Forchel, R.Germann and D.Grutzmacher, Appl.Phys.Lett.**54**, 1522 (1989)
- 5) M.Naganuma, M.Nojima, H.Iwamura, M.Okamoto, T.Nishida and T.Tamamura, J.Cryst.Growth **105**, 254 (1990)
- 6) K.Harada, O.Kogure and K.Murase, IEEE Trans. ED-**29**, 518 (1982)

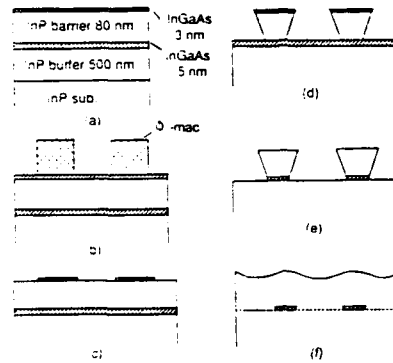


Fig.1 Schematic of fabrication process

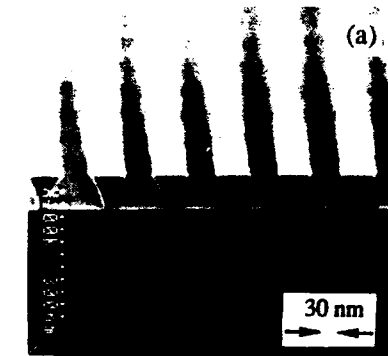


Fig.2 SEM photograph of (a) the as-etched QWWs and (b) the buried QWWs

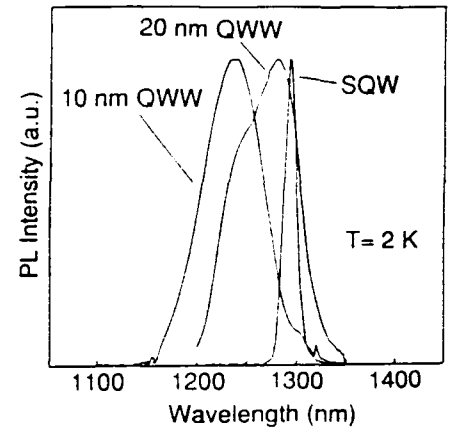


Fig.3 PL spectrum of wires and reference

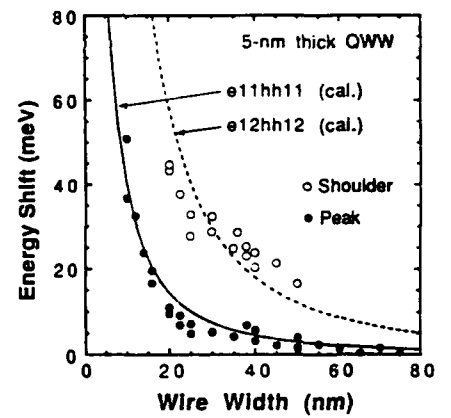


Fig.4 Energy shift of PL main peaks and shoulder structures. Calculated levels are also plotted.

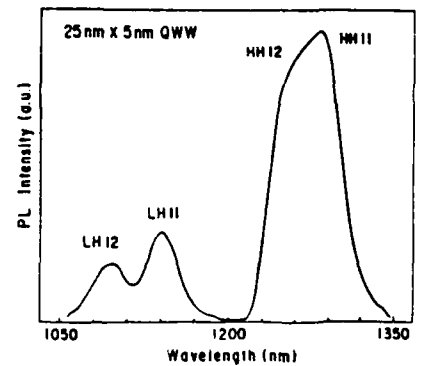


Fig.5 PL spectrum of wires. High-energy peaks are observed.

LASER SCATTEROMETRY FOR PROCESS CHARACTERIZATION

S.M. Gaspar, K.C. Hickman, K.P. Bishop, S.S. Naqvi
and J.R. McNeil

Center for High Technology Materials
University of New Mexico
Albuquerque, NM 87131

Scott Wilson and Yale E. Strausser
Sandia Systems, Inc.
Albuquerque, NM 87111

and

Richard A. Gottscho and Avi Kornblit
AT&T Bell Laboratories
Murray Hill, NJ 07974

Laser scatterometry is a technique which involves shining a light beam on an area to be characterized and measuring the angular distribution of the light that is scattered from that area. A laser is used so that the incident light will be monochromatic and coherent. It is also valuable, in many applications, to be able to confine the probe beam to a selected area, with a diameter of $10\text{ }\mu\text{m}$ or more. The scattered light distribution is typically measured either by scanning a detector over an arc, using a fixed array of photodiodes that are mounted along an arc, or by measuring the scattered light intensity distribution at a hemispherical screen when sample symmetry requires more than a one dimensional distribution measurement. In most cases, a single line measurement along a 90° arc is sufficient, either because of sample symmetry or because of the ability to align the sample in the direction of interest. The wavelength of the light used is a determining factor in the range of feature sizes that will be measured. Thus, different wavelength sources are sometimes valuable. Also, the angle of incidence of the probing light beam is a factor in the range of features that will be characterized.

At the present time laser scatterometry has been used to characterize three different types of features in semiconductor processing. First it has been used to measure random surface roughness and rms slope of the structure. Within the spatial frequency bandwidth of the instrument, which is 0.014 to $1.6\text{ }\mu\text{m}^{-1}$ using 633nm wavelength light, it gives an immediate measure of the rms roughness of a reflecting surface, for rms roughness from approximately 2 to $500\text{ }\text{\AA}$, the spacial frequency distribution of the roughness, and the rms slope of the roughness. This has been used to give a quick, non-destructive characterization of the MBE GaAs, MOCVD AlGaAs, MOCVD InSb, CVD tungsten and tungsten silicide, LPCVD polysilicon and sputtered aluminum films. In each case, defective films (e.g., oval defects from MBE, oxide defects from MOCVD, etc.) have a distinctive signature. A correlation has been observed between Al film roughness determined using the scatterometer and grain size determined by subsequent SEM examination, indicating the optical technique can be used as a fast, non-destructive grain size monitor. Another application to roughness, although not random, is to planarization effectiveness. The scatter technique has been used in a qualitative mode to monitor the remaining non-planarization on chemical-mechanical polish planarized samples.

The second type of feature to which scatterometry has been applied is periodic topographic structures. The best example of this application is the characterization of plasma etch profiles. In a periodic field of topographic features, the scattered light

distribution is very sensitive to small changes in distances and angles. Overcutting and undercutting of line sidewalls are easily recognized. Step height variations are quickly detected. A theoretical analysis of this scatter is underway. However, it isn't needed to effectively use the technique. It is possible to store the signature of a properly etched field and to compare the signal from an unknown area to it. This eliminates the need for destructive, time consuming sample preparation and SEM cross section analysis.

The third type of feature that has been investigated is the 'virtual' structure of an optically transparent sample with scatter originating from topographic structure and from within the sample. Applications include measuring ion implant dosages which have been monitored from $10^{11}/\text{cm}^2$ to $10^{18}/\text{cm}^2$. Implant doses in this range produce a quantitative signature prior to annealing. A second type of subsurface feature, which has been observed, is latent (exposed but undeveloped) images in photoresist. Laser scatterometry has been shown to be able to provide a valuable real time, *in situ* exposure meter for a stepper. We have demonstrated significantly improved CD control over the standard procedure of constant exposure time. In addition, scatterometry provides a significant time and material savings over the usual daily procedure of exposing, processing, preparing and SEMing wafers for calibration of photolithography equipment.

There are a number of very important advantages of laser scatterometry over the various other techniques that can measure certain of these feature types. The technique is rapid, quantitative and very reproducible. This is important in measuring many locations to characterize across-wafer or wafer-to-wafer variations in a feature of interest. It is non-destructive, non-contaminating and non-invasive. No sample preparation is necessary; only a light beam impinges on the surface of interest, and nothing is changed in the sample during the measurement. The measurement apparatus is simple enough that the measurement might be made *in situ* in many wafer processing systems. In some cases it could also be a real time process control monitor.

Study of Epitaxial Growth by UHV-SEM and RHEED-TRAX

Shozo Ino

Department of Physics, Faculty of Science, University of Tokyo, Bunkyo-ku, Tokyo 113, Japan

Abstract

RHEED-TRAXS method has high sensitivity for the elementary analysis. Applying this method we studied the position during adsorption and epitaxial growth of InSb/Si(100) and Ge/Sn/Ge(111) systems. We have UHV-SEM which has a high resolution of about 5 Å. Using the UHV-SEM we can observe directly the details from the two dimensional surface structures such as $\text{Au}, \sqrt{3} \times \sqrt{3}$ -Ag which are formed on Au, Ag/Si(111) system.

1. Surface Elementary Analysis by RHEED-TRAXS

There are no detailed studies on the surface composition during epitaxial growth. It is well known that AES (Auger Electron Spectroscopy) has high sensitivity for surface analysis. AES has, however, some difficulty to perform analysis during epitaxy especially for high gas pressure such as GaAs because of the charging effect of an analyzer due to contaminations by the gases.

During a RHEED experiment [1-2], many X-rays are excited on sample surfaces hit by the electron beam. We have observed a phenomenon that if a X-ray detector is put at the angle corresponding to the critical angle of the total reflection of characteristic X-rays, surface detection sensitivity is high [3,4]. The sensitivity is generally comparable to or higher than that for suitable conditions. We call this method RHEED-TRAXS (Total Reflection Angle X-ray Spectroscopy). In this case, there is no charging problem for the elementary analysis during epitaxial growth since the X-rays excited during experiments are taken out in air through a thin Be window. The UHV and air sides are separated, and are measured by a normal X-ray detector.

Applying RHEED-TRAXS method we have studied adsorption, epitaxial, alloying processes of Au, Ag, InSb etc. on the clean Si(111), Si(100), Si(110), Ge(111) surfaces [5-7]. In the next sections two typical systems, Ge/Sn/Ge(111) and InSb/Si(100) will be described.

2. A RHEED-TRAXS Study of Epitaxial Growth of InSb

Figure 1 shows adsorption curves of In and Sb measured by RHEED-TRAXS.

TRAXS method during epitaxial growth of InSb on a clean Si(100) surface[8]. In and Sb atoms were evaporated separately from different furnaces and exposed simultaneously with a same evaporation speed of 0.1 ML/min.

At room temperature the adsorbed thicknesses of In and Sb increased linearly at first for $\theta \leq 1.0$ (θ : Coverage) with $SP = 1.0$ (SP : Sticking Probability) for each metals. Then the sticking probability decreased gradually with the increase of exposed amount, keeping the same composition of In:Sb = 1:1. At higher temperatures, however, adsorption curves of In and Sb changed drastically depending upon the temperature as shown in Fig. 1. For temperatures higher than 300°C, deposited Sb thickness increased linearly for $\theta \leq 1.0$ and for $TE \leq 2.0$ (TE : Total Exposure Amount of In and Sb: ML) with $SP = 1.0$, and then it stopped to increase, that is, $SP = 0$ thereafter. The similar adsorption curves of Sb were obtained for the temperatures from 300°C to 600°C. On the other hand, In adsorption curves showed complex behaviors depending upon the temperature. As shown in Fig. 1(a), at 400°C-420°C In adsorbed with $SP = 1.0$ at first for $TE \leq 1.0$ and for $\theta \leq 0.5$, and then SP decreased slightly for $TE = 1.0-2.0$, and again increased for $TE = 2.0-8.0$. At about 430°C In desorption began for $TE = 1.0-2.0$, and it became rapid at high temperatures. At 440°C-480°C In adsorbed by 0.5 ML at first, and then decreased quickly for $TE = 1.0-2.0$ and slowly for $TE \geq 2.0$. At 500°C-600°C, as shown in Fig. 1(b), maximum coverage at $TE = 1.0$ decreased as the temperature rise.

3. A RHEED-TRAXS Study of Epitaxial growth of Ge/Sn/Ge(111)

When about a half ML of Sn atoms were deposited on the clean Ge(111)-c(2×8) surface at about 400°C, a new 7×7-Sn superstructure is formed[9]. We deposited Ge on this 7×7-Sn surface. When Ge deposition began, RHEED intensity oscillations of the specular spot were observed for the temperatures between 140°C and 250°C.

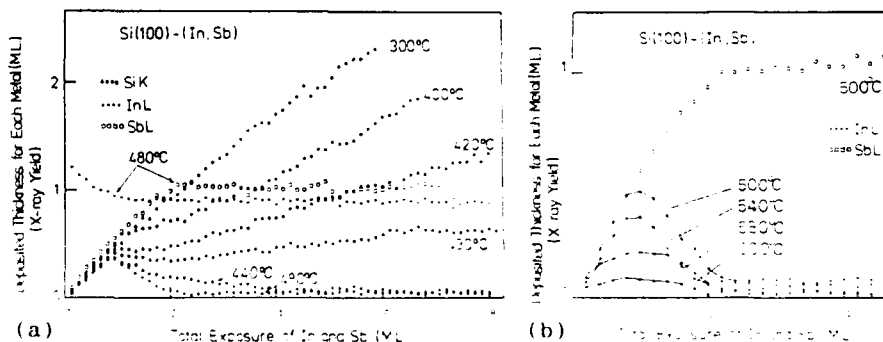


Fig. 1 Adsorption curves of In and Sb on Si(100) surface measured by RHEED-TRAXS method. (a): 300°C - 480°C, (b): 500°C - 600°C.

Thus, Ge grows on this surface in a layer-by-layer fashion through two dimensional nucleation. It is very interesting to study the behavior of the Sn atoms during the growth.

Figure 2 shows the change of SnL α β characteristic X-ray intensity measured by TRAXS method during the growth[10]. The intensity of the GeL α characteristic X-ray showed always a constant value during the growth for temperatures from room temperature to 350°C, whereas SnL α β decreased with the increase of deposited amount of Ge. At the higher substrate temperature, the decreasing rate of SnL α β became smaller. At about 350°C SnL α β intensity remains almost constant during the growth. Taking into consideration the attenuation coefficient of the SnL α β X-ray for Ge, we concluded that Sn atom layer deposited at room temperature remains at the interface between the substrate and the deposited Ge layer. The Sn atoms deposited at a temperature higher than 350°C, however, can move and remain always on the surface[10], which is consistent with the RHEED observations.

4. SEM images of Surface Structures of Au,Ag/Si(111)

We have constructed a high resolution UHV-SEM(Scanning Electron Microscopy)apparatus which can obtain 1.7×10^{-10} Torr through baking all the parts related to the ultra-high vacuum[11-12]. In the STEM (Scanning Transmission Electron Microscopy) mode, a lattice image (1.43 Å) of Au(220) has been clearly observed. In the SEM mode, a resolution of about 5 Å has been obtained for an image taken from deposited Au particles on a carbon film.

When 0.2-0.3 ML of Au was deposited at 600°C on a clean Si(111) surface, the 7×7 and 5×2-Au structures are formed simultaneously [1-2]. This sample was prepared in an another UHV chamber equipped

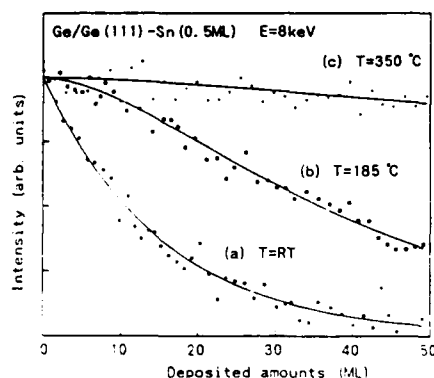


Fig.2 Change of SnL α intensity during epitaxial growth of Ge/Sn/Ge(111).

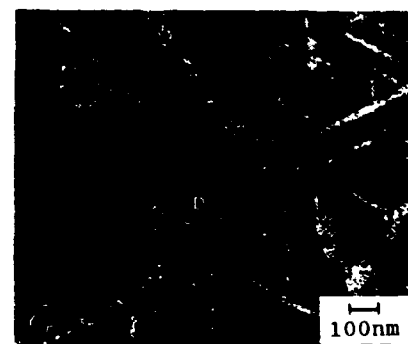


Fig.3 SEM image of Au/Si(111). Three kinds of contrasts, B(Bright), D(Dark) and M(Middle) are seen.

to the SEM column and investigated beforehand by RHEED in detail, and then transferred into the SEM column without exposing to air.

Figure 3 shows a typical SEM image taken from such a sample [12]. The acceleration voltage was 80keV. The electron beam is incident perpendicular to the sample surface. The secondary electrons were spiraled up by a strong magnetic field of a magnetic lens and gathered and detected by an electron multiplier. In Fig. 3, three kinds of contrast, B(Bright), D(Dark) and M(Middle) are observed. The contrasts B and D correspond to the 5×2 -Au and the 7×7 structures, respectively. The domains with the contrast B appear mainly along the surface steps, but are also formed on the terraces. These are three kinds of elongated domains whose directions make a fixed angle 120° to each other. The origin of the contrast M is not clear at present.

When 0.2-0.3 ML of Ag was deposited on a clean Si(111) surface held at 450°C , the 7×7 and $\sqrt{3} \times \sqrt{3}$ -Ag structures were formed simultaneously[2]. Three kinds of domains B($\sqrt{3} \times \sqrt{3}$ -Ag), D(7×7) and M are clearly observed just like in the case of Au. The boundary of the domain D on the terrace makes regular triangles. The domains B are formed along the surface steps and have irregular external forms. The structure of the area M is also observed but the origin is not clear at present.

References

1. S. Ino:Japan. J. Appl. Phys. 16,(1977)891.
2. S. Ino:Proc. NATO Advanced Research Workshop, June 15-19(1987), Netherlands, "RHEED and Reflection Electron Imaging of Surfaces" NATO ASI Series B 188,(1988)p3,(Plenum, New York).
3. S. Ino, T. Ichikawa and S. Okada:Japan. J. Appl. Phys. 19,(1980) 1451.
4. S. Hasegawa, S. Ino, Y. Yamamoto and H. Daimon:Japan. J. Appl. Phys. 24,(1985)L387.
5. S. Hasegawa, H. Daimon and S. Ino:Surf. Sci.186,(1987)128.
6. S. Ino, S. Hasegawa, H. Matsumoto and H. Daimon:Proc. 2nd Int. Con. on the Structure of surfaces(ICSOS II), Amsterdam, The Netherlands, June 22-25,(1987)p334.
7. S. Ino:The Report for "Grant-in-Aid for specially Promoted Research" supported by the Ministry of Education, Science and Culture of Japan, (1988) p(0-290).
8. H. Otaka and S. Ino:to be published.
9. T. Ichikawa and S. Ino:Suf. Sci. 105(1981)395.
10. K. Fukutani, H. Daimon and S. Ino:Proc. 3rd Int. Con. on the Structure of surfaces(ICSOS III), Milwaukee USA, July 9-12,(1990).
11. T. Tomita, Y. Kokubo, Y. Harada, H. Daimon and S. Ino:Proc. 12th Int. Con. for Electron Microscopy, Seattle USA,(1990) I -440.
12. A. Endo, H. Daimon and S. Ino:Proc. 12th Int. Con. for Electron Microscopy, Seattle USA,(1990) I -304.

SPECTROSCOPY and LUMINESCENCE with STM on III-V EPITAXIAL MULTILAYERS

O. Albrechtsen^{*}, S.F. Alvarado, H.P. Meier, Ph. Renaud and H.W.M. Salemink.

IBM Research Division, Zurich Research Laboratory, Säumerstr. 4, CH-8803 Rüschlikon, Switzerland

Atomic registry is observed in heterostructure interfaces and the transition of the valence edge is analyzed at nanometer scale. Also, the STM tip can act as an electron source to excite luminescence in single quantum wells and to probe the bulk conduction bands.

Introduction.

The growth and the characterization of semiconductor heterostructures with atomically controlled interfaces is of great interest in material science and in device applications. The STM technique¹, with its unprecedented spatial resolution and capabilities as a spectroscopic tool, is appropriate to address some of the fundamental aspects of structural and electronic properties of heterojunction interfaces.

Topography and I/V spectroscopy.

The figure 1 shows a constant current image of a GaAs/AlGaAs interface with atomic resolution. The As sublattice is imaged. The multilayer stack is cleaved in ultra high vacuum, and the STM tip is zoomed into the epitaxial layers, employing a SEM. The AlGaAs material displays the electronic effect of composition fluctuations on the atomic scale². The binary/ternary interface as observed, extends over a transition region of 1-2 unit cells (i.e. 0.56 - 1.1 nm) in the $\langle 001 \rangle$ growth direction.

From current-voltage (I-V) spectra, simultaneously acquired with topographic images, the position of the valence and the conduction band at the (110) non-polar surface can be determined. In particular, the continuity of the valence band across the GaAs/AlGaAs transition is monitored (fig.2). In the valence band spectroscopy, the transition occurs over a region of about six unit cells or 3.5 nm. The observed valence band offset of 300 meV is larger than calculated for the bulk: this discrepancy is caused by two effects: 1) Fermi level pinning due to residual gas chemisorption on the AlGaAs³ and 2) tip induced band bending at the (110) surface⁴.

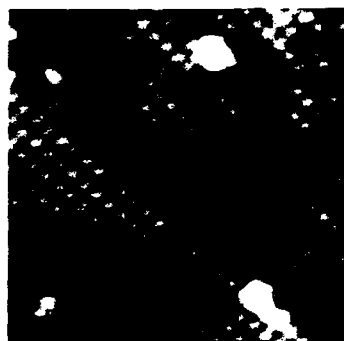


FIG.1 Atomically resolved constant current image of a GaAs/AlGaAs interface (GaAs lower left). Sample voltage +1.8 eV, imaging the As-sublattice.

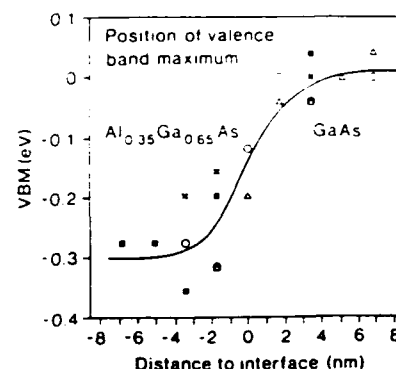


FIG.2 Transition in the valence band maximum, derived from a set of I-V curves, taken over an heterojunction³.

Luminescence:

When tunneling with negative tip voltage, the electrons can be injected into the semiconductor and luminescence may arise by the radiative recombination of these electrons in the material ⁵.

The STM-induced luminescence is described in a three step model⁶: i) Tunneling of electrons from the tip to the surface of the semiconductor. ii) Transport of the electrons from the surface into the bulk conduction band. iii) Diffusion and radiative recombination. When tunneling at energies below the bulk conduction band CB, electrons are reflected back to the surface and thus cannot reach the bulk. No luminescence is expected from the surface where the probability of radiative recombination is very low because of the reduced number of holes available if the band is strongly bent down. The bulk luminescence threshold begins when tunneling at eV_T just above the CB energy. At this energy some electrons are ballistically injected into the bulk where they recombine. Therefore the threshold voltage for luminescence can be associated to the LOCAL CB energy in the bulk. If the electrons are injected into a barrier (i.e. tunnel voltage < CB energy in the barrier), they will diffuse down to a neighbouring well where they are confined until the radiative recombination at the well energy. The figure 3 shows the luminescence intensity map of a series of 15 nm GaAs quantum wells separated with 15 nm $Al_{0.35}Ga_{0.65}As$ barrier. The doping level is $p = 10^{19} cm^{-3}$. The contrast arises from the difference of electron injection efficiency into the bulk between the well and the barrier. For narrow barriers however, the contrast is further reduced by the direct

scattering of the electrons into the well during the initial thermalization. Surface contaminants or defects can trap the electrons and then reduce the fraction which is injected into the bulk. Such surface trapping center are clearly visible as black spots in luminescence pictures (see arrow in figure 3).

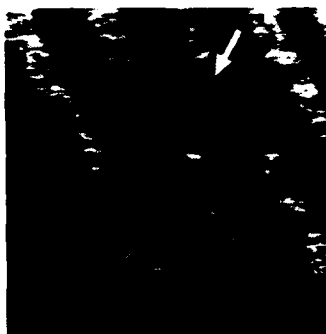


FIG.3 Luminescence image of a series of 15 nm GaAs quantum wells separated by 15 nm $Al_{0.38}Ga_{0.62}As$ barriers.

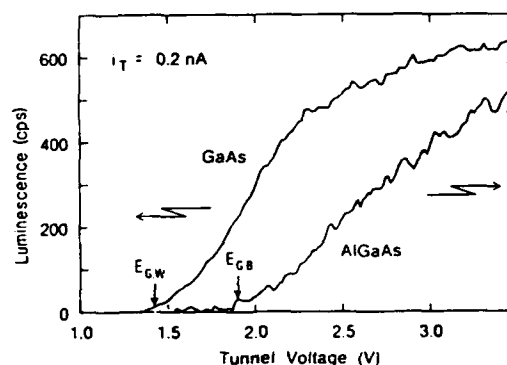


FIG.4 Luminescence intensity versus tunnel voltage on GaAs and AlGaAs. The labels show the respective CB energies⁵.

Figure 4 shows typical luminescence intensity versus tunnel voltage spectra measured at the center of a 50 nm GaAs well and for $Al_{0.38}Ga_{0.62}As$ about 100 nm away from the well. The threshold of luminescence occurs at a potential closely corresponding to the band gap of the III-V compound, $V_T = 1.42$ V for GaAs and $V_T = 1.96$ V for $Al_{0.38}Ga_{0.62}As$, as expected for heavily p-doped concentrations where the Fermi level lies very close to or below the valence band. This proves that the dominant contribution to luminescence is due to recombination of electrons injected deeply into the bulk by penetration the band bending region ballistically^{6,7}.

In conclusion, we have demonstrated the high potential of the techniques related to the scanning tunneling microscopy to determine fundamental properties of the semiconductor heterostructures at a nanometer scale in real space.

* Present address: Telecommunications Research Laboratory, DK-2970 Horsholm, Denmark.

¹ G.Binnig, Ch.Gerber, E.Weibel and H.Rohrer, Phys. Rev. Lett. 50, 120 (1983).

² O.Albrechtsen, D.J.Arent, H.P.Meier and H.W.Salemink Appl. Phys. Lett. 57, 31 (1990).

³ H.W.Salemink and O. Albrechtsen, J. Vac. Sci. Tech. B (to appear in April 1991 issue).

⁴ P.M.Koenraad, O.Albrechtsen and H.W.Salemink, to be published.

⁵ D.L.Abraham, A.Veider, Ch.Schönenberg, H.P.Meier, D.J.Arent and S.F.Alvarado, Appl. Phys. Lett. 56, 1564 (1990).

⁶ S.F.Alvarado, Ph.Renaud, D.L.Abraham, Ch.Schönenberg, H.P.Arent and H.P.Meier, J. Vac. Sci. Tech B (to appear in April 1991 issue).

⁷ Ph. Renaud and S.F.Alvarado, to be published.

Ga_{0.47}In_{0.53}As/InP Multiquantum Well Structures Observed
by Scanning Tunneling Microscopy under Ultrahigh Vacuum

Takashi Kato, Fukunobu Osaka, Ichiro Tanaka and Shunsuke
Ohkouchi

Optoelectronics Technology Research Laboratory

5-5 Tohkodai, Tsukuba, Ibaraki 300-26, JAPAN

Multiquantum wells (MQW's) are being widely applied to various electronic and optoelectronic devices. It is of vital importance to characterize MQW structures such as period, uniformity of barrier and well layers and abruptness of hetero-interfaces as exactly as possible. A scanning tunneling microscope (STM) is considered as a useful tool to observe MQW structures with a high resolution. However, only a few data on this issue have been reported⁽¹⁻³⁾.

We have constructed a new STM having x- and z-inchworms for micro-positioning under an ultrahigh vacuum (UHV) environment, and have observed Ga_{0.47}In_{0.53}As/InP MQW structures. Figure 1 schematically shows a top-view diagram of our STM. x-inchworm was used for both cleaving a sample and moving it to positions of interest, and z-inchworm was used for approaching a tip to the sample surface. For cleavage, the sample was moved toward the block and was pressed against it. A tube-type scanner with three tips was mounted on the z-inchworm. On the x-inchworm were mounted two samples and a tungsten (W) ribbon heater used for in-situ tip cleaning by electron bombardment. Electrochemically etched W tips were used. The maximum travel distances of the x- and z-inchworms were 30 and 10 mm, respectively. The resolution of these inchworms was better than 0.5 μm . The movement of the inchworms was controlled by a personal computer, and the approach to the tunneling region was carried out automatically.

The performance of our STM was first checked by observing a cleaved GaAs (110) surface at a sample voltage (V_s) of -2 V and a tunneling current (I_t) of 100 pA under a pressure of 1×10^{-8} Pa.

Figure 2 shows an atom-resolved STM image of the occupied states on arsenic atoms. It demonstrates that our STM has a sufficient resolution to study cleaved surfaces on the atomic scale.

We then observed GaInAs/InP MQW structures. The MQW samples were grown on n^+ -InP (001) substrates by an organometallic vapor phase epitaxy. An n^+ -InP buffer layer and a few-dozen periods of an n^+ -type GaInAs (10 nm)/InP (10 nm) MQW's were successively grown. The position of the MQW region on the cleaved surface was searched by combining the x-inchworm having the resolution of 0.5 μm and the tube-type scanner having the scan range of 4 μm . Figure 3 (a) and (b) show a wide-range and a narrow-range images, respectively, of the MQW region measured at V_s of -2 V and I_t of 100 pA. The white and the black regions correspond to the GaInAs well layers and InP barrier layers, respectively. This is explained as follows. Electrons tunnel from valence states of the sample surface to empty states above the Fermi level of the tip, since the sample voltage is negative. More electrons can tunnel from a GaInAs well surface than from an InP barrier surface, as can be seen from the valence band structure of the MQW's which is schematically depicted in Fig.4. The position of the tip becomes higher on a GaInAs surface than on an InP surface in order to keep the tunneling current constant. In Fig.3(b) we can clearly observe atomic arrays of the group-V anions. However, at present, we cannot distinguish individual arsenic atoms on a GaInAs well surface and phosphorus atoms on an InP barrier surface. Figure 5 shows a cross-sectional view along line A-B in Fig.3(b). The slowly varying component of the height corresponds to the valence band structure of the MQW's shown in Fig.4, in which the number of valence states contributing to the tunneling gradually changes from a GaInAs well region to an InP barrier region. Therefore, the position of a hetero-interface cannot be exactly identified from this figure. The measurement at a positive sample voltage is thought to be necessary for the identification of the position of a hetero-interface.

In conclusion, we have constructed a compact-sized STM for the observation of a cleaved surface in UHV with an atomic resolution, and have obtained high-resolution STM images of

$\text{Ga}_{0.47}\text{In}_{0.53}\text{As}/\text{InP}$ MQW structures measured in UHV. The images clearly show periodic arrangements of the well and barrier layers, as well as atomic arrays of the group-V anions. It has been shown that the STM images can be explained by the valence band structure of the MQW region.

References

- 1.F.Osaka, I.Tanaka, T.Kato and Y.Katayama, Japan. J. Appl. Phys., 27, L1193 (1988).
- 2.T.Kato, F.Osaka and I.Tanaka, Japan. J. Appl. Phys., 28, 1050 (1989).
- 3.O.Albrechtsen, D.J.Arent, H.P.Meier and H.W.M.Salemink, Appl. Phys. Lett., 57, 31 (1990).

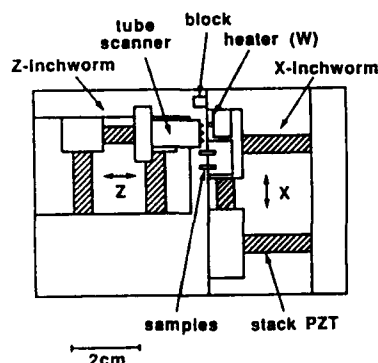


Figure 1. Schematic top-view diagram of our STM.

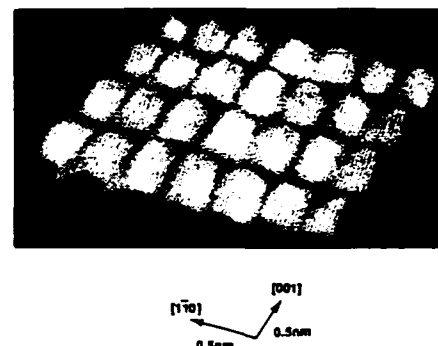
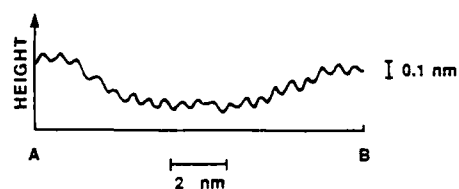
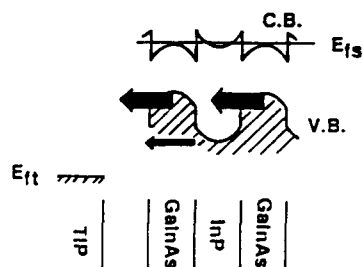
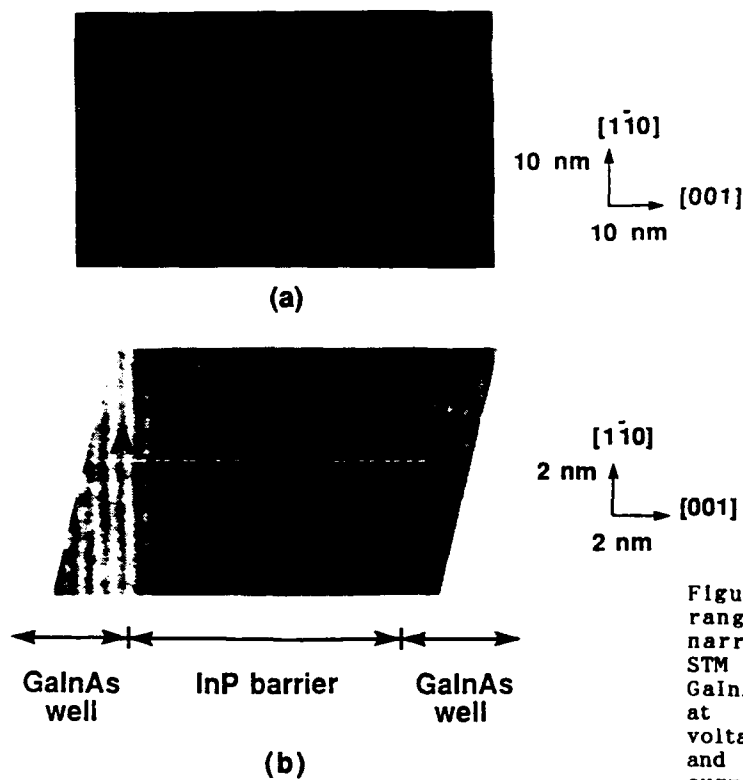


Figure 2. STM image of an n-GaAs (110) cleaved surface at a sample voltage of -2 V and a tunneling current of 100 pA. The topographic height is 0.1 nm.



Characterization of Strained Heterostructures by Cathodoluminescence

D. Bimberg, M. Grundmann and J. Christen
 Institut für Festkörperphysik, Technische Universität Berlin,
 Hardenbergstraße 36, 1000 Berlin 12, Germany

Cathodoluminescence (CL) provides information about the local variation of the defect structure, the impurity incorporation and the electronic bandstructure of semiconductor layers which might be buried below the surface. It is particularly useful for the non-destructive characterization of device structures. In this paper we review some of recent results on strained layer structures. As model systems we investigate $\text{In}_{0.23}\text{Ga}_{0.77}\text{As}/\text{GaAs}$ -, InP/Si - and locally deposited GaAs/Si -layers.

1. Experimental set-up

Our CL setup for spatially, spectrally and time-resolved experiments in the *near infrared* has been described previously [1,2], so we would like to summarize only briefly some of its features.

For *spatially resolved* experiments the exciting electron beam is digitally scanned across the surface of the crystal using the scanning coils of a scanning electron microscope (SEM). The rectangular area under investigation (max. 1 mm x 2 mm) is equally divided into max. 400 x 512 pixels. For *spectrally resolved* measurements the CL is dispersed in a 0.3 m grating monochromator.

For *time-resolved* CL experiments the sample is excited by electron pulses long enough (several 10 ns) so that a quasi-equilibrium of the carriers is reached. The luminescence decay is measured by means of a temperature-stabilized and Peltier-cooled Si-avalanche photodiode and time correlated single photon counting. The time resolution of the whole setup is 350 ps.

In cathodoluminescence wavelength imaging (CLWI) at each pixel not only the luminescence for a *fixed* wavelength is measured but the *whole luminescence spectrum* is simultaneously recorded using an MCP intensified Si-Diode array providing a spectral range from 350 nm - 890 nm. The wavelength interval simultaneously monitored within 512 channels is easily adjusted by selecting adapted gratings ($\Delta\lambda = 113.8$ nm using a 300 lines/mm grating). The amount of data is reduced *online* by extracting some scalars of interest (i.e. peak wavelength, intensities at selected wavelengths) from the recorded spectra. Further technical details are reported in [2]. This technique represents an ideal tool for direct imaging of lateral variations of bandgap.

2. Samples

2.1 Partially relaxed $\text{In}_{0.23}\text{Ga}_{0.77}\text{As}/\text{GaAs}$

We investigate a series of five samples, each one containing a single QW ($L_z = 16, 22, 27, 32$ and 38 nm for samples B1309, ..., B1313 from HP). The growth temperature was 515°C [3]. On top of the $\text{In}_{0.23}\text{Ga}_{0.77}\text{As}$ layer a 50 nm GaAs cap layer was grown.

2.2 GaAs on patterned Si

These samples made at OKI Electric Industries consist typically of a 0.8 μm GaAs layer directly grown onto a (001) Si-substrate (oriented 3° off toward $\bar{1}10$) by a recently developed maskless selective growth technique [13]. V-grooves are etched into the Si along $\langle 1\bar{1}0 \rangle$ and $\langle 110 \rangle$ with a depth and a stripe width of 1.5 μm and 2 μm , respectively. The GaAs is deposited by MOCVD (at 100 Torr) using a two step growth process [4]. The GaAs grows only on top of the (001) facets but not on the {111} sidewalls. In this way large mesas (350 μm x 350 μm) separated by two ridges and three grooves on each side were defined as schematically shown in Fig.1.

2.3 InP on Si

The InP layers on Si (001) are prepared by MOCVD (at TUB) in a two step growth procedure *without* preannealing of the Si substrate [5]. The InP buffer layer was grown at $T=400^\circ\text{C}$. For off-orientations θ larger than 3.5° antiphase-domain (APD) free films are obtained, while films prepared on Si with smaller off-cut exhibit APDs. The size of the APDs increases with increasing InP thickness; in this work we present results on 8 μm thick InP layers, grown on Si (001) with an off-cut of 0.8° and 3.8° with and without APDs, respectively.

3. Results

3.1 Partially relaxed $\text{In}_{0.23}\text{Ga}_{0.77}\text{As}/\text{GaAs}$

In Fig.2 we show spectrally integrated CL images (ICLIs) for the five samples directly visualizing the lateral variation of quantum efficiency. The $L_z=22\text{nm}$ QW shows the misfit dislocations as single distinct straight lines of reduced quantum efficiency (dark line defects). The $L_z=16\text{nm}$ QW shows no dislocations on this scale. ICLIs taken at lower magnification, imaging a larger area, indicate a line dislocation density of $n_L=4\cdot 10^3\text{m}^{-1}$. In QWs with $L_z\geq 27\text{nm}$ single misfit dislocations are no longer observed and the CLI consists of dark line defects at an average distance saturating at about 2 μm corresponding to groups of dislocations [6]. For the determination of n_L at higher dislocation densities, plan-view two-beam TEM experiments are used. The critical thickness [7] is found to be about $L_z=15\text{nm}$ for $x=0.23$ in agreement with theoretical predictions by Matthews and Blakeslee [8].

In all samples the misfit dislocations are preferentially orientated along $[110]$, while the density of dislocations along $[1\bar{1}0]$ is substantially smaller. This explains the striped nature of the ICLIs at high dislocation density. The asymmetric dislocation density causes further anisotropies of structural, electronic and optical properties [9].

3.2 GaAs on patterned Si

In Fig.3a we show the CL peak wavelength image of the GaAs on Si mesa structure (for sample structure see Fig.1) taken at $T=6\text{K}$ together with the secondary electron (SE) image containing the topography contrast on this area (Fig.3b). The grayscale of Fig.3a corresponds to a peak emission wavelength ranging from 807.0nm to 833.7nm across the structure. It is clearly seen that at the boundary of the mesa the emission energy is substantially higher than at the center. Intensity images (Fig.3c and 3d) taken simultaneously in different wavelength windows corresponding to emission from

the boundary and the center exhibit complementary contrast as expected. Fig.4 displays a linescan of the bandgap across the structure (along the black line indicated in Fig.3a) and visualizes the variation of emission energy. The energy shift is due to Si incorporation from the uncovered Si {111} sidewalls ("autodoping"). In the mesa center the average peak emission energy is 1.492eV, corresponding to a Si concentration up to $n_{Si} \approx 1 \cdot 10^{16} \text{cm}^{-3}$ [10]. The shift in emission energy to the mesa boundary is due to an increase of Si concentration to around $n_{Si} \approx 3 \cdot 10^{18} \text{cm}^{-3}$ [11].

3.3 InP on Si

The lateral variation of intensity is imaged in Fig.5. We compare two $8\mu\text{m}$ thick InP layers grown on 3.8° and 0.8° off-cut Si (001), being APD free and showing twisted APD boundaries, respectively. The intensity of emission of the samples without APDs is not directly correlated to the surface topology (Figs.5a,b). The waviness of the surface is somewhat reproduced by the intensity pattern; the most bright areas correspond to regions with flat morphology. In samples with APDs (Figs.5c,d) the CL intensity is very low at the APD boundary while the inner part of the APD (i.e. the region whose distance to the domain boundary is larger than the diffusion length) is very bright because defects like dislocations and stacking faults have been gettered in the boundary.

4. Summary

Several modes of operation of scanning cathodoluminescence have been demonstrated to be useful for the characterization of defects in strained layer semiconductor structures.

Acknowledgement

We are very much indebted to A.Fischer-Colbrie (HP, Palo Alto, USA) and T.Fukunaga (OKI, Tokyo, Japan) for generously supplying excellent samples. The work at TUB has been funded by the DFG in the frame of SFB 6 and by the BMFT under contract no. TK03175.

References

- [1] J.Christen, D.Bimberg, Oyo Buturi 5Z, 69 (1988)
- [2] J.Christen, M.Grundmann, D.Bimberg, Appl.Surf.Sci. 41/42, 329 (1989)
- [3] A.Fischer-Colbrie, J.N.Miller, S.S.Laderman, S.J.Rosner, R.Hull, J.Vac. Sci.Technol. B 6, 620 (1988)
- [4] A.Hashimoto, Y.Kawarada, T.Kamijoh, M.Akiyama, N.Watanabe, M.Sakuta, Appl. Phys. Lett. 48, 1617 (1986)
- [5] M.Grundmann, A.Krost, D.Bimberg, Appl.Phys.Lett. 58, 284 (1991)
- [6] E.A.Fitzgerald, G.D.Ast, P.D.Kirchner, G.D.Pettit, J.M.Woodall, J. Appl. Phys. 63, 693 (1988)
- [7] M.Grundmann, J.Christen, D.Bimberg, A.Fischer-Colbrie, R.Hull, J.Appl.Phys. 66, 2214 (1989)
- [8] J.W.Matthews, A.E.Blakeslee, J.Cryst.Growth 2Z, 118 (1974)
- [9] M.Grundmann, U.Lienert, D.Bimberg, B.Sievers, F.R.Keßler, A.Fischer-Colbrie, J.N.Miller, Proc. ICPS-20 (World Scientific, Singapore) p. 945
- [10] T.Takamori, T.Fukunaga, J.Kobayashi, K.Ishida, H.Nakashima, Jap. J. Appl. Phys. 26, 1097 (1987)
- [11] M.Grundmann, J.Christen, D.Bimberg, A.Hashimoto, T.Fukunaga, N.Watanabe, Appl. Phys. Lett., in print

- Fig.1 Schematic sample structure: Mesa bounded by three V-grooves.
 Fig.2 Integral CL images of single $\text{In}_{0.23}\text{Ga}_{0.77}\text{As}/\text{GaAs}$ QWs. Increasing QW thickness leads to increasing density of dark line defects.
 Fig.3 GaAs mesa on V-grooved Si: a) CLWI, b) SE image, c) CL intensity in wavelength window corresponding to emission at the mesa boundary, d) at the mesa center. All images a)-d) are recorded *simultaneously*.
 Fig.4 CL peak emission energy linescan (along white line in Fig.3a).
 Fig.5 SEM (a,c) and CL intensity (b,d) images of $8\mu\text{m}$ thick InP layers grown on 3.8° (a,b) and 0.8° (c,d) off-cut Si (001) without and with APDs, respectively. Marker represents $5\mu\text{m}$.

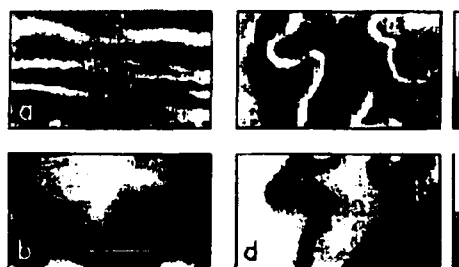
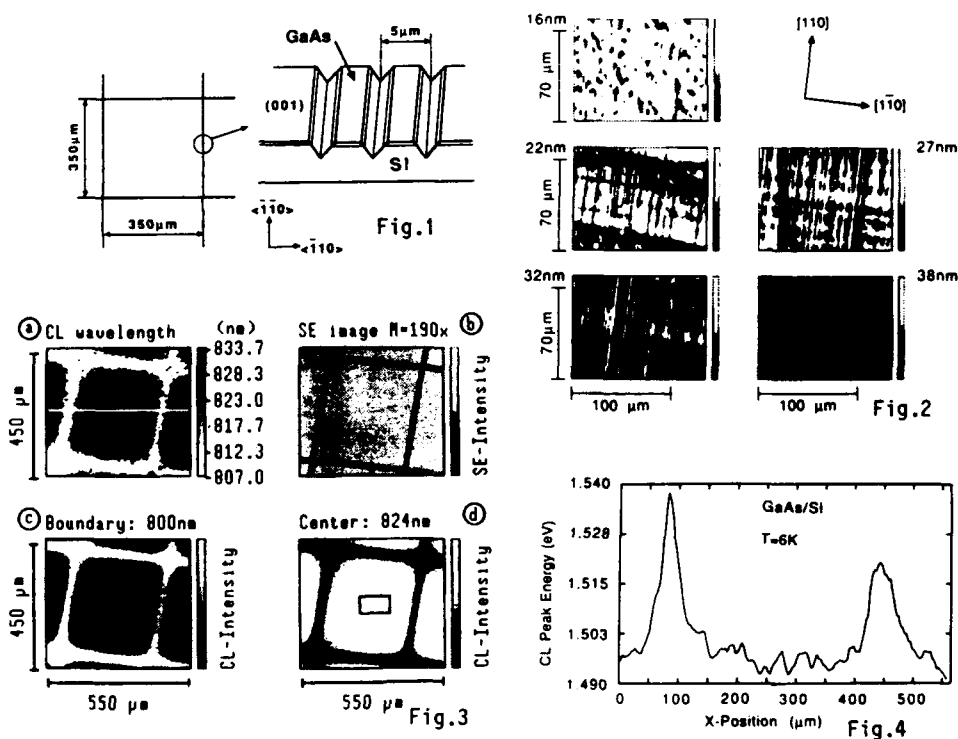


Fig.5

III. PROCESSING

Quantum Sized Structures

| | |
|--|----|
| Formation of AlGaAs Quantum Wire-Like Structures on Vicinal (110) GaAs Substrates by Molecular Beam Epitaxy | 76 |
| <i>H. Nakashima, M. Sato, K. Maehashi, K. Kimura, H. Asahi, S. Hasegawa and K. Inoue</i> | |
| Fabrication of Arrays of High Quality Quantum Filaments by Deep UV Holography and MBE Growth on Channelled Substrates | 80 |
| <i>U. Marti, M. Proctor, R. Monnard, D. Martin, F.K. Reinhard, R. Widmer and H. Lehmann</i> | |
| Mesoscopic Size Fabrication Technology | 84 |
| <i>Y. Arakawa</i> | |
| Lateral Field Effect in Focused-Ion Beam Written In-Plane-Gated Systems | 88 |
| <i>A.D. Wieck, A. Fischer and K. Ploog</i> | |

Applications of Ion Beams and Etching

| | |
|--|-----|
| Focused-Ion-Beam Micromachining: A Fabrication Tool for Prototypal Semiconductor Lasers | 92 |
| <i>R.K. DeFrez</i> | |
| A Novel Vacuum Lithography with SiN_x Resist by Focused Ion Beam Exposure and Dry Etching Development | 96 |
| <i>S. Takahashi, M. Ohashi, S. Fukatsu, Y. Shiraki and R. Ito</i> | |
| ECR Plasma Etching of III-V Optoelectronic Devices | 100 |
| <i>S.J. Pearton</i> | |
| Influence of SiCl₄ Reactive Ion Etching on the Electrical Characteristics of GaAs | 104 |
| <i>D. Lootens, P. Clauws, P. Van Daele and P. Demeester</i> | |
| Electron-beam Writing System for Holographic Optical Elements | 108 |
| <i>Y. Hori, F. Sogawa and M. Kato</i> | |
| Micro Dry Etching Process for Vertical Cavity Surface Emitting Lasers | 112 |
| <i>A. Matsutani, F. Koyama and K. Iga</i> | |

Surfaces and Contacts

| | |
|--|-----|
| Sulfide Treatment on III-V Compound Surfaces | 116 |
| <i>Y. Nannichi</i> | |
| Sulfur Passivation of GaAs Surfaces | 118 |
| <i>Y. Wang and P.H. Holloway</i> | |
| Direct Observation of GaAs Surface Cleaning Process Under Hydrogen Radical Beam Irradiation | 122 |
| <i>H. Iwata and K. Asakawa</i> | |

| | |
|--|-----|
| Near Surface Type Conversion of p-type, Single Crystal InP by Plasma Exposure | 126 |
| <i>X. Li, T.A. Gessert and T.J. Coutts</i> | |
| Advances in Controlling Electrical Contacts for Optoelectronics | 130 |
| <i>L.J. Brillson</i> | |
| Indium Ohmic Contacts to n-ZnSe | 134 |
| <i>Y.X. Wang and P.H. Holloway</i> | |
| Diffusions and Large Areas | |
| A New Method of Zn Diffusion into InP for Optical Device Fabrication | 138 |
| <i>M. Wada, K. Sakakibara and Y. Sekiguchi</i> | |
| Open Tube Double Diffusion for the Fabrication of Bipolar Transistor Waveguide Optical Switch | 142 |
| <i>D.K. Gautam, Y. Nakano and K. Tada</i> | |
| Full-Water Technology for Laser Fabrication and Testing | 146 |
| <i>D.J. Webb, M.K. Benedict, G.L. Bona, P. Buchmann, N. Cahoon, K. Darwyler, H.P. Dietrich, A. Moser, G. Sasso, H.K. Seitz, P. Vettiger, O. Voegeli and P. Wolf</i> | |
| Fabrication Issues and Considerations for High Performance Grating- Surface-Emitting Semiconductor Lasers | 150 |
| <i>G.A. Evans, N.W. Carlson, J.M. Hammer, D.P. Bour, J.B. Kirk, S.K. Liew, H. Lee, W. Reichert, R.K. DeFreez, C.A. Wang, H.K. Choi, J.N. Walpole and J.K. Butler</i> | |
| Epitaxial Liftoff Technology for OEIC's | 154 |
| <i>E. Yablonovitch, W.K. Chan and A. Yi-Yan</i> | |

Formation of AlGaAs Quantum Wire-Like Structures on Vicinal (110) GaAs Substrates by Molecular Beam Epitaxy

Hisao Nakashima, Masamichi Sato, Kenzo Maehashi, Kenta Kimura, Hajime Asahi, Shigehiko Hasegawa and Koichi Inoue

The Institute of Scientific and Industrial Research, Osaka University
8-1 Mihogaoka, Ibaraki, Osaka 567, Japan

Many attempts have been made to fabricate quantum wire or box structures¹⁻⁵), because they are expected to show superior optical properties and unique electronic transport properties. However, these excellent properties have not been experimentally confirmed because of the difficulties in fabricating quantum wire structures.

Recently, we have found that quantum wire-like structures were formed in the AlGaAs/GaAs superlattices grown on cleaved and vicinal (110) GaAs surfaces^{6,7}) by molecular beam epitaxy (MBE). Scanning electron microscopic (SEM) observations and electron probe microanalysis (EPMA) measurements revealed that the (111)A facet formation at giant step edges during growth and orientation dependent AlAs mole fraction of AlGaAs layers induce the quantum wire-like structures. In this paper, we discuss the formation mechanisms of quantum wire-like structures on vicinal (110) surfaces and propose a new approach for fabricating quantum wire structures.

Superlattices composed of 300 Å thick Al_{0.5}Ga_{0.5}As layers and 300 Å thick GaAs layers with 8 periods were grown on vicinal (110) surfaces misoriented 6° toward (111)A and (111)B and nominal (110) surfaces oriented within ±0.5° for comparison, by MBE using AsH₃. Growth temperature, growth rate of GaAs layers and AsH₃ flow rate were 580°C, 0.1 μm/h and 1.5 sccm, respectively. Quantum wire-like structures are observed only for the sample grown on vicinal (110) surfaces misoriented 6° toward (111)B, as shown in Fig. 1. The dark regions in the cross sectional SEM micrograph correspond to AlGaAs layers which were selectively etched by 1 : 21 : 20 solution of HF : H₂O : C₂H₅OH. A precise investigation of the SEM micrograph shown in Fig. 1 indicates that steps are formed during earlier stage of growth and become higher and more coherent as growth proceeds. Two kinds of facets, i.e. (111)A and (111)B are formed at the giant step edges, as schematically illustrated in Fig. 2. The flat surfaces of terraces between giant steps incline about 5° to the interface between the epitaxial layer and substrate, which means that the surface are oriented exact (110).

SEM micrograph of the surface of the same sample as in Fig. 1 shows that almost equally spaced steps are coherently aligned along <110> direction, as shown in Fig. 3. The distance between the steps is about 3000 Å. Allen et al.⁸) have found that the layer nucleation is taking place only at the step edges with Ga-terminated (111)A facets and the epitaxial growth proceeds in a layer-by-layer growth mechanism on vicinal (110) surfaces misoriented 6° toward (111)A. Their result is very consistent with ours that the growth on vicinal (110) surfaces misoriented

6° toward (111)A provides the smooth surface morphology and superlattices without quantum wire-like structures. On the vicinal (110) surfaces misoriented 6° toward (111)B, we considered that the (111)B facets at giant step edges interrupt lateral growth resulting in the formation of (111)A facet at the step edges, as schematically illustrated in Fig. 2. The nominal (110) surfaces are locally misoriented toward different directions. This local misorientation produces the surfaces with differently oriented facets and incoherent superlattices without quantum wire-like structures.

Since the quantum wire-like structures shown in Fig. 1 are induced at this (111)A facet, AlAs mole fraction of AlGaAs layers on (110) surfaces is thought to be different from that on (111)A surfaces, as schematically shown in Fig. 2. Then, a 1 μm thick $\text{Al}_{0.5}\text{Ga}_{0.5}\text{As}$ layer was grown on a GaAs (110) substrate with mesa structures composed of (110), (111)A, (111)B and (100) surfaces. The surface of the $\text{Al}_{0.5}\text{Ga}_{0.5}\text{As}$ layer was covered with a 2500 Å thick GaAs cap layer. EPMA measurements carried out at each surface revealed that the AlAs mole fraction of the AlGaAs layer on (111)A surfaces is smaller than that on (110) surfaces. This result is very consistent with that of cathodoluminescence measurements which showed an orientation dependent AlAs mole fraction in AlGaAs epitaxial layers.⁹⁾ This orientation dependent AlAs mole fraction can be explained by the orientation dependence of the Al sticking coefficient and/or surface diffusion length. The quantum wire-like structures shown in Fig. 1 are considered to be due to the (111)A facet formation and orientation dependent AlAs mole fraction.

Using this phenomenon, quantum wire structures can easily be made without sophisticated process. If $\text{Al}_{x_1}\text{Ga}_{1-x_1}\text{As}/\text{Al}_{x_3}\text{Ga}_{1-x_3}\text{As}$ superlattices ($x_1 > x_3$) are grown on vicinal (110) surfaces misoriented 6° toward (111)B, the small rectangular regions with AlAs mole fraction x_4 less than x_1 , x_2, x_3 are expected to be formed at the giant step edges in the $\text{Al}_{x_3}\text{Ga}_{1-x_3}\text{As}$ layers, as schematically illustrated in Fig. 4. These small rectangular regions are buried in the AlGaAs layers with higher AlAs mole fraction resulting in quantum wire structures.

In conclusion, the quantum wire-like structures were formed in the MBE grown AlGaAs/GaAs superlattices on vicinal (110) GaAs surfaces misoriented 6° toward (111)B. These structures were coherently aligned along $\langle 110 \rangle$ direction with almost equal spacing. SEM observations and EPMA measurements confirm that the (111)A facet formation during growth and orientation dependent AlAs mole fraction of AlGaAs layers induce the quantum wire-like structures. Using this phenomenon, we think that we can easily fabricate quantum wire structures without any sophisticated process.

Acknowledgments ---- The authors would like to thank Dr. N. Fujita and T. Tomikawa of Sumitomo Electric Industry Ltd. for SEM observation, T. Tanaka of Osaka University for EPMA measurements and Y. Okuda of Osaka University for his help in computer control of MBE. They would also like to thank K. Kamon of Sumitomo Electric Industry Ltd. and T. Inada of Hitachi Cable Ltd. for supplying GaAs substrates, and Prof. S. Gonda for his support.

This work was supported by a grant from the Research Program on "Creation of New Materials through Intelligent Design" of ISIR, Osaka University.

References

- 1) J. Cibert, P. M. Petroff, G. J. Dolan, S. T. Pearton, A. C. Gossard and J. H. English, *Appl. Phys. Lett.* **49** (1986) 1275.
- 2) Y. Hirayama, T. Tarucha, T. Suzuki and H. Okamoto, *Phys. Rev. B* **37** (1988) 2774.
- 3) K. Ismail, W. Chu, D. A. Antoniadis and H. I. Smith, *Appl. Phys. Lett.* **52** (1988) 1071.
- 4) P. M. Petroff, A. C. Gossard and W. Wiegmann, *Appl. Phys. Lett.* **45** (1984) 620.
- 5) T. Fukui and H. Saito, *J. Vac. Sci. Technol.* **B6** (1988) 1373.
- 6) M. Sato, K. Maehashi, H. Asahi, S. Hasegawa and H. Nakashima, *Superlattices and Microstructures* **7** (1990) 279.
- 7) S. Hasegawa, M. Sato, K. Maehashi, H. Asahi and H. Nakashima, to be published in *J. Crystal Growth*.
- 8) L. T. P. Allen, E. R. Weber, J. Washburn and Y. C. Pao, *Appl. Phys. Lett.* **51** (1987) 670.
- 9) M. E. Hoenk, H. Z. Chen, A. Yariv, H. Morkoc and K. J. Vahala, *Appl. Phys. Lett.* **54** (1989) 1347.

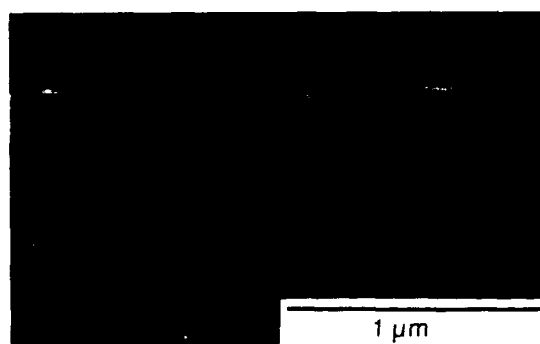


Fig.1 Cross sectional SEM micrograph of the $\text{Al}_{0.5}\text{Ga}_{0.5}\text{As}$ (300 Å) / GaAs (300 Å) superlattice grown on a vicinal (110) GaAs surface misoriented 6° toward (111)B.

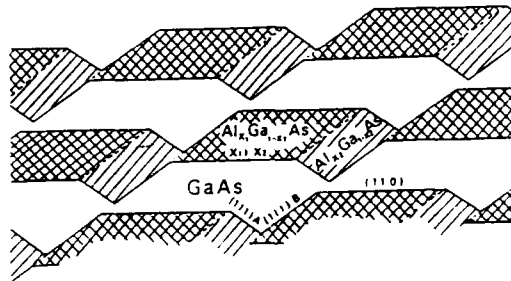


Fig.2 Schematic illustration of the superlattice structure shown in Fig. 1.

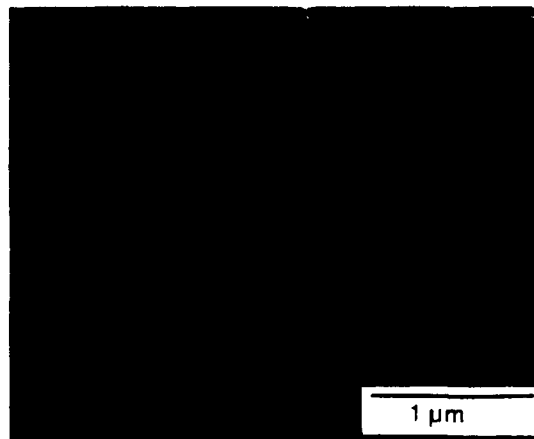


Fig.3 SEM micrograph of the surface of the sample shown in Fig. 1

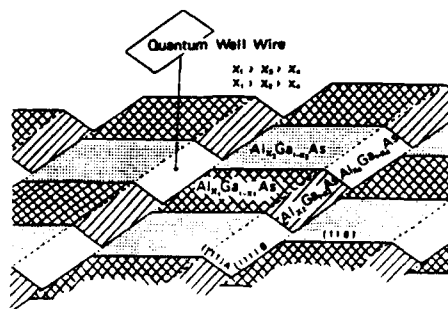


Fig.4 Schematic illustration of the proposed quantum wire structures.

FABRICATION OF ARRAYS OF HIGH QUALITY QUANTUM FILAMENTS BY DEEP UV HOLOGRAPHY AND MBE GROWTH ON CHANNELLED SUBSTRATES

U.Marti, M. Proctor, R. Monnard, D. Martin, F. Morier-Genoud, F.K. Reinhart
Institut de Micro- et d'Optoélectronique,
Ecole Polytechnique Fédérale, CH-1015 Lausanne, Switzerland

R.Widmer, H. Lehmann
PSI c/o Laboratories RCA Ltd, CH-8048 Zürich, Switzerland

Deep UV ($\lambda=257\text{nm}$) holographic lithography is greatly improved by the application of an antireflective coating and a negative (chemical amplification) resist. Deep 90nm period gratings and smallest feature sizes of 40nm are transferred by dry etching to the substrate. Molecular beam epitaxial growth on finely channelled substrates allows us to fabricate high density arrays of buried GaAlAs quantum wires (filaments) (QF) with an optical quality comparable to flat quantum wells. Orientation of the grating lines along the [011] direction is shown to be the most suited for QF with very small lateral dimensions.

1. Introduction

Arrays of quantum well filaments (QF) and dots (QD) hold great potential for improvement of integrated optical devices such as lasers [1] and modulators [2]. Nevertheless the fabrication of QF and QD with an optical quality comparable to standard quantum wells (QW) still remains a challenge [3,4]. One class of possible approaches consists of postgrowth patterning of QW material. This process generally generates defects that are detrimental to the optical properties of QF [3]. A second approach is the fabrication of QF by QW growth on patterned non planar substrates [5,6]. This method has the potential of producing defect free interfaces. However difficulties in crystal preparation before introduction into the growth chamber can lead to detrimental interface roughness and incorporation of impurities, due to thin ($d=60\text{nm}$) buffer layers. Holography with deep UV laser light ($\lambda<257\text{nm}$) shows several interesting features for the efficient fabrication of large arrays of identical nm structures with a high packing density. However, for short period gratings (period $\lambda<200\text{nm}$) standard holographic lithography produces poor resist profiles that allow for less freedom in transferring the pattern to the substrate.

2. Short period holographic lithography

Holography is a highly parallel process that generates independently of the period, fringes of almost 100% contrast by the interference of two laser beams of near equal intensities. Near ideal wave fronts can be produced easily resulting in an interference pattern of excellent uniformity. To take full advantage of these features we eliminate the substrate reflection by an antireflective coating (ARC) using hard baked Novolack. Standing wave patterns parallel to the sample interface destroy the high contrast of the fringes and pinch off very fine resist structures with lateral width $< 100\text{nm}$.

Due to the relatively high optical density of available Novolack resists for $\lambda<300\text{nm}$, vertical resist profiles with high aspect ratios are more readily achieved with a negative rather than a positive process. We have investigated a classical image reversal resist (AZ 5200) and an experimental three component (chemical amplification) material designed for $\lambda=248\text{nm}$ (DN 21, Höchst). The latter shows an increase in sensitivity by a factor of 20 to 50 with respect to AZ 5200, depending on the post exposure bake (PEB) temperature. For both resists, at low PEB temperatures, the lateral feature size can be controlled independently of the period by the control of the exposure dose. We have made 150 nm period gratings with lateral dimension resist lines of about 40-110nm (respectively spaces from 110 to 40nm). When decreasing the grating period, the maximal acceptable PEB temperature has to be decreased and some loss in sensitivity occurs, due to lateral diffusion of the catalyst. An important criteria is the vertical or slightly overhanging resist profile shown for both materials in Fig. 1a and Fig. 1b. The inherent properties of holography allow for further scaling down of the grating period by shortening the laser wavelength. We have successfully applied the prism technique ($\lambda_{\text{fused silica}}=171\text{nm}$) for the fabrication of 90nm period gratings (Fig.2).

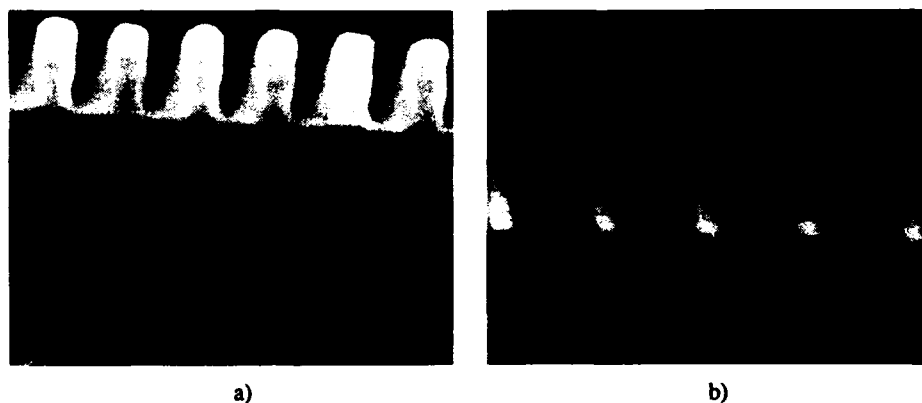


Fig.1: Developed photoresist profile on antireflective coating.

- a) AZ 5200; $L=135\text{nm}$; PEB: 116°C , 3min; Development: AZ Dev: $\text{H}_2\text{O}=1:2$, 90sec.
 b) DN 21 ; $L=185\text{nm}$; PEB: 100°C , 3min; Development: MF 312: $\text{H}_2\text{O}=1:1.5$, 120sec.

A typical fabrication procedure is summarized as follows:

- Application of Novolack ARC
- Application of negative resist
- Holographic exposure ($\lambda=257\text{nm}$, frequency doubled Ar-Laser)
- PEB and development
- Evaporation of NiCr and lift off
- Patterning of ARC by O_2 reactive ion etching.

As a result we obtain a high quality mask for subsequent dry etching of the substrate (Fig.3a,b).



Fig.2

Fig.3a

Fig.3b

Fig.2: Grating with $\Lambda=92\text{nm}$, after patterning of ARC.

Fig.3: Structures etched by MERIE into GaAs.

- a) Dot like structure has been achieved by crossed holograms ($\Lambda=155\text{nm}$).
 b) Grating ($\Lambda=195\text{nm}$) after mask removal.

3. MBE growth of quantum filaments on patterned substrates

GaAs (100) substrates were patterned with this improved holographic method. Gratings with different periods, crystallographic orientations, etching depths and profiles were etched using $\text{CCl}_2\text{F}_2/\text{Ar}$ RIE or SiCl_4 magnetically enhanced reactive ion etching (MERIE). In the first case the DC bias voltage (V_B) was 200V and the $\text{CCl}_2\text{F}_2/\text{Ar}$ ratio was varied over the entire range. In the second case V_B was varied between 40 and 120V. With both methods grating lines with very low sidewall roughness were obtained. After removal of the mask and a standard thermal oxide growth the samples were loaded into the MBE system.

Several sets of experiments were performed with different substrate temperatures between 580°C and 680°C with growth rates of 0.1-1.2 $\mu\text{m}/\text{h}$. One or several QW of different thickness separated by several periods of a short period AlAs/GaAs superlattice (SL) were grown. The samples were analysed by low temperature photoluminescence (PL) at 77K and 5K, photoluminescence excitation spectroscopy (PLE), phase contrast microscopy and scanning electron microscopy (SEM).

We investigated possible PL degradation due to a small thickness of the buffer layer. Enhanced impurity incorporation in such structures is possible due to segregation of surface contaminants (Carbon) and substrate impurities (Si etc). On unprocessed, undoped samples we found using PL a p-type impurity, probably Carbon, within the first 20nm of grown material by PL measurements. The growth rate and temperature were 0.3 $\mu\text{m}/\text{h}$ and 580°C respectively. No extra impurity effects were found in broad area RIE ($\text{CCl}_2\text{F}_2/\text{Ar} < 2:1$) or MERIE etched samples. For a SL buffer thickness of 60nm, analysis of a 5nm QW showed PL intensities and linewidths comparable to standard QW growth with thick buffers.

The overgrown grating samples were analysed by SEM. We observed only a little change of the etched grating profile during a standard pre-growth oxide desorption procedure. However, increasing of the heating time, and lowering the As_4 pressure or raising the temperature before growth started, resulted mainly in a rounding of the corners and a lowering of the modulation depth. For $[01\bar{1}]$ orientated grooves, GaAs grew mainly at the bottom and developed the (100) crystallographic plane (Fig.4a). As a consequence the lateral width of otherwise flat QW became progressively wider with increasing growth. For $[011]$ oriented grooves GaAs growth occurred also on the sidewalls (Fig.4b). A V-shaped profile is formed and subsequent planarisation occurs by the development of sidewalls with a higher crystal index. This clearly indicates that GaAs grows fastest in the corner of the V-groove to produce crescent cross-section layers (Fig.4c). Growth on gratings with deep and narrow grooves showed peculiarities due to facet dependent Ga adatom migration.

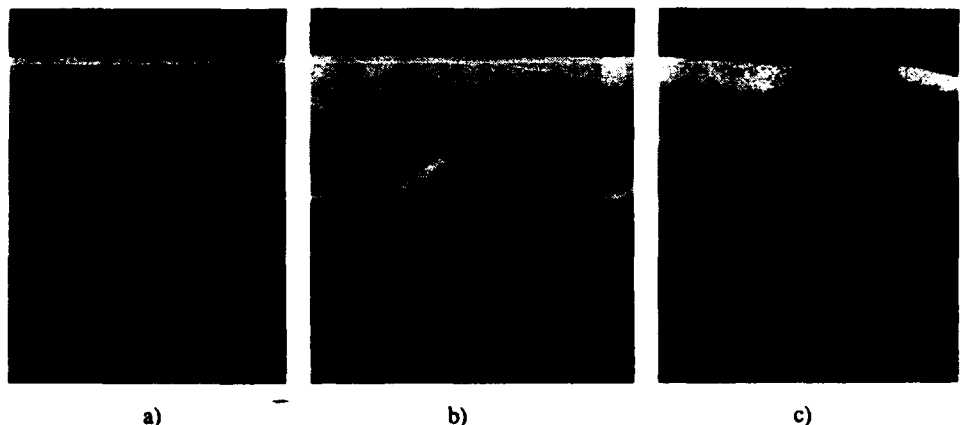


Fig.4: SEM cross-sectional micrographs of layers grown on grooved substrates (GaAs: dark, AlAs/GaAs SL bright).

- a) Orientation of the grating lines: $[01\bar{1}]$; b), c) Orientation of the grating lines: $[011]$.
- c) Crescent cross-section GaAs filament ($\lambda=180\text{nm}$).

Grating samples with near vertical profiles show very poor PL. Good results are obtained for sidewall angles smaller than about 45° . For these samples the following was established:

- The intensities of the QW peaks are similar for growth on grooved and flat substrates in both crystallographic orientations. For both cases the peaks have comparable line width and are less than 9meV for a 4.5nm well at 5K). For [011] orientation the minimal peak width was 5.5meV (6.5nm well, 5K).
- For short period gratings only one QW related PL peak corresponding to a QW in the groove and not on the mesa was found.
- For [01 $\bar{1}$] oriented grooves the photon energy of the QF PL peak was close to that grown on flat substrates. For [011] orientation the PL peak energy corresponded to considerably thicker QW.
- The Stokes shift between PL and PLE spectra was for [01 $\bar{1}$] oriented grooves in the range 3-5meV, however, for the [011] orientation we normally found Stokes shifts smaller than 2meV. This indicates that the well fluctuations may not be significant [8].

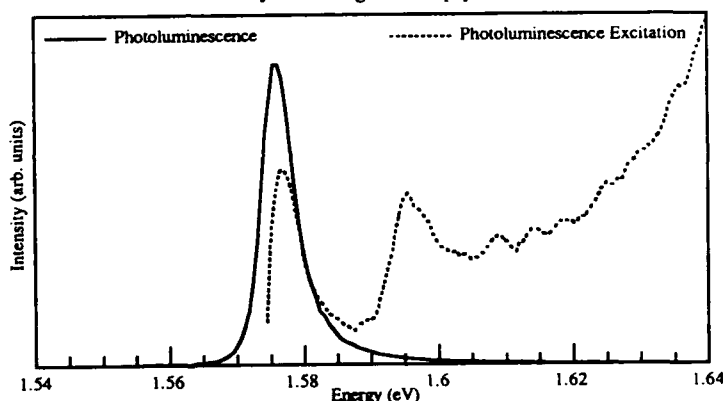


Fig.5: PL and PLE (5K) for QF with [011] orientation (grating period $\Lambda=140\text{nm}$). The PL peak (5K) for planar growth was at 1.649meV in this experiment.

4. Conclusions

We have demonstrated improved deep UV holographic lithography to be an efficient technique for the fabrication of large arrays of identical nm-structures with a high packing density. We achieved periods as short as 90nm and feature sizes for lines and dots near 30-40nm, and they have excellent uniformity. Chemical amplification resists have in addition to their high sensitivity a resolution capability better than 40nm. MBE growth on finely channeled substrates produces QF material with a quality comparable to standard QW growth with thick buffer layers. The [011] orientation of the grooves allows the fabrication of crescent profile quantum filaments with very small lateral dimensions and high optical quality.

This work was made possible through a collaboration with Thomson-CSF. We wish to thank P.C.Silva for assistance in MBE growth and grating fabrication, J.Bergheuer and G.Pawlowsky (Höchst) for providing DN 21 sample.

- [1] M.Asada, Y.Miyamoto, Y.Suemsatsu, IEEE J.Quantum Electron. QE-22, (1986) 1915.
- Y.Arakawa, A.Yariv, IEEE J. Quantum Electron. QE-22 (1986) 1887.
- [2] D.A.B.Miller, D.S.Chemla, S.Schmitt-Rink, Appl. Phys. Lett. 52(25), (1988) 2145.
- K.Matsubara, K.G.Ravikumar, M.Asada, Y.Suemsatsu, Trans. IEICE E 72(25), (1988) 2145.
- [3] B.E.Maile, A.Forchel, R.Germann, et al., J. Vac. Sci. Technol. B6, (1988) 2308.
- [4] F.S.Turco, S.Simhony, K.Kash, D.M.Hwang, et al. J.Crystal Growth 104 (1990) 766.
- [5] S.Nilson, E.Van Gison, D.J.Arent, H.P.Meier, et al., Appl. Phys. Lett. 55 (11), (1989), 972.
- [6] E.Kapon, M.C.Tamargo, D.M.Hwang, Appl. Phys. Lett. 50 (1987) 347.
- [7] C.V.Shank, R.V.Schmidt, Appl. Phys. Lett. 23 (1973) 154.
- [8] G.Bastard, C.Delalande, M.H.Meynadier, et al. Phys. Rev. Lett. 29(12), (1984), 7042.

Mesoscopic Size Fabrication Technology

Yasuhiko Arakawa

Research Center for Advanced Science and Technology, University of Tokyo

4-6-1 Komaba, Meguro-ku, Tokyo 153 Japan

1. Introduction

Mesoscopic and/or quantum microstructures have recently received great attentions, since new physical phenomena with possible applications to optical devices are expected in these structures^[1]. For this purpose, fabrication technologies including fractional layer superlattice growth^[2], the laser assisted atomic layer epitaxy^[3], and the facet wire growth^[4,5] are intensively investigated. In particular, use of both metal-organic chemical vapor deposition (MOCVD) selective growth technique and electron beam (EB) lithography technique would play important roles. In this paper, we discuss fabrication technologies for quantum wires and quantum boxes with emphasis on these electron-beam assisted MOCVD technologies. In addition, physics of the mesoscopic structures for laser applications is also discussed.

2. Electron-Beam Assisted MOCVD^[6]

Recently we have been investigating possibility of a selective growth named electron beam assisted MOCVD (EBI-MOCVD), in which irradiation of electron beam enhances or suppresses adsorption and/or decomposition of source materials on the substrate surface, resulting in formation of sub-nanometer-scale structures. Here, discussed are the selective growth condition, the source material dependence and the substrate temperature dependence of the deposition on GaAs substrates.

In our system, source materials are the same as the conventional MOCVD system; These are AsH₃, tri-methyl-gallium (TMG) and tri-methyl-aluminium (TMA) carried by H₂ gas flow. The gas flows are controlled by the mass flow controllers. AsH₃ can be cracked by a cracking cell up to 1200°C. The growth chamber and the electron beam gun are evacuated separately by the differential exhaust systems which consist of diffusion pumps and rotary pumps. The back-ground pressure in the chamber is about 10⁻⁷ torr and the pressure during the growth is about 10⁻⁴ torr. As regards the pressure, the growth mode in this method should be similar to that in metal organic molecular beam epitaxy (MOMBE) method. The electron beam can be irradiated onto the substrate surface during the growth. An electron beam current density is within the range from 1 to 100 A/cm², depending on an acceleration voltage. Substrates can be heated up to 700°C by the radiation heater.

We investigated the source material dependence and the temperature dependence of the selective growth on GaAs substrates. A wire structure was successfully formed when only TMA is supplied into the chamber at 400°C substrate temperature. The electron beam irradiation time is 1 hour. The dimension of the wire is about 1000 Å, which is not determined by the diameter of the

electron beam but by some evaporation problems in the system. Similar formation of the wire can be achieved at the temperature range between room temperature and 700°C. On the other hand, when only TMG is supplied, the selective growth is realized below 400°C. Thus, there exists difference in the temperature dependence between TMA and TMG.

There are several mechanisms which are considered for this selective formation, although it is not clear which mechanism is dominant. One is that TMG or TMA is directly decomposed into Ga, Al and CH₃ by the electron beam irradiation. In this case, TMG or TMA might be also completely decomposed into Ga or Al, C and H. Another is that TMG which is on the surface of the substrate is decomposed by electrons or holes generated by irradiation of the electron beam.

3. In-Situ Patterning of Contamination Resists in MOCVD⁽⁷⁾

An in-situ processes for fabrication of semiconductor quantum wire structures is also investigated, combining contamination resists and selective growth in MOCVD. We have succeeded in forming GaAs quasi-quantum wires with the width as narrow as 700 nm. In addition, Auger electron spectroscopy is used for identifying material of the contamination resists.

The fabrication system is the same as EBIMOCVD, discussed above. The time sequences of the growth are 1) electron beam irradiation onto the substrate surface to form contamination resists at room temperature, 2) heating the substrate up to 700 °C for thermal cleaning for a few minutes, 3) setting at the growth temperature, 4) supplying the source materials and crystal growth, and 5) cooling down to room temperature. AsH₃ cracked at 1000°C is supplied before heating to avoid the desorption of As atoms from the substrate surface. Using this procedure, semiconductor crystals are selectively grown after forming contamination resist without exposing the sample to the air. This method is one of *in-situ* selective growth processes. A selective growth was achieved by this process sequence. The source materials used are AsH₃ and TMG. The substrate temperature is 500 °C and growth time is 1 hour. We find that GaAs crystal is grown outside of the electron beam irradiated area. The grown crystal formed outside of the region where the electron beam is irradiated is confirmed to be the *mono*-crystal by means of the observation of the electron channeling pattern.

We apply this in-situ selective growth phenomena to a fabrication of the quantum wire structures using the following method. First, we irradiate the electron beam onto the separated regions of the substrate surface in order to form contamination resists without supplying source materials, and secondly the crystal growth is performed. As a result, a GaAs quasi-quantum wire structure whose width is as narrow as 700 nm. was successfully formed. The dimension of the wire demonstrated here is still large compared to the dimension which can achieve the real quantum confinement. However, we believe that this technology has potential capability of forming quantum wires and boxes by scanning the electron beam on the substrate just before the growth.

The micro Auger electron spectroscopy analysis revealed that the selective ungrowth in the region where the electron beam is irradiated results from the contamination resists consisting of carbon whose thickness is thinner than 10 Å.

AD-A254 162

ADVANCED PROCESSING AND CHARACTERIZATION TECHNOLOGIES
FABRICATION AND CHA. (U) FLORIDA UNIV GAINESVILLE
P H HOLLOWAY JUL 92 ARO-28953. 1-EL-CF DAAL03-91-G-0142

2/3

UNCLASSIFIED

NL

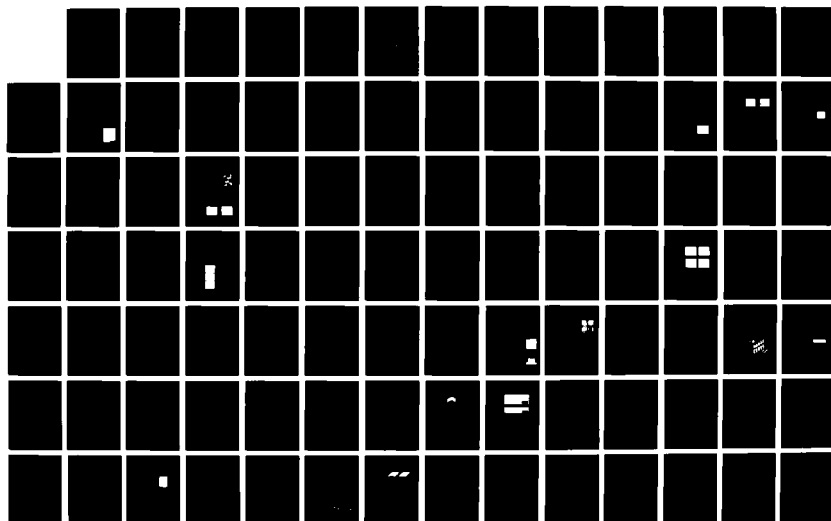
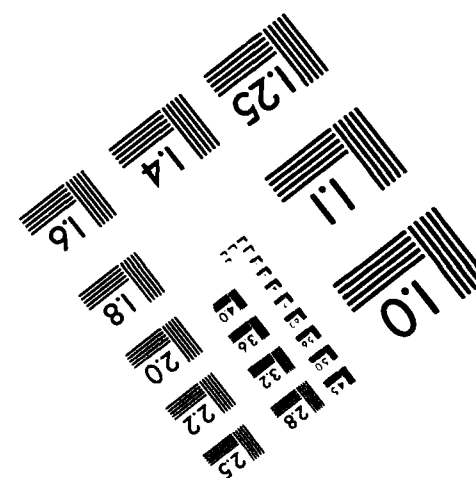
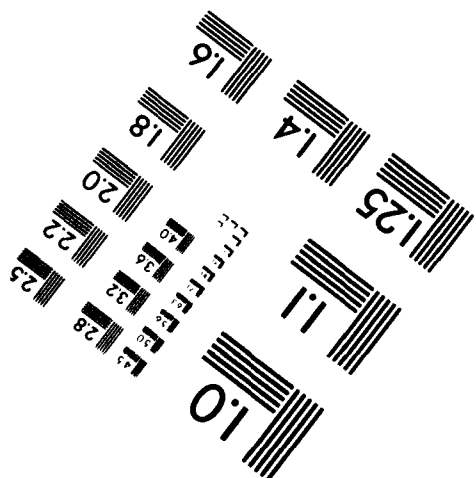
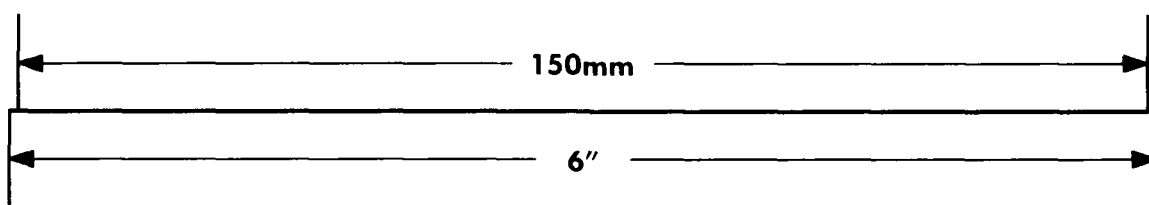
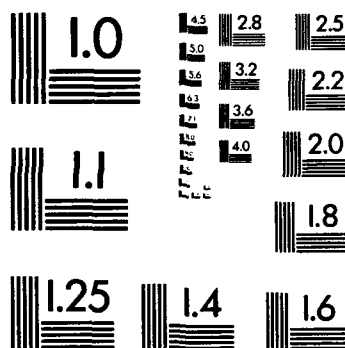
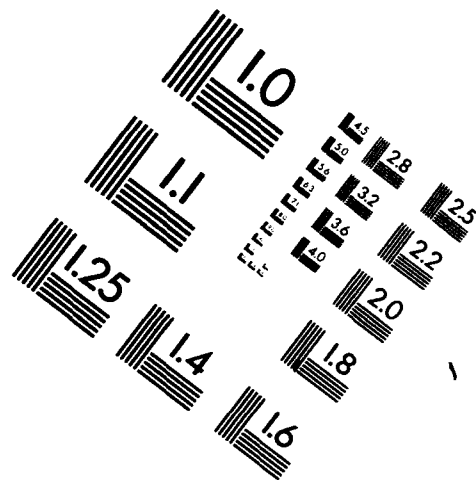
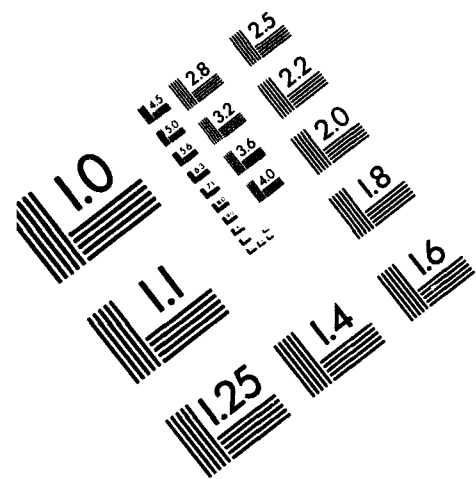


IMAGE EVALUATION TEST TARGET (MT-3)



PHOTOGRAPHIC SCIENCES CORPORATION
770 BASKET ROAD
P.O. BOX 338
WEBSTER, NEW YORK 14580
(716) 265-1600

4. Fabrication of Buried GaAs Wire array on SiO₂-Patterned Substrate formed by Electron Beam Lithography^[8]

In this section, we discuss recent successful fabrication of GaAs trigonal prism-like quantum wire (TPQW) arrays which are buried in Al_{0.4}Ga_{0.6}As layer using the MOCVD and the EB lithography. The minimum base width obtained for the wire is 300Å. The 55° tilted facet sidewalls correspond to crystallographic (111)B.

Fabrication process is as follows. First, a SiO₂ mask of 400 Å thickness was formed by plasma deposition method on a semi-insulating (100) GaAs substrate. Arrays of 650-μm-long PMMA wires with 1000Å line and spaces parallel to the reverse mesa <011> direction were lithographically defined on SiO₂ mask by the EB lithography technique, followed by a wet chemical etching. Then the TPQWs was grown on this substrate by the MOCVD. At the initial stage, GaAs trapezoids on the substrate through the mask window were formed and the upside of the trapezoid (i.e., [100] facet) diminishes in size, resulting the formation of trigonal prisms. After disappearing of the [100] facet, the [100] facet growth stops for a time. During this time, the wires do not overlap each other, although the SiO₂ wire width is only 300Å. The continuation of the growth flattens (111)B facet sidewalls, making the dimension of wires uniform. Because of small width of the SiO₂ masking wires, the space between the trigonal prisms can be finally filled up by the further continuation growth of Al_{0.4}Ga_{0.6}As without changing growth parameters. As a result, the buried TPQWs is formed without being exposed to the air. Since the EB lithography enables us to produce 50nm period pattern and this unexposed TPQWs has excellent crystalline characteristics, the TPQWs is obviously one of the most attractive candidates for quantum wire semiconductor laser devices.

5. Conclusion

In this paper we have discussed three kinds of electron beam assisted MOCVD technologies which we are recently developing for mesoscopic and/or quantum microstructures. We believed use of both MOCVD and electron beam technique will be important for fabrication of mesoscopic structures. In the presentation, we will also discuss our recent results on device physics of quantum wire and box lasers including band theory and nonlinear gain effects will be also discussed^[9-14].

This work was supported in part by a Grand-in-Aid for Scientific Research on Priority Area, "Electron Wave Interference Effects in Mesoscopic Structures" from the Ministry of Education, Science and Culture and university-industry joint research project "Mesoscopic Electronics".

References

- [1] Y. Arakawa and H. Sakaki, Appl. Phys. Lett., **40**, 939 (1982).
- [2] P. M. Petroff, A. C. Gossard and W. Wiegmann, Appl. Phys. Lett. **45**, 620 (1984).
- [3] Y. Aoyagi, S. Masuda, S. Namba and A. Doi, Appl. Phys. Lett. **47**, 95 (1985).
- [4] H. Asai, S. Yamada and T. Fukui, Appl. Phys. Lett. **51**, 1518 (1987).
- [5] E. Kapon, S. Simhony, R. Bhat and D. M. Hwang, Appl. Phys. Lett., **55**, 2715 (1989).
- [6] T. Takahashi, Y. Arakawa, M. Nishioka and T. Ikoma, Proc. of 1990 Fall Meeting of the Materials Research Society, November 1990, Boston, USA
- [7] T. Takahashi, Y. Arakawa, and M. Nishioka, Appl. Phys. Lett. to be published (1991)
- [8] S. Tsukamoto, Y. Nagamune, M. Nishioka, and Y. Arakawa to be presented at the 7th International Conference on Crystal Growth and Vapor Deposition, Nagoya, Japan (1991)
- [9] T. Yamauchi, Y. Arakawa, and J. N. Schulman, Appl. Phys. Lett. **57**, pp. 1224 (1990)
- [10] T. Yamauchi and Y. Arakawa, to be published in Superlattice and Microstructures (1991)
- [11] Y. Arakawa, T. Yamauchi, and J. N. Schulman, to be published in Phys. Rev. B **43**, February (1991)
- [12] Y. Arakawa, T. Yamauchi, and J. N. Schulman, submitted to Phys. Rev. B
- [13] T. Yamauchi, T. Takahashi, and Y. Arakawa, IEEE J. of Quantum Electronics, June (1991)
- [14] T. Yamauchi, Y. Arakawa, and M. Nishioka to be published in Appl. Phys. Lett. (1991)

Lateral Field Effect in Focused-Ion-Beam Written In-Plane-Gated Systems

A.D. Wieck, A. Fischer, and K. Ploog

Max-Planck-Institut für Festkörperforschung
D-7000 Stuttgart 80, Germany

We define one dimensional channels and adjacent In-Plane-Gates in a single step preparation by linewise insulating an $Al_{0.3}Ga_{0.7}As/GaAs$ n-type heterostructure. Channel and gates consist of the same electronic layer, which leads to lateral electric field effect with high flexibility in microstructure design.

The present technology of microstructured devices is based on lithographic processes, which use masks and photoresist layers. The power of this techniques is the parallel production of many structures in a chip unit and many chip units on a wafer in a single run, once the complex masks have been fabricated. However, there are two essential inconveniences inherent to this technology: First, one needs not one, but several complex masks, which have to be precisely aligned with the permanent risk of contamination with particles. Second, all resist processes are indirect ones, i.e. the resist pattern serves as a further mask for subsequent etching or implantation steps, also sensitive to contamination on a rough as well as on a submicron scale. For this reason, it is highly desirable to fabricate semiconductor microstructures with a minimum number of process steps.

Recently, we proposed and realized field-effect devices which are defined in a single technology step by implantation of Focused Ion Beams (FIB).[1] The starting modulation-doped heterostructure consists of 10nm $GaAs$, 50nm Si-doped and 23nm undoped $Al_{0.3}Ga_{0.7}As$, and $2\mu m$ $GaAs$ grown on a semi-insulating $GaAs$ substrate by molecular beam epitaxy (MBE). At room temperature the electron density and mobility of the 2-dimensional electron gas (2DEG) are $n = 4.5 \times 10^{11} cm^{-2}$ and $\mu = 7800 cm^2/Vs$, respectively. The as-grown samples are mesa-etched with optical lithography to define a $150\mu m$ -wide Hall bar with $150\mu m$ spaced $50\mu m$ -wide potential probes (Fig.1). This starting structure is a standard system easily producible in MBE systems.

The conductivity of the electronic layer, situated 83nm below the sample surface, can be strongly laterally modulated by implantation of accelerated ions.[1] A single line, written across the Hall-bar by 100keV Ga^+ ions focused to a spot diameter of 100nm, increases the resistance of the electronic layer by a factor of 10^6 at room temperature and more than 10^9 at low temperatures, respectively. With a beam current of 100pA, we write lines with a dot spacing of 32nm and dwell times of $1\mu s$, yielding an ion dose of $2 \times 10^{13} cm^{-2}$. This insulation writing is performed along two U-shaped paths on the as-grown mesa, defining a conducting channel between their adjacent corners (Fig.1). We denote the distance between the center points of the FIB-exposed dots in these two corners the geometrical width W_{geo} .

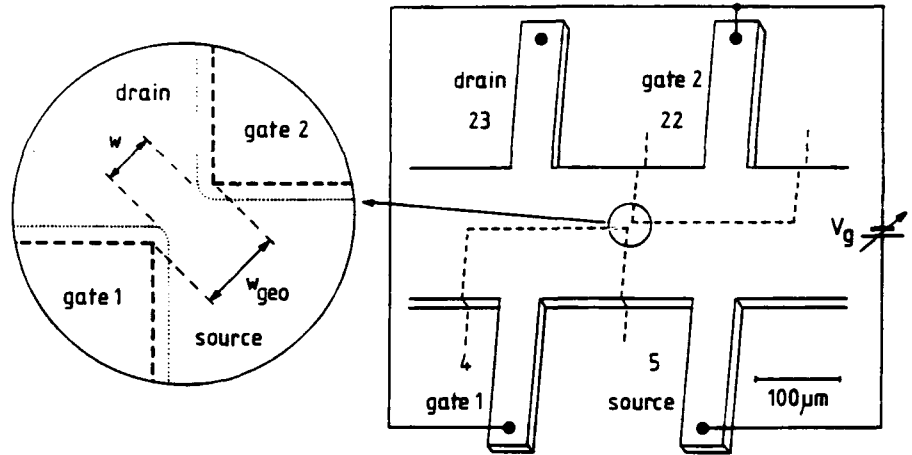


Fig.1: Sketch of the mesa-etched sample. Broken lines indicate the FIB-written paths, defining a narrow channel between source and drain. On the left hand side of the figure, the channel region is magnified.

The two regions of the 2DEG isolated by the U-shaped paths are now considered as field-effect gates, which can electrostatically influence the carrier density and the width of the channel between their adjacent corners. As these gates are in the same plane as the channel itself, we call them "In-Plane-Gates" (IPG). With the setup depicted in Fig.1, we measure the drain-source current-voltage characteristics for different gate voltages shown in Fig.2. The behavior of the device is typical for an unipolar field-effect transistor and at voltages $V_{DS} > 2V$ clear saturation occurs. This structure with a geometrical width of a few μm exhibits a "normal on" channel, which can be enhanced by a positive or depleted by a negative gate voltage, respectively. If W_{geo} is chosen to be $1.5\mu m$ or lower, the channel is "normal off" and can be

enhanced to a finite conductance by a positive gate voltage. Thus, the IPG transistor can also be operated as an inverter and fulfills requirements for logical as well as analog functions. From the fabrication point of view, the IPG transistor offers several inherent advantages: As we define gate and channel areas in the same insulation writing process, no second positioning is necessary. This means that there is no alignment and the whole process including the MBE growth and FIB writing can be performed in ultrahigh vacuum without exposure to air or particles. This allows even subsequent MBE-overgrowth of the FIB structures extending to 3-dimensional devices.

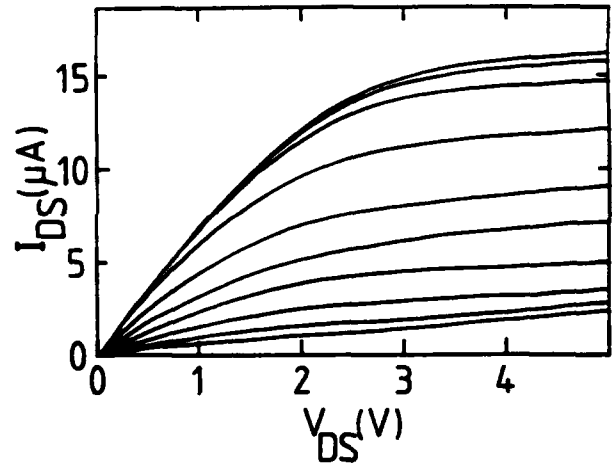


Fig.2: Drain-source current I_{DS} versus drain-source voltage V_{DS} , measured at room temperature in an IPG-transistor with $W_{geo} = 4.2\mu m$. The gate voltage V_g is taken as parameter and changed in steps of $-1V$ from $+3V$ (upper curve) to $-6V$ (lowest curve).

Furthermore, the maskless and computer-controlled beam deflection of the FIB allows an easy-to-change pattern design. With a writing speed of $0.3m/s$ and an effective gate length of $3\mu m$, we can write 10^6 IPG transistors in 10s. The single IPG-structure depicted in Fig.1 is written with rather long, "inactive" FIB-paths, because only the IPG regions close to the channel contribute to the field effect. However, the sample is FIB-written already in a few milliseconds, thus mechanical vibrations of the stage or the whole setup up to $\approx 100Hz$ do not disturb the fabrication process. Starting from a given heterostructure, this method of creating a field effect device is probably the simplest and fastest ever reported. Very recently we provided a further example of the general-IPG principle described here, fabricated by electron beam lithography and subsequent mesa etching.[2]

An undesirable detail is the gate1-gate2 crossover connection shown in Fig.1. The structure

can be modified to a three-terminal device by simply connecting gate2 with the source. A voltage at gate1 leads now to an asymmetric potential across the channel, which also varies its conductivity. In Fig.3 a possible application of the so modified IPG transistor is shown.

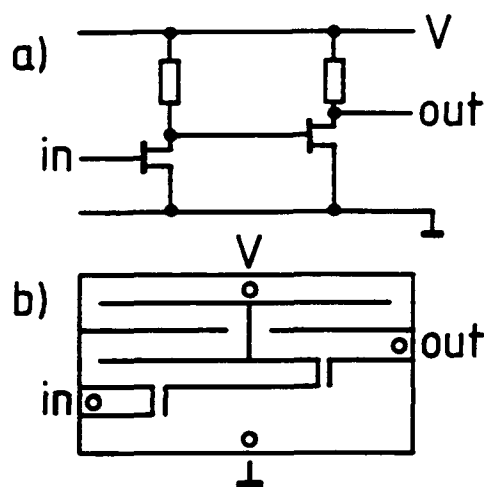


Fig.3: Equivalent circuit (a) and FIB-written paths (b) on a heterostructure, both representing a two-stage amplifier with supply voltage V , input in , and output out , respectively. Open circles in (b) represent ohmic contacts to the 2DEG. Note that lines in (a) indicate electrical connections, whereas lines in (b) symbolize FIB-written, insulating paths.

In only FIB writing, we define two active elements and two resistors, which are interconnected by omitting FIB lines, representing a simple two-stage amplifier. This example shows that once at the edge of the chip contacts are prepared in a classical manner, the whole microstructure can be written by FIB. In this way, the IPG transistor can be a key element in future microstructure technology.

We gratefully acknowledge financial support of the Bundesministerium für Forschung und Technologie.

[1] A.D. Wieck and K. Ploog, Appl. Phys. Lett. **56**, 928 (1990).

[2] J. Nieder, A.D. Wieck, P. Grambow, H. Lage, D. Heitmann, K.v. Klitzing, and K. Ploog, Appl.Phys.Lett.**57**, 2695 (1990).

Focused-Ion-Beam Micromachining: A Fabrication Tool for Prototypal Semiconductor Lasers

Richard K. DeFreez
Oregon Graduate Institute of Science and Technology
19600 NW Von Neumann Drive
Beaverton, OR 97006-1999

Focused-ion-beam micromachining is a technique for forming optical quality surfaces in semiconductor laser materials and has been used to fabricate several types of prototypal semiconductor laser structures. Diode laser output mirrors of quality comparable to that of cleaved facets have been fabricated¹. Focused-ion-beam micromachined (FIBM) single stripe coupled cavity lasers have demonstrated widely and continuously tunable single mode operation². Tunable single longitudinal mode optical power has been achieved with FIBM coupled cavity phase-locked arrays of AlGaAs semiconductor lasers³. Hundreds of milliwatts of pulsed optical power has been observed from surface-emitting phase-locked arrays with FIBM turning and oscillator mirrors⁴. The use of vector scanning of the ion beam to produce arbitrary surface contours, such as linear and curved turning mirrors and micron pitch gratings with various profiles, has been demonstrated⁵. Results from elevated temperature aging tests suggest that FIBM does not cause significant damage to transverse junction stripe laser diodes and that it can be a promising tool for fabrication of mirrors for prototypal optoelectronic integrated circuits⁶. Recently, two-dimensionally coherent arrays of semiconductor lasers in both serpentine⁷ and ring⁸ configurations have been fabricated using total-internal-reflection turning mirrors.

Most recently, the very high quality surfaces created by FIBM were exploited to fabricate low magnification unstable resonator semiconductor

lasers which operate in a nearly-diffraction-limited mode to five times lasing threshold and to record optical powers. Attempts to re-create these structures with reactive ion etching of various curvatures mirrors have met only limited success in large part, it is believed, due to mirror surface roughness associated with mask-edge irregularities.

FIBM exploits the precise, computer controlled, maskless, sputter-etching afforded by a beam of 15 - 25 keV Ga^+ ions focused to a 30 to 250 nm spot to fabricate features in semiconductor laser dice and wafers. Current densities of the order of 1 A/cm² are readily achieved. The focused beam of ions can be deflected under computer control over areas approaching 1 mm² with a precision comparable to or smaller than the spot size. This allows the removal of material by sputter-etching to form submicron features with optically smooth surfaces. A significant advantage of FIBM is that it is a completely maskless process and no photolithography, wet chemistry, or other processing is required so that mounted and partially packaged devices can be modified without fear of adverse interactions with heatsink or packaging materials.

On the other hand, FIBM is inherently slow since it is an intrinsically serial process relegating it to prototypal applications. Typical FIBM sputter rates for III-V semiconductor compounds are approximately 1 μm^3 per second. Recent, and previously unreported, experimental work at Oregon Graduate Institute indicates that an increase in the sputter rate by approximately a factor of ten is attainable in GaAs using chemically assisted FIBM, but still machining times typically are too long to consider "production runs".

The ability to deflect the ion beam under computer control provides added flexibility for producing features with arbitrary surface profiles. For simple shapes this is not so important since the ion beam can be raster scanned at a uniform rate over a field to remove a thin laminar layer over the entire field and adjusting subsequent fields scanned to form the topography desired. For example a V-shaped groove can be formed by rastering the ion beam over a sequence of successively narrower rectangles on a common center. For more complex shapes it is useful to be able to control the beam

dwel time at each pixel of the field of view. Topographical features such as sinusoidal gratings can be micromachined using this method^{5,9,10}. However, it has been found¹¹ that crystal damage induced below the surface of gratings so formed is sufficient to preclude lasing action in grating surface emitting laser arrays.

In summary, focused ion beam micromachining is a highly useful tool for the fabrication of a wide variety of prototypal semiconductor lasers if the machining process is designed to leave beam-induced damage in an area that is not critical to device operation.

References

1. J. Puretz, R. K. DeFreez, R. A. Elliott, and J. Orloff, "Focused-ion-beam micromachined AlGaAs semiconductor laser mirrors," *Electron. Lett.*, vol. 22, pp. 700-702, 19 June 1986.
2. R. K. DeFreez, J. Puretz, R. A. Elliott, J. Orloff, and L. W. Swanson, "CW operation of widely and continuously tunable micromachined-coupled-cavity diode lasers," *Electron. Lett.*, vol. 22, pp. 919-921, 14 August 1986.
3. R. K. DeFreez, J. Puretz, R. A. Elliott, J. Orloff, and T. L. Paoli, "Focussed-ion-beam micromachined coupled-cavity and surface-emitting arrays of diode lasers," *Technical Digest of CLEO '87*, pp. 134-135, Baltimore, Maryland, 26 April to 1 May 1987. Paper WG3
4. J. Puretz, R. K. DeFreez, R. A. Elliott, J. Orloff, and T. L. Paoli, "300 mW operation of a surface-emitting phase-locked array of diode lasers," *Electron. Lett.*, vol. 23, pp. 130-131, 29 January, 1987.
5. G. Crow, J. Puretz, J. Orloff, R. K. DeFreez, and R. A. Elliott, "The use of vector scanning for producing arbitrary surface contours with a focused ion beam," *J. Vac. Sci. Technol. B*, vol. 6, pp. 1605-1607, September/October 1988.

6. R. K. DeFreez, J. Puretz, J. Orloff, R. A. Elliott, H. Namba, E. Omura, and H. Namizaki, "Operating characteristics and elevated temperature lifetests of focussed ion beam micromachined transverse junction stripe lasers," *Appl. Phys. Lett.*, vol. 53, pp. 1153-1155, 26 September 1988.
7. R. K. DeFreez, H. Ximen, D. J. Bossert, J. M. Hunt, G. A. Wilson, R. A. Elliott, J. Orloff, G. A. Evans, N. W. Carlson, M. Lurie, J. M. Hammer, D. P. Bour, S. L. Palfrey, and R. Amantea, "Spectral locking in an extended area two-dimensional coherent grating-surface-emitting laser array fabricated using focused ion beam micromachining," *IEEE Photonics Technol. Lett.*, vol. 2, pp. 6-8, January 1990.
8. D. J. Bossert, R. K. DeFreez, H. Ximen, R. A. Elliott, J. M. Hunt, G. A. Evans, N. W. Carlson, M. Lurie, J. M. Hammer, D. P. Bour, S. L. Palfrey, and R. Amantea, "Grating surface emitting lasers in a ring configuration," *Appl. Phys. Lett.*, vol. 56, pp. 2068-2070, 21 May 1990.
9. R. A. Elliott, R. K. DeFreez, J. Puretz, J. Orloff, and G. A. Crow, "Focused-ion-beam micromachining of diode laser mirrors," *Proceedings of the SPIE Symposium on Communications Networking in Dense Electromagnetic Environments*, vol. 876, pp. 114-120, 14-15 January 1988.
10. H. Ximen, R. K. DeFreez, J. Orloff, R. A. Elliott, G. A. Evans, N. W. Carlson, M. Lurie, and D. P. Bour, "Focused ion beam micromachined three-dimensional features by means of a digital scan," *J. Vac. Sci. Technology*, vol. B 8, pp. 1361-1365, November/December 1990.
11. H. Ximen, "A study of focused ion beam micromachining by development of a 3-D computer simulation and a 3-D digital scan strategy," *Ph.D. Thesis, Oregon Graduate Institute of Science and Technology, 1990.*

A Novel Vacuum Lithography with SiN_x Resist by Focused Ion Beam Exposure and Dry Etching Development

S. Takahashi^{*,**}, M. Ohashi^{*}, S. Fukatsu^{*},
Y. Shiraki^{*}, and R. Ito^{*}

^{*}RCAST, The University of Tokyo
4-6-1, Komaba, Meguro-ku, Tokyo, 153, Japan

^{**}Toshiba R&D Center

1, Komukai Toshiba-cho, Saiwai-ku, Kawasaki, 210, Japan

1. Introduction

There has been increasing interest in in-situ processing to avoid interface degradation which is an important problem in the III-V semiconductor technology.¹⁻³ For in-situ processing involving regrowth of semiconductor layers, lithography techniques which can be integrated into vacuum processes are essential. In-situ pattern processing using focused ion beams (FIB)² and electron beams (EB)³ has been demonstrated recently. In those works, however, very thin semiconductor oxide films which act as resists are not durable enough to allow the fabrication of fine and high-aspect-ratio patterns on substrate surfaces. Moreover, maskless pattern formation by FIB-assisted etching has a serious problem of ion-induced damage.⁴ We propose here a novel lithography technique applicable to in-situ processing, where plasma-CVD (P-CVD) deposited SiN_x is used as a resist, Ga-FIB implantation as exposure, and CF_4 dry etching as development. We describe its lithographic properties and demonstrate deep anisotropic pattern etching of a GaAs substrate. In addition, we show that the SiN_x resist makes ion-induced substrate damage minimal.

2. Mechanism of the lithography

Figure 1 shows the mechanism of the proposed lithography. Ga ion beams are implanted into the SiN_x resist. Almost all the Ga ions stay near the resist surface. During subsequent CF_4 dry etching, a nonvolatile compound GaF_x is formed in the implanted region of the resist providing an in-situ mask. On the other hand, a volatile compound SiF_x is formed in the nonimplanted region of the resist. Thus, SiN_x acts as a negative resist. By using reactive ion etching (RIE) under anisotropic etching

conditions, the resist can be developed with a high aspect ratio profile.

3. Lithographic properties and GaAs pattern formation

An 800 nm thick SiN_x resist was deposited on Si and GaAs substrates by P-CVD. The SiN_x resist was exposed to focused Ga ion beams: accelerating voltage was varied 40-80 kV, beam diameter was about 1 μm , and the exposed regions were 0.1-1 mm regular squares and line-and-space patterns. Subsequently, the SiN_x resist was developed by chemical dry etching (CDE) or RIE using a CF_4 gas. Figure 2 shows the difference between the resist thickness on the implanted region (T_{GI}) and that on the nonimplanted region (T_{NI}) as a function of the ion dose for two accelerating voltages, 40 kV and 80 kV. As the dose increases, $T_{\text{GI}} - T_{\text{NI}}$ increases nonlinearly, exhibiting a threshold dose. That is, at the ion doses above the threshold, the initial resist thickness almost remains. This result indicates a strong suppression of SiN_x etching in the implanted region at higher doses, and can be interpreted by the mechanism shown in Fig.1. As the accelerating voltage becomes higher, the threshold dose shifts to a higher level and the slope becomes gentle. This is because, at higher ion energies, the depth profile of Ga ions becomes broader and the peak ion concentration decreases as a result of the increase in the ion penetration depth.

Figure 3 shows an exposure characteristic around the threshold dose for an accelerating voltage of 40 kV. The normalized film thickness remaining is plotted against the ion dose. We obtain a contrast (γ) of 4.0 from the slope. This is much better than that for conventional ion beam resists.⁵ Therefore, it will be possible to fabricate high resolution patterns as fine as 0.1 μm or better, with the finest beam of the FIB system.

We also examined the substrate damage caused by FIB exposure by measuring the photoluminescence (PL) intensity of MQW GaAs samples. The MQW samples had 6 QWs whose width became wider as their positions became deeper. FIB was implanted into SiN_x -deposited MQW samples at 80 kV with a dose of $5 \times 10^{16} \text{ cm}^{-2}$. The PL peak intensity ratios for the implanted region over the nonimplanted region are plotted against the depth in Fig.4. The PL intensities of the implanted and nonimplanted regions are almost the same for SiN_x thickness of 720 nm and 410 nm. This

means that the FIB exposure does not induce significant damage in the substrates due to the presence of the SiN_x resist.

The SiN_x mask fabricated by the present lithography was used for GaAs etching. A $5\mu\text{m}$ line-and-space pattern was fabricated on a SiN_x resist by FIB exposure with an accelerating voltage of 80 kV followed by CF_4 -RIE development. Subsequently, GaAs was dry etched by reactive ion beam etching using a Cl_2 gas. Figure 5 shows a dry-etched GaAs line-and-space pattern whose sidewalls are seen to be nearly vertical. Because the selectivity of GaAs to the SiN_x mask is about 8 even under anisotropic etching conditions, high-aspect-ratio GaAs etching is realized even when thinner SiN_x masks are used for very fine pattern formation.

4. Summary

We have demonstrated that P-CVD deposited SiN_x acts as a negative resist using Ga-FIB implantation as exposure and CF_4 dry etching as development. This lithography technique is not only suitable for in-situ pattern processing but also for high resolution lithography because of its high contrast property and exquisite convergence of FIB. Moreover, the GaAs substrates are not damaged by FIB exposure because of the presence of SiN_x resist. A Deep dry-etched GaAs patterns with nearly vertical sidewalls were obtained using a SiN_x mask fabricated by this lithography technique. We believe that this technique is applicable to the fabrication of very fine structures such as optical gratings and quantum effect devices.

References

- 1) A. Takamori, E. Miyauchi, H. Arimoto, Y. Bamba, and H. Hashimoto, Jpn. J. Appl. Phys. **23**, L599 (1984)
- 2) H. Temkin, L. R. Harriott, R. A. Hamm, J. Weiner, and M. B. Panish, Appl. Phys. Lett. **54**, 1463 (1989)
- 3) Y. Sugimoto, K. Akita, M. Taneya, and H. Hidaka, Appl. Phys. Lett. **57**, 1012 (1990)
- 4) M. Taneya, Y. Sugimoto, and K. Akita, J. Appl. Phys. **66**, 1375 (1989)
- 5) H. Ryssel, K. Habberger, and H. Kranz, J. Vac. Sci. Technol. **19**, 1358 (1981)

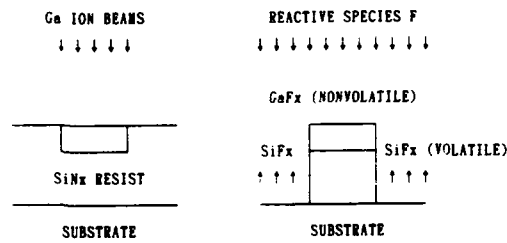


Fig.1 Mechanism of the lithography.

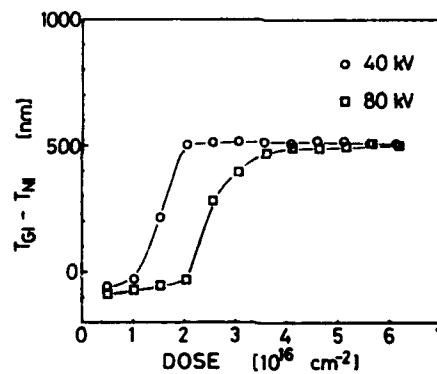
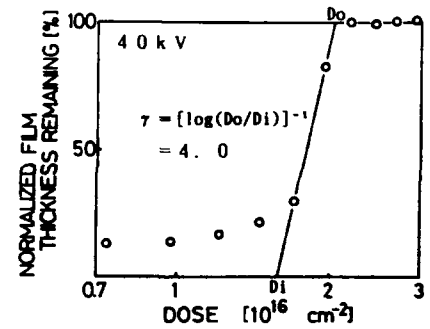
Fig.2 Dose dependence of resist thickness. T_{GI} : Thickness of implanted region. T_{NI} : Thickness of nonimplanted region.

Fig.3 Exposure characteristic.

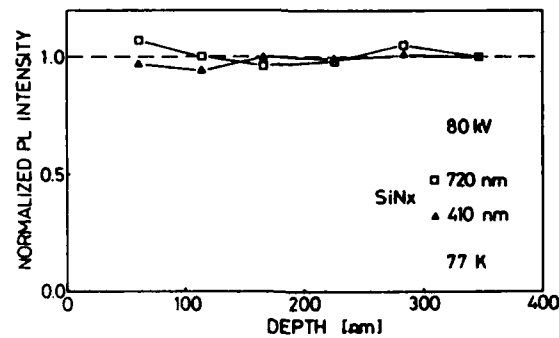
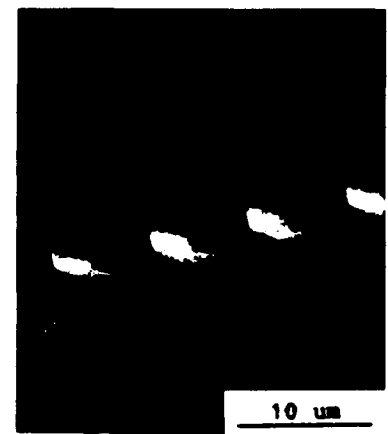


Fig.4 Normalized PL intensity of MQW samples.

Fig.5 SEM image of dry-etched GaAs pattern using SiN_x mask.

ECR Plasma Etching of III-V Optoelectronic Devices

S. J. Pearton

AT&T Bell Laboratories
Murray Hill, New Jersey 07974

SUMMARY

The dry etching of GaAs, InP and related compounds is gaining a resurgence of interest, largely due to the need to achieve high resolution, anisotropic etching in device applications. There are a variety of requirements of this etching, such as fast etch rate for creation of deep ($\geq 1 \mu\text{m}$) trenches, high selectivity for one material over another (say GaAs over AlGaAs) or conversely equi-rate etching for these materials.

There are two basic classes of gas mixtures used for etching of III-V materials. The first is based on chlorine or bromine, particularly the former because gallium and other group III chlorides are volatile at relatively low temperatures, as opposed to the stable gallium fluorides. It is common then to use Cl_2 -based etching for III-V materials, in contrast to the F-based etching prevalent for Si. Most of the Cl-containing gases also contain carbon and often problems are encountered with the deposition of polymer films during etching. Some of the gas mixtures used include Cl_2 , CCl_4 , BCl_3 , $\text{SiCl}_4/\text{Cl}_2$, $\text{SiCl}_4/\text{SF}_6$, CHCl_3 , COCl_2 and CCl_2F_2 (with O, He or Ar). The advantages of using Freon 12 (CCl_2F_2) are that it is a nontoxic noncorrosive gas which contains both Cl for etching and F to provide an etch stop upon reaching an underlying AlGaAs or AlInAs layer. The etch stop mechanism involves the formation of an involatile AlF_3 layer, allowing selectivities of GaAs-to-AlGaAs and InGaAs-to-AlInAs of several hundred.

The second general class of gas mixture is based on methane or ethane and hydrogen. This has attracted considerable recent attention for etching both Ga- and In-based semiconductors. This nonchlorinated mixture shows controlled, smooth, highly anisotropic etching of all III-V materials. The etch products are thought to be AsH_3 or PH_3 for the group V element and most likely some form of methyl adduct (eg. $(\text{CH}_3)_n\text{Ga}$) for the group III species. A list of the comparative etch rates of GaAs, $\text{Al}_{0.3}\text{Ga}_{0.7}\text{As}$, InP and InGaAs in the various gas mixtures at low pressure (4 mTorr), and power densities ($0.56 \text{ W}\cdot\text{cm}^{-2}$, self-biases of $\sim 300 \text{ V}$) are shown in Table 1.

One of the major issues with dry etching of III-V materials is the introduction of surface damage by energetic ion bombardment. This has been investigated for a variety of dry etching methods using inert ion and reactive ion bombardment. The degree of damage has been found to be inversely proportional to the ion mass, and directly proportional to the ion energy. Sidewall damage during dry etching has also been studied [10,11]. The most obvious effect of near-surface damage is a reduction in the carrier concentration between 200-1000 Å from the surface. This is considerably deeper than the projected range of ions crossing the plasma sheath and is ascribed to channeling of these relatively low-energy particles, and recombination-enhanced motion of defects. In at least some cases where H_2 is involved in the etch mixture, there appears also to be passivation of donors and acceptors by hydrogen association. This is a well-known effect from studies of the role of atomic hydrogen in passivating shallow level dopants.

Table 1 Typical etch rates of GaAs, InP, $\text{Al}_{0.3}\text{Ga}_{0.7}\text{As}$ and InGaAs in different gas mixtures at 4 mTorr and $0.56\text{W}\cdot\text{cm}^{-2}$.

| Mixture | Etch Rate ($\text{\AA}\cdot\text{min}^{-1}$) | | | |
|-------------------------------------|--|---|-----|--------|
| | GaAs | $\text{Al}_{0.3}\text{Ga}_{0.7}\text{As}$ | InP | InGaAs |
| Cl_2/Ar | 20,000 | 5,000 | 150 | 150 |
| SiCl_4/Ar | 5,000 | 3,000 | 130 | 320 |
| $\text{CCl}_2\text{F}_2/\text{O}_2$ | 750 | 500 | 650 | 1,000 |
| CH_3Br | 600 | 400 | 220 | 300 |
| CH_4/H_2 | 190 | 140 | 220 | 280 |
| $\text{C}_2\text{H}_6/\text{H}_2$ | 220 | 160 | 250 | 320 |
| $\text{CHCl}_2\text{F}/\text{O}_2$ | 600 | 300 | 300 | 320 |
| $\text{CHClF}_2/\text{O}_2$ | 400 | 250 | 110 | 130 |

The near-surface carrier profiles in etched GaAs are shown in Fig. 1 as a function of post-RIE annealing temperature. The results for $\text{CCl}_2\text{F}_2:\text{O}_2$ RIE are relatively straightforward. There is a reduction in the net carrier concentration within 1500 Å of the surface which is recovered by annealing at 300°C. Any form of ion bombardment of GaAs with energies above the threshold for displacement (~ 15 eV) will create midgap deep levels which trap free carriers and are not thermally ionized at room temperature. This effect is widely used in isolating GaAs devices using ion implantation with nondopants ions like O, B, or H. Under our conditions there appears to be annealing of the damage-related levels near 300°C. In the case of $\text{C}_2\text{H}_6-\text{H}_2-\text{Ar}$ RIE the evolution of the carrier profiles with annealing is more complicated. The reduction in the doping concentration is now due to two effects; damage-related deep levels and passivation of the Si donors in the material by atomic hydrogen. The as-etched sample appears to show an increase in carrier concentration right at the surface, but this is an artifact of the C-V measurement, judging from the phase angle at low reverse biases. A more reliable profile is obtained at depth > 1000 Å. Upon annealing at 200°C the carrier reduction moves to greater depth, which we ascribe to motion of near-surface atomic hydrogen further into the sample. For annealing above 300°C the carrier profile recovers towards its unetched shape. Annealing of deep levels again appears to begin at $T \geq 300^\circ\text{C}$, whereas reactivation of hydrogen passivated donors occurs at $\sim 400^\circ\text{C}$. Even after 500°C annealing the profile is not fully recovered, presumably due to residual near-surface disorder.

Reverse voltage-current characteristics from InP ($n = 6 \times 10^{15} \text{ cm}^{-3}$) etched in $\text{C}_2\text{H}_6/\text{H}_2$ or $\text{CCl}_2\text{F}_2/\text{O}_2$ are shown in Fig. 2. Upon RIE, Au contacts no longer showed rectifying behavior for InP etched in $\text{C}_2\text{H}_6/\text{H}_2$ but were essentially ohmic for either polarity of bias applied to the contact. Once again this is presumably due to the creation of a nonstoichiometric near-surface region. Chemical analysis of the surface showed a deficiency of phosphorus to a depth of ~ 150 Å. By sharp contrast, RIE in a $\text{CCl}_2\text{F}_2/\text{O}_2$ discharge leads to an approximately fivefold increase in reverse bias current, but the I-V characteristic is still rectifying. Chemical analysis of the near-surface

region of InP etched in this type of discharge showed only a slight deficiency of P within 20 Å of the surface. The difference between the two gas mixtures is clearly the high concentration of atomic hydrogen which can preferentially remove phosphorus from InP in the form of PH_3 . This appears to be a fundamental problem with the $\text{C}_2\text{H}_6/\text{H}_2$ mixture, since the use of lower hydrogen concentrations leads to increasing polymer deposition.

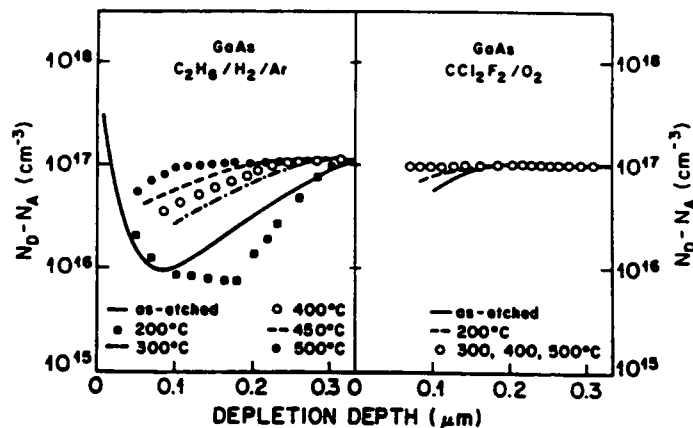


Figure 1. Carrier profiles in n-type ($n = 10^{17} \text{ cm}^{-3}$) GaAs etched in either a 19:1 $\text{CCl}_2\text{F}_2:\text{O}_2$ or 1:10:3 $\text{C}_2\text{H}_6:\text{H}_2:\text{Ar}$ discharge (4 mTorr, 0.85 W cm^{-2}), as a function of post-RIE annealing temperature. The profiles before etching were uniform at a level of 10^{17} cm^{-3} .

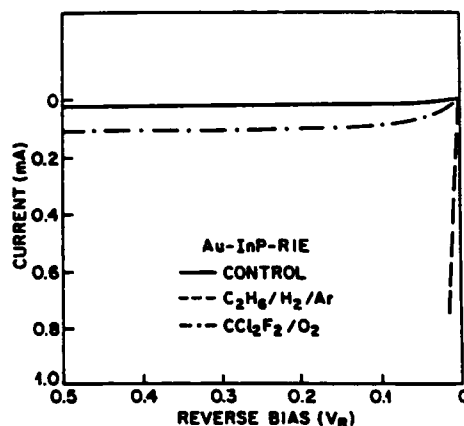


Figure 2. Reverse bias I-V characteristics from Au contacted n-type InP ($n = 6 \times 10^{15} \text{ cm}^{-3}$) after etching in 1 $\text{C}_2\text{H}_6/10\text{H}_2$ or 19 $\text{CCl}_2\text{F}_2/\text{O}_2$ discharges prior to Au deposition. The reverse breakdown voltage on the control sample was -2.5 V .

Lower levels of ion-induced damage are present when microwave Electron Cyclotron Resonance (ECR) discharges are used because of the lower ion energies relative to conventional RF plasmas. An example of the relatively benign nature of ECR etching with regard to InP is given by the forward current-voltage (I-V) measurements shown in Fig. 3. Samples etched under ECR conditions with no additional biasing gave I-V characteristics very close to those of an unetched control sample, with a Schottky barrier height (ϕ_B) of 0.48 eV and diode ideality factor (n) of 1.1, both derived from the forward I-V plots assuming thermionic emission. Once again our past experience with RIE of InP using this type of gas chemistry has been that Au deposition onto the RIE surface results in ohmic behavior, and a rectifying characteristic is not observed until at least 100 Å is removed from the sample by wet etching prior to the Au deposition. With RIE we also observe substantial In enrichment of the near-surface region, but to much greater depths than with ECR. Even with the addition of 100 V substrate bias during the ECR etching we observe only a relatively small reduction of the Schottky barrier height to 0.44 eV, while the ideality factor shows a greater degradation, to a value of 1.6. This is a convincing demonstration of the much lower degree of disruption to the semiconductor surface using ECR discharges compared to conventional RIE.

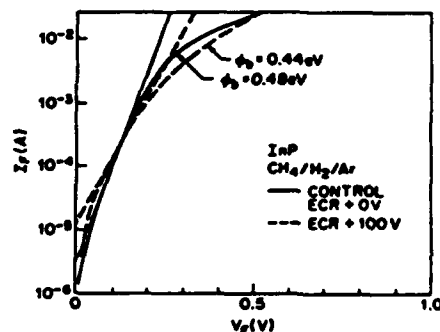


Figure 3. Forward current-voltage characteristics from Au-InP Schottky diodes etched in ECR 5 CH₄/15 H₂/7 Ar discharges (0 or 100V substrate self-bias) prior to deposition of the Au contacts. The straight lines in each case are used to give the intercept and slope of the characteristic. The ECR + 0 V sample had forward I-V curves very close to those of an unetched control sample.

A dry-etch fabrication technology for high-speed AlInAs/InGaAs Heterojunction Bipolar Transistors (HBT's) utilizing low-damage Electron Cyclotron Resonance (ECR) CH₄/H₂/Ar plasma etching has been developed. Small-area ($2 \times 4 \mu\text{m}^2$ to $3 \times 9 \mu\text{m}^2$) devices demonstrated current gains up to 160, unity gain cut-off frequency (f_T) of 57 GHz and a maximum oscillation frequency (f_{max}) of 35 GHz. The dry etch process uses triple self-alignment of the emitter and base metals and the base mesa, minimizing the base-collector capacitance (C_{BC}). These results represent the first report of a truly scalable process for InP-based HBT's and demonstrate the ability of ECR plasma etching to provide smooth, degradation-free etching of III-V semiconductors.

We will also detail the etching of GaAs-AlGaAs high power lasers in which the ohmic metal contact is used as the dry etch mask. In this situation it is desirable to have equal-rate etching of both GaAs and AlGaAs and we have used PCI₃/Ar mixtures to achieve anisotropic mesa formation.

INFLUENCE OF SiCl_4 REACTIVE ION ETCHING ON THE ELECTRICAL CHARACTERISTICS OF GaAs.

D. Lootens⁽¹⁾, P. Clauws⁽²⁾, P. Van Daele⁽¹⁾, P. Demeester⁽¹⁾

(1): University of Gent - Interuniversity Micro-Electronics Center (IMEC), Laboratorium voor Elektromagnetisme en Acoustica (LEA), Sint-Pietersnieuwstraat 41, B-9000 Gent, Belgium.

(2): University of Gent, Laboratorium voor Kristallografie en Studie van de Vaste Stof, Krijgslaan 281, B-9000 Gent, Belgium.

ABSTRACT.

SiCl_4 -RIE causes electrical damage to GaAs strongly related to doping type and level. Changes in C-V and DLTS-measurements can be related to EL2-defects. Explanations for observed differences in n-type and p-type material will be presented.

I. Introduction.

As the dimensions in optoelectronic components continue to shrink, more and more dry etching processes are used for patterning of the semiconductor material. Unfortunately the need for smaller dimensions requires anisotropic etching and so the use of energetic particles to stimulate the etching. Although RIE makes use of particles with relatively small energies (typically 200eV), the damage effects start playing a role, both in vertical direction and in lateral direction, as dimensions become smaller, like in quantum dots and wires. In literature, already a lot of work on RIE-damage in GaAs has been reported, but only a few deal with the physical nature of the defects⁽¹⁾ or with different doping types, although remarkable differences in the effect of particle bombardment on n-type and p-type have been reported^(2,3) and although the study of the different electrical behaviour of n- and p-type material, can reveal new information. The damage induced by the RIE-process can also be related to the chemistry of the reactive gases used. Our study covers electrical damage after SiCl_4 -RIE both in n- and p-type GaAs, involving capacitance-voltage (C-V) measurements on Schottky barriers and Deep Level Transient Spectroscopy (DLTS) measurements.

II. Experimental.

The experiments were carried out in a RIE80-system of Plasma Technology, operating at a pressure of 10mTorr, a SiCl_4 flow of 10sccm, a power density of 0.2W/cm² and a DC_{bias} of 170V. The samples were mounted on the electrode (covered by a quartz plate and kept at 40°C), using photoresist as a heat conductor. This results in a perfect anisotropic etching process for GaAs with perfect surface morphology⁽⁴⁾. The samples were highly doped substrates (10^{19}cm^{-3}), with a 2 μm thick MOCVD-grown epitaxial layer with varying doping concentration on top. The ohmic contacts (AuGe/Ni for n-type and Zn/Au for p-type) were evaporated, alloyed (450°C resp. 420°C) and the samples scribed (for reference) before loading in the RIE-chamber. All samples were dry etched during 2.5 min removing approximately 500nm GaAs, or, for reference, wet etched (also 500 nm) using $\text{H}_2\text{SO}_4:\text{H}_2\text{O}_2:\text{H}_2\text{O}$ (1:1:18). After etching square Au (n-type) or Al (p-type) Schottky contacts (100 μm x 100 μm) were defined. C-V measurements were carried out on a Hewlett Packard 3497A Capacitance bridge at 1MHz and classical capacitance DLTS was applied with the rate window implemented by double lock-in filtering. The sample was mounted in the helium contact-gas of a continuous-flow LHe or LN₂ cryostat, allowing temperature sweeps between 10 and 400K.

III. Experimental results.

1) C-V measurements.

The free carrier concentration profiles as a function of depth, calculated from the C-V measurements show no change for the n-type material, indicating a low concentration of defects induced by RIE (compared to the dopant concentration) or a small depth over which the defects are induced (compared to the zero bias depletion depth). For the p-type, on the other hand, the free hole concentration is significantly lowered over a depth, depending on the original doping level (figure 1). For all doping levels examined, this depth exceeds the expected penetration depth of the plasma ions (only a few nm). The original dopant concentration is obtained at larger depths.

2) DLTS measurements.

a) Deep levels in p-GaAs.

The DLTS measurements were carried out on samples with an original doping level of approximately $1.5 \times 10^{17} \text{ cm}^{-3}$. As can be seen from the spectra (figure 2) only level H2 is related to the RIE-process. Figure 3 shows the Arrhenius plot of the emission rate e_p for the trap H2 using $e_p = K_1 T^2 \exp(-\Delta E/kT)$. We obtain $\Delta E = (538 \pm 8) \text{ meV}$ and $K_1 = (1.4 \pm 0.4) \times 10^6 \text{ K}^{-2} \text{ s}^{-1}$ with an apparent capture cross-section $\sigma_a = (8 \pm 3) \times 10^{-16} \text{ cm}^2$.

H2 shows, as a function of depth, a concentration profile similar to the reduction in free hole concentration. The density amounts to $3 \times 10^{16} \text{ cm}^{-3}$ at a depth of 150nm below the barrier interface indicating a close relation to the observed carrier removal. In the literature several defects have been reported with a signature very close to H2 (5): the Fe(-/o) acceptor level (6), the EL2(+/-) donor level (7) and an I_{AS} -impurity complex (8).

The concentration of the defect is too high to be related to any (if there is any) incorporation of Fe which would come from stainless steel parts in the reaction chamber and from the gas leads. Additionally, Fe is known to be an acceptor in GaAs (6,9) and so it cannot explain the reduction in free carrier concentration seen in the C-V measurements. SIMS measurements carried out on p-type RIE-etched samples did not show the presence of Fe above the detection limit of the system.

On the other hand the assignment of H2 to EL2, located at $E_v + 0.52 \text{ eV}$, would very well explain the carrier removal in the p-type samples. An EL2 density of $3 \times 10^{16} \text{ cm}^{-3}$ would compensate 6×10^{16} shallow acceptors, in fair agreement with the electrical data. Verification of the assignment to EL2 by DLTS observation of the well known EL2(o/+) band is however impossible in p-type material(10).

The signature of H2 is almost identical with the signature of the H3 level in ref.8 so that in fact the same defect may have been observed in both cases. The assignment of H2 to a complex involving an impurity already present before the RIE etch seems however rather improbable regarding the high density required: there is no evidence for such an impurity except Zn to be present at densities of a few times 10^{17} cm^{-3} .

b) Deep levels in n-GaAs.

Typical DLTS results for RIE and wet etched n-type GaAs are shown in figure 4. Of the four bands present in the reference sample, only E4 is seen after RIE where its concentration has increased by less than a factor of two. In both cases the total concentration of deep levels remains however small with respect to the doping level, which is in agreement with the C-V result. The band E4 occurs at the well-known DLTS position of the EL2(o/+) level at about $E_c - 0.75 \text{ eV}$, also indicating an increased

concentration of EL2. The concentration remains however more than two orders of magnitude below the concentration of H2 in p-type material, at least in the range accessible by DLTS which is about 50 to 200nm below the barrier interface. An EL2 concentration of a few 10^{14}cm^{-3} following $\text{CCl}_2\text{F}_2/\text{O}_2$ RIE etching of n-GaAs was also observed by Pearton et al.⁽¹⁾.

IV. Discussion.

It seems obvious from the DLTS measurements on p-GaAs, that during the etching process, EL2-defects are created, and these defects can explain the observed decrease in free hole density. The density of these traps seems to be proportional to the original dopant concentration and the penetration depth of the damage increases as the dopant concentration decreases. A correlation between damage induced by RIE and EL2 was already seen after CHF_3 RIE⁽¹¹⁾ and $\text{CCl}_2\text{F}_2/\text{O}_2$ RIE⁽¹⁾.

For the n-type GaAs the changes in deep level concentration are at least two orders of magnitude smaller than the shallow level concentration, and so this will have only a minor effect on the electrical characteristics of the material, in agreement with the unchanged free carrier concentration.

At least two mechanisms can explain the large penetration depth of the damage in p-type material. The first is recombination enhanced migration⁽¹²⁾, which has been invoked to explain the higher mobility of I_{AS} in p- than in n-type GaAs^(5,8). Since I_{AS} is thought to be a constituent of the H3 level found in ref.8 and of the EL2-defect, which both have a signature close to our H2 level, this may also explain the difference in damage depth found in our results. On the other hand it is at this moment not clear how this mechanism alone could explain the dopant concentration dependence of the damage depth. A second possible explanation is given by field-diffusion of the defects due to surface fields which are present at the semiconductor surface during the RIE. These surface fields can be caused by the difference in penetration depth between the plasma ions and electrons, and so will have a opposite direction for opposite material type⁽¹³⁾. The latter mechanism can explain the dependence both on the dopant type as well as the dopant concentration reported before, suggesting a high EL2-mobility at relatively low temperature.

V. Conclusions.

In this paper we presented an electrical study of damage induced by SiCl_4 -RIE in both n- and p-type GaAs. Using DLTS, we have observed large concentrations of defects in p-GaAs, probably the native defect EL2. The presence of this defect and the estimated concentrations, can explain the observed changes in free carrier concentrations and changes in barrier heights. For n-GaAs no mayor changes in deep level concentrations are observed. The difference between n- and p-type material, can be explained by both recombination enhanced migration and field-diffusion of defects.

Acknowledgements.

We would like to thank C. Eechout (LEA-IMEC) for device fabrication, A. Ackaert and L. Buydens (LEA-IMEC) for MOCVD growth and W. Vandervorst (IMEC) for SIMS measurements. Part of this work was supported by the European Community Esprit Basic Research Action nr 3133.

¹ S.J. Pearton, A.B. Emerson, U.K. Chakrabati, E. Lane, K.S. Jones, K.T.Short, A.E. White, T.R. Fullowan, J. Appl. Phys. 66, 3839 (1989).

² L.L. Yeh, Y. Xie, P.H. Holloway, J. Appl. Phys. 65, 3568 (1989).

³ Y.X. Wang, P.H. Holloway, J. Vac. Sci. Technol., A2, 567 (1984).

⁴ P. Van Daele, D. Lootens, P. Demeester, Vacuum 41, 906 (1990).

⁵ J.C. Bourgoin, H.J. von Bardeleben, D. Stievenard, J. Appl. Phys. 64, R65 (1988).

- 6 M. Kleverman, P. Omling, L.-Å Ledebo, H.G. Grimmeiss, J. Appl. Phys. 54, 814 (1983).
- 7 J. Lagowski, D.G. Lin, T.P. Chen, M. Skowronski, H.C. Gatos, Appl. Phys. Lett. 47, 929 (1985).
- 8 D. Stievenard, X. Boddaert, J.C. Bourgoin, Phys. Rev. B 34, 4048 (1986).
- 9 A.G. Milnes, Deep Levels in Semiconductors, J. Wiley, New York 1973, p61.
- 10 D.E. Bliss, D.D. Nolte, W. Walukiewicz, E.E. Haller, J. Lagowski, Appl. Phys. Lett., 56, 1143 (1990).
- 11 T. Ikoma, Y. Hagihara, Materials Science Forum 38-41, 67 (1989).
- 12 M. Lannoo, J. Bourgoin, Point Defects in Semiconductors I, Solid-State Sciences 22, Springer Berlin 1981, p232.
- 13 D. Lootens, F. Depestel, P. Van Daele, P. Demeester, Proceedings of the twelfth state-of-the-art program on compound semiconductors (SOTAPOCS XII), The Electrochem. Soc. vol. 90-15 (1990), p38.

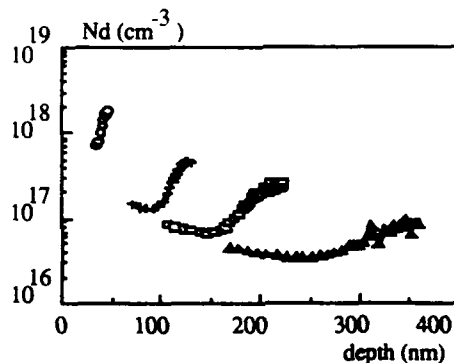


Figure 1: Free-carrier concentration as a function of depth, for RIE etched p-GaAs of different dopant concentrations (approx. 2×10^{18} , 5×10^{17} , 3×10^{17} and $1.5 \times 10^{17} \text{ cm}^{-3}$ resp.).

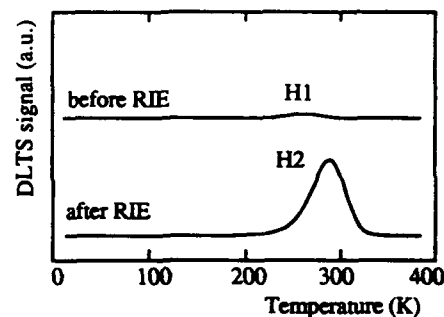


Figure 2: DLTS of p-GaAs; original material: $p = 1.5 \times 10^{17} \text{ cm}^{-3}$; $\tau_{\text{window}} = 6 \text{ ms}$, before (=wet etched) and after RIE. Both spectra are drawn on the same scale

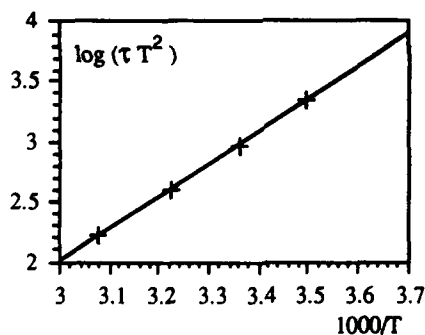


Figure 3: Arrheniusplot of the emission rate of trap H2 (experimental points are indicated).

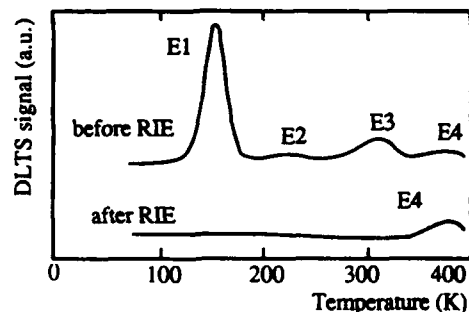


Figure 4: DLTS of n-GaAs; original material: $n = 2 \times 10^{17} \text{ cm}^{-3}$; $\tau_{\text{window}} = 14 \text{ ms}$, before (=wet etched) and after RIE. Both spectra are drawn on the same scale

Electron-beam Writing System for Holographic Optical Elements

Yoshikazu HORI, Fumihiko SOGAWA, and Makoto KATO
 Opto-Electronics Research Lab., Semiconductor Research Center,
 Matsushita Electric Industrial Co. Ltd.
 Moriguchi, Osaka, 570 Japan.

Abstract

A highly accurate and versatile electron-beam(EB) writing system suitable for fabrication of holographic optical elements (HOEs) with arbitrary patterns is developed. New HOEs with multiple functions are successfully fabricated by the EB system, and their unique applications are introduced.

I. Introduction

Holographic optical elements (HOEs), which have planar structures and multiple functions, will play important roles in photonics by not only miniaturizing conventional optical systems but also improving their properties. Therefore, the development of a novel technology suitable for fabricating arbitrary HOEs is required, and applications of HOEs to improve the properties of conventional optical systems are expected to be introduced. Electron-beam(EB) lithography is considered to be the most promising fabrication technology, because direct writing of the hologram patterns with grating periods from submicrons to submillimeters is possible. Since HOEs generally consist of gratings with curved and chirp structures, conventional EB exposure systems, which are optimized for ultra large scale ICs' (ULSIs') patterns with rectangular units, are difficult to be applied for HOEs especially with submicron grating periods. Therefore, EB writing systems optimized for HOEs must be newly developed. Some systems designed for some optical elements have been already reported, however, the drawable patterns are limited to simple cases^[1,2].

For the fabrication of arbitrary HOEs, the necessary functions in the EB systems are (A)arbitrary hologram pattern writing, (B)accurate beam deflection distortion calibration, (C)precise dose control for blazed cross-sectional structure formation^[3] and for proximity effects calibration, in addition to high resolution lithography and high speed writing. In this paper, we report having developed a highly accurate and versatile EB writing system suitable for fabrication of arbitrary HOEs. Then, we introduce new HOEs with multiple functions, which have been successfully fabricated by the EB systems, and demonstrate their unique applications.

II. Developed electron-beam writing system for HOEs

A schematic block diagram of the EB writing system is shown in Figure 1. The system consists of a personal computer (PC) for hologram pattern generation, a minicomputer for line data generation of each grating line in hologram patterns, for numerical data processing and for data transfer, a D/A converter system for beam scanning, a scanning electron microscope (SEM) for lithography. The most important and novel feature of the EB system is the employment of a full digital beam scanning method by dual 16 bit-D/A converters with 64K-word static RAMs for both x and y coordinates of the grating lines of hologram patterns. We believe the method is the most versatile for arbitrary hologram pattern writing, beam deflection distortion calibration, and dose control. The calibration of beam deflection distortion of SEM, and dose control is feasible by means of numerical processing in the minicomputers. Besides this point, we employed a 150M-Byte hard disk for storage, of the sampled data generated by the PC, and a beam deflection

distortion measurement system of the SEM for precise beam deflection distortion calibration. The electrical noises caused by such as electrical connection between the instruments, which degrades the resolution of the lithography, is suppressed as much as possible.

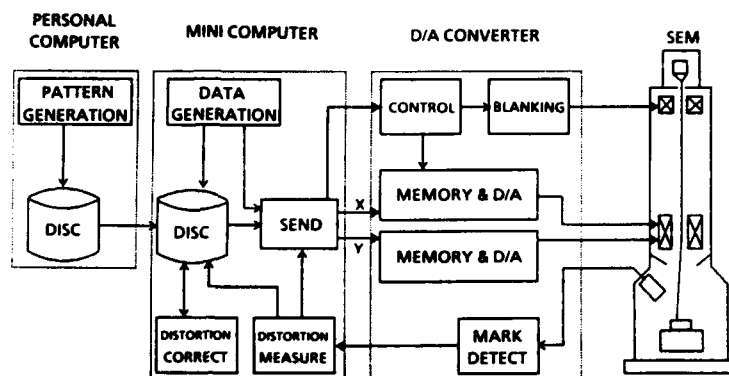


Fig.1 Block diagram of the developed EB writing system

III. Deflection distortion calibration

Before HOE pattern writing, we measured the beam deflection distortion of the SEM for calibration. The result is shown in Fig.2, in which the values for distortion are expanded by twenty times. Based on the results, two dimensional table of the calibration coefficients, which we denote by $a_x(x,y)$ and $a_y(x,y)$ is obtained. The calibration is performed by replacing the x and y data by minicomputer to $x' = a_x(x,y) + b_x x$ and $y' = a_y(x,y) + b_y y$ ^[4]. Here, b_x and b_y are the beam deflection adjustment coefficients. Fig.3 shows the beam traces before and after the calibration. The beam distortion after the calibration is suppressed to less than 0.1% in the area of $1 \times 1 \text{ mm}^2$.

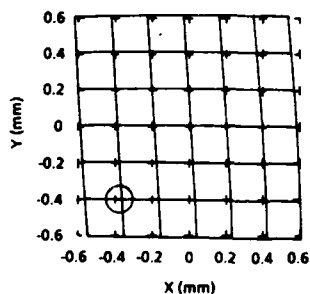


Fig.2 The beam deflection distortion in SEM.



Fig.3 The beam traces before and after the calibration for the point indicated by the circle in Fig.2.

IV. HOE with arbitrary hologram patterns

We show examples of HOEs with arbitrary hologram patterns written by the EB system to demonstrate the functions and properties of the system. Fig.4 is a part of a focusing grating coupler without aberration^[4], which convert a guided wave to a spherical wave. Fig.5 is an example of HOEs with arbitrary hologram patterns, in which two concentric gratings with half wavelength phase shift are drawn by the EB systems.

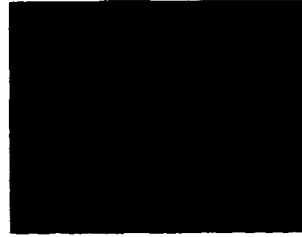


Fig.4 A part of the focusing grating coupler.

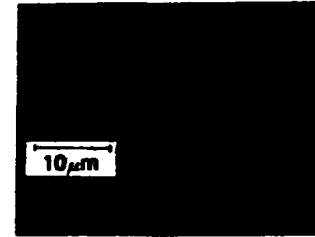


Fig.5 Examples of HOE with arbitrary patterns by EB.

V. Applications of HOEs fabricated by EB writing system

We propose and introduce new applications of HOEs with functions of lens and grating^[5], which have been realized by our EB system.

(A) Short External Cavity Semiconductor Laser^[6]

External cavity semiconductor lasers with grating for selective wavelength optical feedback, which enables single wavelength oscillation, are indispensable light sources in wavelength division multiplexing and coherent optical communication systems. The problems in conventional external cavity semiconductor lasers^[7], which use collimating lenses and linear gratings, are the large size and the limited modulation frequency due to the long external cavity length owing to the existence of collimating lenses. The limitation of the external cavity length was 7mm and the modulation frequency limit was about 1GHz^[7]. We introduce the application of the HOEs with above functions to the external cavity lasers for realizing the cavity length as short as 2mm, which is shown in Fig.6. The grating lines of the HOE are given by

$$x^2 + (y - f \cos \theta)^2 = (m \lambda_0 / 2 + f)^2 - (f \cos \theta)^2. \quad (\text{Eq.1})$$

We fabricated the HOE with parameters of $f = 2\text{mm}$, $\theta = 45^\circ$, $\lambda_0 = 1.3\mu\text{m}$ and with area of $1.4 \times 1.4\text{mm}^2$, in which the grating periods ranges from 0.8 to $1.5\mu\text{m}$, and the grating height is $0.3\mu\text{m}$. Dose control to keep a constant line and space ratio is performed by controlling the beam scan speed according to the grating periods by make use of the full digital scan method. A diffraction efficiency of 60% was obtained for $1.3\mu\text{m}$. The fabricated HOE was combined with an InGaAsP/InP semiconductor laser of $1.3\mu\text{m}$ wavelength region. Single mode oscillation with side mode suppression ratio of 30dB and high frequency modulation up to several GHz has been realized. The small signal response of the new external cavity laser at $I = 1.05 \times I_{th}$ is shown in Fig.7 by solid line, in which the properties of the conventional external cavity laser with cavity length of 7mm is also shown by the broken line for comparison. The modulation frequency limit of external cavity lasers is successfully extended by employing the HOE.

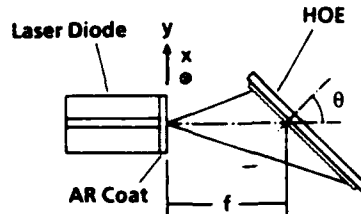


Fig.6 New external cavity laser with HOE.

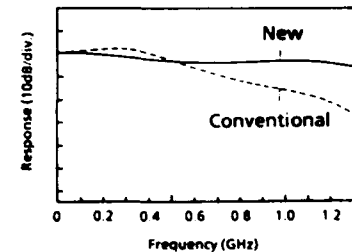


Fig.7 Small signal responses of the ext. cavity lasers.

(B) Small Size Polychromator^[8]

Polychromators are widely used as compact spectrometers. The size reduction of polychromators will expand their applications to such as color sensors. However, the size is limited by the focal length of the concave mirror on which surface gratings may be uniformly fabricated. We introduce the application of the HOE with functions of lens and grating for realizing a small size polychromator as shown in Fig.8. The grating lines of the HOE are given by

$$\sqrt{x^2 + y^2 + 2yf_1 \sin \theta_1 + f_1^2} + \sqrt{x^2 + y^2 - 2yf_2 \sin \theta_2 + f_2^2} = m \lambda_0 + f_1^2 + f_2^2. \quad (\text{Eq.2})$$

We fabricated the HOE with parameters of $f_1 = 2.6\text{mm}$, $f_2 = 30\text{mm}$, $\theta_1 = 65.4\text{deg.}$, $\theta_2 = 0\text{deg.}$, $\lambda_0 = 0.62\mu\text{m}$ and with area of $1 \times 1\text{mm}^2$, in which the grating periods ranges from 0.65 to $0.73\mu\text{m}$, and the grating height is $0.2\mu\text{m}$. The diffraction efficiency of 30% for the entire visible spectrum was obtained. The measured spectrum of mercury lamp is shown in Fig.9 as an example. The wavelength resolution of the polychromator is less than 20nm .

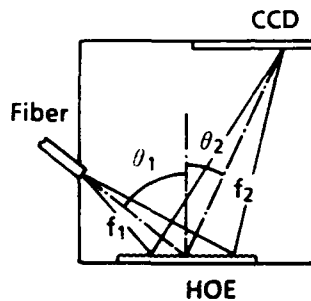


Fig.8 New small size polychromator with HOE.

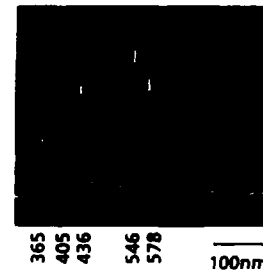


Fig.9 The measured spectrum of mercury lamp.

VI. Summary

We have developed a novel EB system suitable for fabrication of HOEs with arbitrary hologram patterns. New multiple functional HOEs with submicron grating periods are fabricated by the EB system, and their applicability to external cavity lasers and polychromator is demonstrated.

Acknowledgement

The authors are grateful to Prof. H.Nishihara, Dr. T.Suhara, and Dr. S.Ura of Osaka University for the useful advice in the development of the EB system. They acknowledge the support of Dr. T.Shiono in the Central Research laboratory and H.Asakura in the Audio-Video Development Center of Matsushita Electric Industrial Co., Ltd.

- [1]T.Suhara et al., IEEE J. Quantum Electron. Vol.QE-22, 845 (1986)
- [2]T.Shiono et al., Appl. Opt. Vol.26, 587 (1987)
- [3]H.Nishihara et al., "Micro Fresnel Lens " in Progress in Optics, Vol.24, E.Wolf Ed., North-Holland, Amsterdam, Chapt.1 (1987)
- [4]F.Sogawa et al., to be published in Appl. Opt. Dec. (1990)
- [5]Y.Hori et al., Appl. Opt. Vol.29, 2522 (1990)
- [6]Y.Hori et al., IEEE J. Quantum Electron. Vol.QE-26, 1747 (1990)
- [7]H.Asakura et al., 1989 Autumn National Convention Record, IEICE of Japan, C-162 (1986)
- [8]F.Sogawa et al., Submitted to Appl. Opt.

Micro Dry Etching Process for Vertical Cavity Surface Emitting Lasers

A. Matsutani, F. Koyama and K. Iga
Tokyo Institute of Technology
4259 Nagatsuta, Midori-ku, Yokohama 227, Japan

1. Introduction

A microcavity surface emitting (SE) laser is very attractive for future optoelectronic applications such as optical parallel processing and optical interconnections¹⁾. In order to realize such a low threshold SE laser, micro-fabrication providing a low damage etch is one of important issues. We have introduced a reactive ion etch (RIE) and reactive ion beam etch (RIBE) technique to fabricate a tiny dielectric multilayer reflector and micro-resonator for surface emitting lasers. In most of SE laser structures, a $\text{SiO}_2/\text{TiO}_2$ dielectric multilayer reflector or semiconductor multilayer mirror is used as high reflective mirrors. However, it has been difficult to fabricate the microcavity with steep side walls by wet chemical etching since each material has different etching rates. Dry etch techniques for multilayer structures, especially for GaInAsP/InP semiconductors, have not been fully studied. In this paper, micro dry etch processes for $\text{SiO}_2/\text{TiO}_2$ and GaInAsP/InP multilayers have been developed to form microcavities.

2. Formation of Micro Dielectric Multilayer Mirror by RIE

$\text{SiO}_2/\text{TiO}_2$ and Si/ SiO_2 dielectric multilayer reflectors have been used for GaAs/GaAlAs and GaInAsP/InP SE lasers, respectively. To reduce the diffraction and scattering losses at the multilayer reflector, it is necessary to make a tiny mirror with a steep and smooth wall. Here, we investigated a RIE technique to etch such a dielectric hetero-structures. Table 1 shows the etch rates of Si, SiO_2 , TiO_2 , GaAs substrate and a Cr metal as a mask material, respectively. The employed etching gas is CF_4 . The samples were etched with a pressure of 0.12 Torr and rf power of 100 W. The target used here is made of Teflon (C_nF_{2n}) which is effective to decrease the influence of free fluorine radicals²⁾. Figure 1 shows an SEM photograph of dielectric multilayer reflector array of $5\mu\text{m}$ in diameter. A steep vertical shape was ob-

tained with a good uniformity. This micromirror has been used in GaAs/GaAlAs SE lasers resulting in the threshold to 18 mA from 30 mA which was previously reported.

We have investigated RIE induced damages of a GaAs substrate by a PL measurement. A He-Ne laser ($\lambda = 633\text{nm}$) was used as a pumping source. The processed GaAs substrate was damaged, but the induced damage was recovered to some degree by thermal annealing in H_2 at 400°C ³⁾. On the other hand, any damages of GaAlAs/GaAs DH wafer was not observed, because the GaAs active layer in DH structure was located $1\mu\text{m}$ from the surface³⁾. Figure 2 shows the change of PL intensity for the GaAs substrate etched by RIE versus the distance from the surface. The depression of PL intensity was observed. The damage depth is estimated to be $0.3\mu\text{m}$.

3. RIBE of Quaternary Semiconductor Materials

RIBE is a promising technique for semiconductor micro-fabrication for SE lasers. So far, some RIBE etching conditions for GaAs and InP have been studied^{5,6)}, but data for GaInAsP are not enough yet. Figure 3 shows the measured etch rates of InP, GaAs and $\text{Ga}_{0.73}\text{In}_{0.27}\text{As}_{0.6}\text{P}_{0.4}$ ($\lambda_g = 1.3\mu\text{m}$) for various substrate temperatures and extraction voltages. The sample was etched with a gas pressure of 8×10^{-4} Torr and Cl_2 gas flow rate of 10 sccm. The etch rates increase in proportional both to the extraction voltage and etching temperature. The etch rate of GaInAsP was found to be in between InP and GaAs in each temperature. The etch rate of GaInAsP is closed to that of InP at 100°C , however it approaches to that of GaAs at 250°C . The etch rate looks strongly depend on the In concentration at low temperatures.

4. RIBE of Semiconductor Multilayer

Figure 4 shows a cross-section of a strip of 15 pair GaInAsP/InP semiconductor multilayer etched by RIBE. This semiconductor multilayer was grown by a chemical beam epitaxy (CBE)⁴⁾. The sample was etched with a gas pressure of 8×10^{-4} Torr, sample temperature of 170°C , and extraction voltage of 400V. The etching time of GaInAsP/InP multilayer was 15 min. The straight side wall was obtained, although the etch rate of GaInAsP is quite different from that of InP as described above. Figure 5 shows an SEM photograph of circular array pattern of GaInAsP/InP DH wafer with $2\mu\text{m}$ thick GaInAsP layer etched by RIBE. The diameter is $5\mu\text{m}$. This wafer was grown by LPE and

etched by RIBE by the same condition as indicated in Fig. 4. The profile near the edge of substrate shows a reasonably vertical shape. However, the wall near the center looks like a taper shape near the bottom. This effect may be originated from the high mask pattern density.

5. Conclusion

We have established RIE and RIBE dry etch processes for making microcavity SE lasers. A tiny circular structure of $\text{SiO}_2/\text{TiO}_2$ multilayer reflector was fabricated by RIE. We have shown that the active layer in DH wafer was not damaged by the RIE process. The damage of the cladding layer can be relaxed by thermal annealing. Thus obtained tiny dielectric mirror has been used for SE laser devices and it is shown to be very effective for low threshold operation and transverse mode control of SE lasers.

In addition, we have examined RIBE for GaInAsP for the first time, in order to fabricate microresonator composed of semiconductor multilayer. The straight side wall of GaInAsP/InP multilayer was obtained. The RIBE is very effective for producing a semiconductor microresonator. The induced damage on the side wall is a remaining problem, which is now under investigation.

Acknowledgment

The authors acknowledge Prof. Y. Suematsu, the president of Tokyo Institute of Technology for encouragement. This work was partly supported by a Grant-in-Aid for Encouragement of Young Scientists (B) #02918036 from the Japanese Ministry of Education, Science and Culture given to one of the authors (A.M.).

References

- 1) K. Iga, F. Koyama, and S. Kinoshita : IEEE J. Quantum Electron. **24** (1988) 1845
- 2) S. Matsuo and Y. Takenaka : Jpn. J. Appl. Phys. **16** (1977) 175
- 3) A. Matsutani, F. Koyama and K. Iga : Jpn. J. Appl. Phys. **30** (1991) (to be published)
- 4) T. Uchida, T.K.Uchida, N. Yokouchi, T. Miyamoto, F. Koyama and K. Iga : The Japan Society of Applied Physics the 51st Autumn Meeting 27aV8 (1990)
- 5) K. Asakawa and S. Sugata : J. Vac. Sci. Technol. **B3**(1) Jan/Feb (1985) 402
- 6) T. Tadokoro, F. Koyama and K. Iga : Jpn. J. Appl. Phys. **27** (1988) 389

Table I Etching Rate of dielectric,
GaAs and Cr by RIE

| Materials | Etching Rate |
|------------------|---------------|
| SiO ₂ | 1800 (Å /min) |
| TiO ₂ | 880 |
| Si | 850 |
| GaAs | 25 |
| Cr | 20 |



Fig.1 SiO₂/TiO₂ multilayer
reflector (D=5 μm)

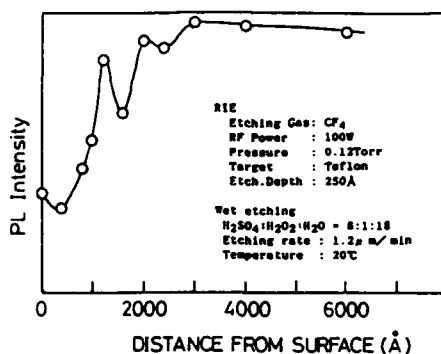


Fig.2 PL intensity vs. distance
from surface

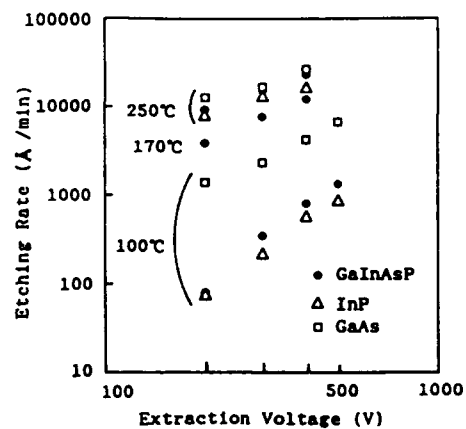


Fig.3 RIBE etch rate for InP,
GaAs and GaInAsP

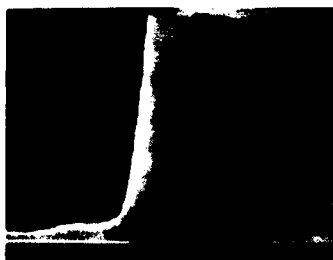


Fig.4 Cross section of GaInAsP/InP
semiconductor multilayer etched
by RIBE

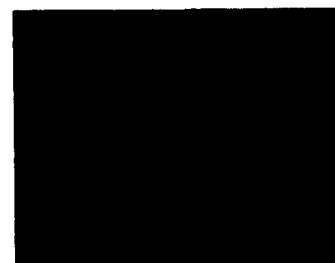


Fig.5 SEM photograph of circular
pattern GaInAsP/InP DH wafer
etched by RIBE

SULFIDE TREATMENT ON III-V COMPOUND SURFACES

Yasuo NANNICHI

Institute of Materials Science, University of Tsukuba

1-1-1, Tennodai, Tsukuba, 305 JAPAN

I. INTRODUCTION

The treatment of GaAs with a sulfide solution was initiated by Sandroff and others in 1987. They used Na_2S as the magic agent. After soaking the GaAs crystal, photoluminescence (PL) signal was drastically intensified and the current amplification factor in a bipolar transistor increased, meaning the suppression of carrier recombination velocity at the surface. However, it was soon known that the treatment effect was lost by rinsing the surface with water. They suggested the use of other sulfides, but we were the first to observe the more reliable effect of $(\text{NH}_4)_2\text{S}$ as well as its variation, $(\text{NH}_4)_2\text{S}_x$.

In this talk I should like to clarify the difference in the effects of the latter two from Na_2S , in the light of electrical characteristics, and data on surface analyses. Preliminary theoretical results support what we interpret from the observation, so far. The effects of $(\text{NH}_4)_2\text{S}_x$ are similarly observed on many III-V compounds. Comments are also extended to the effect of other VI elements on III-V compounds. Finally, a few words should be added on the applicational aspects of this process.

II. SURFACE RECOMBINATION VELOCITY; BAND BENDING vs. DEFECT DENSITY

Decrease in the surface recombination velocity is observed by the increase in PL intensity, as well as its variation with band-bending modulation, EBIC measurement on diffusion length, and other means. However, the cause of this decrease remains disputable. That is, whether it is due to the band bending or to the real reduction in the surface or interface defect density. In the case of Na_2S , this is really difficult to tell, as the treated surface is covered with a crusty film of polar crystalline Na_2S .

In the case of $(\text{NH}_4)_2\text{S}_x$, even though the effect of band bending seems to remain, its effect seems much less compared with Na_2S . GaAs Schottky barrier heights reveal more distinct dependency on the work function of the metal on the sulfide treated surface, which is, in part, an evidence that the interface state density decreases after the treatment. Also observed is the reduction in the interface state density of MIS structures roughly by a factor of 10^2 , from 10^{13} to $10^{11} \text{ cm}^{-2} \text{ eV}^{-1}$ after $(\text{NH}_4)_2\text{S}_x$ treatment. In-situ observation by UV PES on the variation of the surface potential of the $(\text{NH}_4)_2\text{S}_x$ surface with deposition of aluminum must be interesting data.

III. SURFACE STRUCTURE; EXPERIMENTAL DATA AND THEORETICAL APPROACH

Combining all the surface analysis data obtained by RHEED, LEELS, AES, SIMS, PES, CAICISS, slow positron annihilation spectrum, etc., the change in the surface structure of $(\text{NH}_4)_2\text{S}_x$ -treated surface is getting clarified. The distinct difference of $(\text{NH}_4)_2\text{S}_x$ solution from Na_2S is that the former solution etches the natural oxide as well as GaAs. After the treatment, the GaAs surface is terminated with sulfur atoms, which reject adsor-

bing oxygen atoms. There are five states of the sulfur-covered surface.

1) Immediately after removing the wafer out of the solution, the surface is covered with a yellowish film. It is difficult to analyse the nature of this film, as it disappears immediately after putting the sample in a vacuum chamber for analysis. However, it should be reasonable to assume this an amorphous film of sulfur. 2) Most of amorphous sulfur atoms sublime in vacuum leaving a few atomic layer of sulfur. A strong PES signal of S-S bonds is observed. 3) Heating below 250°C, the layer is almost one monolayer thick. A strong signal of As-S bond and a weak one of Ga-S are observed. 4) At the reconstruction temperature of 250°C, the surface structure observed by RHEED suddenly changes from 1x1 to 2x1, and at the same time the PES signal intensities switch to a stronger Ga-S and a weaker As-S signal. 5) The above state remains up to the desorbing temperature of ca. 530°C, where sulfur atoms begin to desorb from GaAs surface.

As long as the surface is covered with sulfur, oxygen are prevented from adsorbing on the otherwise active surface of GaAs. This nature of adsorption free surface of $(\text{NH}_4)_2\text{S}_x$ -treated surface of GaAs seems essential to the reduction in the interface defect density, but it still remains open to more discussions.

Determination of the exact position of sulfur atoms on top of the GaAs surface is much sought about without apparent success, yet. In order to avoid technical difficulties with CAICISS, we made observation on the InAs surface, in stead of GaAs, in which similarity is ascertained. Our tentative interpretation is that below the reconstruction temperature the surface is rich with As atoms which are not exactly located on crystalline sites. Above the critical temperature sulfur atoms replace the surface As atoms to sit on the As site of InAs crystal.

Very encouragingly, our colleagues performed theoretical calculations to support our interpretation. Their calculations tell that when S-As bond is formed, the As-Ga bond is weakened. Thus by heating at the reconstruction temperature, the As more easily sublimates and S-Ga bonds stabler than S-As ones replace them.

IV. UNIVERSALITY OF THE SULFUR TREATMENT

There are similarities as well as differences among the effects by surface treatments on various III-V compounds. Data are accumulating but more systematic study is needed. The situation seems quite the same on the effect of Se and Te with III-V's.

VI. CONCLUSION

Sulfide treatment started as a very unique wet process, which does not have the weakness of oxidation. It even has the merit of 1) easiness of the treatment, 2) possibility of producing smooth surface and fine pattern definition of three-dimensional structures, when combined with epitaxial processes, 4) capability of dry process. Stabilization technique of the treated surface is necessary before this treatment is more widely adopted.

In conclusion, I should like to stress that sulfide treatment offered an adequate theme which bridges the science and technology of III-V compounds.

Sulfur Passivation of GaAs Surfaces

Yun Wang and Paul H. Holloway
Dept. of Materials Science & Engineering
University of Florida
Gainesville, FL 32611

Abstract

Passivation of GaAs (100) surfaces with chemical solutions containing P_2S_5 has been studied using photoluminescence, electrical tests (I-V, C-V), Auger electron and X-ray photoelectron spectroscopies, and scanning electron microscopy. The time stability of the interfacial passivation was a particular concern, and passivation protocols were developed to prolong the effects. The lifetime of passivation at contact interfaces were studied in particular. In addition, techniques to improve the uniformity of passivation and reduce surface morphology in the contact area have been developed.

Introduction

Passivation of GaAs surfaces with sulfur to reduce the density of surface states and the surface recombination velocities has attracted a lot of attention recently.¹⁻⁸ The most common sources of sulfur have been sodium sulfide, ammonium sulfide and hydrogen sulfide, however the mechanism(s) of passivation are not very clear nor is the lifetime of the passivity very long. Recently Lee, et al.⁹ has shown that a new source of sulfur (P_2S_5) is able to passivate GaAs (100) surfaces over longer times. Furthermore, Li and Hwang¹⁰ have shown that combining P_2S_5 with $(NH_4)_2S$ leads to much better unpinning of the Fermi level of Schottky contacts of Au to GaAs (determined from I-V and C-V measurements), and this passivation effects last a longer time in room temperature room air (as contrasted to the above mentioned single sulfide treatments). In this study we have used $P_2S_5/(NH_4)_2S$ solutions to passivate GaAs (100) surfaces, then examined the samples with a variety of analytical techniques to determine the mechanism of passivation and degradation, plus examine the topography induced by passivation and method to make the passivated surface more planar.

Experimental

The samples used in this study were Si doped n-type to 2×10^{17} - 3×10^{18} cm^{-3} . The substrates were cleaned prior to passivation with a trichlorethane, acetone, methanol and DI water rinse followed by etching for 20 sec. in an $NH_4OH:H_2O_2:H_2O$, rinsed in DI water, dipped in an $NH_4OH:H_2O$ solution, etched in an $HNO_3:H_2O$ solution, and blown dry with a nitrogen jet. The cleaned sample was immediately passivated with one of the following solutions: [1] 0.1 g/ml P_2S_5 in NH_4OH , or [2] 0.1 g/ml P_2S_5 in $(NH_4)_2S$.

The analytical techniques used to characterize these samples were scanning electron microscopy (SEM), angle-resolved X-ray photoelectron (XPS) or Auger electron spectroscopy (AES) and

photoluminescence analysis (PL). The time dependent of the passivation layer was determined using both PL and XPS by analyzing samples immediately after passivation (within 10 min.) and after selected periods of time in laboratory air (up to 3 weeks). A Mg anode was used for XPS in a Perkin Elmer Model 5100 spectrometer, while the PL data were collected using an argon ion laser emitting at 457 nm with an output power between 24 and 250 mW in a 2 mm spot and good linearity of the signal was observed (see Fig. 1). Normally the power out was 120 mW since this power level was shown to maximize the signal to noise ratio while still not degrading the PL intensity.

Results and Discussion

Even using the P_2S_5 containing solution, there was a relatively low signal from the surface from P, indicating that this element was not the species responsible for improved passivation lifetimes. In fact, there were no bonds detected between the GaAs substrate and P on the surface. The detected P was bound only to O (presumably as a phosphate) and was non-uniformly distributed over the surface. This indicates clearly that if P_2S_5 -containing solutions are to be used for passivation, a method to planarize the surface is necessary.

The XPS data show that S was bound both to Ga and As on the surface, but was not bound to the P. Thus the P_2S_5 molecule dissociates upon striking the surface, but the P does not bind strongly to the surface when S is available in sufficient abundance. With exposure to laboratory air, the PL intensity decreased with time and the XPS data showed an increasingly large concentration of O on the surface due to an increasing number of O-Ga bonds. Thus the mechanism of degradation appears to be oxygen-Ga bond formation at the expense of Ga-S and As-S bonds. Formation of Ga-O bonds obviously allow the reformation of surface states with high concentrations and high recombination velocities.

The rate of degradation versus the sources of S as, measured by PL, is shown in Table 1 and Fig. 2. As is obvious, the sample passivated in the ammonium sulfide solution was much more stable as compared to ammonium hydroxide. Both of these samples yielded higher PL signals, even after 8 days in air, as contrasted to as received samples. The passivation also increased the observed Schottky barrier heights, as shown in Table 2. The increase persisted with no sign of degradation even after exposure of the diodes to 7 days in air.

The SEM photomicrographs of the passivated treatments showed a very rough surface, apparently from crystals adhered to the surface from the solution. Some of these may have resulted from precipitation of crystals as the P_2S_5 /ammonium hydroxide or sulfide solutions were evaporating after the passivation treatment. However some of these may have resulted from saturation of the passivation solution by reaction and precipitation on the surface prior to rinsing or blowing with N_2 . A variety of washing treatments were attempted to remove the precipitates and retain the passivation, however rinsing was only successful when a sulfide solution was used. Specifically, washing with a $(NH_4)_2S$ solution

allowed the PL intensity to remain high. However washing with DI water or with an ammonium hydroxide solution caused the surface to exhibit a very low PL signal.

Summary

Polished surfaces of (100)GaAs was passivated with phosphorus sulfide in solutions of ammonium hydroxide or ammonium sulfide. The $P_2S_5/(NH_4)_2S$ solutions were more effective immediately and over times of several days in passivating the surface as measured by the intensity of photoluminescence. X-ray photoelectron data showed that the S bonded to both Ga and As on the surface, however the P did not bond to the semiconductor. Instead it bonded to O, presumable to form phosphates. This suggests that the improved stability of passivated GaAs surfaces resulting from the use of P-containing compounds results from a solution chemistry effect(s) not from interfacial chemistry effects.

References

1. C. J. Spindt, R. S. Besser, R. Cao, K. Miyano, C. R. Helms, and W. E. Spicer, Appl. Phys. Lett. 54, 1148 (1989).
2. M. S. Carpenter and M. r. Melloch, J. Vac. Sci. Technol. B7, 845 (1989).
3. M. S. Carpenter, M. R. Melloch, M. S. Lundstrom and S. P. Tobin, Appl. Phys. Lett. 52, 2157 (1988).
4. D Liu, T. Zhang, R. A. LaRue, J. S. Harris and T. W. Sigmund, Appl. Phys. Lett. 53, 1059 (1988).
5. R. J. Nelson, J. S. Williams, H. J. Leamy, B. Miller, H. C. Casey, B. A. Parkinson and A. Heller, Appl. Phys. Lett. 36, 76 (1980).
6. J. R. Waldrop, J. Vac. Sci. Technol. B3, 1197 (1985).
7. C. J. Sandroff, R. N. Nottenburgf, J. C. Bischoff and R. Bhat, Appl. Phys. Lett. 51, 33 (1987).
8. C. J. Sandroff, M. S. Hegde and C. C. Chang, J. Vac. Sci. Technol. B7, 841 (1989).
9. H. H. Lee, R. J. Racicot and S. H. Lee, Appl. Phys. Lett. 54, 724 (1989).
10. K. C. Hwang and S. S. Li, J. Appl. Phys. 67, 2162 (1990).

Table 1
Relative Photoluminescence Intensity vs Solution and Time

| Solution | PL Intensity | | |
|--------------------|--------------|--------|--------|
| | 1.5 hrs | 5 hrs. | 8 days |
| As Received | 1.0 | 1.0 | 1.0 |
| P_2S_5/NH_4OH | 7.0 | 1.5 | 1.5 |
| $P_2S_5/(NH_4)_2S$ | 14. | 7.4 | 2.5 |

Table 2
Schottky Barrier Height(eV) for Au on n-GaAs

| Solution | Initial Values | | Seven Days | |
|--|----------------|------|------------|------|
| | I-V | C-V | I-V | C-V |
| $\text{NH}_4\text{OH}/\text{HF}$ | 0.94 | 0.94 | 0.96 | 0.97 |
| $\text{P}_2\text{S}_5/(\text{NH}_4)_2\text{S}$ | 1.12 | 1.21 | 1.10 | 1.22 |

Figure 1
Photoluminescence Intensity vs. Irradiation Power Density

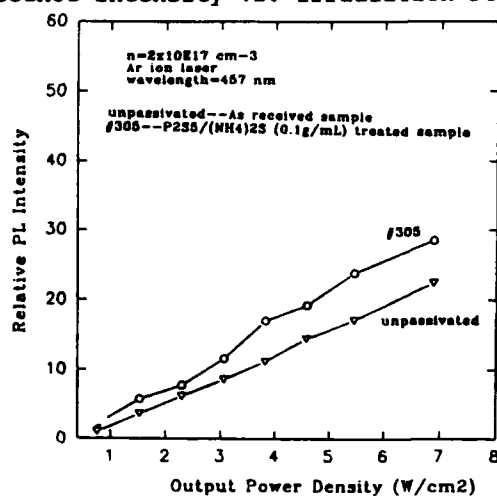
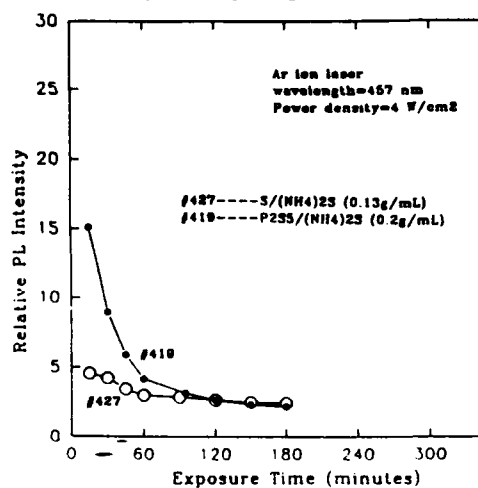


Figure 2
Relative PL Intensity vs Ageing Time in Laboratory Air



Direct observation of GaAs surface cleaning process under hydrogen radical beam irradiation

Hiroshi Iwata and Kiyoshi Asakawa

Opto-Electronics Research Laboratories, NEC Corporation

34, Miyukigaoka, Tsukuba, Ibaraki, Japan 305

Recently dry etching techniques have been adopted for surface cleaning of III-V compound semiconductors.¹⁻³ The effectiveness of hydrogen (H) radical beam produced by electron cyclotron resonance (ECR) plasma for low-temperature surface cleaning has been successfully demonstrated.^{4,5} Removal of oxygen contamination on the GaAs substrate has been performed by H radical beam irradiation. This radical beam, which consists of only neutral radicals, is supposed to be free from surface damages caused by ion bombardment.⁵ Although the deoxidation of the native oxide layer resulting from the introduction of the H radical has been attributed as the factor leading to the removal of the oxygen contamination, there has yet to be any direct observation of such a chemical reaction.

In this work, we show, for the first time, an obvious increase in H₂O partial pressure under ECR H plasma radical beam irradiation. The increase in H₂O partial pressure is closely related to the removal of oxygen contamination on the GaAs surface. This phenomenon enables us to directly observe the surface cleaning process.

The cleaning chamber, with a radical beam gun and a quadrupole mass spectrometer (QMASS), is connected to an analysis chamber equipped with an Auger electron spectrometer (AES) as shown in Fig. 1. The vacuum is 1×10^{-9} Torr in the cleaning chamber and 3×10^{-10} Torr in the analysis chamber. H₂ ECR plasma can be excited in the compact plasma chamber with a microwave emitter and a permanent magnet, which is shown in Fig. 2. H radicals, released through a 10mm diam orifice with thermal energies, are irradiated onto a heated sample. The H₂ pressure can be controlled in a range between 3×10^{-5} Torr to 5×10^{-4} Torr. A 2.45GHz microwave input of 30-50W was used.

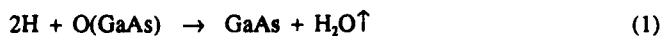
The samples were cut from (100)-oriented Cr-O doped GaAs wafers. Before being introduced into the vacuum chamber, the samples were first rinsed with organic solvents and deionized water, then etched in a solution of H₂SO₄ : H₂O₂ : H₂O = 4:1:1. After

rinsing in deionized water, the samples were mounted on a Mo block with In.

Figure 3 shows the change of QMASS H_2O intensity during the cleaning procedure. First, to remove the adsorbed H_2O molecule, the GaAs substrate was heated to $400^\circ C$ and then cooled without H_2 irradiation. An increase in H_2O partial pressure was observed as indicated by (A). Next the sample was heated to $350^\circ C$ under H_2 molecule irradiation of 1×10^{-4} Torr. Very few increases in H_2O were observed in this case (B). The adsorbed H_2O molecules were almost entirely removed by the first thermal treatment. As a result, there is no obvious increase in H_2O from H_2 molecule irradiation. After the sample temperature reached $350^\circ C$, an H radical beam was irradiated onto the GaAs surface for 10 minutes. As shown in (C), a rapid increase of H_2O was observed. This increase cannot be observed when the GaAs substrate does not exist. The rate of increase strongly depends on the sample temperature. From these results we concluded that this increase of H_2O was caused by a reaction between the H radical beam and materials on the GaAs surface.

The amount of increase in H_2O is in the order of 10^{-9} Torr. This increase could be observed only after reducing the incorporation of H_2O to a value of 1×10^{-10} Torr. To accomplish this, a filter was attached to the H_2 pipeline leading to the vacuum chamber. Once the filter had been set, the pipeline was baked at $300^\circ C$ first in vacuum and then with H_2 gas. Following this, H_2 gas was allowed to flow through the pipeline for one week.

The increase in H_2O can be attributed to the deoxidation of the oxide layer on the GaAs surface by the H radical. To clarify the relationship between the H_2O partial pressure and the oxygen on the GaAs surface, H radical beams a few minutes in length were irradiated several times onto the same GaAs substrate. The QMASS H_2O intensity and the AES intensity ratios of the oxygen and the gallium lines are shown in Fig. 4 and Fig. 5 respectively. The irradiation periods of time are illustrated in the upper side of Fig. 4 by straight lines. As each irradiation time was not same, the peak values cannot be compared with. An interesting points are that the H_2O rising rates decreased as the AES oxygen intensity decreased and that the shape of H_2O rising curves resemble. The AES oxygen intensity decreased exponentially as a function of the H radical beam irradiation time. The H_2O generation is directly related to the oxygen on the GaAs surface. This process can be written by the following chemical reaction⁴



Here, $O(GaAs)$ represents the oxygen-included GaAs layer.

As the reaction on the GaAs surface is not yet clearly understood, a simple reaction

model that the reaction rate will be proportional to the amount of oxygen on the GaAs surface N_{ox} is useful. When the vacuum chamber is pumped at a constant rate β , the H_2O molecules in the vacuum chamber $N_{\text{H}_2\text{O}}$ follow the equation

$$\frac{dN_{\text{H}_2\text{O}}}{dt} = kN_{\text{ox}} - \beta N_{\text{H}_2\text{O}} \quad (2)$$

Here, k and t represent reaction constant and time, respectively. Solutions are

$$N_{\text{H}_2\text{O}}(t) = \frac{kN_{\text{ox}}(0)}{\beta - k} [\exp(-kt) - \exp(-\beta t)] \quad (3)$$

$$N_{\text{ox}}(t) = N_{\text{ox}}(0)\exp(-kt) \quad (4)$$

where $N_{\text{ox}}(0)$ represents the amount of oxygen on the GaAs surface at $t=0$.

As equations (3) and (4) agreed well with the results of QMASS and AES measurements, this simple model is valid. The intensity of $N_{\text{H}_2\text{O}}(t)$ and $N_{\text{ox}}(t)$ are simply proportional to the initial oxygen value $N_{\text{ox}}(0)$, and those time dependence are determined by k and β . Equation (3) shows that the QMASS H_2O measurement is a quantitative and direct observation of cleaning process. The H_2O partial pressure is a good index of the reaction process. For a cleaning technique to be practically useful, the k value is desired to be larger than 0.1 min^{-1} . The value of k was estimated to be 0.23 min^{-1} from Fig. 5, making clear the efficiency of the H radical beam for GaAs surface cleaning.

In conclusion, an increase in H_2O partial pressure was observed under H radical beam irradiation. This increase can be attributed to the deoxidization of oxygen on the GaAs surface. This phenomenon can be observed by reducing the incorporation of H_2O . By measuring the H_2O partial pressure, the progress of cleaning can be directly observed. This phenomenon will become a useful technique for monitoring the cleaning process.

References

- 1) R. Z. Bachrach, *Prog. Cryst. Growth Charact.* 2, 115(1979)
- 2) R. P. Chang, C. C. Chang, and S. Darack, *J. Vac. Sci. Technol.* 20, 45(1982)
- 3) I. Suemune, A. Kishimoto, K. Hamaoka, Y. Honda, Y. Kan, and M. Yamanishi, *Appl. Phys. Lett.* 56, 2393(1990)
- 4) K. Asakawa and S. Sugata, *J. Vac. Sci. Technol.* A4, 677(1986)
- 5) S. Sugata, A. Takamori, N. Takado, K. Asakawa, E. Miyauchi, and H. Hashimoto, *J. Vac. Sci. Technol.* B6, 1087(1988)

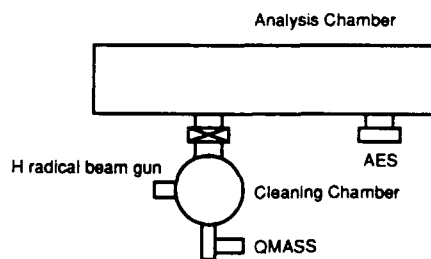


Fig. 1. Schematic diagram of cleaning chamber and analysis chamber.

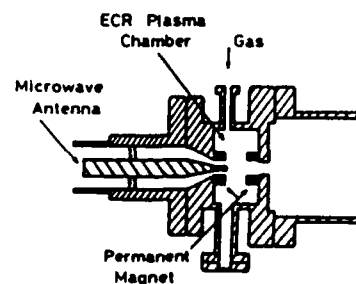


Fig. 2. Schematic diagram of a radical beam gun.

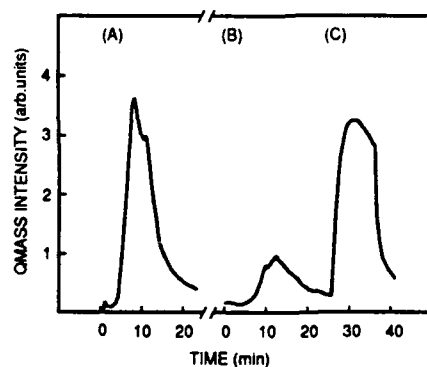


Fig. 3. QMASS H₂O intensity during the cleaning procedure; (A) sample was heated to 400°C in vacuum, (B) heated to 350°C under 1×10^{-4} Torr H₂ molecule irradiation, (C) irradiated 10 minutes H radical beam at 350°C substrate temperature.

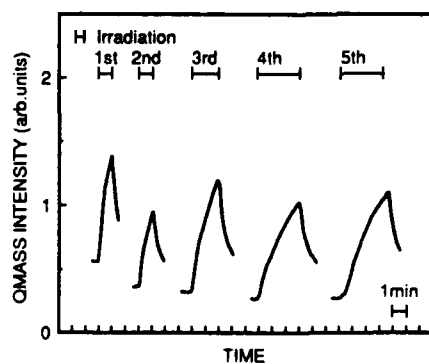


Fig. 4. QMASS H₂O intensity during H radical beam irradiation. H radical beams were irradiated five times.

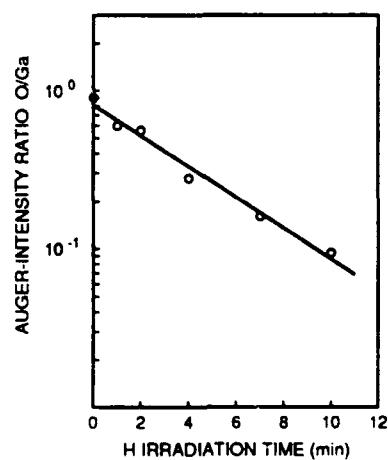


Fig. 5. AES intensity ratios of the oxygen and the gallium lines as a function of H radical beam irradiation time.

Near-Surface Type Conversion of p-type Single-Crystal InP by Plasma Exposure

X. Li, T.A. Gessert and T.J. Coutts.

Solar Energy Research Institute, 1617 Cole Blvd. Golden, CO 80401

Introduction

During the past several years considerable work has gone into describing why a buried homojunction forms during direct current (dc) magnetron sputter deposition of indium tin oxide (ITO) on single-crystal, p-type InP. Several mechanisms have been suggested to account for the resulting device behavior. Bachmann suggested that type conversion may be due to substitutional doping by Sn,¹ while Tsai et al. believed that sputter damage was a possibility.² In our own work, Sn-free In₂O₃ was substituted for the ITO, resulting in devices with very similar photovoltaic response to their ITO/InP counterparts, indicating that Sn is not the cause of type conversion.³ To investigate this junction formation process further, photovoltaic solar cells have been fabricated by exposing p-type InP substrates to a pure hydrogen plasma (without any deposition procedure involved). In this paper we report how this H₂ plasma exposure (PE) affects the InP surface properties. The results confirm that deposition is not necessary to cause the type conversion which forms the buried homojunction, and suggest a fabrication process that may be useful with other relevant materials.

Experimental

The InP substrates were purchased for Nippon Mining and had a carrier concentration of $1.6\text{--}1.9 \times 10^{16} \text{ cm}^{-3}$ [Zn-doped, (100) orientation]. The PE was performed in a Technics Planar Etch II rf plasma system with the InP substrates mounted on an 8 inch diameter grounded electrode. It should be noted that the rf frequency of this system is 30 kHz, much lower than 13.56 MHz commonly used. Thus the plasma potential is higher and effects due to ion bombardment are expected to be stronger. The hydrogen pressure used was 200 mTorr and the flow rate was 6 sccm. The rf power level was varied between 10 and 200 Watts (0.03–0.62 Watt-cm⁻²), and the exposure time was varied between 0.5 and 90 min. Except where noted, the substrates were not heated; however, temperature increases of up to ~20 °C were observed during the higher power and/or longer plasma exposures. Following PE, Hall (van der Pauw technique), electron channeling (EC), photoluminescence (PL), and deep level transient spectroscopy (DLTS) measurements were performed. Also, to assess device characteristics, small solar cells (0.1 cm²) were fabricated and analyzed using light and dark I-V and quantum efficiency (QE) measurements.

Results and Discussion

Our initial evidence that the hydrogen plasma effects the InP surface came from Hall measurements. These indicated that both p- and semi-insulating surfaces became n-type during PE. By assigning a nominal thickness of 100 nm to the type-converted layer,⁴ the mobility, carrier concentration and resistivity were found to be ~600 cm² V⁻¹ s⁻¹, $1.5 \times 10^{17} \text{ cm}^{-3}$ and $7 \times 10^{-2} \Omega\text{-cm}$.

respectively. Since effects due to ion bombardment were expected during PE, efforts to identify the mechanism of type conversion began with measurements to monitor changes in the surface quality as a function of PE parameters. EC analysis has been used to qualitatively study near surface damage (<100 nm) on the InP caused by the PE.⁵ Figure 1 shows a sequence of EC photographs illustrating how the pattern changes as the sample is exposed to increasing plasma power densities for a 30 min. exposure. This figure shows that surface damage increases as the plasma power increases. Although InP samples with different doping densities were studied, the effect of doping on the surface crystal structure is small, and thus EC analysis did not identify any dependence on doping level. However, EC comparisons made between the PE samples and samples exposed to a planar dc magnetron sputtering source (ITO deposition) indicate that relatively little surface damage occurs during sputtering.

Additional information about the PE-induced, near-surface damage was acquired through PL analysis. These measurements were used to determine if the dominant mechanism of type conversion is passivation of acceptor levels (in our case, Zn), or is somehow related to plasma damage. If passivation is the dominant mechanism, then the PL lifetime would increase. Although increases in PL response have been observed by others after similar PE treatments (but using Sn-doped [n-type] material),⁶ we found that the minority carrier lifetime decreased after PE. Furthermore, Figure 2 illustrates that this decrease is systematic with increasing power density. A likely explanation for both the PL and EC observations is that the PE causes plasma damage such as preferential etching of the phosphorus on InP, leaving an In-rich layer, as observed by others.⁷

The measurements discussed thus far have examined some electrical and structural properties of the type-converted region which forms very near the surface (<100 nm) of the InP after plasma exposure. Additionally, it has been found that although type conversion stops at ~70-100 nm from the surface,⁴ the effects of the plasma extend much deeper into the InP. Indeed, DLTS measurements that probe the defect behavior at the outer edge of the depletion width (for 2×10^{16} doping density and assuming an abrupt junction, the depletion width at zero voltage bias is ~300 nm) indicate that during PE, at least four defect levels form in the p-InP. One is an electron trap and three are hole traps. Two of the hole traps demonstrate considerable temperature instability and therefore were difficult to identify. However, due to their positions relative to the dominant (and temperature-stable) hole trap, we believe that they are H₃ and H₅, following standard identification conventions.⁸ The electron trap (minority carrier) has been identified as EPX, with a concentration of $N_T = 1.1 \times 10^{12} \text{ cm}^{-3}$ and an ionization energy of $E_i = 0.199 \text{ eV}$ below the conduction band. Also, the temperature-stable hole trap (majority carrier) has been identified as H₄, with a concentration of $N_T = 3.6 \times 10^{12} \text{ cm}^{-3}$ and an ionization energy of $E_i = 0.386 \text{ eV}$ above the valence band. It has been suggested that both of these traps are associated with a point defect such as a phosphorus vacancy. Specifically, it is speculated that EPX and H₄ relate to the phosphorus vacancy (V_P) and the interstitial phosphorus (P_i), together forming a Frenkel-pair of V_P-P_i .⁸ Theoretical and experimental studies of interstitial-vacancy Frenkel-pair centers suggest that they can act as singly- or doubly-ionized donor species and also as nonradiative recombination centers.^{9,10,11}

The device properties were found to be sensitive to the PE parameters used. Specifically, it was found that for a plasma power of 20-70 Watts, the optimum exposure time is ~10-20 min. Longer exposure time, higher power density and/or substrate temperatures higher than 150°C resulted in decreased device performances. Although most of the devices were fabricated using a pure H₂ plasma, some devices were fabricated using a pure-Ar plasma. These Ar cells also demonstrated photovoltaic response (although inferior to the hydrogen cells) supporting the speculation that ion bombardment is the dominant type conversion mechanism. Performance comparisons between PE cells and similar ITO/InP cells are difficult because after PE, the plasma-formed solar cells do not have the advantage of an ITO layer, which reduces both reflection and emitter sheet resistance losses. To solve these problems, a single PE cell (H₂ plasma) was fabricated with a grid design that accounted for the higher emitter sheet resistance, and with a ZnS/MgF₂ AR coating to compensate for differences in reflection. When this was done, the measured fill factor (FF) of the PE cell was found to be very similar to that of an ITO/InP cell (~82%). This indicates that the low FF of the typical test structures (fabricated with a grid designed for ITO/InP cells) is not due to poor junction quality but, as expected, due to the high series resistance of the emitter. However the open-circuit voltage and the short circuit current for the PE cells are both slightly lower than the ITO/InP cells. When these performance parameters are combined and compared to the best ITO/InP cell efficiency (18.9%, global), the best PE efficiency of 16.2% is lower, yet still remarkable.¹² The result that the PE cells are of poorer quality than the ITO/InP cells suggests that ion bombardment limits the performance of the PE cells.

Conclusions

This work has shown that exposure to a pure H₂ or pure Ar plasma causes p-InP surfaces to be converted to n-type. EC and PL measurements indicated that considerable surface damage occurs during PE, and that this damage is more severe than that observed to occur in similar ITO/InP devices where the junction is formed during dc magnetron sputter deposition of ITO. DLTS measurements indicate that at least four defect traps are introduced into the p-InP base during PE. Two of these traps have been identified as EPX and H₄, and have been proposed to be a Frenkel-pair V_P-P_i generated via ion bombardment. Taken together, these results indicate that the dominant mechanism of type conversion in p-InP is likely phosphorus depletion. However, type conversion may also be assisted by other mechanisms, such as hydrogen passivation of Zn acceptors.

Acknowledgements

This work was supported by the U.S. Department of Energy under Contract No. DE-AC02-83CH10093, and by NASA Lewis Research Center under Interagency Order No. C-3000-K. The authors also wish to thank B. Keyes, A. Bakry and R. Matson for PL, DLTS and EC measurements and analysis, respectively.

References

1. K.J. Bachmann, H. Schreiber Jr., W.R. Sinclair, P.H. Schmidt, F.A. Thiel, E.G. Spencer, G. Pasture, W.L. Feldman, and K.S. Sree Harsha, *J. Appl. Phys.*, Vol. 50, p. 3441 (1979).
2. M.J. Tsai, A.L. Fahrenbruch, and R.L. Bube, *J. Appl. Phys.*, Vol. 51, p. 2696 (1980).
3. T. A. Gessert, X. Li, M. W. Wanlass, A. J. Nelson and T. J. Coutts, *J. Vac. Sci. Technol. A*, Vol. 8, No. 3, Part 1, p. 1912 (1990).
4. T.A. Gessert, X. Li, M.W. Wanlass and T.J. Coutts, *Proc. 2nd Int. Conf. InP and Rel. Mat.*, Denver, CO, April 1990, (IEEE Cat. No. 90CH2859-7,1990) p. 260.
5. D.C. Joy, D.E. Newbury and D.L. Davidon, *J. Appl. Phys.*, Vol 53, No. 8, p. R81 (1982).
6. T. Sugino, A. Boonyasirikool, J. Shirafuji, and H. Hashimoto, *Electronics Lett.*, Vol. 25, No. 9, p. 590 (1989).
7. C.W. Tu, R.P.H. Chang and A.R. Schlier, *Appl. Phys. Lett.*, Vol. 41, p. 80 (1982).
8. M. Yamaguchi and K. Ando, *J. Appl. Phys.*, Vol. 63, No. 11, p. 5555 (1988).
9. E. Luis and L.A. Verges, *Phys. Rev.*, Vol. B24, p. 6020 (1981).
10. J. Van Vechten, *J. Electrochem. Soc.*, Vol. 122, p. 423 (1975).
11. H.P. Gislason and G.D. Watkins, *Phys. Rev.*, Vol. B33, p. 2957 (1986).
12. T.A. Gessert, X. Li, M.W. Wanlass and T.J. Coutts, *Proc. 21st IEEE Photovoltaics Specialists Conf.*, Orlando, Florida, May 1990 (IEEE, New York, 1990), p.153.

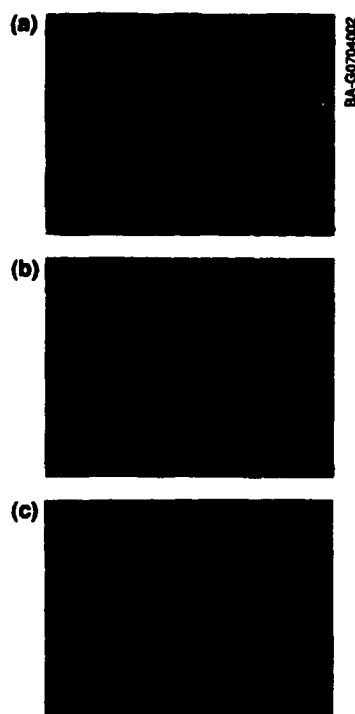


Figure 1

Fig.1. Electron channeling patterns observed as a p^- InP substrate ($1.4 \times 10^{16} \text{ cm}^{-3}$) is exposed to a pure hydrogen plasma. (a) Untreated InP surface. (b) Treated at 20 Watts, 30 min. (c) Treated at 90 Watts 30 min.

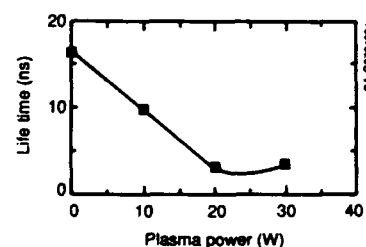


Figure 2

Fig.2. Effect of increasing plasma power on the minority carrier life time in the emitter of a PE cell (30 min PE treatment).

Advances in Controlling Electrical Contacts for Optoelectronics

L.J. Brillson

Xerox Webster Research Center

800 Phillips Rd. 114-41D, Webster, NY 14580

Abstract

Recent advances in fabricating and characterizing metal / III-V compound semiconductor contacts have led to a variety of new techniques for controlling contact electrical properties and a more refined perspective of the atomic - scale mechanisms involved.

Summary

Rectifying or ohmic contacts with stable electrical and chemical properties and low boundary recombination are key requirements for optoelectronic devices. Such devices typically involve III-V compound semiconductors, the control of whose electronic properties presents a formidable challenge. Over the past few years, researchers have developed several new techniques for controlling contact electronic properties which may significantly improve device performance and enlarge our perspective of the fundamental mechanisms involved. Categories of research embodying these developments are: shallow ohmic contacts via low temperature metallurgy, epitaxial metal-alloy contacts via high temperature molecular beam epitaxy (MBE) growth, surface passivation by wet-chemical techniques, interface passivation by atomic-scale interlayers, and semiconductor crystal modification via growth and processing techniques. Here we summarize major developments within each category, with particular emphasis on atomic-scale chemical approaches to controlling macroscopic electrical properties.

Traditional methods of contact formation to III-V compound and other semiconductors involve single or multilayer contacts with appropriate processing

aimed at forming tunnel diodes, localized state-assisted contacts, or graded composition, reduced barrier junctions.¹ Several new approaches have afforded very low resistance contacts while minimizing the penetration of the contact chemistry into the semiconductor bulk. Such techniques include solid - phase epitaxy yielding non-alloyed and low resistance contacts to GaAs², as well as refractory metal compound layers to form thermally stable, ohmic contacts by virtue of the lack of interface reaction.³ Indeed the use of refractory metal alloys with good lattice match to the semiconductor affords low chemical activity at elevated temperatures, in addition to an ordered template on which additional epitaxial growth may occur.⁴ An alternative approach to controlling interface chemistry involves atomic interlayers of reactive metal, which modifies the stoichiometry of semiconductor outdiffusion via "chemical trapping".⁵ Furthermore, such processes alter the barrier heights⁶ and the densities of deep levels otherwise created by the metal-semiconductor interaction.⁷ Wet chemical techniques have also demonstrated dramatic effects in passivating interface states against both Fermi level "pinning" and high surface recombination velocities - either by removing surface chemical constituents⁸ or by forming thin, stable overlayers with the otherwise electrically-active species.⁹ Researchers have also achieved improved control of GaAs Schottky barrier heights by employing As capping and thermal cleaning of GaAs (100) surfaces

Such treatments yield ranges of barriers which increase with decreased chemical interactions, according to several electronic and electrical techniques.¹⁰ By virtue of their wider electrical response, such interfaces permit identification of additional contributions to interface state formation, e.g., chemically-active step sites at misoriented growth surfaces.¹¹ Indeed, control of such misorientation can yield dramatic changes in Schottky barrier height.^{11,12} Similar atomic-scale bonding features are now seen to be a major factor in controlling heterojunction band offsets as well. Hence, progress in controlling electrical contacts for optoelectronic

materials has been made in several arenas, enabled by a more refined understanding and control of interface atomic bonding.

References

1. C. J. Palmström and D.V. Morgan, in Gallium Arsenide, Edited by M.J. Howes and D.V. Morgan (John Wiley & Sons Ltd, New York, 1985) Ch. 6.
2. E.D. Marshall, B. Zhang, L.C. Wang, P.F. Jiao, W.X. Chen, T. Sawada, S.S. Lau, K.L. Kavanaugh, and T.F. Kuech, *J. Appl. Phys.* **62**, 942 (1987).
3. M. Murakami, H.J. Kim, Y.-C. Shih, W.H. Price, and C.C. Parks, *Appl. Surface Sci.* **41/42**, 195 (1989).
4. T. Sands, *Materials Science and Engineering*, **B1**, 289 (1989).
5. L.J. Brillson, G. Margaritondo, and N.G. Stoffel, *Phys. Rev. Lett.* **44**, 667 (1980).
6. L.J. Brillson, C.F. Brucker, A.D. Katnani, N.G. Stoffel, and G. Margaritondo, *Appl. Phys. Lett.* **38**, 784 (1981).
7. J.L. Shaw, R.E. Viturro, L.J. Brillson, and D. LaGraffe, *Appl. Phys. Lett.* **53**, 1723 (1988).
8. S.D. Offsey, J.M. Woodall, A.C. Warren, P.D. Kirchner, T.I. Chappell, and G.D. Pettit, *Appl. Phys. Lett.* **48**, 475 (1986).
9. E. Yablonovitch and T.J. Gmitter, *Proc. Electrochem. Soc.* **88-20**, 207 (1988).
10. R. E. Viturro, J. L. Shaw, C. Mailhot, L. J. Brillson, N. Tache, J. McKinley, G. Margaritondo, J. M. Woodall, P. D. Kirchner, G. D. Pettit, and S. L. Wright, *Appl. Phys. Lett.* **52**, 2052 (1988).
11. S. Chang, L. J. Brillson, Y. J. Kime, D. S. Rioux, D. Pettit, and J. M. Woodall, *Phys. Rev. Lett.* **64**, 2551 (1990).
12. C.J. Palmström, T.L. Cheeks, H.L. Gilchrist, J.G. Zhu, C.B. Carter, and R.E. Nahory, *Mat. Res. Soc. Extended Abstract (EA-21)*, 63 (1990).

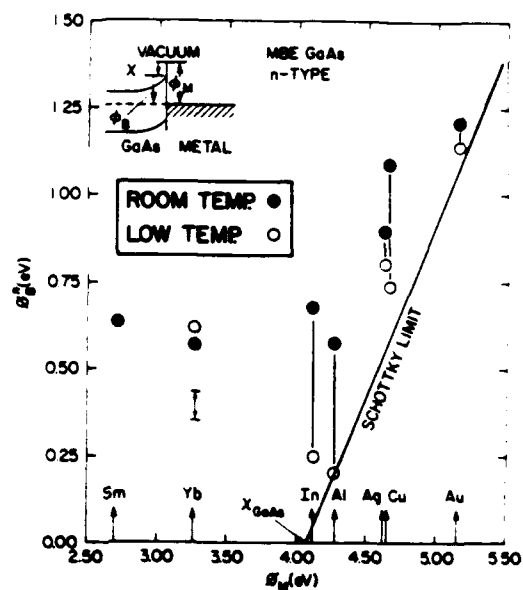


Fig.1. Barrier heights vs. metal work function for As-decapped, MBE-grown GaAs (100) at 100K and room temperature.¹⁰

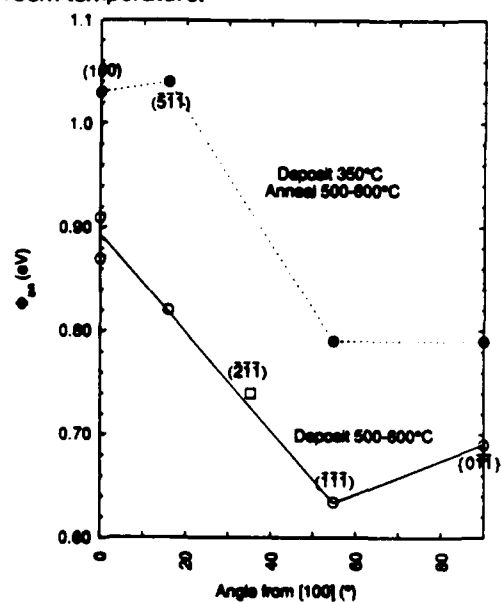


Fig. 2. Schottky barrier height of $\text{Sc}_{1-x}\text{Er}_x\text{As} / \text{GaAs}$ vs. crystal orientation.¹² With permission.

Indium Ohmic Contacts to n-ZnSe

Y.X. Wang* and Paul H. Holloway
Dept. of Materials Science & Engineering
University of Florida
Gainesville, FL 32611

ABSTRACT

The reaction between an indium overlayer and high purity MBE grown n-ZnSe chlorine doped ($2 \times 10^{18} \text{ cm}^{-3}$) epilayers has been investigated using X-ray diffraction, Rutherford backscattering spectroscopy, X-ray photoelectron and Auger electron spectroscopy, and by electrical function tests (I-V and C-V). Good ohmic contacts were formed after annealing at 250°C or 300°C for a few minutes in forming gas. Annealing at lower or higher temperatures resulted in higher resistance or rectifying contacts. The data show that no compounds were formed at the interface; instead In appeared to diffuse into the ZnSe. High surface doping densities appear to allow an ohmic contact, but the electrical data suggest that compensation effects are also very significant in formation of the contact. These effects must be considered for successful formation of the ohmic contact.

*--Visiting Scientist from the Institute of Semiconductors, Academia Sinica, Beijing, China.

Introduction

Metal/semiconductor contacts have often been studied since they are critical for the successful fabrication of electronic and optoelectronic devices. Formation of low resistance ohmic contacts is very important for successful operation of devices since this allows lower working voltages and minimizes dissipation of power with resulting increased efficiency and lower operating temperatures. General requirements to achieve good ohmic contacts were established in the 1970's by Sze, et al^{1,2}, and the general principles have been applied to both elemental and compound semiconductors. A good ohmic contact were formed when the interfacial current transport is dominated by a large tunneling component² and this is achieved when any interfacial barrier is minimized in height and width. This has been achieved regularly on elemental semiconductors, however the case for compound semiconductors has been more difficult because of Fermi level pinning in the mid-gap region leading to high interfacial barrier heights³. The technology of ohmic contacts to ZnSe is particularly lacking because, to date, production of p-n junctions has not been possible, therefore the need for the contact has not controlled the rate of development of devices. This is no longer true with our demonstration of MBE-grown p-type layers and the fabrication of a blue LED from ZnSe⁴. Thus it is now necessary to develop the technology for production of ohmic contacts to ZnSe, and this is the subject of the present research.

With respect to ohmic contacts in the ZnSe system, the extent

of knowledge is very small. A common material for contacts is indium (In), which has been used for n-ZnSe since 1961^{5,6}. Annealing is required to form an ohmic contact with In, but the optimum reported temperature for this procedure varies from 220°C to 400°C. In addition, the data are all for formation of contacts to bulk material and are often contradictory⁷⁻⁹. It is clear, however, that In will form ohmic contacts of reasonably low resistance to n-type ZnSe. The mechanism(s) by which In induces an ohmic contact is unclear; near-surface doping has been suggested by Friberg, et al⁹, while interfacial compound formation has been postulated by Kaufman and Dowber⁷. A number of authors⁷⁻⁹ have reported that annealing temperatures above 400°C induce Zn vacancies which destroy the desirable contact properties. Additional data also suggests that the interfacial native oxide layer significantly affects the formation of ohmic contacts. Ohmic contacts were formed at the lowest annealing temperatures when the In was deposited on freshly cleaved ZnSe surfaces⁷. Thicker interfacial oxide left by other interfacial treatments lead to the requirement of higher annealing temperatures¹⁰. Tyagi⁸ suggests that use of Ga-In alloys for contact formation will allow reduction of interfacial ZnO by Ga and therefore will promote ohmic formation. However there are currently no data relating to compound rearrangement at the contact interface, except those reported by Brillson, et al.³

Experimental

Epitaxial layers of n-ZnSe were grown by MBE heteroepitaxed to a GaAs substrate and protected by a 1 μ m buffer layer, then doped to 2×10^{18} cm⁻³ with a ZnCl₂ source. The mobility of electron carriers at this doping concentration were shown to be in excess of 200 cm²/V-sec. After cleaning the surface with a bromine/NaOH two step etch, the samples were quickly inserted into a high vacuum chamber and approximately 100nm of In deposited by physical vapor deposition. The samples were then characterized using scanning Auger electron spectroscopy (SAM), Rutherford backscattering spectroscopy (RBS), scanning electron microscopy (SEM), X-ray diffraction (XRD), and I-V measurements. The samples were characterized both before and after heat treatment at temperatures between 200°C and 500°C for times up to 1 hour in forming gas.

Results

Good ohmic contacts were formed after heating the 100 nm thick films to 250°C in forming gas (see Fig.1). However, the data in Fig. 1 show that if the In is heated to temperatures as high as 350 to 400°C, the resistance of the contact increases and in fact it will become rectifying again. We believe that this strong dependence upon temperature indicates the formation of compensating point defects for heating the uncapped samples in a forming gas environment at $T > 350^\circ\text{C}$. In separate experiments, we found by photoluminescence evidence for point defect generation in ZnSe after such heat treatments. We also determined that defect formation could be suppressed by heat treating under the appropriate Zn overpressure.¹¹ Data from SAM is shown in Fig. 2 and it is clear that no compound has formed at the interface. This

conclusion is consistent with the lack of new compounds being detected using either XRD or RBS techniques. As a result we postulate that the mechanism of formation of the ohmic contact is diffusion of dopant concentrations of In into the ZnSe layer in order to increase the surface carrier density. This carrier increase will cause a change in the charge transport limit from thermionic emission to tunneling through a shorter depletion distance. The SAM, RBS and C-V data are consistent with this postulate, and we are currently using secondary ion mass spectrometry (SIMS) to verify that this is the true explanation. We are also using different contact areas to attempt to determine for the first time the specific contact resistance for In on n-ZnSe. Our current data suggest a value of approximately $0.05 \Omega\text{-cm}^2$. Finally, it must be pointed out that In makes a good ohmic contact whereas Al and rare earth materials do not to n-ZnSe, probably due to minimization of compensation effects for In but not for the other metals.¹²

Summary

Indium thin films (100 nm thick) have been shown to form ohmic contacts to MBE grown epitaxial layers doped n-type by chlorine ($2 \times 10^{18} \text{ cm}^{-2}$). Heat treatments to temperatures in excess of 200°C in forming gas were necessary to convert them from rectifying to ohmic, but heat treatments in excess of 350°C resulted in higher resistance contacts and/or rectifying rather than ohmic contacts. Preliminary estimates of the specific contact resistance is $0.05 \Omega\text{-cm}^2$. The mechanism of ohmic contact formation appears to be near surface doping by In to reduce the depletion distance and allow tunneling transport of charge carriers without inducing compensation.

References

1. C. Y. Fang, Y. K. Fang and S. M. Sze, *Sol. State Electron.*, **14**, 541 (1971).
2. S. M. Sze, *Physics of Semiconductor Devices* (J. Wiley and Sons, NY, 1983) p. 304.
3. L. J. Brillson, *Surf. Sci. Reports*, **2**, 123 (1982).
4. R. M. Park, M. J. Troffer, C. M. Rouleau, J. M. DePuydt and M. A. Haase, *Appl. Phys. Lett.* **57**, 2127 (1990).
5. M. Aven, D. T. F. Marple and B. Segall, *J. Appl. Phys. Suppl.*, **32**, 2261 (1961).
6. Y. S. Park and B. K. Shin, *Topics Applied Phys.* **17**, 133 (1977).
7. R. G. Kaufman and P. Dowbor, *J. Appl. Phys.*, **45**, 4487 (1974).
8. M. S. Tyagi, *J. Inst. Electron. Telecomm. (India)*, **25**, 491 (1979).
9. A. Friberg, I. Holwech and B. Nost, *Appl. Phys.*, **A26**, 239 (1981).
10. M. E. Ozsan and J. Woods, *Sol. State Electron.*, **18**, 519 (1975).
11. K. Jones, Private Communications, Gainesville, FL, Dec. 1990.
12. R. K. Swank, M. Aven and J. Z. Devine, *J. Appl. Phys.* **40**, 89 (1969).

Figure 1. In/n-ZnSe (#1068)
 Annealed at specified temperature and time in forming gas.
 ($y = 1 \text{ mA/cm}$; $x = 1 \text{ V/cm}$)



(a) 250°C, 10 min.



(b) 300°C, 10 min.

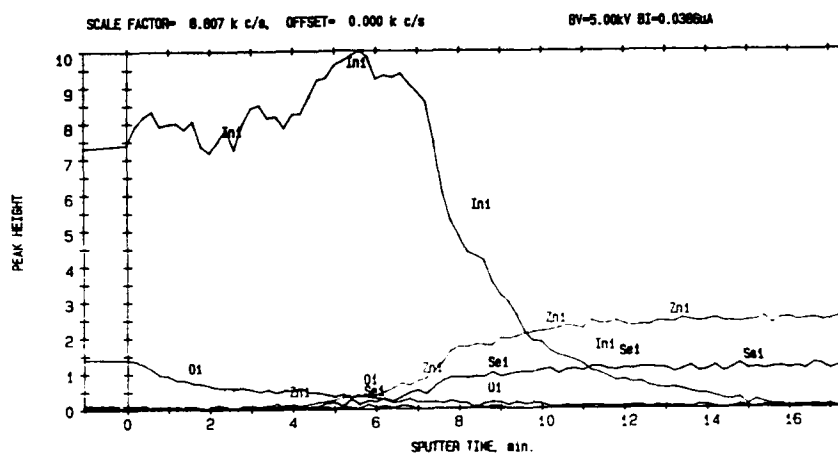


(c) 350°C, 10 min.



(d) 400°C, 10 min.

Figure 2
 Auger Electron Sputter Profile of Indium on ZnSe
 Heated to 250°C for 30 min.



A New Method of Zn Diffusion into InP for Optical Device Fabrication

Morio Wada, Katsutoshi Sakakibara and Yoichi Sekiguchi

Optical Measurement Technology Development Co., Ltd.

11-13 NAKA-CHO 2-CHOME MUSASHINO-SHI TOKYO, 180 JAPAN

1. Introduction

Zn diffusion into InP or InP-based materials has been the subject of many investigations, most of which have involved the open tube method performed in a less closed boat under a flow of hydrogen or nitrogen, and the sealed ampule technique. A relatively new technique for III-V semiconductors is the use of Zn-doped spin-on film of SiO_2 ¹.

In present work, we have developed a new method of Zn diffusion into InP using the open tube diffusion in a flow of N_2+H_2 mixture gases containing dimethylzinc(DMZ) and PH_3 ², and studied Zn incorporation mechanisms in this method. The conventional MOVPE system is used as the diffusion system so that the temperature and gas flow can be controlled precisely and uniformly. SIMS, C-V and photoluminescence(PL) measurements were carried out to investigate the diffusion profiles and donor-acceptor(D-A) emission bands in the Zn-diffused region. The results strongly support the diffusion model of interstitial Zn donors, compensating substitutional Zn acceptors in bulk InP³. For the diffusion at a high PH_3 flow rate, the enhanced diffusion and the increased PL intensity of a new D-A emission band localized near the surface region were observed. These results suggest that the different Zn incorporation mechanism occurs near the surface region in InP. The fabrication of PIN photodiodes as an application of this diffusion method are also described⁴.

2. Experimental procedures

The samples used for the diffusion were undoped (100)InP with room-temperature carrier concentrations of $1-5 \times 10^{16} \text{cm}^{-3}$. DMZ(1500ppm in He) with flow rates of 50-200sccm was used as a Zn source and carrier gases were 50% H_2 and 50% N_2 . The total flow rate was 4.6slm. After chemically etching, the substrate was put on a SiC coated graphite susceptor heated by RF-induction in a cold-wall horizontal reactor. Zn diffusion was carried out at 76Torr with a temperature range from 500 to 570°C. During the heating up stage, PH_3 (20 or 40% in H_2) with a flow rate of 200sccm was turned on below 150°C to protect the sample surface and switched off at 200°C during the cooling off stage. The DMZ was switched into the reactor and PH_3 flow rate was changed when the diffusion temperature was reached. After the diffusion time, the DMZ and RF-induction were turned off simultaneously. PH_3 overpressure was maintained throughout the diffusion process.

3. Results and Discussion

Figure 1 shows diffusion profiles of (a)Zn and (b)hole concentrations at 500°C, a DMZ flow rate of 200sccm and a PH_3 flow rate of 200sccm for diffusion time varying 0.05-2h. Figure 2 shows plots of diffusion depth, evaluated at a fixed carrier concentration of $1 \times 10^{17} \text{cm}^{-3}$ vs the square-root of diffusion time. The dotted lines were calculated by solving the diffusion equation for

singly ionized interstitials.

The diffusion profiles become deeper and the concentrations increase with increasing the DMZ flow rate as shown in Figs.3 and 4(a). Both the surface Zn concentration and substitutional concentration are proportional to the DMZ flow rate while the interstitial concentration rapidly decreases as the DMZ flow rate decreases. Solid line shows the calculated interstitial concentration which was fitted to the experimental data.

As the PH_3 flow rate increased, the diffusion profiles increased and the intensity of a new deep donor-related donor-acceptor emission, which we refer to as BEB in the text, rapidly increased as shown in Figs.5, 6 and 7. BEB is observed only in the thin surface region of the Zn-diffused InP, and after this peak disappears, an another broad emission band(AEB) at 1.332eV is observed through the Zn-diffused region where the hole concentration is measured constantly higher than 10^{18}cm^{-3} . From the measured temperature and excitation intensity dependence of the PL peak energy, AEB can be identified with the low energy emission band(LEB) found in a Zn-doped InP substrate⁵ and MOVPE Zn-doped InP layers. In this diffusion method, in order to explain the enhanced Zn diffusion and the increased PL intensity of BEB for Zn diffusion at a high PH_3 flow rate, the incorporation mechanism near the surface region where most of substitutional Zn acceptors are compensated, must be more fully understood and different from that in bulk InP.

We have demonstrated GaInAs PIN photodiodes fabricated by selective Zn diffusion of this diffusion method and LP-MOVPE. The external quantum efficiency was 60-80% in the 0.95-1.55 μm wavelength range. A reverse leakage current of 30pA at -2V base was measured and a -3dB cutoff frequency of 1.4GHz was obtained for 110- μm -diam diodes.

4.Conclusion

A new method of Zn diffusion into InP using dimethylzinc as a Zn source has been developed to fabricate optical devices. This method provides precise control over both diffusion depth and Zn concentration. The interstitial-substitutional model can also explain Zn diffusion into bulk InP. However, for Zn diffusion at a high PH_3 flow rate, the enhanced diffusion and a new deep donor-related donor-acceptor emission band were observed, suggesting that the different Zn incorporation mechanism takes place near the surface region. The measured characteristics of the PIN photodiodes fabricated by this diffusion method provide evidence that this new method is suitable for optical device fabrication.

References

1. U. Konif, H. Haspeklo, P. Marschall and M. Kuissl: J. Appl. Phys. 65(1989) 548.
2. M. Wada, M. Seko, K. Sakakibara and Y. Sekiguchi: Jpn. J. Appl. Phys. 28 (1989)L1700.
3. G. J. van Grup, T. van Dongen, G. M. Fontijn, J. M. Jacobs and D. L. A. Tjaden: J. Appl. Phys. 65(1989)553.
4. M. Wada, M. Seko, K. Sakakibara and Y. Sekiguchi: Jpn. J. Appl. Phys. 29 (1990)L401.
5. V. Swaminathan, V. M. Donnelly and J. Long: J. Appl. Phys. 58(1985)4565.

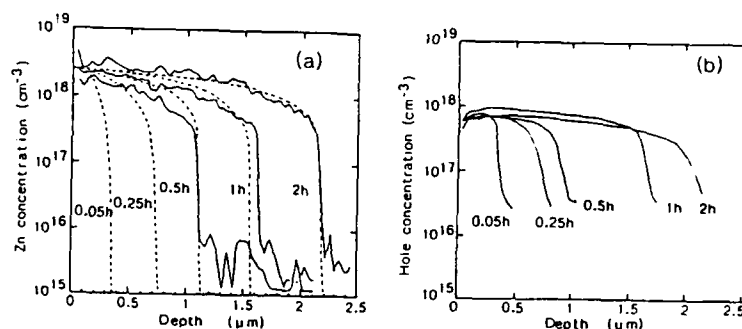


Fig.1 Diffusion profiles at 500°C and a DMZ flow rate of 200sccm for 0.05, 0.25, 0.5, 1 and 2h. (a) Zn concentrations were obtained by SIMS analysis. The dotted lines denote the calculated profiles using the interstitial-substitutional model, assuming that all of the interstitial Zn is singly ionized. The calculations were fitted at the surface. (b) Hole concentrations were obtained by C-V measurement.

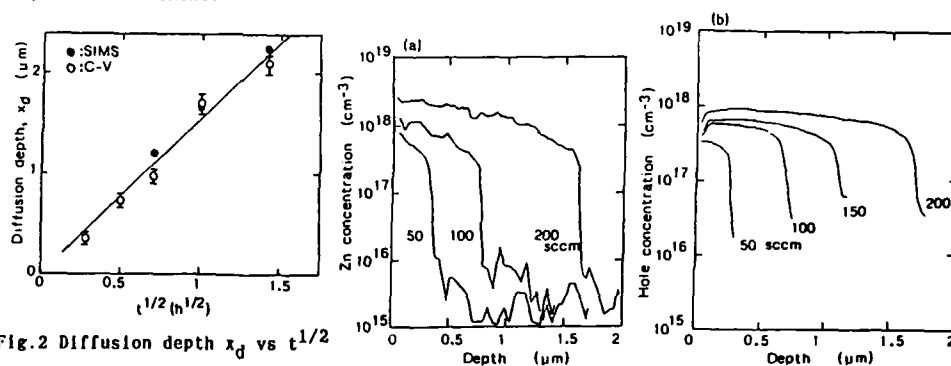


Fig.2 Diffusion depth x_d vs $t^{1/2}$

Fig.3 Diffusion profiles for 1h at 500°C and DMZ flow rates of 50, 100, 150 and 200sccm. (a) Zn concentrations were obtained by SIMS analysis and (b) hole concentrations were obtained by C-V measurement.

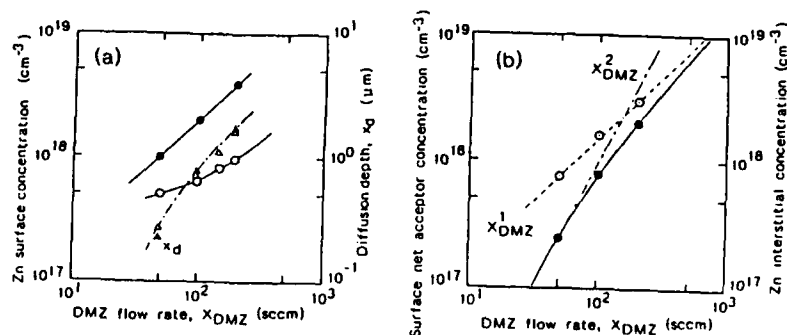


Fig.4 (a) Hole (○) and Zn (●) surface concentrations and diffusion depths (Δ, ▲) as a function of the DMZ flow rate for the 500°C diffusions. (b) Surface net acceptor concentrations (○), and Zn interstitial concentrations (●) as a function of the DMZ flow rate. Surface net acceptor concentration is proportional to the DMZ flow rate (the Zn pressure). Solid line shows the Zn interstitial concentration calculated with the model of interstitial Zn compensating substitutional Zn. In this model a C-V measurement yield the difference of the concentrations ($C_0 - C_1$) and the Zn concentration is equal to their sum ($C_0 + C_1$).

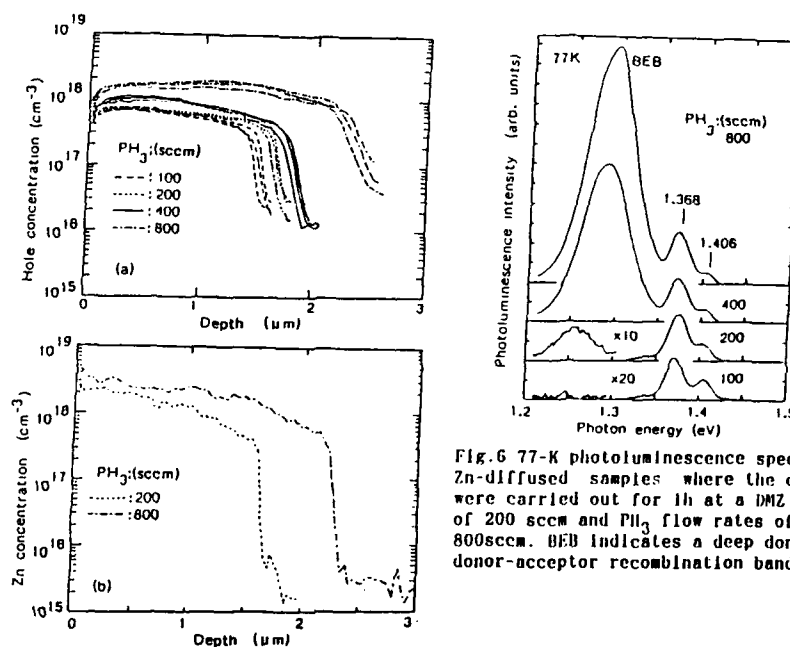


Fig.5 Diffusion profiles for 1h at 500°C. a DMZ flow rate of 200sccm and PH₃ flow rates of 100-800sccm. (a) Hole concentrations were obtained at three locations spanning the 10-mm length along the gas flow direction by C-V measurement. (b) Zn concentrations were obtained by SIMS analysis.

Fig.6 77-K photoluminescence spectra from Zn-diffused samples where the diffusions were carried out for 1h at a DMZ flow rate of 200 sccm and PH₃ flow rates of 100-800sccm. BEB indicates a deep donor-related donor-acceptor recombination band.

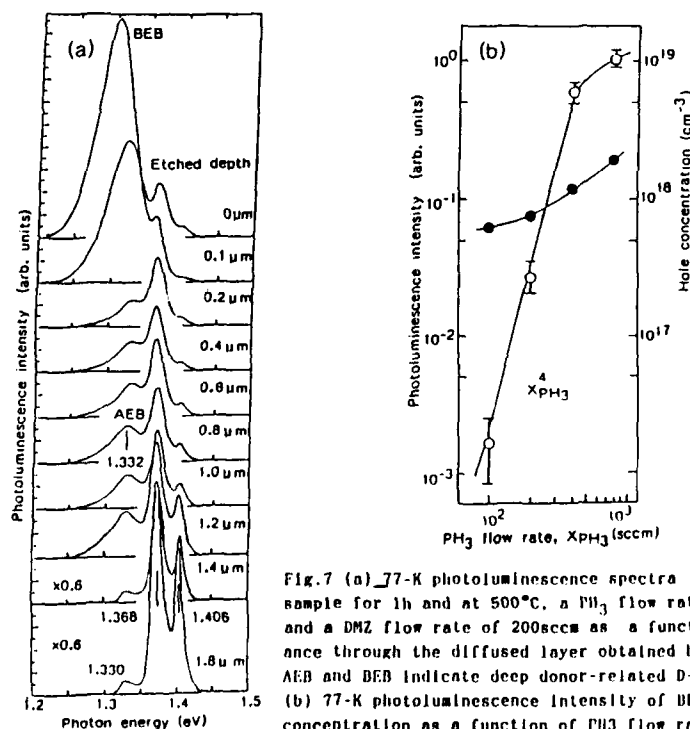


Fig.7 (a) 77-K photoluminescence spectra of a diffused sample for 1h and at 500°C, a PH₃ flow rate of 800sccm and a DMZ flow rate of 200sccm as a function of the distance through the diffused layer obtained by sequential etching. AEB and BEB indicate deep donor-related D-A emission bands. (b) 77-K photoluminescence intensity of BEB and surface hole concentration as a function of PH₃ flow rate.

OPEN TUBE DOUBLE DIFFUSION FOR THE FABRICATION OF BIPOLAR TRANSISTOR WAVEGUIDE OPTICAL SWITCH

D. K. GAUTAM, Y. NAKANO, and K. TADA
Department of Electronic Engineering, University of Tokyo
7-3-1 Hongo, Bunkyo-Ku, Tokyo, 113, Japan

Abstract

Experimental results of a new method for the double diffusion into GaAs in an open tube have been presented. New techniques developed for the low concentration Zn diffusion at relatively higher values of the temperature and high concentration Sn diffusion in an open tube system can be convenient for the fabrication of bipolar transistor waveguide optical switches and other self-aligned bipolar devices needed for photonic integrated circuits.

1 Introduction

Recently, the high speed optical switches have received the significant interest because of their high demands in the systems of optical communication, photonic switching, optical information processing and optical computing. The need for encoding and transmitting large amounts of data or processing light with low switching energy has lead to a search for compact optoelectronic devices which could be used for the monolithic integration. The heterostructure bipolar transistor (HBT) structures have shown their excellent performance [1] for high speed logic applications. The application of the HBTs is not only limited for the high speed electronic circuit operation, but they have also been used as the highly efficient multifunctional optical devices such as the photo transistors [2] and laser transistors [3]. Double heterostructure bipolar transistors (DHBTs) using heterostructure collectors are also of interest both for electronic and optoelectronic applications. Tada and Okada have proposed a waveguide optical switch in a DHBT [4]. This device is expected to improve

the switching speed by several times and will be a promising component for photonic integrated circuit. The optical modulator in a DHBT has also been reported [5].

Low temperature Zn diffusion is frequently used as an acceptor impurity in GaAs. As examples p-n junctions are formed using Zn diffused layers in solar cells, lasers and varactor diodes. But for the fabrication of devices like bipolar transistors where the second time diffusion concentration profile must be higher than the previous diffusion profile, the low temperature Zn diffusion is not applicable as the high concentration n-type profile is very difficult to obtain even at very high temperature values in GaAs. In this work, we report for the first time the experimental results of the open tube double diffusion techniques at the high values of the temperature to fabricate a waveguide optical switch in a bipolar transistor structure.

2 Experimental Method

Semi-insulating (S.I.) GaAs substrates oriented in the (100) direction were used for the

diffusion experiments. The diffusion for both p type impurity (Zn) and n type impurity (Sn) were carried out in an open tube system at high temperature values in presence of the flowing N_2 atmosphere. To get the low p-type concentration profile at high temperature, 1% Zn doped SiO_2 (commercially available) was used as a diffusion source. A protective layer of SiO_2 (250Å) was deposited on the surface of the substrate first by plasma-assisted chemical vapor deposition (PCVD) technique. A second layer of 1% Zn doped SiO_2 (2000Å) was then spin coated and baked at 250°C for 30 min. A third cap layer of SiO_2 (2000Å) was again deposited by PCVD. The wafers completely covered with SiO_2 were loaded into a single zone furnace. Intensive care was taken in increasing the substrate temperature at a very slow rate while loading the wafer into the furnace. Otherwise; the SiO_2 layers would be so hard that it will be difficult to remove them with the buffer HF. The diffusion was carried out for a period of 45 minutes and then the wafers were taken out and cooled down rapidly by the flowing N_2 . The SiO_2 layers were etched by buffer HF. The surface of the substrate was found to be as shiny as it was before and no surface degradation was observed.

To convert the p^+ type region into n^{++} type region, tin diffusion was carried out at the same or lower values of the temperature with the following techniques using elemental Sn as a diffusion source. A SiO_2 (250Å) layer was deposited on the surface of the substrates by PCVD. A second layer of tin (500Å) was then deposited by evaporation. A third cap layer of SiO_2 (5000 Å) was again deposited by PCVD. The special care was taken in growing the SiO_2 cap layer by PCVD so that the deposited Sn layer could not be evaporated into the vacuum when the substrate temperature is increased higher than the melting point of Sn. Wafers were, then, loaded into the furnace at 1000°C or 950°C in a flowing N_2 atmosphere under the same precautions described above. After 20 minutes diffusion period, the samples were taken out and cooled down rapidly by the flowing N_2 gas. The SiO_2

layers were then etched by buffer HF which causes the simultaneous removal of the sandwiched Sn layer also. The concentration profile of the electrically activated substrates by diffusion were analyzed by an electrochemical profiler.

3 Results and Discussion

Zinc diffusion was carried out on several samples using 1% Zn doped SiO_2 as a diffusion source. It was observed that the source layer coated directly on the surface of the substrate during diffusion process causes many number of surface stress defects. Hence a protective SiO_2 layer (250 Å) was first deposited on the surface before coating the diffusion source oxide. The carrier concentration profile of a sample with Zn diffused at 1000°C is shown in Fig.1. The concentration profile exhibits a steep front and a concave region near the surface which is necessary for the reproducible diffusion and to make a good quality of p-n junction. The surface concentration and the diffusion coefficient were measured to be $6 \times 10^{18} \text{cm}^{-3}$ and $3.67 \times 10^{-13} \text{cm}^2 \text{s}^{-1}$.

High concentration n type impurity diffusion was carried out on the Zn diffused and S.I. substrates using elemental Sn as a diffusion source. Fig.2. shows the concentration profile of a S.I. substrate with Sn diffused at 1000°C. The surface concentration on various samples under the same conditions was measured to be $9 \times 10^{19} \text{cm}^{-3}$ and the diffusion coefficient was found to be $9.18 \times 10^{-14} \text{cm}^2 \text{s}^{-1}$.

Figures 3 and 4 show the concentration profile of the double diffused samples. Tin diffusion temperature for these samples were taken 1000°C and 950°C respectively while keeping the Zn diffusion temperature constant (1000°C). In the first case, Fig.3, the junction depth was measured to be 0.4 μm with the sharp fall of the p type concentration after the junction. At 950°C, Fig.4., the junction depth was measured to be at 0.23 μm . In this case the concentration of electrons was measured to

be $3 \times 10^{18} \text{cm}^{-3}$. Due to the shallow diffusion and the low surface concentration of the n type impurity at the reduced Sn diffusion temperature, the carrier profile showed a shape different from that in Fig.3. Near the junction the profiler does not measure the exact number of carriers and gives a shape of hill peak. But the measurements carried at different positions on the same sample show the junction to be quite uniform.

4 Conclusion

In this work, we have presented, for the first time, the experimental results of the double diffusion into GaAs to fabricate the bipolar transistor optical switch. Our new techniques can be useful to fabricate several number of self-aligned devices required for photonic integrated circuits.

Acknowledgment

The technical support of Mr. K. Sato is greatly acknowledged by the authors.

References

- [1] T.Nitto, K.Nayata, O.Nakajima and T.Ishibashi, IEEE Electron Device Lett. 10, 506 (1989).
- [2] T.Ohnishi, K.Mukaiyama, M.Yamanishi, N.Ochi, Y.Ono, Y.Kan, H.Ishikawa and I.Suemune, IEEE Photonics Technology Lett. 2, 546 (1990).
- [3] Y.Mori, J.Shibata, Y.Sasai, H.Serizawa, and T.Kajiware, Appl. Phys. Lett. 47, 649 (1985).
- [4] K.Tada and Y.Okada, IEEE Electron Device Lett. EDL-7, 605 (1986).
- [5] Y.Okada, T.Ishikawa and K.Tada, Appl. Phys. Lett. 55, 2591 (1989).

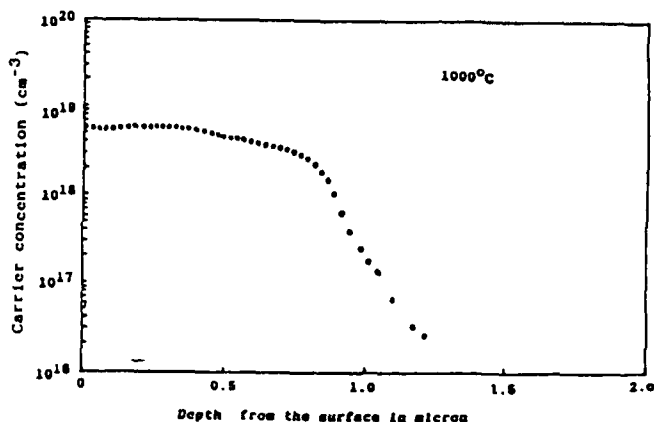


Fig.(1)- Concentration profile of a Zn diffused GaAs S.I. substrate (as measured with the electrochemical profiler)

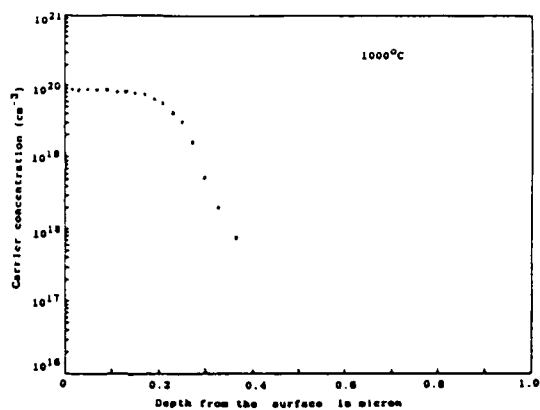


Fig. (12)- Concentration profile of a tin diffused GaAs S.I. Substrate (as measured with the electrochemical profiler)

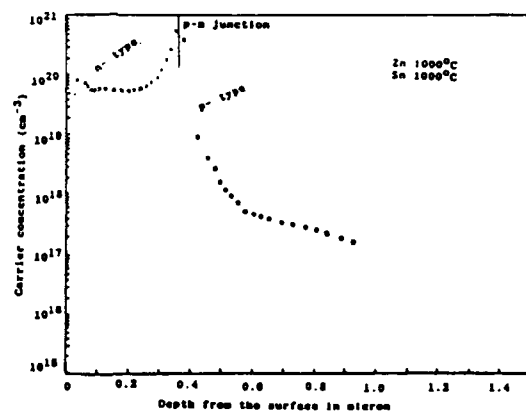


Fig. (13)- Concentration profile of a double diffused GaAs S.I. substrate (as measured with the electrochemical profiler)

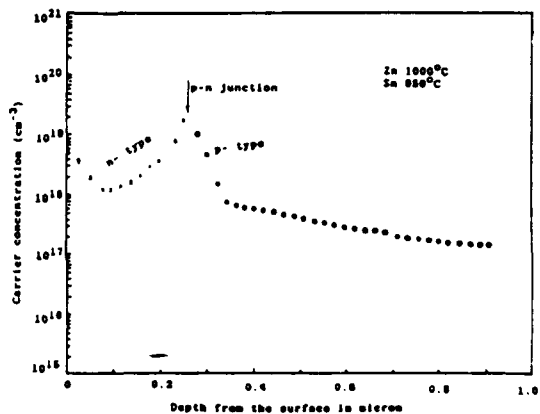


Fig. (14)- Concentration profile of a double diffused GaAs S.I. substrate (as measured with the electrochemical profiler)

Full-Wafer Technology for Laser Fabrication and Testing

D.J. Webb, M.K. Benedict, G.L. Bona, P. Buchmann, N. Cahoon, K. Dätwyler,
H.P. Dietrich, A. Moser, G. Sasso, H.K. Seitz, P. Vettiger, O. Vogeli, P. Wolf

IBM Research Division, Zurich Research Laboratory, Säumerstrasse 4,
8803 Rüschlikon, Switzerland

Summary

Full-wafer fabrication of AlGaAs lasers, which have mirrors etched by chemically assisted ion-beam etching and passivated by ion-beam sputtered Al_2O_3 , is described. Full-wafer testing techniques for both laser parameters ($P-I$, far-field, spectrum, T_0), as well as other test sites for process development and control (critical dimensions, overlay, etch depths, sheet resistances) have been developed. The lasers have excellent beam quality, with an rms phase-front distortion ($\delta\lambda/\lambda$) of less than 0.04. Operation in a single transverse mode at output powers up to about 50 mW and catastrophic optical damage thresholds of about 120 mW have been demonstrated. Full-wafer testing of 1400 lasers with a yield of functioning lasers of over 90%, and with good uniformity of $P-I$ characteristics over a wafer will be shown. These fabrication and testing techniques are being developed with the aim both of improving the fabrication of discrete lasers, and of laying the basis for future developments towards optoelectronic integration.

Full-wafer laser fabrication

Full-wafer laser fabrication technology using etched mirrors can be applied to almost any laser structure. The structure we have used is an MBE-grown single quantum-well GRINSCHE structure, in which lateral optical and current confinement is provided by etched ridges which are typically $3.2\text{ }\mu\text{m}$ wide. For a single lateral mode, the upper cladding layer is etched to within 400 nm of the graded-index region. The lasers are typically $720\text{ }\mu\text{m}$ long.

Mirror Etching—The requirements for the etching process are severe. The etched mirror surfaces should be smooth, and have the correct shape; crystal damage and chemical contamination must also be minimized. For maximum smoothness, the etch mask must be erosion-resistant and have smooth vertical sidewalls. Photo-resist baked at $200\text{ }^\circ\text{C}$ has been found to be most resistant to edge erosion, and is patterned using a multi-layer resist technique. The mirrors are etched by chemically assisted ion-beam etching (CAIBE). A beam of 500 eV argon ions, generated by a Kaufman ion source, is directed at the substrate, together with a flow of Cl_2 molecules from a ring of small jets. The directionality of the ion beam ensures the anisotropic etching needed to produce the vertical sidewalls. The dependence of the etch rate on Ar-ion current density is shown in Fig. 1, which also shows that it can be made independent of the Al concentration in the substrate. This is necessary for smooth sidewalls as the different AlGaAs layers are etched through. The Cl_2 provides a chemical component which increases the etch rate by a factor of over 100 compared to the sputter etching from the ion beam alone. This minimizes surface damage. The physical sputtering component from the 500 eV Ar-ion beam, although small, together with a background pressure of oxygen or moisture below 10^{-8} mbar prevent roughness due to the formation of etch-resistant oxides on the AlGaAs surface. The residual roughness of the mirrors is of the order of 20 nm. It results mainly from the roughness of the chromium mask used for the photoresist exposure, which is done by contact printing. In order to ensure that the mirrors are flat a 'flared' ridge waveguide is employed. The ridge waveguides are up to $1.8\text{ }\mu\text{m}$ high. The photoresist for the mirror etch-mask is not uniform over this large step and this results in a waviness of the edge of the mask and hence of the etched mirror surface. The last $2\text{ }\mu\text{m}$ of the ridge waveguide is therefore flared out to a width of $24\text{ }\mu\text{m}$, thus displacing the perturbed regions well away from the part of the mirror through which the beam emerges. The structure is shown in the SEM image in Fig. 2.

Lasers with uncoated etched mirrors have been compared directly with lasers with uncoated cleaved mirrors from the same wafer. The output power vs. drive current ($P-I$) curves are practically identical up to output powers of 40 mW. The reflectivity (R) and scattering losses (S) of the mirrors have been measured by comparing the differential quantum efficiencies. The etched mirrors of straight waveguides (without flare) have low R (about 0.1) and high S values (about 0.25). The mirrors of flared waveguides have almost the same reflectivity (0.3) as cleaved mirrors. The scatter loss (S), which includes the insertion

loss of the flared section as well as the loss from the small residual mirror roughness, is very low (< 0.03). Finally, the phase variation of the laser far-field radiation pattern was measured after chip parting. The output beam was collimated using a 0.62 N.A. lens and the phase-front analyzed using a Mach-Zehnder scanning interferometer having a resolution of $\sim \lambda/100$. The total rms phase-front distortion was between 0.03 and 0.04 for four uncoated and one coated laser, each from a different run. It was independent of power up to 50 mW as is illustrated in Fig. 3. For comparison, values of up to 0.04 are measured for cleaved uncoated mirrors.

Mirror Coating— The etched laser mirrors are coated to passivate them and to modify their reflectivity. Aluminum oxide (Al_2O_3), deposited by ion-beam sputter deposition, is used for passivation. Here, an Ar-ion beam sputters material from a solid target onto the substrate. The advantage of ion beam, as compared to other sputtering techniques, is that the deposition is directional, and thus allows the front and rear mirrors of the lasers to be coated differently as shown in Fig. 4. Sputtering is preferred over e-beam evaporation, which is also a directional technique, since it produces denser, less porous films, which should improve reliability. The plasma is contained in the ion source. Bombardment and possible damage of the substrate by energetic ions is therefore minimized. The Ar-ion beam energy is 1000 eV. Experiments on cleaved mirrors have shown that at much lower energies, the films are more porous, and that at much higher energies the pulsed catastrophic optical damage (COD) power of the lasers starts to drop. When oxides are sputtered, oxygen is bled into the chamber at a rate of 10% of the total gas flow, otherwise the films are metal-rich. Al_2O_3 ($n = 1.66$), SiO_2 ($n = 1.48$), and Si ($n = 3.8$), are sputtered from targets of the respective material. The deposition system was arranged to optimize the uniformity of deposition on the sidewalls of the mirror trenches. For Al_2O_3 , uniformities of thickness and refractive index of 2.7% and 0.3% ($1-\sigma$) respectively over a 40 mm diameter have been obtained. For mirrors with lower reflectivity ($2\% < R < 30\%$), the thickness of the Al_2O_3 passivation is appropriately adjusted. For mirrors with high reflectivity ($R > 30\%$), the Al_2O_3 passivation is the first low-index layer in a quarter-wave high-reflectivity stack. The high index material is amorphous silicon (a-Si). The contact pads are coated along with the mirrors so subsequent low-index layers in this stack are made of SiO_2 , which has a much higher etch rate in the CF_4 -RIE used to etch the necessary contact vias. The output-power vs. drive current for two lasers with passivated ($R \sim 30\%$) etched mirrors are shown in Fig. 5. The $P-I$ curves are linear up to almost 80 mW and the lasers operate in a single lateral mode up to about 50 mW. CW operation is demonstrated at over 100 mW, and the ramped COD power of such lasers ranges from 105 to over 120 mW.

Full-Wafer Testing

A processed 2" wafer is shown in Fig. 6, where typical laser chips (inset) are mixed with other test sites. Full laser testing is done using a specially adapted semiconductor wafer tester. It consists of a stepping probe station, a switch matrix for addressing the device under test, and units both to apply and measure voltages and currents. All these items are controlled from a computer. To this is added a large-area photodiode for the measurement of $P-I$ curves, a diode array for measuring vertical and horizontal far fields, and an optical spectrum analyzer for the measurement of the longitudinal mode spectrum. Laser characteristics are measured as shown schematically in Fig. 7. The front mirror trenches of the lasers are made about 200 μm wide, allowing nearly all the output beam to be picked up both directly and by reflection from the floor of the mirror trench. Horizontal far fields are not affected by the reflection; vertical far fields contain interference fringes from the reflection in the mirror trench but this can be compensated in the data analysis. Fig. 8 shows the measured characteristics of 1457 lasers obtained from on-wafer testing of a full 2 inch diameter wafer, the lasers on which have etched mirrors. These mirrors are coated for a front reflectivity of 10% and a rear reflectivity of $> 90\%$. The average threshold currents are 20.3 mA with a std. dev. of 5.1 mA. Differential front facet efficiencies have a mean of 0.81 W/A with a std. dev. of 0.1 W/A. The distributions are quite narrow and include all sources of variation, from epitaxial growth, through the processing of the lasers, to etching and coating of the mirrors. Full-wafer testing is very advantageous, since the wafer is loaded on the tester only once as a unit, and the testing accomplished in only a few hours with no further handling. Other test sites allow a wide range of process parameters to be obtained, such as the sheet resistances of various layers, critical dimensions and overlay accuracy. These test sites have the form of a Wheatstone bridge whenever possible, so that only the parameter of interest will cause a bridge imbalance. Since they are on the same wafer as the lasers, wafer-to-wafer parameter variations do not affect the interpretation of the results. These data augment and contribute to the interpretation of the laser measurements. Wafer maps of the distributions of various quantities aid the

development and control of the process. Other test sites are available to allow on-wafer measurements of the facet reflectivity ratio as well as the internal laser parameters such as absorption and internal quantum efficiency. Back-facet monitor diodes are also integrated onto the laser chips. They can be used for certain on-wafer measurements, and also packaged together with the lasers as integrated power monitors.

Acknowledgements

The authors gratefully acknowledge the excellent contributions of Theodor Forster, Heinz P. Meier, Albertus Oosenbrug, Louis Perriard, Heinz Richard, and W. Walter. We are also very pleased to thank Volker Graf for his continued encouragement and support.

References

- [1] P. Vettiger, M.K. Benedict, G.L. Bona, P. Buchmann, N. Cahoon, K. Dätwyler, H.P. Dietrich, A. Moser, H.K. Seitz, O. Voegeli, D.J. Webb, P. Wolf, IEEE J. Quantum Electronics, to be published, June 1991.
- [2] D.J. Webb, M. Benedict, G.L. Bona, P. Buchmann, K. Daetwyler, H.P. Dietrich, A. Moser, G. Sasso, P. Vettiger, O. Voegeli, *Proc. SPIE "OE LASE 91,"* Los Angeles, CA, Jan. 20-25, 1991, to be published.

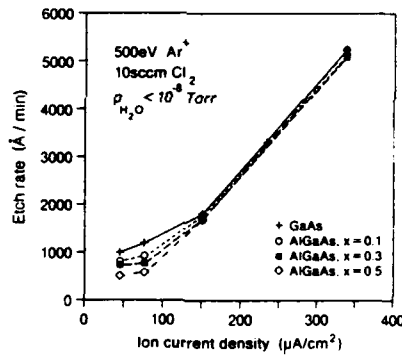


Fig. 1. Etch rate of AlGaAs as a function of ion beam current density and Al concentration. From Ref. 1.

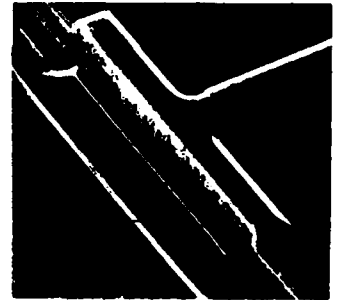


Fig. 2. SEM picture of etched mirror showing the flared end section of the waveguide.

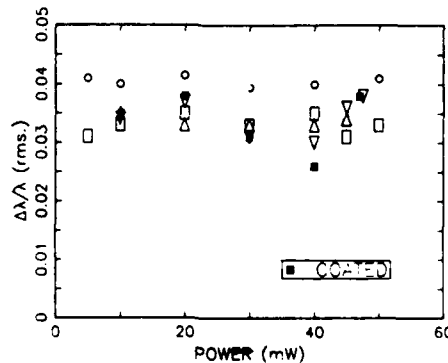


Fig. 3. Phase front distortion for uncoated (open symbols) and coated (filled symbols) etched mirrors (with flared ends) as a function of output power.

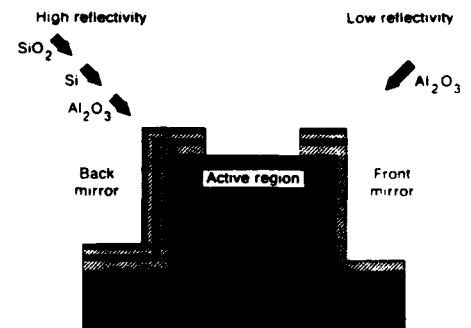


Fig. 4. Film deposition sequence for reflectivity modification of etched mirrors. From Ref. 1.

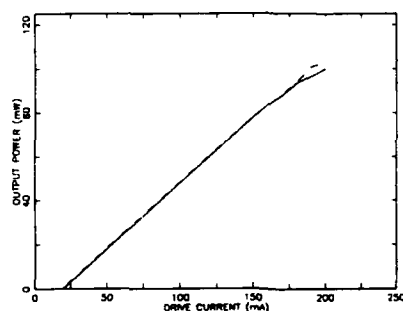


Fig. 5. Light-current ($P-I$) curves for lasers with coated etched mirrors: the mirror reflectivity is 30%. From Ref. 2.

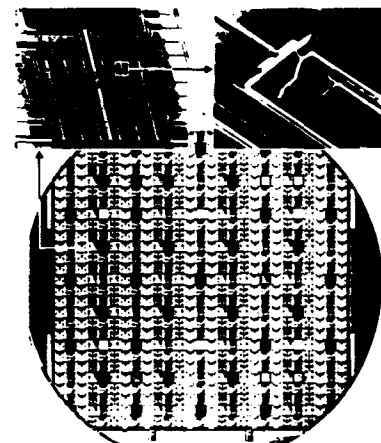


Fig. 6. A completed 2" wafer with lasers chips (inset) and a view of a rear laser mirror showing integrated monitor diode. From Ref. 1.

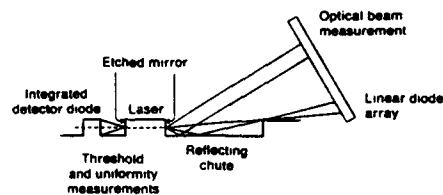


Fig. 7. A schematic view of on-wafer laser measurements. From Ref. 1.

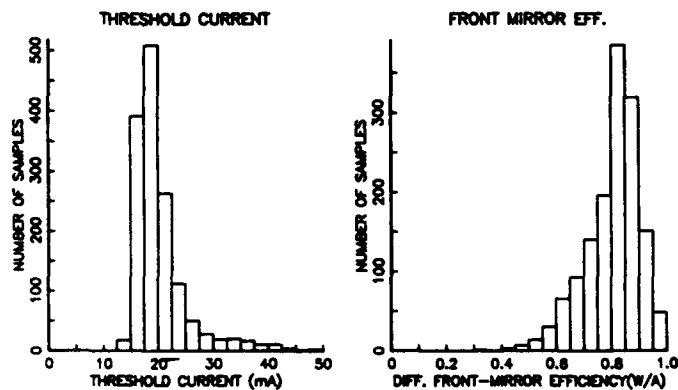


Fig. 8. Histogram of threshold current and differential front-facet efficiency for lasers with front and rear facet reflectivities of 0.1 and 0.9 respectively.

Fabrication Issues and Considerations for High Performance Grating-Surface-Emitting Semiconductor Lasers

G. A. Evans, N. W. Carlson, J. M. Hammer, D. P. Bour,
J. B. Kirk, S. K. Liew, H. Lee, W. Reichert, R. K. DeFreez*,
C. A. Wang** H. K. Choi**, J. N. Walpole**, and J. K. Butler***

David Sarnoff Research Center
CN 5300
Princeton, NJ 08543-5300

*Oregon Graduate Institute of Science and Technology
19600 N.W. von Nueman Drive
Beaverton, OR 97006-1999

**Lincoln Laboratory
244 Wood Street
Lexington, MA 02173-0073

***Southern Methodist University
Dallas, TX 75275

SUMMARY

A sketch of a grating-surface-emitting (GSE) laser is shown in Fig. 1. The gratings between the gain sections provide feedback for laser oscillation in second order and couple out the laser radiation perpendicular to the surface in both directions in first order. With proper choice of grating parameters, a portion of the light is passed completely through each grating section and serves to injection lock additional gain sections in the longitudinal direction. GSE laser array technology has experienced steady progress over the last two years [1]. Improvements in material quality and uniformity have made it possible to coherently couple two dimensional GSE lasers over distances larger than 1 cm. Figure 2a shows a peak output of 32 W per surface with differential quantum efficiencies of 40 % per surface during pulsed operation. The same device provides a continuous power output of 3.4 W per surface, as shown in Fig. 2b. Variations on the basic GSE laser concept have resulted in Master Oscillator Power Amplifier (MOPA) GSE arrays [2,3] and continuous grating (CG)-GSE laser arrays [4, 5]. GSE arrays with 10 elements per gain section and 20 gain sections have obtained cw threshold current densities of under 140 A/cm² with cw differential quantum efficiencies of 20 to 30% per surface. Linewidths in the 40 to 100 MHz range have been obtained with output powers of 100 to 250 mW/surface.

An epitaxial structure typically used for GSE arrays (and for the devices reported in this paper) is a graded index separate confinement heterostructure (GRIN SCH) geometry with a single quantum well. The complete epitaxial structure, corresponding to a cross section along one of the ridges in a gain section (Fig. 1), shown in Fig. 3a, has 66% AlAs in the cladding layers, and the top of the graded region has 8% AlAs. On either side of the 100 Å thick strained layer quantum well, which contains 14% In, are 60 Å GaAs barrier layers. The total width of the graded regions is about 0.3 μm. With this general structure, 60 μm wide broad area lasers have threshold current densities of about 110 to 130 A/cm² for 500 μm long lasers and as low as 65 A/cm² for 1.5 mm long lasers [6].

To provide index guiding of the array elements in each gain section and to provide the proper location for the grating, the GaAs cap layer and part of the p-clad layer is etched away.

Typically, all but about 1400 Å of the p-clad layer above the graded region is removed. After fabrication of a ~ 400 Å deep grating, an index difference of about 8×10^{-3} exists between the regions that are not etched and those that are etched, providing index guiding in the ridges of the gain sections. The transmission electron micrograph (Fig. 3b) shows the top graded region, p-clad thickness, and a ~ 300 Å deep grating, which was formed in the 300 μm long passive regions between the gain sections. Each of the ten ridges in a gain section are 2 μm wide on 4.6 μm centers and the length of each gain section is 300 μm .

Variations in the material compositions and layer thicknesses of the device can prevent coherent operation of the array. Assuming the layer thickness variation is a tightly controlled $\pm 1\%$, variations in the graded region thickness result in a calculated wavelength variation (detuning) of ± 1.5 Å for single, independent GSE emitters. A variation in the p-clad layer after ion-beam etching of ± 300 Å results in a similar shift of ± 6 Å. The wavelength detuning sensitivity of the p-clad thickness (after etching to the grating level) can be reduced to about ± 3 Å by increasing the thickness of the graded regions from 0.15 μm to 0.2 μm , although at the expense of increased detuning due to variations in the thickness of the graded regions. Calculations indicate that for tightly controlled variations in the material composition ($\pm 0.05\%$), the resulting detuning is about 0.5 Å. If a two-step growth process is used, the p-clad thickness variation is due to growth thickness variation and not etching variations. In this case, overall detuning can be limited to about ± 1.5 Å for both graded region variations and p-clad thickness variations.

In GSE arrays, adjusting the individual currents to obtain narrow spectral linewidths also adjusts the phases between the emitting regions. As a result, the individual currents that correspond to the narrowest linewidth (and highest coherence) may produce a far-field pattern with less visibility than a far-field with a wider linewidth, but with currents adjusted to provide a far-field pattern with high visibility. One modification to GSE devices to simultaneously achieve a narrow linewidth and high visibility in the far-field would be the addition of a separate phase-adjusting section between each gain and grating section. Focussed ion beam micromachining has been used to modify regular GSE gain sections to allow a short (~ 50 μm) phase adjusting section before each grating region.

The basic GSE array shown in Fig. 1 couples light perpendicular to the surface in both directions. If the substrate is transparent, the device can be mounted junction-down for optimum cooling. The use of a strained quantum well emitting at ~ 0.97 μm allowed junction down mounting and substrate emission for the device whose characteristics are shown in Fig. 2. In addition to thermal considerations, junction down mounting on a patterned, insulated submount allows multiple electrodes without exposing numerous, vulnerable bond wires to the external system. Because of the thermal and other packaging advantages of junction down mounting, high-reflect coatings for the grating side and anti-reflect coatings for the substrate side have been developed to improve power and efficiency. Figure 5a shows the reflectivity of a GaAs substrate (no epi-layers) with a quarter-wave thickness (~ 1300 Å at $\lambda = 9500$) of Si_3N_4 on both surfaces as a function of wavelength. For several hundred Angstroms centered around 9500 Å, the reflection is less than 1%. Figure 5b shows the reflectivity of a GaAs wafer with an anti-reflect coating on one side (the input side) and a high reflect coating on the other side for two cases. The high reflect coating consists of a quarter wavelength (~ 1300 Å) of Si_3N_4 followed by 2000 Å of Au. In one case there is a grating (period ~ 3000 Å) on the surface of the GaAs. The two different experimental curves for the grating case correspond to two different polarizations of the incident beam. The other case shown in Fig. 5b is for a GaAs wafer without a grating on the surface. In this case, as in Fig. 5a, no difference in the reflectivity as a function of polarization is distinguishable. To test these coatings, devices were first probe tested junction up at the wafer level and the power and threshold for each array measured. Next, high reflect coatings were applied to the grating surface and individual arrays were sawn from the wafer. After junction down mounting, the power and threshold were again measured. Preliminary results of using high-reflect and anti-reflect coatings on 10×10 GSE arrays show that the high reflect coatings resulted in a power increase of 60 to 63% out the substrate side and a threshold current reduction of 17 to 46%.

REFERENCES

1. G. A. Evans, N. W. Carlson, J. M. Hammer, M. Lurie, J. K. Butler, S.L. Palfrey, R. Amantea, L. A. Carr, F. Z. Hawrylo, E. A. James, C. J. Kaiser, J. B. Kirk, and W. F. Reichert, "Two Dimensional Coherent Laser Arrays Using Grating Surface Emission," *IEEE Journal of Quantum Electronics*, Vol. 25, No. 6, pp. 1525-1538, June, 1989.
2. N. W. Carlson, J. H. Abeles, D. P. Bour, S. K. Liew, W. F. Reichert, P. S. D. Lin, A. S. Gozdz, "Demonstration of a monolithic, grating-surface-emitting laser master-oscillator-cascaded power amplifier array," to be published in October 1990, *Photonics Technology Letters*.
3. D. F. Welch, D. Mehuys, R. Parke, R. Waarts, D. Scifres, and W. Streifer, "Coherent operation of monolithically integrated master oscillator amplifiers" *Electronics Letters*, Vol. 26, No. 17, 16th August 1990, pp.1327-1329.
4. J. S. Mott, and S. H. Macomber, "Two-Dimensional Surface Emitting Distributed Feedback Laser Arrays," *IEEE Photonics Technology Letters*, Vol. 1, No. 8, pp.202-204, August 1989.
5. N. W. Carlson, S. K. Liew, R. Amantea, D. P. Bour, G. A. Evans, E. Vangieson, "Mode Discrimination in Distributed Feedback Grating Surface Emitting Lasers Containing a Buried Second Order Grating," submitted to *IEEE Journal of Quantum Electronics*.
6. C. A. Wang and H. K. Choi, "Organometallic Vapor Phase Epitaxy of High-Performance Strained-Layer InGaAs/AlGaAs Diode Lasers," *IEEE Journal of Quantum Electronics*, accepted for publication.

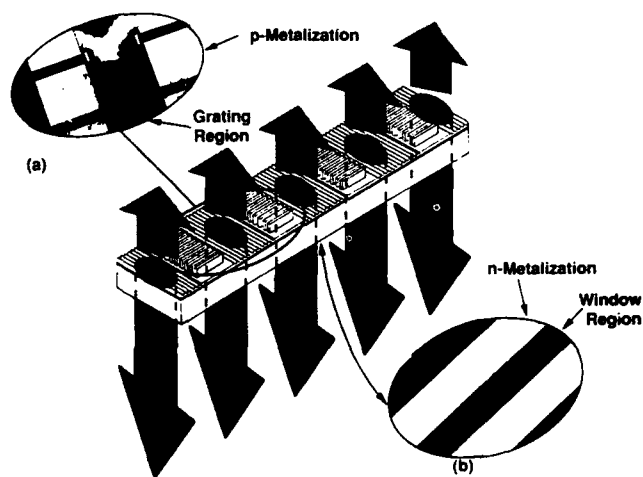


Figure 1 Several sections of a basic two dimensional array. Groups of 10 parallel ridge guide lasers are laterally coupled evanescently in each gain section. Inset photograph a) shows completed gain sections with contact pads and inset b) shows the substrate side metalization and emission window.

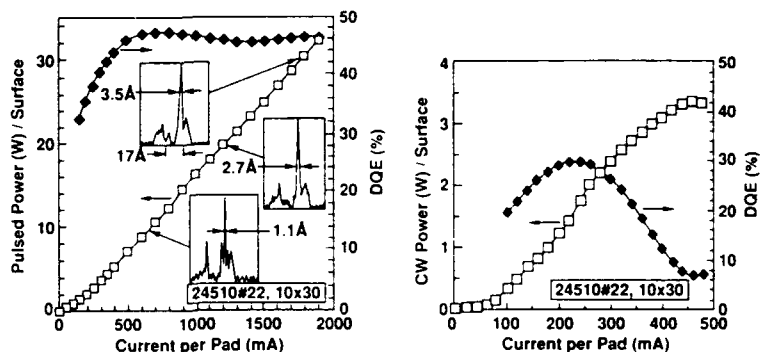


Figure 2 a) power-current curve of a 10x30 GSE array operating with 100 ns pulses, 10 kHz repetition rate, and at a coolant temperature of -2.8 C; b) cw power-current curve for the same device at -2.8 C. The longitudinal aperture of the array is 1.83 cm.

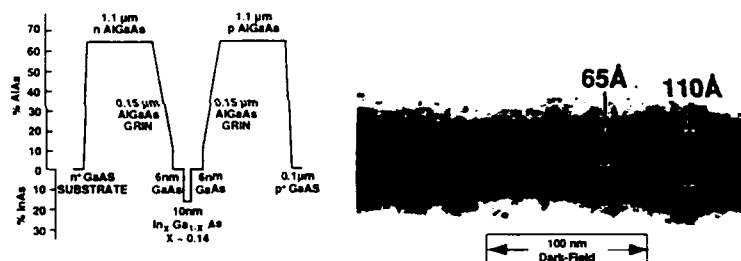


Figure 3 a) the thickness and composition profile of the laser structure b) TEM of the quantum well region.

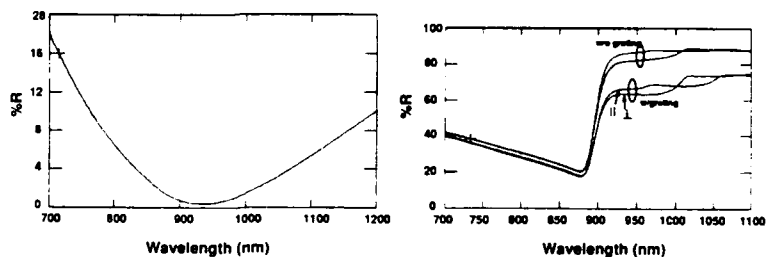


Figure 4 a) power reflectivity from a 100 μm thick GaAs substrate with an anti-reflect layer of quarter wave thick ($\sim 1300 \text{ \AA}$) Si_3N_4 on both surfaces; b) power reflectivity from a 100 μm thick GaAs substrate with an anti-reflect layer on one GaAs surface and a high reflect layer ($\sim 1300 \text{ \AA}$ of Si_3N_4 and 2000 \AA of Au) on the opposite surface. A slight difference in reflectivity is observed for different incident polarizations if a grating is present at the high-reflect interface.

EPITAXIAL LIFTOFF TECHNOLOGY FOR OEIC's

by

E. Yablonovitch, W.K. Chan and A. Yi-Yan

*Bell Communications Research**Navasink Research Center**Red Bank, N.J. 07701-7040*

Epitaxial liftoff permits the integration of III-V films and devices onto arbitrary material substrates. This paper will review Bellcore's work on opto-electronic integration of III-V optical transmitter and receiver devices onto LiNbO₃, glass, Silicon and sapphire substrates.

In the field of electronic materials there has been a persistent interest in the integration of high quality epitaxial thin film semiconductor layers with arbitrary crystalline or glass substrates. For example, thin film GaAs layers on crystalline Silicon substrates would allow the combination of the two technologies. This has led to a massive effort on lattice mis-matched heteroepitaxial growth. Recently, however, a new and more flexible approach¹ has been attracting increasing² attention.

In this new approach, perfect epitaxial quality AlGaAs thin films are lifted off lattice-matched GaAs growth substrates by means of an ultra-thin AlAs release layer. Advantage is taken of the extremely selective etching ($\geq 10^7$) of AlAs in dilute Hydrofluoric acid, permitting large area (cm²) epitaxial AlGaAs films to become undercut. The GaAs substrate is left intact and can be re-used if so desired, while the epitaxial thin film can be cemented or "Van der Waals bonded" by surface tension to any arbitrary substrate. In this

paper we report the implementation of examples of this technology involving the marriage of a number of different opto-electronic devices and materials.

Among the devices and material systems which have been demonstrated are GaAs double heterostructure GaAs thin film lasers on glass and Silicon substrates³, MESFET's on glass⁴, InGaAs strained quantum well HEMT's on Silicon and glass², GaAs LED's on Silicon⁶, InGaAs/InP p-i-n photodetectors on sapphire⁷, GaAs photodetectors integrated with LiNbO₃ and glass waveguides^{8,9}. In addition, the regrowth of quantum wells on GaAs on Silicon has been shown to be feasible.

Unlike lattice mis-matched heteroepitaxy, there is no compromise in the epitaxial quality¹ of the liftoff films. We anticipate that the epitaxial liftoff approach will find use wherever there is a desire to combine thin film III-V semiconductor crystals with other materials and substrates.

This work was partially supported by DARPA and ONR under Contract N0014-90-C-0048.

1. "Extreme Selectivity in the Lift-Off of Epitaxial GaAs Films", E. Yablonovitch, T. Gmitter, J. P. Harbison, R. Bhat, Appl. Phys. Lett. 51, 2222 (1987).
2. "(AlGa)As/(InGa)As Strained Quantum Well on Silicon Dioxide by Selective Device Liftoff as an Alternative to Hetero-epitaxy", D. R. Myers, J. F. Klem, J. A. Lott, Tech. Dig. of the 1988 Int. Elec. Dev. Mtg. (IEEE, Piscataway, N.J., 1988)
3. "Double Heterostructure GaAs Thin Film Lasers on Glass Substrates", E. Yablonovitch, E. Kapon, T. J. Gmitter, C. P. Yun, R. Bhat, IEEE

Phot. Tech. Lett. 1, 41, (1989)

4. "MESFET Liftoff from GaAs Substrate to Glass Host", C. Van Hoof, W. D. Raedt, M. Van Rossum, G. Borghs, Electron. Lett. 25, 136 (1989)
5. "Regrowth of GaAs Quantum Wells on GaAs Liftoff Films 'Van der Waals Bonded' to Silicon Substrates", E. Yablonovitch, K. Kash, T. J. Gmitter, L. T. Florez, J. P. Harbison and E. Colas, Electron. Lett. 25, 171 (1989)
6. "Integration of GaAs LED's on Si by Epi-lift-off", I. Pollentier, P. De Dobbelaere, F. De Pestel, P. van Daele and P. Demeester, Proceedings of ESSDERC '89 (Berlin, 1989)
7. "A High-Speed InP/InGaAs Photodiode on a Sapphire Substrate", H. Schumacher, T. J. Gmitter, H. P. LeBlanc, R. Bhat, E. Yablonovitch and M. Koza, Elec. Lett. 25, 1653 (1989).
8. "Grafted GaAs Detectors on Lithium Niobate and Glass Optical Waveguides", A. Yi-Yan, W. K. Chan, T. J. Gmitter, L. T. Florez, J. L. Jackel and E. Yablonovitch, IEEE Phot. Tech. Lett. 1, 379 (1989).
9. "Optical Coupling of GaAs Photodetectors Integrated With Lithium Niobate Waveguides" W. K. Chan, A. Yi-Yan, T. J. Gmitter, L. T. Florez, J. L. Jackel, E. Yablonovitch, R. Bhat and J. P. Harbison, IEEE Phot. Tech. Lett. 2, 194 (1990).

IV. DEVICES

Lasers

| | |
|--|-----|
| Submilliampere-threshold Multi-Quantum-Well AlGaAs Laser and Their Integration of More than 100 Lasers | 160 |
| <i>S. Hirata, H. Narui and Y. Mori</i> | |
| Fabrication of Low-Threshold InGaAs/GaAs Ridge Waveguide Lasers by Using In-Situ Monitored Reactive Ion Etching | 164 |
| <i>C.P. Chao, S.Y. Hu, P. Floyd, K-K. Law, J.L. Merz and A.C. Gossard</i> | |
| Fabrication of GaAlAs/GaAs Single Quantum Well Gain-Coupled Distributed Feedback Lasers | 168 |
| <i>Y. Luo, H.L. Cao, M. Dobashi, H. Hosomatsu, Y. Nakano and K. Tada</i> | |
| Effect of Window Diffusion Stripe Structure on Reduction of Temperature Rise at Laser Facet | 172 |
| <i>A. Shima, Y. Kokubo and M. Aiga</i> | |
| Differential Gain and Damping in High Speed 1.55μ Quantum Well Lasers | 176 |
| <i>M.C. Tatham, N.C. Fletcher, D.M. Cooper and L.D. Westbrook</i> | |
| Fabrication of GaInAs(P)/InP Quantum-Wire Structures for Lasers and Electro-Optical Devices | 180 |
| <i>S. Arai and Y. Suematsu</i> | |
| Polarization-Controlled Semiconductor Photonic Devices by Strained-Barrier Superlattice Structure | 184 |
| <i>M. Okamoto, K. Magari and Y. Itaya</i> | |

Integrated Structures

| | |
|---|-----|
| Fabrication and Characteristics of Tunable Twin-Guide DFB Lasers by All MOVPE | 188 |
| <i>M. Hamada, E. Yamamoto, K. Suda, S. Nogiwa and T. Oki</i> | |
| Buried Interconnect Structure for Symmetric SEEDs | 192 |
| <i>L.A. D'Asaro, L.M.F. Chirovsky, R.F. Kopf and S.J. Pearton</i> | |
| Tailoring of Electron and Hole Energies in Strained GaAsP/AlGaAs Quantum Wells using Fluorine Impurity Induced Layer Disordering | 195 |
| <i>U. Das, S. Davis, J-T. Hsu, R.V. Ramaswamy and F.A. Stevie</i> | |

Waveguides, Switches, and Modulators

| | |
|---|-----|
| Semiconductor Waveguide Switches and Modulators | 199 |
| <i>K. Tada</i> | |
| Properties of Waveguides, Routing Structures and Switches Fabricated by Impurity Induced Layer Disordering | 203 |
| <i>T.A. DeTemple</i> | |

| | |
|---|-----|
| Room Temperature Stark-Ladder Transitions and Electro-Optic Bistability in GaAs/AlAs Superlattices with Different Miniband Widths | 206 |
| <i>K. Kawashima, K. Fujiwara, T. Yamamoto, M. Sigeta and K. Kobayashi</i> | |
| Very Low-Voltage MBE-Grown Asymmetric Fabry-Perot Reflection Modulator Based on Superlattice Wannier-Stark Localization | 210 |
| <i>K-K. Law, J.L. Merz and L.A. Coldren</i> | |
| Room Temperature Excitonic Transitions and Electro-Optical Bistability in Strained $\text{In}_x\text{Ga}_{1-x}\text{As}/\text{Al}_{0.15}\text{Ga}_{0.85}\text{As}$ Multiple Quantum Wells | 214 |
| <i>K. Kawashima, K. Fujiwara, K. Kobayashi and N. Sano</i> | |
| Ultrafast Measurements of Tunneling Dynamics in a GaAs/AlGaAs MQW Pin Optical Modulator | 218 |
| <i>C.B. Park, A. Miller, D.C. Hutchings and P. LiKamWa</i> | |

Submilliampere-threshold Multi-Quantum-Well AlGaAs Lasers and Their Integration of More Than 100 Lasers

Shoji Hirata, Hironobu Narui and Yoshifumi Mori

Sony Corporation Research Center, Hodogaya-ku, Yokohama 240, Japan

Extremely low threshold lasers are very much in demand for opt-electronic integrated circuits (OEICs), such lasers can realize dreams of optical parallel processing systems and optical computing, because very dense integration of optical devices requires low heat generation and low electric power consumption. Recently, submilliampere lasers have been reported from several laboratories [1]-[3], but these lasers require high-reflection facet coating, which prevents high light output power. The lowest threshold current achieved with an uncoated device had been 1.8mA under pulsed operation [4] and 2.5mA under continuous wave (CW) operation [5]. We have developed a new type buried heterostructure (BH) laser using single-step MOCVD on a nonplanar GaAs substrate [6],[7]. Our laser has the lowest threshold current value of 0.88mA and the highest energy conversion efficiency of 42% at 1mW/facet at room temperature (RT) under CW conditions without facet coating. Then we have fabricated 102 laser arrays and realized their uniform operations[8].

Figure 1 shows the structure of our laser. A triangular prism-shaped region appeared on the ridge is an active region as a laser diode and surrounding layers are confinement layers of optical wave and injection current. In order to realize the submilliampere lasers, we injected currents into the active region effectively and introduced optimized multi-quantum-well (MQW) structure as the active layer.

Figure 2 shows an outline of the fabrication process. The ridged substrate whose stripe is parallel to the $\langle 011 \rangle$ direction was prepared using chemical etching as shown in Fig.2(a). The width and height of the ridge are both about $4\mu\text{m}$. Then we use atmospheric pressure MOCVD to grow the laser structure. Trimethyl aluminum, trimethyl gallium and arsine were used as sources and hydrogen selenide and dimethyl zinc as dopants. First, the n-type GaAs buffer layer, the n-type $\text{Al}_{0.4}\text{Ga}_{0.6}\text{As}$ cladding layer, the active layer and the p-type $\text{Al}_{0.4}\text{Ga}_{0.6}\text{As}$ cladding layer were formed on the nonplanar GaAs substrate. The triangular prism-shaped double heterostructure (DH) surrounded by $(111)\text{B}$ planes was formed on the ridge and another DH was formed on the rest of the ridge, as in Fig.2(b). Since no layers can be grown directly along the $\langle 111 \rangle$ direction with MOCVD, the active layer on the ridge is separate from the active layer on the rest of the ridge. The MQW active layer was composed of the p-type $\text{Al}_{0.2}\text{Ga}_{0.8}\text{As}$ guided layer (1000\AA), the n-type $\text{Al}_{0.2}\text{Ga}_{0.8}\text{As}$ guided layer (1000\AA), two $\text{Al}_{0.2}\text{Ga}_{0.8}\text{As}$ barrier layers (80\AA) and three GaAs well layers (60\AA). Next, the n-type $\text{Al}_{0.45}\text{Ga}_{0.55}\text{As}$ current blocking layer was formed to concentrate the injection current in the active layer on the ridge. This current blocking layer was divided by the triangle prism-shaped region with $(111)\text{B}$ planes, as in Fig.2(c). Finally, the p-type $\text{Al}_{0.45}\text{Ga}_{0.55}\text{As}$ cladding layer and the p-type GaAs capping layer were formed, as in Fig.2(d). Individual lasers are cleaved to a length of $150\mu\text{m}$ and mounted p-side up on a copper heat sink without any facet coating.

Figure 3 shows the light output power / current characteristics. We obtained threshold current of 0.88mA at room temperature and 0.30mA at 77K in CW operation. The energy conversion efficiency from input electric power to light output

power is estimated to be 42% at the light output power of 1mW/facet as shown in Fig. 4. The curved line in Fig.4 shows the theoretical upper limit of the energy conversion efficiency at 1mW/facet. To obtain the higher efficiency of more than 50%, we have to reduce the threshold current of less than 1mA. The characteristic temperature was 122K in the temperature range between -20°C and 50°C. Figure 5 shows the far field pattern measured at an output power of 3mW/facet. In this laser we could obtain the result of $\theta_{//} > \theta_{\perp}$, which meant that a perfectly round beam could be obtained by controlling the laser parameters. The astigmatic difference was negligible. The laser oscillated at the wavelength of about 845nm in TE mode.

Using the extremely low threshold laser structure, we could get uniform laser array with 102 beams with a period of 4.5 μ m, as shown in Fig.6. To get this structure, first we prepared periodic-ridge-shaped stripes parallel to the <011> direction on the GaAs substrate using RIE, then we grew the laser structure using single-step MOCVD as we shown before in Fig.2. The laser arrays have cavity length of 200 μ m and have no facet coating.

All of 102 lasers were operated simultaneously under CW condition at RT. Figure 7 shows the near-field pattern of the 102 laser array operated at 600mA. Each laser operated in a stable fundamental mode and at uniform power of about 2.5mW/facet. The total light output and current characteristics and their temperature dependences are shown in Fig.8. The total CW threshold current were 180mA and 48mA at 300K and 77K, respectively. The differential quantum efficiency was estimated to be 87%. The maximum output power obtained at the injection current level of 2A was 850mW/facet. The characteristic temperature was estimated to be 158K. The laser arrays could operate at temperatures of more than 80°C because of their very low threshold current and good characteristic temperature.

Figure 9 shows the lasing characteristics of five of the lasers in the laser array. We measured the light output power from each laser using a spacial filter at various current levels, and we estimated the threshold current. These values were then divided by 102 and the calculated values were called reduced threshold currents. The average value of the reduced threshold currents was 1.8mA. Lasing spectra were obtained at total current level of 600mA. It should be pointed out that the average lasing wavelength for the 102 laser arrays was 861nm, longer than that of 845nm for a single laser with the same MQW structure. The QW active layer of any laser of the 102 laser array becomes thicker than the QW active layer of a single laser because of the strong migration effect during MOCVD growth.

We have realized a submilliampere-threshold laser without facet coating and its integration of 102 lasers. The lasers can be fabricated using single step MOCVD. These lasers are expected to be key devices for optical parallel processing systems.

- 1) E.Kapon, S.Simhony, J.P.Harbison, L.T.Florez, and P.Worland, Appl. Phys. Lett., 56, pp1825, 1990.
- 2) K.Y.Lau, P.L.Derry, and A.Yariv, Appl. Phys. Lett., 52, pp88, 1988
- 3) E.Marclay, D.J.Arent, C.Harder, H.P.Meier, W.Walter, and D.J.Webb, Electron. Lett., 25, pp892, 1989
- 4) E.Kapon, C.P.Yun, J.P.Harbison, L.T.Florez, and N.G.Stoffel, Electron. Lett., 24, pp985, 1988
- 5) K.M.Dzurko, E.P.Menu, C.A.Beyler, J.S.Osinski, and P.D.Dapkus, IEEE J.Q.E., 25, pp1450, 1989
- 6) H.Narui, S.Hirata, T.Ohata, and Y.Mori, Digest of intl. meeting on APCT'89, Tokyo, H-3, 1989
- 7) H.Narui, S.Hirata, and Y.Mori, Digest of 12 intl. semicon. laser conf., Davos, F-1, 1990
- 8) S.Hirata, H.Narui, and Y.Mori, Appl. Phys. Lett., 58, pp319, 1991

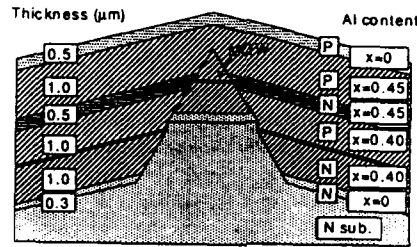


Fig.1 Schematic representation of laser structure

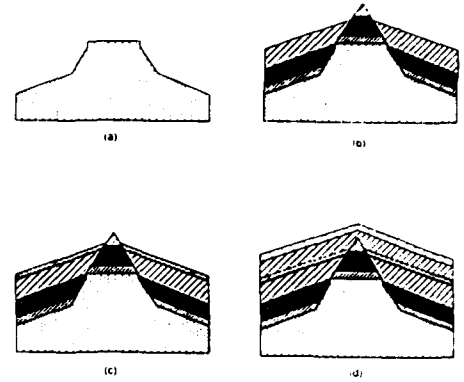


Fig.2 Outline of fabrication process

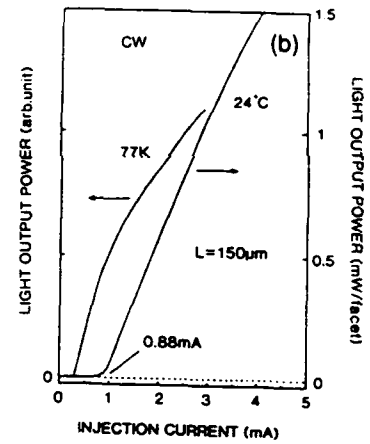
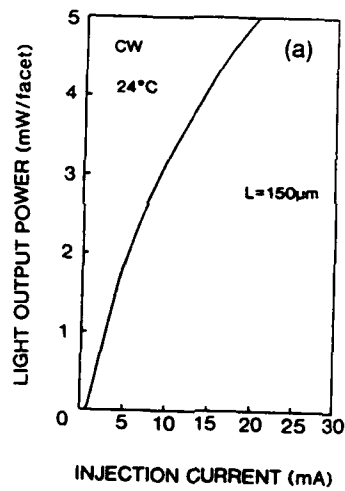


Fig.3 Light output power/current characteristics. Fig.(b) is an expansion of Fig.(a).

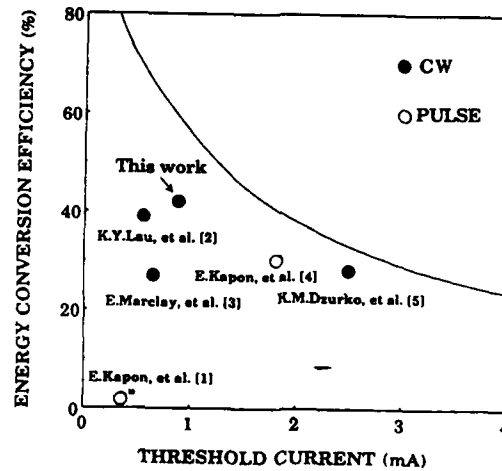


Fig.4 Relation between threshold current and energy conversion efficiency

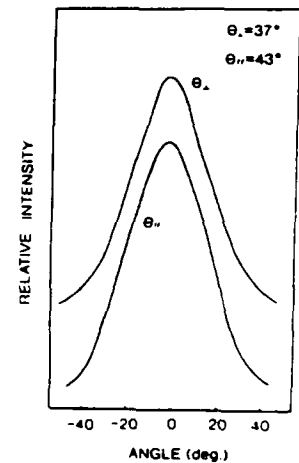


Fig.5 Far-field pattern parallel and perpendicular to junction plane

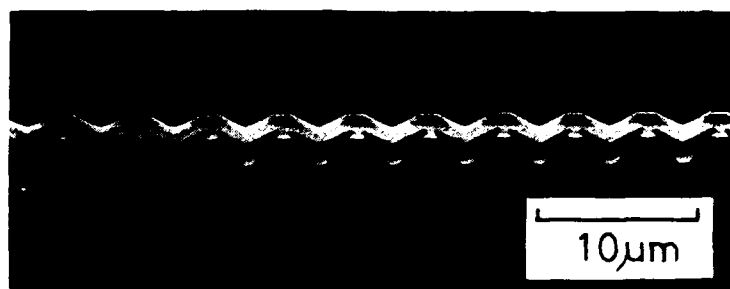


Fig.6 Cross-sectional SEM micrograph of a 102-laser array



Fig.7 Near-field photograph of a 102-laser array

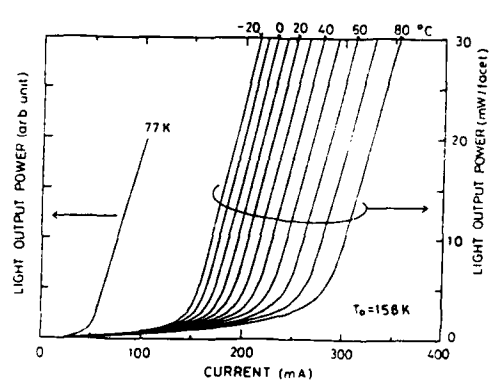
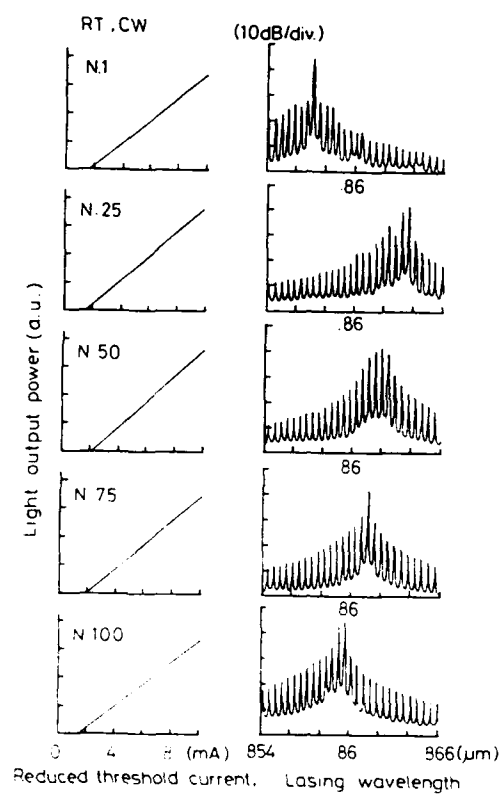


Fig.8 Light output power/current characteristics of a 102-laser array

Fig.9 Lasing characteristics of five of the lasers in a 102 laser array



**Fabrication of low-threshold InGaAs/GaAs ridge waveguide lasers by using
in situ monitored reactive ion etching**

C.P. Chao, S.Y. Hu, P. Floyd, K-K. Law, J.L. Merz, and A.C. Gossard

Department of Electrical and Computer Engineering
University of California, Santa Barbara
Santa Barbara, CA 93107

In general, fabrication of ridge waveguide lasers is simpler than that of other structures such as diffusion and buried heterostructure lasers. Either wet etching or dry etching processes are generally used for ridge formation. Since the height of the ridge determines the optical confinement as well as the surface recombination and lateral diffusion of the injected carriers, it is important to control the ridge formation properly to optimize the device performance. Recently, an *in situ* laser-monitored dry etching technique has been widely used in device processing[1-3], and various monitoring techniques have been developed to accomplish precise etching-depth control such as growing a stop-etch layer which makes a clear difference in the monitored signal[1]. With the ability of accurate ridge etching, high performance ridge waveguide lasers are expected. However, the reported ridge lasers did not have the low threshold current predicted theoretically even though very good results were obtained for the material threshold current density and for buried heterostructure lasers[6,8]. This was particularly true for strained-layer InGaAs/GaAs structures. [4-7]

In this paper we report a low-threshold InGaAs/GaAs strained single quantum well (SQW) ridge waveguide laser fabricated using single laser-monitored dry etching for ridge formation. Precision of ridge etching was controlled within 150Å. Continuous wave (CW) threshold current (I_{th}) as low as 3.6mA was obtained for 3.3µm wide, 240µm long lasers with cleaved facets. With 96%-70% high reflectivity (HR) coatings on both facets I_{th} dropped to 2.1mA.

The laser structure, as shown in Fig. 1, was grown by molecular beam epitaxy (MBE) on a (100) n⁺-GaAs substrate. It is a conventional double heterostructure single quantum well (DHSQW) ridge laser. To make the monitoring process suitable for general use in other device fabrication there is no extra stop-etch indicating layer. To reduce the threshold current we stopped the ridge etching at the interface between the doped p-type cladding layer and the undoped active region (including guiding layers) since the surface recombination of GaAs is severe[9]. This requires precise etching depth control in the ridge formation. A He-Ne laser ($\lambda = 6328\text{\AA}$) was installed for *in situ* etch monitoring.

Shown in Fig. 2b is the etching curve obtained to characterize the etching process. The active region and the cladding regions are clearly distinguished by their different average reflectivity. Theoretically the etching curve can be calculated by using a transmission matrix method[10], and Fig. 2a is the calculated curve which matches the experimental data quite well. From the theoretical calculation the interface of every layer is clearly identified on the etching curve, therefore the etching depth can be very precisely decided. Ridge dry etching was carried out by Cl_2 plasma RIE at a flow rate of 4sccm, 1mtorr, 60W and 350V DC bias. The etching rate is about $1500\text{\AA} / \text{min}$, and at this rate the etching depth can be easily controlled within 150\AA (10 seconds), which is good enough for ridge laser fabrication. The ridge formation stops at about 1300\AA above the quantum well. Due to the rather sparse lithographic pattern of ridge-lines the monitoring laser light was directed onto the patterned sample instead of using an unpatterned reference sample. The uniformity of the etched sample shows no obvious difference between the laser monitored region and the rest of the sample which means that the monitor light did not disturb the etching. Hence the detected signal provides an accurate *in situ* information from the as-etched surface. After dry etching SiO_2 was deposited for contact isolation. The dry etching mask was then used for the self-aligned lift-off process of SiO_2 on top of the ridge. Cr/AuZn/Au and AuGe/Ni/Au were evaporated for p-contact and n-contacts separately. The sample was thinned and cleaved for measurement. Si / SiN_x dielectric films was finally sputtered on the facets as HR coatings.

The lasing wavelength was measured at about 9880\AA . At this wavelength the detector response was calibrated for the light vs current (L-I) measurement. Shown in Fig. 3 is the room temperature CW L-I curve of a $240\mu\text{m}$ long, $3.3\mu\text{m}$ wide, ridge laser. The as-cleaved $I_{\text{th}}=3.6\text{mA}$ and the external quantum efficiency (η_d) was about 70%. Also shown in Fig.3 are the L-I curves of the same device using different coating conditions. For 96%-70% HR-HR coating $I_{\text{th}}=2.1\text{mA}$ which is the lowest threshold current obtained on strained InGaAs/GaAs ridge waveguide lasers. The reduction of threshold current by coating is less significant than other published results.[7,9] This occurs because the laser bar ($240\mu\text{m}$) is not as short as those in ref. 6 and 9 ($150\mu\text{m}$, $198\mu\text{m}$, respectively) and the internal loss ($\alpha_i = 10\text{cm}^{-1}$ obtained by analyzing the different η_d from each coated facet) is relatively high.

In conclusion, *in situ* laser monitored dry etching was successfully used for precise ridge formation in fabricating low-threshold strained InGaAs/GaAs ridge waveguide lasers. The lowest as-cleaved CW threshold current is 3.6 mA on a $240\mu\text{m}$ long device, and HR-HR coating reduces the I_{th} to 2.1mA. The great reduction in threshold current in strained InGaAs/GaAs ridge lasers further proves the expected advantages of this material system. These low-threshold lasers are suitable for OEIC applications for which simplified

processing is preferred. With the availability of improved strained-layer material, lower threshold current and higher efficiency is expected for InGaAs/GaAs strained-layer quantum well lasers.

References :

1. M. Jost, G. L. Bona, P. Buchmann, G. Sasso, P. Vettiger, and D. Webb, "Ridge formation for AlGaAs GRIN-SCH lasers by Cl_2 reactive ion etching," IEEE Photon. Tech. Lett., 2, No. 10, 697-698 (1990).
2. J. Landreau, and H. Nakajima, "*In situ* reflectivity monitoring of antireflection coatings on semiconductor laser facets through facet loss induced forward voltage changes," Appl. Phys. Lett., 56, No. 24, 2376-2378 (1990).
3. T. R. Hayes, P.A. Heimann, V. M. Donnelly, and K. E. Strege, "Maskless laser interferometric monitoring of InP/InGaAsP heterostructure reactive ion etching," Appl. Phys. Lett., 57, No. 26, 2817-2819 (1990).
4. S. E. Fischer, D. Fekete, G. B. Feak, and J. M. Ballantyne, "Ridge waveguide injection laser with a GaInAs strained layer quantum well ($\lambda=1\mu\text{m}$)," Appl. Phys. Lett., 50, 714-716 (1987).
5. A. Larsson, S. Forouhar, J. Cody, and R.J. Lang, "High-Power operation of highly reliable narrow stripe pseudomorphic single quantum well lasers emitting at 980nm," IEEE Photon. Tech. Lett., 2, No. 5, 307-309 (1990).
6. T. Takeshita, M. Okayasu, O. Kogure, and S. Uehara, "Low-Threshold strained-layer ridge waveguide lasers," Japan J. Appl. Phys., 29, No. 7, L1138-L1140 (1990).
7. I. Suemune, L. A. Coldren, M. Yamanishi, and Y. Kan, "Extremely wide modulation bandwidth in a low threshold current strained quantum well laser," Appl. Phys. Lett. 53, No. 15, 1378-1380 (1988).
8. T. R. Chen, L. Eng, B. Zhao, Y. H. Zhuang, S. Sanders, H. Morkoc, and A. Yariv, "Submilliamp threshold InGaAs-GaAs strained layer quantum-well laser," IEEE J. Quantum Electron. 26, No. 7, 1183-1190 (1990).
9. G. P. Agrawal, and N.K. Dutta, Long-Wavelength semiconductor lasers, (Van Nostrand Reinhold, New York, 1986), p. 116.
10. P. Yeh, Optical waves in layered media, (Wiley, New York, 1988), Chap. 6.

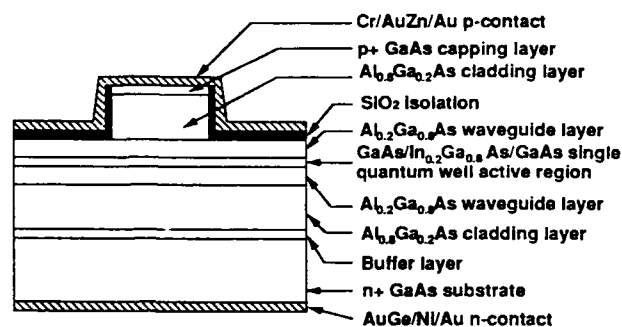


Fig. 1 Schematic diagram of the InGaAs/GaAs DHSQW ridge waveguide laser.

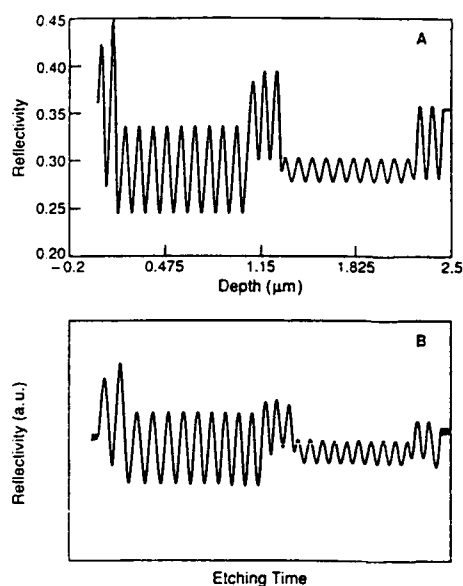


Fig. 2 Change of surface reflectivity during etching : monitored etching curve.
(a) Theoretical calculation.
(b) Experimental data of characterization etching.

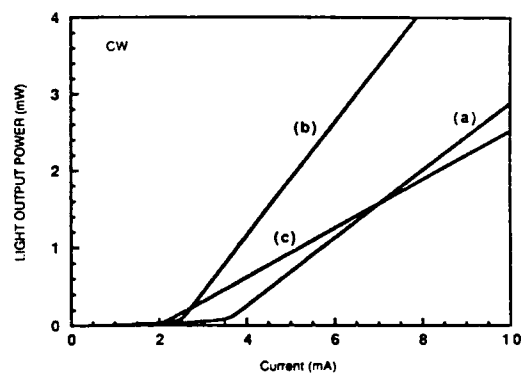


Fig. 3 CW L-I curves of a 240 μm long and 3.3 μm wide ridge laser diode at different facet-coated reflectivities:
(a) $R_1=R_2=0.3$, (b) $R_1=0.3$, $R_2=0.96$, (c) $R_1=0.7$, $R_2=0.96$

Fabrication of GaAlAs/GaAs Single Quantum Well Gain-Coupled Distributed Feedback Lasers

Y. Luo*, H. L. Cao, M. Dobashi*, H. Hosomatsu*
Y. Nakano, and K. Tada

Department of Electronic Engineering, University of Tokyo
7-3-1 Hongo, Bunkyo-ku, Tokyo, 113, Japan

**Optical Measurement Technology Development Co., Ltd.*
2-11-13 Naka-cho, Musashino-shi, Tokyo, 180, Japan

1. Introduction

The gain-coupled distributed feedback (DFB) semiconductor laser is regarded as a promising light source for applications such as optical communication and optical measurement, because of its unique features such as complete single longitudinal mode property¹⁻³, immunity to facet reflection⁴, and resistance to external optical feedback⁵.

The introduction of the quantum well structure to the gain-coupled DFB laser is thought to bring further advantages. We are trying to fabricate gain-coupled DFB lasers with a single quantum well (SQW) active layer. In this paper, we report the preliminary experiment on the fabrication procedure and the characteristics of the SQW gain-coupled DFB laser.

2. Device Structure and Fabrication Procedure

Recently, we demonstrated a purely gain-coupled DFB laser, whose active layer was furnished with a diffraction grating directly on it but still retained sufficient emission efficiency. This has been done by utilizing the organo-metallic vapor phase (OMVPE) technique on patterned substrates^{2,6}. In this experiment, the similar technique has been used. The laser's longitudinal cross sectional structure we propose here is shown in Fig.1. As can be seen, the quantum well active layer is bent, and its thickness is changed periodically. The periodic gain modulation is expected due to the difference in electronic confinement between the thin and thick quantum wells. We adopted a graded-index (GRIN) separate carrier and optical confinement heterostructure (SCH)

SQW. The GRIN layers were designed so as to have a parabolic energy band.

The epitaxial layers of the laser were grown in a low pressure, horizontal, RF heated OMVPE reactor using trimethylgallium (TMG), trimethylaluminum (TMA), arsine, monosilane for n-type doping, diethylzinc (DEZ) for p-type doping, and Pd-diffused hydrogen as a carrier. Total gas flow rate and growth pressure were 10 slm and 100 Torr. In the first OMVPE step, n^+ -GaAs ($1 \times 10^{18} \text{ cm}^{-3}$, $0.5 \mu\text{m}$) buffer, $n\text{-Ga}_{0.55}\text{Al}_{0.45}\text{As}$ ($5 \times 10^{17} \text{ cm}^{-3}$, $1.2 \mu\text{m}$) lower cladding, and undoped $\text{Ga}_{0.75}\text{Al}_{0.25}\text{As}$ ($5 \times 10^{17} \text{ cm}^{-3}$, $0.087 \mu\text{m}$) pattern-providing layers were grown successively on an n^+ -GaAs (100) substrate at 780°C . Next, a second-order diffraction grating with a 244nm period was formed on the epitaxial wafer in parallel with $[0\bar{1}1]$ direction by holographic exposure and wet chemical etching. The groove reached the lower cladding layer. The etchant, $\text{H}_2\text{SO}_4 : \text{H}_2\text{O}_2 : \text{H}_2\text{O} = 9 : 1 : 1$, disclosed (111) and $(1\bar{1}\bar{1})$ planes.

During the second OMVPE step, after bringing growth rate down to half of that in the 1st growth, thin undoped $\text{Ga}_{0.55}\text{Al}_{0.45}\text{As}$ ($0.1 \mu\text{m}$) buffer, undoped $\text{Ga}_{1-x}\text{Al}_x\text{As}$ lower GRIN ($x = 0.45 \sim 0.25$, $0.15 \mu\text{m}$), undoped active (averaged thickness is 80 nm), undoped $\text{Ga}_{1-x}\text{Al}_x\text{As}$ upper GRIN ($x = 0.25 \sim 0.45$, $0.15 \mu\text{m}$) layers were grown at 780°C . During this growth step, the slower growth on the etched facets provided a bent active layer. The growth rate was then restored to the original value used in the 1st OMVPE step for growing $p\text{-Ga}_{0.55}\text{Al}_{0.45}\text{As}$ ($5 \times 10^{17} \text{ cm}^{-3}$, $1.0 \mu\text{m}$) upper cladding and p^+ -GaAs ($1 \times 10^{19} \text{ cm}^{-3}$, $0.5 \mu\text{m}$) contact layers at 780°C and 680°C , respectively. Figure 2 shows an example of the cross-sectional micrograph of the structure thus fabricated, where we observe an SQW active layer with periodically changing thickness.

The epitaxial wafer was made into ridge waveguide DFB lasers. The ridge width and the length of the device were $4 \mu\text{m}$ and $400 \mu\text{m}$, respectively. Both facets were left as cleaved.

3. Device Characteristics

The DFB lasers were operated under pulsed current ($0.4 \mu\text{s}$, 2.5 kHz) at room temperature. Their threshold current were distributed around 40 mA . Figure 3 shows a typical light output vs. current curve. A threshold current of 38 mA and an external differential quantum efficiency of 21% per facet has been obtained. These results are of preliminary experiments, and further improvement is expected through the

optimization of the fabrication process.

Complete single longitudinal mode oscillation has been obtained in all the measured devices. A typical lasing spectrum at an injection level of 1.6 times the threshold (output power of 8 mW) is shown in Fig.4. Excellent single longitudinal mode oscillation, which is of a high side-mode suppression ratio exceeding 35 dB, has been achieved. In the spectrum near the threshold, it was very difficult to observe side modes⁶. From this facts, we judged that these lasers were equipped with sufficient gain coupling. Thus, we have shown the applicability of the quantum well structure to our gain-coupled DFB lasers, and we expect the advantages stemming from the quantum size effects

4. Conclusions

We have reported the first realization of gain-coupled DFB lasers having quantum well active layers, placing emphasis on the proposal of the structure and its fabrication method. Room temperature pulsed operation with a threshold current of 38 mA and a single longitudinal mode oscillation of over 35 dB side-mode suppression has been demonstrated. The merits of the quantum well lasers, in addition to the unique features of the gain-coupled structure, are expected.

References

- 1 H. Kogelnik and C. V. Shank, J. Appl. Phys. **43**, 2327 (1972).
- 2 Y. Luo, Y. Nakano, K. Tada, T. Inoue, H. Hosomatsu, and H. Iwaoka, Appl. Phys. Lett. **56**, 1620 (1990).
- 3 Y. Luo, Y. Nakano, K. Ikeda, K. Tada, T. Inoue, H. Hosomatsu, and H. Iwaoka, Conference Digest, 12th IEEE International Semiconductor Laser Conference, E-6, pp.70-71, Davos, Sept. 1990.
- 4 Y. Nakano, Y. Luo, and K. Tada, Appl. Phys. Lett. **55**, 1606 (1989).
- 5 Y. Nakano, Y. Deguchi, K. Ikeda, Y. Luo, and K. Tada, Conference Digest, 12th IEEE International Semiconductor Laser Conference, E-7, pp.72-73, Davos, Sept. 1990.
- 6 Y. Luo, Y. Nakano, K. Tada, T. Inoue, H. Hosomatsu, and H. Iwaoka, Tech. Digest, 1st International Meeting on Advanced Processing and Characterization Technologies, H-5, pp.223-226, Tokyo, Oct. 1989.

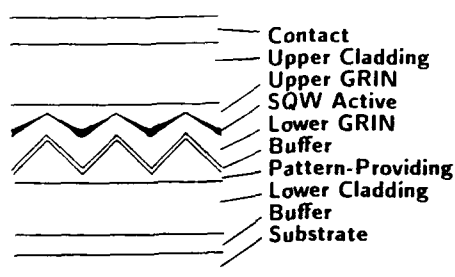


Fig.1 Schematic structure of the longitudinal cross section of the GRIN-SCH-SQW gain-coupled DFB laser proposed.

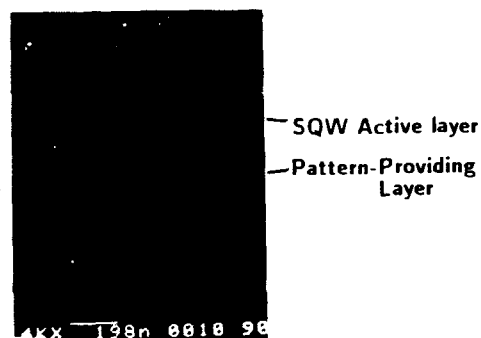


Fig.2 Example of a scanning electron micrograph showing the longitudinal cross section of the epitaxial layers.

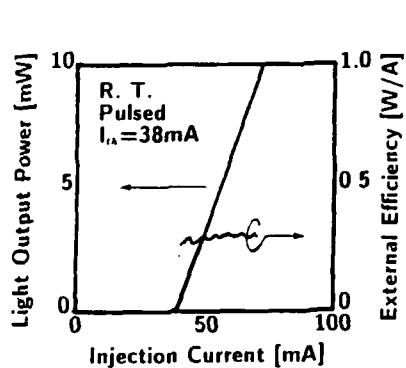


Fig.3 Light output vs. injection current characteristics. External efficiency per facet is plotted together.

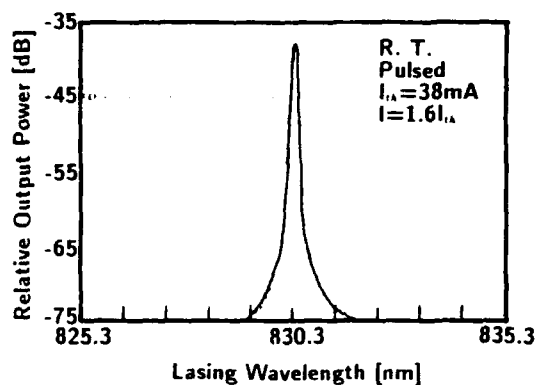


Fig.4 Example of a lasing spectrum at 8 mW.

Effect of Window Diffusion Stripe Structure on Reduction of Temperature Rise at Laser Facet

Akihiro Shima, Yoshihiro Kokubo and Masao Aiga

Optoelectronic & Microwave Devices R&D Laboratory
Mitsubishi Electric Corporation
4-1, Mizuhara, Itami Hyogo, 664 Japan

1. Introduction

Recently, optical data processing systems have increasingly required higher-power and more reliable short wavelength laser diodes. However, the major problem in high-power and long-term operation of the AlGaAs lasers is the degradation of the active layer in the vicinity of the mirror facet. This degradation is considered to be caused by heat generation due to the optical absorption resulting from the surface recombination at the mirror surface. The facet temperature rise of loss-guided stripe lasers such as a channeled substrate planar (CSP) laser was investigated, using laser Raman spectroscopy [1,2]. It was confirmed that the optical absorption in the GaAs substrate outside the channel (stripe) region also increased the facet temperature [1,2], and the facet degradation began from the outside of the channel [1]. On the other hand, window diffusion stripe (WDS) laser [3] has a non-absorbing region near the mirror and hardly absorbs the optical flux in the outside of the stripe region. This laser proved to emit the maximum output power density of 16MW/cm² without the facet degradation, which was several times higher than that of the non-window, loss-guided stripe lasers as mentioned above.

This report describes the effect of the WDS structure on the reduction of the facet temperature rise. The facet temperature measured by an infrared (IR) radiometric microscope is compared with that of the loss-guided laser, and discussed in conjunction with the optical absorption near the facet.

2. Experiment and laser structures

An IR radiometric microscope detects the IR power generated by the temperature on a material surface. Figure 1 shows a schematic diagram of the system for the measurement of the temperature at the laser mirror. In this system the spatial resolution is 8μm while the resolution for the temperature is 0.5°C. The lasing output power and the IR power which are emitted from the laser mirror, are directly collected into the microscope while the objective lens is focused at the facet. The IR power whose wavelength is longer than 1.8μm, is selectively detected by an InSb detector through an optical filter. The laser is attached on an x-y scanning stage which is able to move at intervals of 2μm.

The T³ (thin-tapered thickness active layer) laser [4] is chosen as a loss-guided stripe laser. The structure near the mirror in the each laser is shown in Fig. 2. In the T³ laser, the optical flux is absorbed both in the GaAs layer outside the channel region and at the mirror facet. To reduce the absorption in the active layer at the mirror, the thickness of the active layer is thinned near the mirror. The cavity length of the T³ laser is 350μm. On the other hand, the WDS laser has the Zn diffused stripe region except the vicinity of the mirror. The bandgap energy of the Zn diffused stripe region is narrower than that of the non-diffused region. Therefore, the optical flux is not absorbed both outside the stripe and near the mirror. Moreover, the injected current is blocked near the window region. The cavity length is 400μm, including the 15μm window regions at the both facets.

The lasers are mounted in junction down configuration on a silicon submount which is bonded on a silver block. The front facet is coated with the Al₂O₃-SiO₂ films of the reflectivity resulting in 13%. The reflectivity of the

coated rear facet is higher than 90%. The facet temperature is measured under conditions of the various optical output power less than 50mW.

3. Results & Discussions

Temperature rise in the active region (ΔT) is given by the following equations:

$$\begin{aligned} T &= R_{th} \Delta P \\ P &= (V_{op} I_{op} - P_{out}), \end{aligned}$$

where R_{th} is the thermal resistance, ΔP is the difference between the electrical input power and the optical output power, V_{op} is the operating voltage, I_{op} is the operating current, and P_{out} is the optical output power.

Figure 3 shows the two-dimensional distribution of the facet temperature rise of the T³ laser and the WDS laser in the continuous wave (CW) operation of 30mW output power. The ΔP in the 30mW operation of the T³ laser and that of the WDS laser are 0.164W and 0.117W, respectively. The position of the peak temperature corresponds to the radiative spot (stripe) in the each laser. The peak temperature of T³ laser is higher by 19°C, than that of the WDS. A small difference of the background temperature rise at the facets of the both lasers is presumably due to the difference of the electrical input power. In the T³ laser, slight increase of temperature along the active layer is observed. This increase may be attributed to the influence of the injected carrier spreading over the active layer outside the stripe.

The dependence of the measured temperature rise on the ΔP is shown in Fig.4. The closed triangles show the facet temperature rise at the radiative spot. The closed circles show the temperature rise at a distance of 100μm from the radiative spot, which is marked by the open circle in Fig.3. The theoretical distribution of the temperature rise of the laser is calculated by a two-dimensional finite difference method. The mesh size is chosen to be 10μm for this method, taking the spatial resolution of the microscope into account. The calculated values correspond to the average temperature rise along the cavity. Therefore, the theoretical temperature distribution is considered to represent the distribution in the inner region of the laser. The solid lines show the theoretical values at the stripe and those at a distance of 100μm from the stripe. The theoretical R_{th} is 60°C/W which agrees well with the experimental R_{th} obtained by a ΔV_f method. The facet temperature rise at the radiative spot of the T³ laser drastically increases even before the lasing threshold. Compared to the inner temperature rise in the active region which is determined by the R_{th} , it should be noted that the facet temperature at the radiative spot is protrusively increased. On the contrary, the facet temperature rise at the radiative spot of the WDS laser is slightly lower than the inner temperature rise determined by the R_{th} even in high-power operation. The facet temperature rise at a distance of 100μm from the radiative spot agrees well with the theoretical temperature rise at 100μm position from the stripe. This proves that the facet temperature rise of the WDS laser is determined by the entire chip temperature, and the protrusive increase of the facet temperature rise at the stripe is suppressed.

In order to investigate the dependence of the local facet temperature rise at the radiative spot on the optical output power, it is necessary to eliminate the background temperature rise of the laser chip increased by the electrical input power from the facet temperature rise. We define the local facet temperature rise at the radiative spot as the difference between the peak temperature at the radiative spot and the facet temperature at a distance of 100μm from the radiative spot (T_{s-100}) since that at 100μm position nearly agrees with the background temperature of the laser chip, as shown in Fig.3. Figure 5 shows the dependence of the T_{s-100} on the optical output power. The T_{s-100} of the T³ laser increases up to 18°C as the optical output power is increased up to

30mW. On the contrary, that of the WDS laser is little increased in the range of the output power less than 50mW. This reduction of temperature rise of the WDS laser is considered due to the reduction of the optical absorption both near the mirror and outside the stripe. Moreover, the little increase of the temperature rise for various optical power proves that the optical beam of the laser has very little influence on the measurement of the temperature.

4. Summary

We have evaluated the facet temperature rise of the WDS laser as compared with that of T^3 laser, using the IR radiometric microscope. As a result, it was confirmed that the facet temperature rise at the radiative spot of the WDS laser is much lower than that of the conventional loss-guided stripe laser. Moreover, the local facet temperature rise at the radiative spot of the WDS laser is not protrusive even in high-power operation. Even at the very high optical power density of $16\text{MW}/\text{cm}^2$ reported previously [3], the WDS laser can be operated without the facet degradation as a result of the reduction of the facet temperature rise.

References

- [1] S.Todoroki, M.Sawai and K.Aiki: J.Appl.Phys., 58, pp.1124-1128, 1985.
- [2] H.Kawanishi, T.Morimoto, M.Yamaguchi, S.Kaneiwa, N.Miyauchi, T.Yoshida, H.Hayashi, S.Yano and T.Hijikata: Jpn.J.Appl.Phys., 27, pp.L1310-1312, 1988.
- [3] K.Isshiki, T.Kamizato, A.Takami, A.Shima, S.Karakida, H.Matsubara and W.Susaki: IEEE J.Quantum Electron. 26, pp.837-842, 1990.
- [4] A.Shima, T.Yamawaki, H.Saito, H.Matsubara, H.Kumabe and W.Susaki: Jpn.J.Appl.Phys., 28, pp.L105-107, 1989.

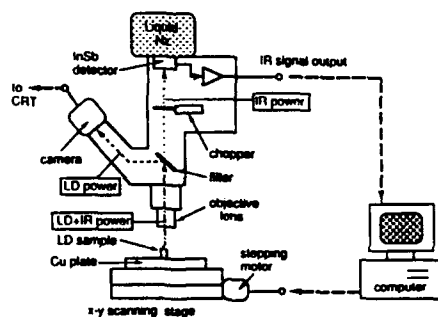


Fig.1
The schematic diagram of the system for the measurement of the temperature at the laser mirror.

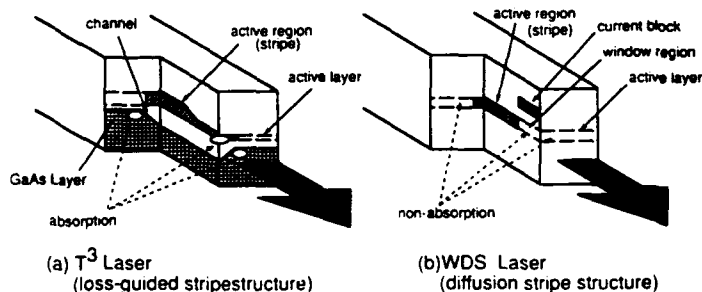


Fig.2 The structures near the mirror facet of the lasers.

- (a) T^3 laser: The optical flux is absorbed both in the GaAs layer outside the channel region and at the mirror facet.
- (b) WDS laser: The optical flux is neither absorbed outside the stripe nor at the mirror facet. The injected current is blocked near the mirror.

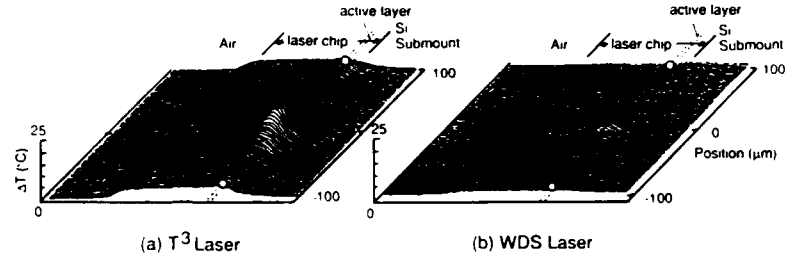


Fig.3 The two-dimensional distribution of the temperature rise at the mirror surface in the condition of 30mW optical output power. The open circle shows the position at a distance of 100μm from the radiative spot. The peak position corresponds to the radiative spot.
 (a) T³ laser: The peak temperature rise is 25 °C. The difference between the electrical input power and the optical output power (ΔP) is 0.164W.
 (b) WDS laser: The peak temperature rise is 6 °C. The ΔP is 0.117W.

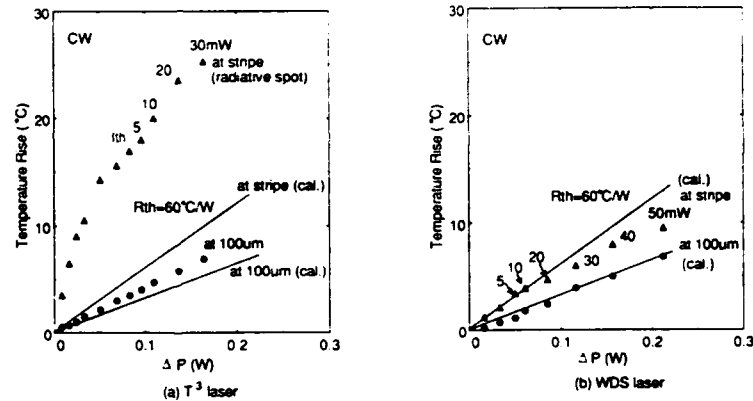


Fig.4 The dependence of the temperature rise of the T³ laser (a) and the WDS laser (b) on the ΔP . The triangles and the circles show the facet temperature rise at the radiative spot and that at a distance of 100μm from the radiative spot, respectively. The solid lines show theoretical average temperature rise along the cavity. The theoretical R_{th} agrees with the experiment R_{th} determined by the ΔV_f method.

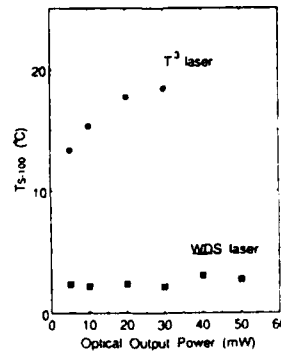


Fig.5 The dependence of the local facet temperature rise at the radiative spot on the optical output power.

DIFFERENTIAL GAIN AND DAMPING IN HIGH SPEED 1.55 μ QUANTUM WELL LASERS

M.C. Tatham, N.C. Fletcher, D.M. Cooper and L.D. Westbrook.
British Telecom Research Laboratories,
Martlesham Heath, Ipswich IP5 7RE
UNITED KINGDOM.

SUMMARY

The use of multiple quantum wells in the active region of semiconductor lasers has been predicted to give rise to large improvements in their intrinsic frequency response [1-3]. Such improvements arise from the increased differential gain possible in MQW lasers which has been shown theoretically to lead to an increase in the resonant frequency and to a reduction in the damping of the modulation response. A reduction in the damping is important insofar as this determines the maximum intrinsic bandwidth of the device, given no saturation of output power. There have, however, been few experimental reports of such improvements in MQW structures. In this paper we present experimental results on a large number of MQW lasers which, firstly, demonstrate the optimisation in the performance of high speed lasers and, secondly, show qualitative agreement with the theoretical predictions.

The devices measured were all multimode buried heterostructure lasers with wavelengths in the region of 1.55 μ . The active regions were composed of InGaAs quantum wells with 1.3Q InGaAsP barriers embedded between 1.3Q InGaAsP layers forming the separate confinement structure. The frequency response of the devices was determined by measuring the relative intensity noise (RIN) spectrum. The resonant frequency and damping values obtained from these parasitic-free measurements were found to be in good agreement with those obtained from direct small-signal modulation response measurements.

The resonant frequency, f_0 , of a laser increases linearly with the square-root of the facet power, P_f , with a constant of proportionality D . The parameter D usefully characterises the device performance. Figure 1 shows the variation of D as a function of the number of quantum wells in the active region for several different wafers, for devices of lengths 200-300 μ . Devices with large numbers of wells clearly give higher resonant frequencies for given output power.

Such a monotonic increase in D coefficient with numbers of wells would be expected simply through the increase in the total confinement factor for the active regions and the associated increase in internal losses. However the D coefficient depends also upon the square-root of the differential gain, dg/dn , and it is possible to obtain an estimate of dg/dn from the value of D , by taking into account its dependence upon the confinement factor, internal loss and active layer volume. Figure 2 shows the differential gain, estimated from the D coefficients of 1.55 μ MQW lasers (lengths

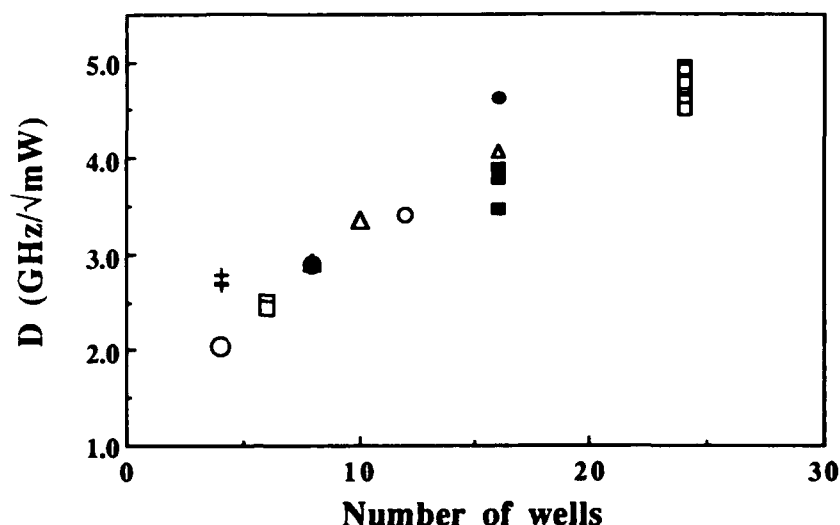


Fig.1 D coefficients for 1.55 μ multimode MQW lasers, lengths 200-300 μ , as a function of the number of wells in the active region, as determined from RIN measurements. The symbols indicate different wafers.

90 - 1000 μ) as a function of the number of wells. The figure shows a surprisingly large variation in dg/dn , with a substantial increase in the values for large numbers of wells. Such an effect is of considerable importance in determining the device performance. As the quantum wells for each wafer have similar parameters, it is probable that the increase in dg/dn results from a reduction in the threshold carrier density per well. When comparison is made with lasers with bulk active layers (1.3 μ and 1.55 μ) it is found that the values of dg/dn for large numbers of wells is substantially higher than the highest values from the bulk devices (typically $3 - 4 \times 10^{16} \text{cm}^{-2}$), though by a smaller factor than has been predicted theoretically [3].

The damping of the frequency response is found to be well described by the relation [4]:

$$\Gamma = K f_0^2 + \Gamma_0$$

with the limiting intrinsic 3dB bandwidth given by $(2\pi\sqrt{2}/K)$. Theories of spectral holeburning have predicted that the value of K is inversely proportional to the value of dg/dn , and hence should display a reduction in quantum well lasers [3,5,6]. There has been a remarkable uniformity in the values of K reported, typically 0.2 - 0.3ns, for a large range of different structures [4,7,8]; there has also been no evidence to substantiate the prediction of reduced damping in quantum wells. In Fig. 3 the K coefficients for the same devices as in Fig. 2 have been plotted against the estimated values of dg/dn . Despite the large scatter in the data, there is clearly a trend to lower values of K for increasing dg/dn , the damping parameter being up to twice as large for devices with low dg/dn . In fact the 2 well

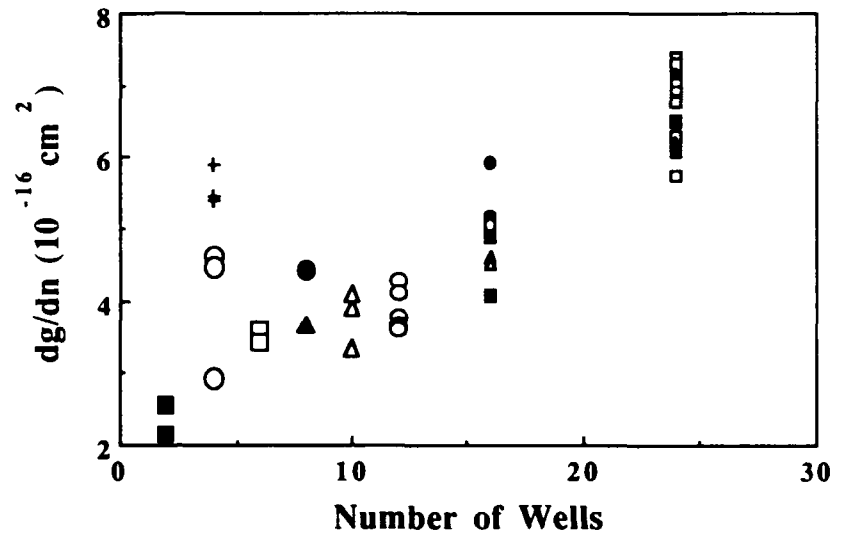


Fig.2 Differential gain dg/dn , estimated from D coefficients for 1.55μ multimode MQW lasers (lengths $90\text{-}1000\mu$). The symbols indicating different wafers correspond to those of Fig.1

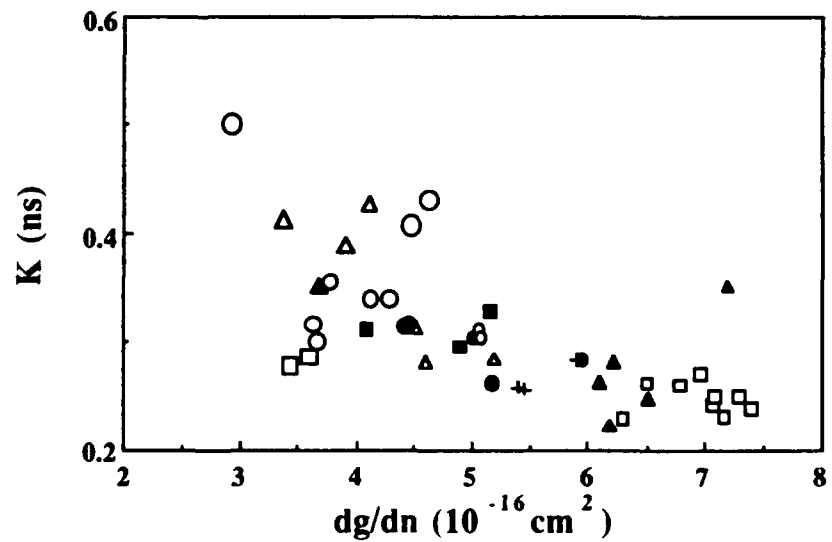


Fig.3 Damping parameter \bar{K} for the devices shown in Fig. 2, plotted as a function of the estimated differential gain.

devices with low dg/dn ($2.4 - 2.8 \times 10^{-16} \text{cm}^2$) show values of K as large as $1.2 - 1.4 \text{ns}$, omitted from Fig. 3 for clarity. It is important to note that despite the increase in differential gain for the devices with large numbers of wells, there is no measurable reduction in damping, compared with bulk devices.

In conclusion, it has been shown that considerable improvements in the frequency response characteristics of 1.55μ MQW lasers may be obtained by optimisation of the structure. Devices with larger numbers of wells show a substantially higher D coefficient than those with smaller numbers. This was shown to arise not only from the increase in confinement factor and the internal losses, but also from an increase in the differential gain, which, for large numbers of wells, was considerably higher than in bulk devices. A systematic trend in the damping was also observed, devices with higher differential gain displaying lower damping. These considerations have led to the fabrication of a MQW laser with a 3dB bandwidth of 18-19GHz at room temperature.

The authors would like to gratefully acknowledge the many people involved in the growth, overgrowth and fabrication of devices at BTRL, and Dr. P.W.A. McIlroy for invaluable assistance with the analysis.

REFERENCES

- [1] Y. Arakawa, K. Vahala and A. Yariv, *Appl. Phys. Lett.* **45**, 950, 1984.
- [2] Y. Arakawa and A. Yariv, *IEEE J. Quantum Electron.* **QE-21**, 1666, 1985.
- [3] K. Uomi and N. Chinone, *Jap. J. Appl. Phys.* **28**, L1424, 1989.
- [4] R. Olshansky, P. Hill, V. Lanzisera and W. Powazinik, *IEEE J. Quantum Electron.* **QE-23**, 1410, 1987.
- [5] M. Yamada, *IEEE J. Quantum Electron.* **QE-19**, 1365, 1983.
- [6] G.P. Agrawal, *IEEE J. Quantum Electron.* **QE-23**, 860, 1987.
- [7] R. Olshansky, P. Hill, V. Lanzisera and W. Powazinik, *Appl. Phys. Lett.* **50**, 653, 1987.
- [8] J. Eom, C.B. Su, J.S. LaCourse and R.B. Lauer, *IEEE Photonics Tech. Lett.* **2**, 692, 1990.

Fabrication of GaInAs(P)/InP Quantum-Wire Structures for Lasers and Electro-Optical Devices

Shigehisa ARAI⁺ & Yasuharu SUEMATSU

*+Department of Physical Electronics
Tokyo Institute of Technology
2-12-1 O-Okayama, Meguro-ku
Tokyo 152, Japan*

Realization of high performance optical devices based on lower dimensional electron systems in quantum-well structures essentially requires two key technologies, an ultra-fine lithography including an etching process and a growth of quality crystals on a patterned substrate, even though there are several methods reported[1]-[3] to obtain those devices.

We reported a lasing action of GaInAs/InP quantum-wire (10nm thick, 30nm wide) lasers at 77K fabricated by employing an EBX direct writing, a wet chemical etching, and an OMVPE regrowth[4]. However the threshold current was too high to operate at room temperature due to poor regrown interface.

In this paper we present effective methods to improve the regrown interface, introduction of a pre-heating process in pure H₂ atmosphere and a growth of an InP thin (~3nm) layer prior to the growth of a GaInAsP optical confinement layer. As the result, a room temperature operation of multiple quantum-well GaInAs/InP lasers with the active region width of ~100nm was obtained for the first time. By using a high vacuum ECR-RIBE and the OMVPE regrowth, an anisotropic property of field induced refractive index variation of a GaInAs/InP quantum-wire structure (~30nm wide) was measured.

Experiments and Results

Figure 1 shows the outline of the fabrication process used in these experiments. First a GaInAs/InP multiple quantum-film (MQF) wafer was grown on an n-InP substrate by a low pressure OMVPE. A thin (3nm) InP layer was grown on the top to protect the surface and the bandgap wavelength of barrier layers and optical confinement layers (OCLs) was 1.15-1.18 μ m. Then 20nm thick SiO₂ was deposited and a grating pattern (200-230nm pitch) along $\langle 011 \rangle$ direction was transferred by a conventional holographic lithography and a BHF etching so as to form an etching mask. After an etching of the MQF wafer, it was underwent a regrowth process by the OMVPE again.

Since we supposed that poor lasing characteristics of GaInAs/InP quantum-wire (QW) lasers[4] was attributed to remaining of water vapor during the regrowth and the growth of locally lattice mismatched GaInAsP on the patterned substrate, a pre-heating process at 200°C for 30minutes under pure H₂ atmosphere (76Torr) and a growth of enough thin (3nm) InP layer just before the growth of the GaInAsP OCL were introduced.

Figure 2 shows a cross sectional SEM view of thus fabricated 5-layered GaInAs/InP MQF laser. An etching of the active region was carried out by Br-methanol and a slight etching (3nm) was added to clean the surface just before loading it into the OMVPE reactor. The active region was completely separated and buried in GaInAsP OCLs with the width of 70nm on the top and 140nm in the bottom.

Figure 3 shows the cavity length dependence of the threshold current density at room temperature of 4 different groups of SiO₂ defined stripe lasers; (a)1-step grown MQF lasers, (b)2-step grown MQF lasers, (c)2-step grown wire-like MQF lasers with a thin InP cover layer (as same as shown in Fig.3), and (d)2-step grown wire-like MQF lasers directly buried with a GaInAsP OCL. Even though there still remains little difference between (a) and (b) groups, the threshold current of group (b) samples was drastically reduced by introducing the pre-heating and the growth of the InP cover layer. As can be seen from groups (c) and (d), this improvement was much clearly observed in samples with wire-like active region.

By applying above mentioned OMVPE regrowth process to quantum-wire structures, we used a high-vacuum ECR-RIBE dry etching system with Cl₂ gas. As the result, an anisotropic property of field induced refractive index variation as well as a large index variation was obtained in GaInAs/InP 3-layered quantum-wire structure.

Figure 4 shows a schematic structure and a cross sectional SEM view of a GaInAs/InP 3-layered quantum-wire structure with the width of 25~35nm. The etching was done at the substrate temperature of 350°C with the extraction voltage of 20V so as to reduce damage induced by ion bombardment. Cl₂ gas flow rate was controlled so as to maintain the pressure of 10⁻⁵Torr. InP was used for both the barrier layer (4nm) and the OCLs (40nm each).

Figure 5 shows the PL spectra of MQF and quantum wire structures both fabricated from the same wafer. The PL peak wavelength shift of 20nm was observed in the quantum-wire structure and the PL intensity normalized by the volume of GaInAs region was almost 70% of original MQF structure.

Figure 6 shows the field induced refractive index variation spectrum for 2 different incident light conditions, (a)TE-polarized light across the quantum-wire and (b)along the quantum-wire. The maximum refractive index variation of around 4% (across) and 2% (along) was observed at 1.52μm wavelength whereas that for the wavelength shorter than 1.48μm could not be measured due to large absorption. This anisotropic and

large index variation property can be attributed to the quantum confined Stark effect in quantum-wire structures.

Conclusion

A room temperature operation of GaInAs/InP multiple quantum-film lasers with the active region width of $\sim 100\text{nm}$ was achieved by introducing a pre-heating process under H_2 atmosphere and a thin InP cover layer growth into the OMVPE regrowth.

Anisotropic field induced refractive index variation property with a large value of around 4 percent was observed in a GaInAs/InP quantum-wire structure.

Acknowledgment

The authors thank to Profs. K.Iga, K.Furuya, and Assoc. Prof. M.Asada for fruitful discussions, and Drs. Y.Miyamoto, K.G.Ravikumar, Mr. Y.Miyake, and Mr. H.Hirayama for their experimental works. They also acknowledge the Ministry of Education, Science & Culture, Japan, for continuous support to this research.

References

- [1] Y.Miyamoto et al.: Jpn. J. Appl. Phys., 26, 4, p.L225 (1987)
- [2] E.Kapon et al: Appl. Phys. Lett., 55, 26, p.2715 (1989)
- [3] M.Tsuchiya et al.: IEEE Trans., ED-36, 11, p.2612 (1989)
- [4] M.Cao et al.: Trans. IEICE-J, E73, 1, p.63 (1990)

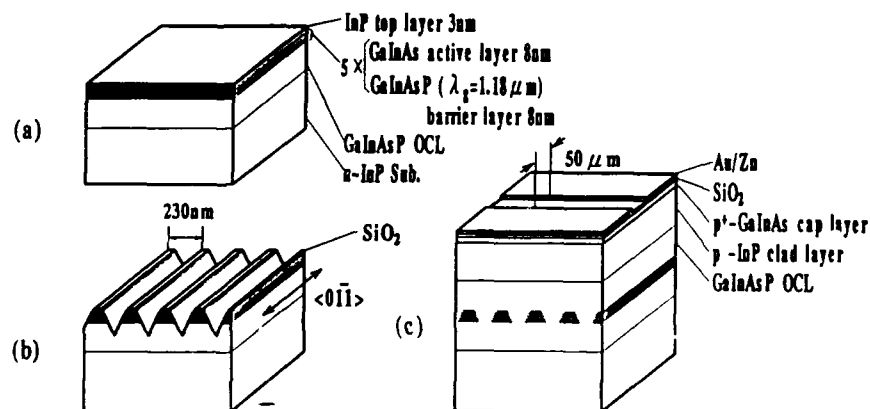


Fig.1 Fabrication process of GaInAs/GaInAsP/InP SCH-MQF laser with wire-like active region.

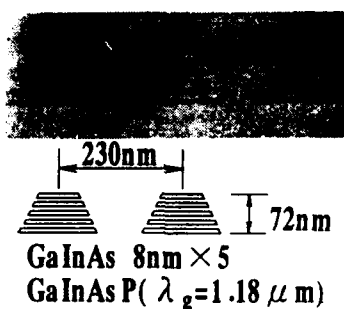


Fig.2 SEM cross-sectional view of GaInAs/GaInAsP/InP SCH-MQF laser with wire-like active region.

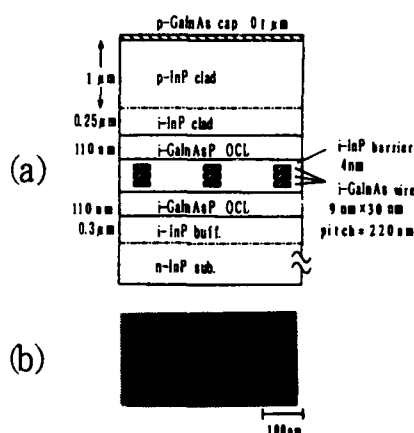


Fig.4 (a) Schematic diagram of the multi-layered quantum wire structure, and (b) its SEM view.

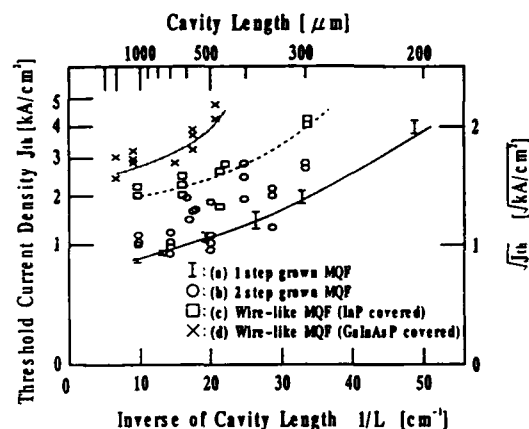


Fig.3 Threshold current densities of 4 different groups of lasers as a function of inverse of the cavity length.

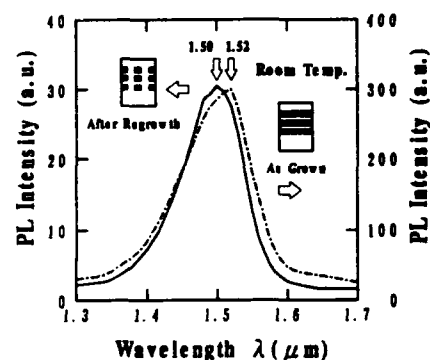


Fig.5 PL spectra from as-grown and multi-layered quantum wire structure.

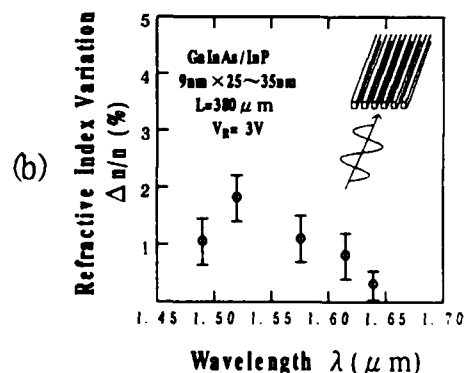
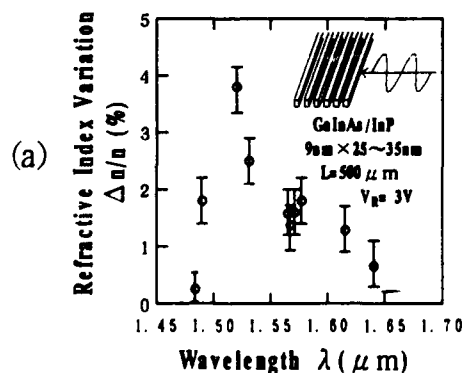


Fig.6 Field induced refractive index variation spectrum.

(a) With light propagated across quantum wires,
(b) With light propagated along quantum wires.

**Polarization Controlled Semiconductor Photonic Devices
by Strained-Barrier Superlattice Structures**

M.Okamoto, K. Magari and Y. Itaya*

NTT Opto-electronics Laboratories

3-1 Morinosato Wakamiya

Atsugi, Kanagawa Pref. 243-01, Japan

1. Introduction

Strained layer superlattice (SLS) structures offer excellent versatility for tailoring different energy-band structures^{1),2)}. For example, the difference between TE and TM modes can be readily controlled by selecting layer lattice parameters to produce tensile strain in the structures³⁾. This approach can be exploited to fabricate polarization-insensitive amplifier with high gain.

2. Band-structure Engineering

Valence-band degeneration in the $\text{Ga}_x\text{In}_{1-x}\text{As}_y\text{P}_{1-y}$ system can be solved by inducing biaxial stress. Under tensile strain, the energy level of the light-hole band becomes less than that of heavy holes⁴⁾. Recombination between the conduction band and the light hole band then becomes dominant so that the TM-mode emission is enhanced⁵⁾.

To control the mode gain difference, a tensile strained layer superlattice (SLS) of $\text{Ga}_{0.47}\text{In}_{0.53}\text{As}/\text{Ga}_x\text{In}_{1-x}\text{As}$ ($x > 0.47$) has been proposed⁶⁾. The band structure was calculated using the

method proposed by Asai and Oe for a GaInP/GaAs system⁷⁾. A schematic band diagram to emerge from the calculation is shown in Fig. 1. As apparent from the figure, the light hole band has a slightly lower energy in the strained barrier layers than the valence band edge in the lattice matched well layers. TM mode DFB lasers that exploit the tensile SLS structure³⁾ have already been reported.

3. Crystal Growth and Device Structure

The structure for this study was epitaxially grown by low-pressure MOVPE on n-type (100) InP substrates in a vertical reactor. The pressure in the reactor was controlled at 50 Torr, and reactant gas sources were TMIn, TEGa, AsH₃, and PH₃. N- and p-type dopants were supplied in the form of H₂Se and DEZn, respectively. The resulting band diagram structure is shown in Fig. 2. The active region is composed of 50-Å-thick Ga_{0.47}In_{0.53}As well layers and 50-Å-thick Ga_{0.72}In_{0.28}As strained-barrier layers. The lattice mismatch value ϵ of the barrier was -0.017. A 1.5- μ m-wide stripe region was buried with p-InP, and n-InP current blocking layers were fabricated by LPE⁸⁾. A window structure 30 μ m in length was fabricated on both sides with TiO₂/SiO₂ films for anti-reflection. Residual reflectivity was about 0.007%. The total length of the device was 660 μ m. A cross-sectional view of the traveling wave type amplifier (TWA) incorporating the device is shown in Fig. 3.

4. Results and Discussion

A signal light of 1.56 μ m wavelength from an external

grating cavity laser was coupled into the tensile SLS TWA by a GRIN rod lens. Polarization of the input power could be alternated between TE and TM modes by a $\lambda/2$ plate and a polarizer. The measured signal gain characteristics are shown in Fig. 4. The fiber-to-TWA coupling loss was on the order of 7 dB/facet. More than 10-dB fiber-to-fiber gain was obtained at 1.56 μm where the gain difference between TE and TM mode was kept to less than 0.5 dB.

Acknowledgements

The authors would like to thank Y. Noguchi for the LPE-grown crystal. They also acknowledge O. Mikami, Y. Imamura, M. Naganuma, K. Kurumada, H. Tsuchiya and T. Ikegami for their valuable observations and continuous encouragement.

References

- 1) E. Yablonovitch and E.O. Kane, "Band Structure Engineering of Semiconductor Lasers for Optical Communications," J. Lightwave Technol., vol.6, pp.1292-1299, 1988.
- 2) A.R. Adams, "Band-structure Engineering for Low-Threshold High-Efficiency Semiconductor lasers," Electron. Lett., vol.22, pp.249-250, 1986.
- 3) M. Okamoto, K. Sato, H. Mawatari, F. Kano, K. Magari, Y. Kondo and Y. Itaya, "TM-Mode Gain Enhancement in GaInAs/InP Lasers with Tensile Strained-Layer Superlattice," to be published in IEEE J. Quantum Electron. 1991.
- 4) for review, E.P. O'Reilly, "Valence band engineering in strained-layer structure," Semicond. Sci. Technol., vol.4, pp.121-137, 1989.
- 5) T. C. Chong and C.G. Fonstad, "Theoretical Gain of Strained-Layer Semiconductor Lasers in the Large Strain Regime", IEEE J. Quantum Electron. vol.QE-25, pp.171-178, 1989.
- 6) K. Magari, M. Okamoto, H. Yasaka, K. Sato, Y. Noguchi and O. Mikami, "Polarization Insensitive Traveling Wave Type Amplifier Using Strained Multiple Quantum Well Structure," IEEE Photon. Technol. Lett., vol.2, pp.556-558, 1990.
- 7) H. Asai and K. Oe, "Energy band-gap shift with elastic strain in $\text{Ga}_x\text{In}_{1-x}\text{P}$ epitaxial layers on (001) GaAs substrates," J. Appl. Phys., vol.54, pp.2052-2056, 1983.
- 8) K. Magari, S. Kondo, H. Yasaka, Y. Noguchi, T. Kataoka and O. Mikami, "A High Gain GRIN-SCH MQW Optical Semiconductor Laser Amplifier," IEEE Photon. Technol. Lett., vol.2, pp.792-793, 1990.

*present address: NTT Opto-electronics Labs. Tokai-mura, Nakagun, Ibaraki Pref. 319-11 Japan.

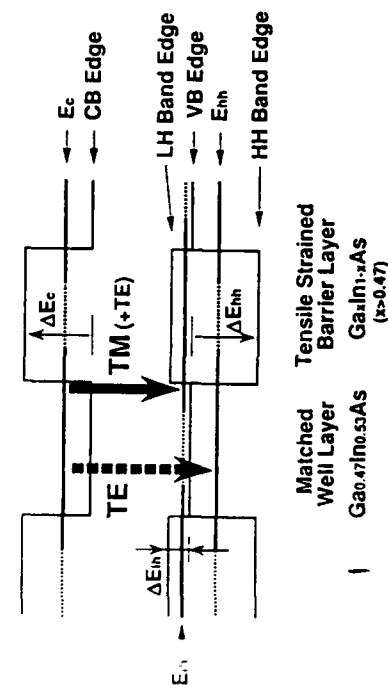


Fig.1. Band Diagram of the Tensile SLS.

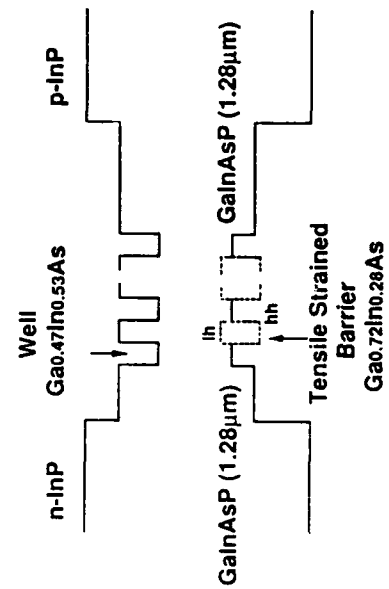


Fig.2. Band Diagram of the Tensile SLS TWA.

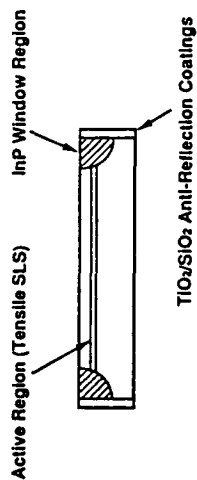


Fig.3. Structure of Traveling Wave type Amplifier (TWA)

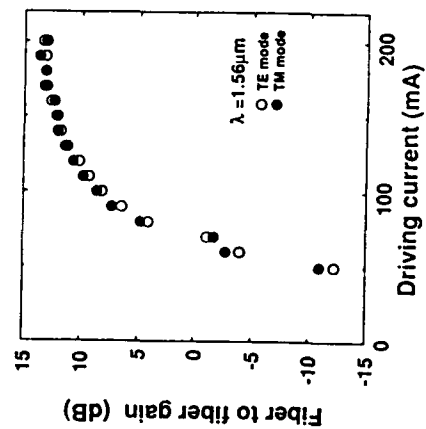


Fig.4. Fiber-to-Fiber Gain vs Driving Current of the Tensile SLS TWA.

Fabrication and Characteristics of Tunable Twin-Guide DFB Lasers by All MOVPE

Madoka Hamada, Elji Yamamoto, Kazuya Suda, Seiji Nogiwa, and Tokukoh Oki

Optical Measurement Technology Development Co., Ltd.
2-11-13, Naka-cho, Musashino-shi, Tokyo, 180 Japan

1. Introduction

Wavelength tunable lasers are expected to be used as the key devices for coherent optical transmission systems. Continuous tuning range of 7nm has been reported in tunable twin-guide (TTG) laser¹⁾ and we have reported 2.6nm continuous tuning range in TTG laser fabricated by all MOVPE²⁾. Here, we report on the tuning characteristics of the TTG-DFB lasers fabricated by an improved process. The TTG-DFB lasers were fixed by 9-fold MOVPE. The threshold current was 16mA, and the continuous tuning range exceeded 5.3nm.

2. Device Structure and Fabrication

The structure of the TTG-DFB laser is shown in Fig. 1. This structure has pnp heterojunctions in the vertical direction. The MQW active layer and the modulation layer were placed at the lower and upper pn junctions, respectively. The current blocking layer was used as the constriction window of the active layer injection current. The upper cladding layer mesa width of the improved TTG was wider than that of previous TTG²⁾. When the resistance along the current injection pass decreases, the injection current efficiency of the modulation increases in the improved devices. Two types of lasers, that is broad (10μm) cladding layer mesa (type W) and narrow (1.5μm) (type N) were fabricated and compared.

The fabrication process was as follows. All epitaxial growths were carried out by MOVPE. Initially, a p-InP buffer layer (1.5μm) was grown on a p-InP substrate. Then, mesa stripe was formed by a patterned SiO₂ mask and then buried with the current blocking layer (n-InP) by selective epitaxial growth. Next, the second p-InP buffer layer (1μm), 1.3μm-InGaAsP confining layer

(80nm), InGaAs/1.3 μm -InGaAsP MQW active layer (six wells), 1.3 μm -InGaAsP confining layer (50nm), n-InP separation layer (200nm), 1.4 μm -InGaAsP modulation layer (290nm), p-InP separation layer (100nm) and 1.3 μm -InGaAsP guiding layer (40nm) were grown successively. Next, the grating on the guiding layer was formed by EB lithography³⁾ and wet etching. After growing the p-InP layer (200nm), the lower mesa stripe was formed to maintain a single transversal mode and buried by n-InP layer. After the p-InP cladding layer (1 μm) was grown, the broad cladding layer mesa stripe was formed and buried by n-InP layer. The n⁺-InGaAs and p⁺-InGaAs contact layer were formed by similar selective epitaxial growth. Finally, Au/Cr for p-contact and AuGeNi for n-contact were patterned by the lift-off method.

3. Experimental Results

The 525 μm long TTG-DFB laser with cleaved facets is characterized as follows. The threshold current was 16mA, the lasing center wavelength was approximately 1.55 μm and the maximum output power was 5mW per facet. The near-field pattern (NFP) and the far-field pattern (FFP) are shown in Fig. 2. Both horizontal and vertical mode are fundamental. The spectral linewidths without modulation as measured by the delayed self-heterodyne method are as shown in Fig. 3. The minimum spectral linewidth was 8.5MHz at the output power of 3.3mW. The spectra variation versus the modulation current at constant laser driving current are as shown in Fig. 4. The main mode wavelength shifts continuously by 4.9nm, and the wavelength shifts as a function of the modulation current are as shown in Fig. 5. The continuous wavelength shift of type W was 5.3nm, and was larger than that of type N. These results show that the modulation efficiency of type W is superior to that of type N. Figure 6 shows the output power as a function of the wavelength shift at a constant laser driving current of 60mA. A 4.3nm tuning range was recorded with the side mode suppression ratio (SMSR) exceeding 20dB.

4. Conclusions

1.5 μm range TTG-DFB lasers were fabricated using 9-fold MOVPE growth. Threshold current was 16mA, and a continuous tuning performance of 5.3nm/40mA was obtained using the improved process.

Acknowledgements

The authors wish to thank Dr. M. Morimura and Dr. H. Iwaoka for their continuous encouragement.

References;

- 1) S. Illek, W. Thulke, C. Schanen, H. Lang and M. C. Amann : Electron. Lett. 26(1990) 46.
- 2) E. Yamamoto, M. Hamada, S. Nakajima, S. Nogiwa, K. Suda and T. Oki : Jpn. J. Appl. Phys. 29(1990)L2063.
- 3) M. Suehiro, W. Narazaki, S. Iio, M. Hamada and H. Hosomatsu : APCT '89 P-21 179.

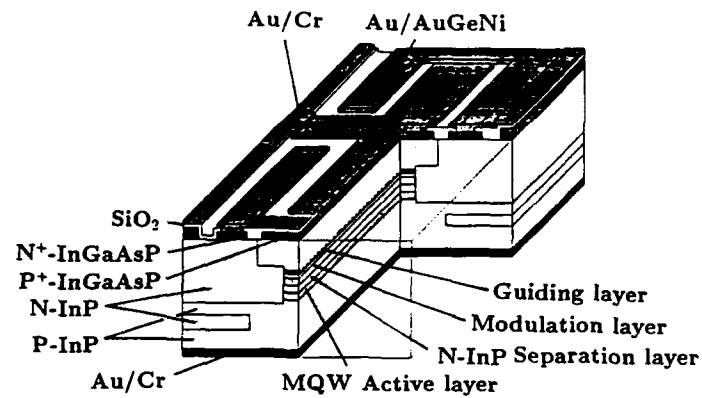


Fig. 1 Schematic structure of a TTG-DFB laser.

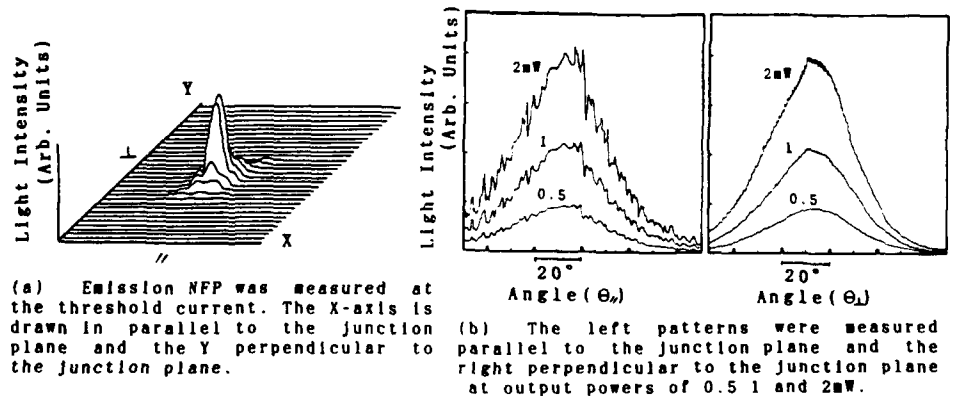


Fig. 2 Observed NFP(a) and FFP(b) of a TTG-DFB laser.

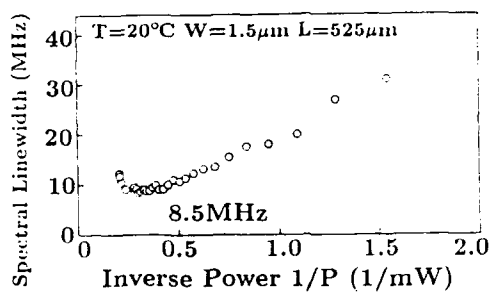


Fig. 3 Spectral linewidths versus inverse output power.

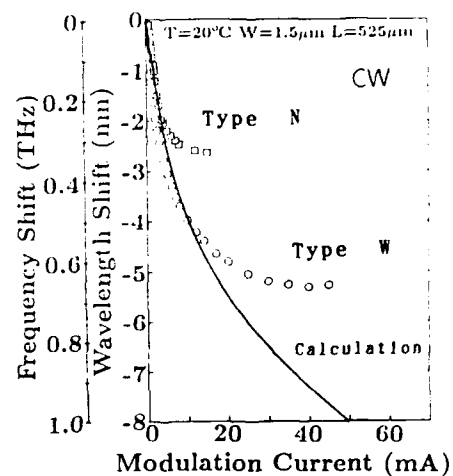


Fig. 5 Wavelength shifts versus modulation current.

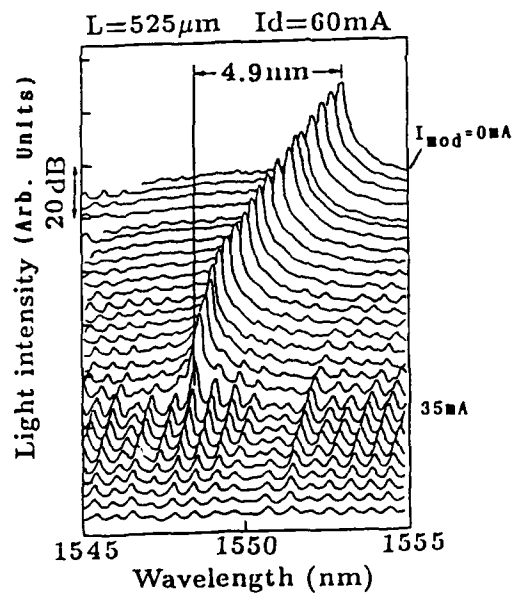


Fig. 4 Emission spectra at various modulation currents (I_{mod}) with driving current, held constant at 60mA.

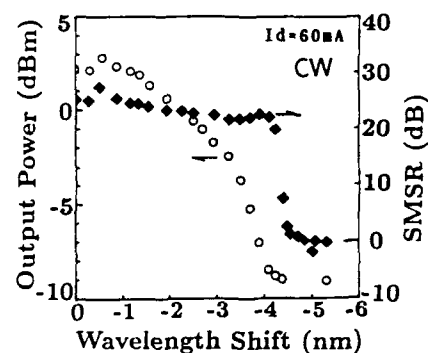


Fig. 6 Output power and SMSR versus wavelength shift.

Buried Interconnect Structure for Symmetric SEEDs

L. A. D'Asaro, L. M. F. Chirovsky, R. F. Kopf, and S. J. Pearton

AT&T Bell Laboratories
Murray Hill, New Jersey 07974**Introduction**

The mesa structure previously published¹ for S-SEED arrays has a number of disadvantages for future integration with electronic circuits on the same chip. These problems arise from the large ($\approx 1 \mu\text{m}$) height of the mesas: (1) the angle on the sides of the mesas takes up valuable real estate, (2) the metallization of the mesa sidewall for interconnect can introduce a yield problem because of difficulty in covering, (3) the etching of the sidewall is a critical step which requires accurate control to expose the buried N-layer for contacting, (4) the lithography resolution is degraded by the large topography, and (5) the mesa sidewall presents a surface where minority carriers recombine and thereby reduce the photocurrent collection efficiency.

We have developed a nearly planar structure which overcomes these problems. The new structure is made by ion implantation for isolating and contacting the active regions. Figure 1 shows the structure, which we call "buried interconnect" because the connection between the two SEED diodes in series to make an S-SEED is made through a buried layer of P-type AlGaAs. Contact to the buried P-layer is made by a P-type implant. The layers in this structure form an NIP diode, in contrast with the previously published PIN SEED diode.

Fabrication

The process steps to produce the buried interconnect structure are: MBE growth, etch, Be implant and anneal, proton isolation implant and anneal, ohmic metallization and anneal, interconnect insulation and metallization, and anti-reflection coating. Some details of these steps are as follows.

The MBE growth is similar to the growth for the previously described mesa design,¹ with the exception that the top contact layer of heavily doped $\text{Al}_{.11}\text{Ga}_{.89}\text{As}$ is N-type, while the bottom contact layer of heavily doped $\text{Al}_{.11}\text{Ga}_{.89}\text{As}$ is P-type. The layers, from the substrate up, are: the reflector stack made of undoped AlAs and $\text{Al}_{.30}\text{Ga}_{.70}\text{As}$, the heavily doped P-type layer, the undoped multi-quantum-well structure (typically 60 pairs of alternating GaAs 100 Å thick and $\text{Al}_{.30}\text{Ga}_{.70}\text{As}$ 60 Å thick), followed by the heavily doped top N-type layer.

The photolithographically defined chemical etch isolates the top N-type regions for each active SEED structure. This etch depth is only a few thousand Å, needed to remove the 3000 Å thick top N-layer of $\text{Al}_{.11}\text{Ga}_{.89}\text{As}$ between the active regions.

The Be implant to contact the buried P-layer is masked with photoresist. Several implant energies are used to assure a conducting path from the surface to the buried P-layer.² The Be is annealed by rapid thermal annealing.³ This P-implant process replaces the previously used critical etch.

The isolation between SEED active regions is completed by proton isolation implant,⁴ again masked by photoresist. Several implant energies are used to compensate the acceptors in the

buried P-layer by introducing traps. The implant is followed by a rapid thermal anneal to optimize the isolation.³

Ohmic contacts to the P and N-regions are similar to those previously described.¹ A photolithographically defined final metal interconnect is deposited over an insulating film in order to connect the SEEDs in series and to bring in the bias potentials from bonding pads.

Testing

Despite the advantages of a nearly planar structure, the buried interconnect would be preferred only if it had equivalent or better performance than the mesa structure. Figure 2 shows a comparison of the responsivity versus voltage and reflectivity versus voltage curves for two SEED diodes, of identical size, made with identical MQW and contact regions. The difference is that one is a buried interconnect NIP diode, while the other is a PIN mesa diode. The data was taken with 3 μm diameter beams delivering 100 μW of power at the exciton absorption wavelength. The buried interconnect diode shows deeper modulation of the reflectivity and, most importantly, a larger responsivity than the mesa diode in the range from 1 volt forward bias to 3 volts reverse bias. The buried interconnect also shows deeper modulation of the responsivity in the preferred range of operation, which is 0 to 6 volts of reverse bias.

Conclusions

The test results show that S-SEEDs fabricated by the buried interconnect method would be expected to have better performance due to lower bistability thresholds and higher contrast than mesa diode S-SEEDs. The results also show that the photocurrent is collected more efficiently by the buried interconnect structure. These results are consistent with a model in which the boundaries of the active region, formed by ion implantation, have a lower density of hole-electron recombination sites than the sidewall surface of a mesa diode.⁵ In addition to the good operating characteristics, the nearly planar surface avoids the fabrication problems which would interfere with the integration of S-SEEDs with FETs or other devices to form electronic circuits on the same chip. This integration is very desirable for improving systems applications of SEEDs.

References

1. L. M. F. Chirovsky, L. A. D'Asaro, C. W. Tu, A. L. Lentine, G. D. Boyd, and D. A. B. Miller "Batch-Fabricated Symmetric Self-Electro-Optic Effect Devices" in *OSA Proceedings on Photonic Switching*, J. E. Midwinter and H. S. Hinton, eds. (Optical Society of America, Washington, D. C., 1989), 3, 2.
2. R. Anhold, P. Balasingam, S. Y. Chou, T. W. Sigmon, and M. Deal "Ion Implantation into Gallium Arsenide", *J. Applied Physics* 64, 3429 (1988).
3. J. S. Williams and S. J. Pearton in *Energy Beam-Solid Interactions and Transient Thermal Processing*, Materials Research Society Symposium 35, 427 (1985).
4. S. J. Pearton, "Ion Implantation for Isolation of III-V Semiconductors" *Materials Science Reports* 4, 315 (1990).
5. V. Swaminathan, J. M. Freund, L. M. F. Chirovsky, T. D. Harris, N. A. Kuebler, and L. A. D'Asaro, "Evidence for Surface Recombination at Mesa Sidewalls of Self-Electro-Optic Effect Devices" *J. Applied Physics* 68, 4116 (1990).

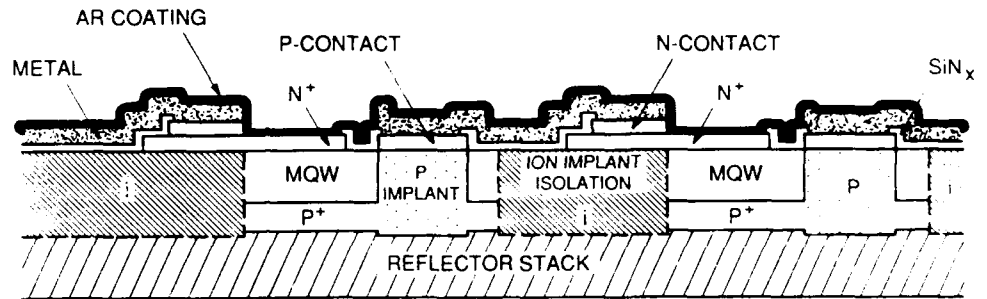


Fig. 1. Schematic cross section of a buried interconnect reflective S-SEED.

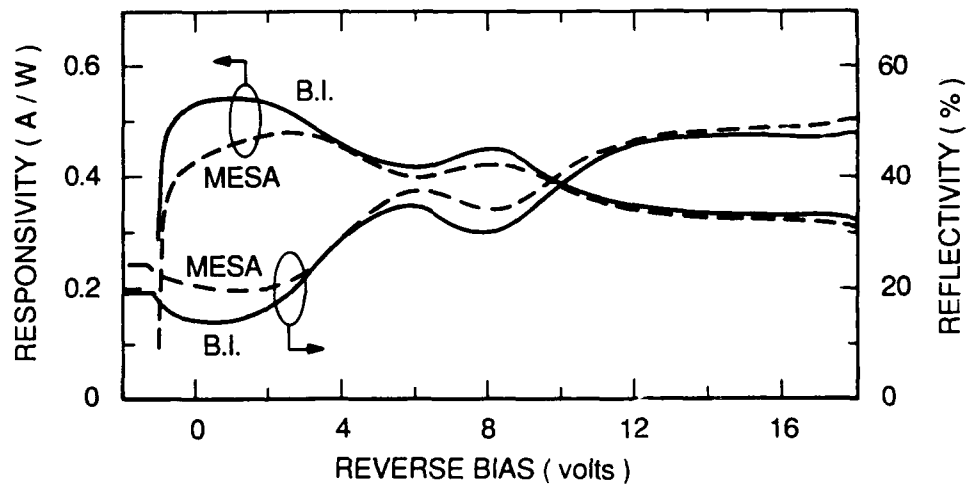


Fig. 2. Responsivity and reflectivity versus voltage for a buried interconnect SEED (solid curve) and a mesa SEED (dashed curve).

Tailoring of Electron and Hole Energies in Strained GaAsP/AlGaAs Quantum Wells using Fluorine Impurity Induced Layer Disordering

Utpal Das, Steve Davis, Jia-T. Hsu, and Ramu V. Ramaswamy
University of Florida, Electrical Engineering Department, Gainesville, Florida 32611

Fred A. Stevie
AT&T Bell Laboratories, Allentown, Pennsylvania 18103

Electroabsorption in GaAs/AlGaAs quantum well (QW) waveguides is known to be strongly polarization dependent [1]. Electro-optic effects for the polarization perpendicular to the layer (which shows a strong light-hole (LH) exciton peak) is negligible for the (100) grown QWs. For polarization parallel to the layers the oscillator strengths of the excitons are smaller due to the presence of both the LH and the heavy-hole (HH) exciton transitions. This necessitates a modification of the quantum wells so that stronger oscillator strengths can be obtained for polarization parallel to the layers. This can be accomplished by introducing a small amount of biaxial tensile strain in coherently grown QWs [2]. The influence of biaxial tensile strain in tailoring the hole energies in GaAs [3] and GaAsP [4] QWs has been reported. When a strained GaAsP is used in a quantum well, due to size quantization, the valence bands move down. This movement is in the same direction incurred by the HH but opposite to that incurred by the LH, due to shear strain. Thus for selected values of the strain and well size, it is possible to restore the degeneracy of the two valence bands at the Brillouin Zone center as shown in Fig. 1. It is possible to split the degeneracy for a small applied electric field and reduce the absorption by half. The effects of modulating the degeneracy of the LH and HH transitions on the electro-optic coefficients in this strained material is promising because of larger changes in the absorption coefficient with the applied electric field. A practical approach to move the device from the electroabsorption to the electro-optic regime at a fixed operating wavelength is to tailor the bandgap itself, as would be required in optoelectronic integration. A method of achieving this with minimum processing steps is to use impurity induced layer disordering (IILD) in the QWs [5]. Interdiffusion of the constituent species of the quantum well and the barrier materials in a QW structure reduces the well width. This in turn modifies the quantized energies in the well and moves the bandgap to higher energies. Fluorine (F) implantation was used to enhance interdiffusion of GaAs/AlGaAs quantum wells [6, 7]. F is a neutral impurity in III-V semiconductors, therefore waveguide losses (arising from free carrier scattering) are expected to be much lower than with the use of Si or Zn IILD.

In this work, we present a study of the optical properties of interdiffused $\text{GaAs}_{0.91}\text{P}_{0.09}/\text{Al}_{0.3}\text{Ga}_{0.7}\text{As}$ single QWs, induced by F implantation. A schematic structure of the single QWs is shown in Fig. 2. The layers have been grown by atmospheric pressure MOCVD at 750°C . The unintentional background doping is measured to be $\sim 5 \times 10^{15}\text{ cm}^{-3}$. F has been implanted at 200 keV with a dose of 10^{14} cm^{-2} in the QW structures. Sealed tube annealing under Arsenic overpressure of implanted and as-grown layers has been used for comparison purposes. Annealing temperature was 750°C and the annealing time was between 15 minutes to 2 hours. Photoluminescence (PL) measurements at 13K were used to determine the band energies for the control and the implanted and annealed layers. An Argon-ion laser ($\lambda=5145\text{ \AA}$) was used for the PL measurements. Fig. 3 shows a

typical PL plot for a 15 minute annealing time. The peaks are dominated by the LH and HH transitions. After annealing, however, the peaks for the 80 Å well which are aligned before annealing loses its degeneracy but for the 110 Å well the degeneracy is almost restored. For higher annealing times (up to 2 hours) the PL measurements only show single peaks for each well. The peak energies are also found not to increase monotonically with increasing annealing time. The change in the band energies is therefore due to the interdiffusion of both the Group III as well as the Group V species. SIMS measurements were performed on both implanted+annealed and as-grown+annealed layers. They indicate, that unlike InGaAsP/InP heterostructures there is a strong interdiffusion of As and P, as shown in Fig. 4. It is also evident from the SIMS results that a depletion of As at the surface is associated with an out diffusion of P. However the decrease of Al concentration and increase of Ga concentration at the surface contradicts the plausible explanation that one is tempted to make, namely, that the layers were annealed at low As overpressure. The explanation may well be associated with defects generated by F implantation. SIMS measurements of the F concentration shown in Fig. 5 clearly indicate that with only a 15 minute anneal there is an increase of F concentration, by an order of magnitude, close to the surface. Study of the interdiffusion in the GaAsP/AlGaAs QWs for various F implant energies is in progress to explain the dependence of the interdiffusion on the impurity profile.

In conclusion we have shown for the first time, that Fluorine induced IILD can be used to restore or remove the LH-HH degeneracy in a strained GaAsP/AlGaAs QW. This is particularly useful for integrated opto-electronics where bandgap tailoring is required across the wafer. Restoring the degeneracy of LH and HH in a QW is important for potential applications in efficient electro-optic integrated devices.

1. "Strong polarization-sensitive electroabsorption in GaAs/AlGaAs quantum well waveguides" J.S. Weiner, D.A.B. Miller, D.S. Chemla, T.C. Damen, C.A. Burrus, T.H. Wood, A.C. Gossard, and W. Wiegmann, Appl. Phys. Lett. 47, 1148 (1985).
2. "Theoretical Studies of polarization dependent electro-optical modulation in lattice matched and strained multi-quantum well structures", S. Hong and J. Singh, Superlattices and microstructures 3, 645 (1987).
3. "Enhancement of excitonic absorption due to overlap in heavy-hole and light-hole excitons in GaAs/InAlGaAs quantum well structures", G.P. Kothiyal, S. Hong, N. Debbar, P.I. Bhattacharya and J. Singh, Appl. Phys. Lett. 51, 1091 (1987).
4. "Tailoring of hole eigenenergies in strained GaAsP/AlGaAs single quantum wells by atmospheric pressure Organometallic chemical vapor deposition", D.C. Bertolet, J.K. Hsu, and K.M. Lam, Appl. Phys. Lett. 53, 1501 (1988).
5. "Monolithic Waveguide Coupled Cavity Lasers and Modulators Fabricated by Impurity Induced Disorder", R. L. Thornton, W. J. Mosby, and T. L. Paoli, IEEE J Lightwave Technol. 6, 786 (1988).
6. "MQW optical waveguides with large absorption edge blue shift produced by Boron and Fluorine impurity-induced disordering", M. O'Neill, A. C. Bryce, J.M. Marsh, R.M. DeLaRue, J.S. Roberts and C. Jeynes, Appl. Phys. Lett. 55, 1373 (1989).
7. "Ion-species dependence of interdiffusion in ion-implanted GaAs-AlAs superlattices", Y. Hirayama, Y. Suzuki, and H. Okamoto, Jap. J. Appl. Phys. 24, 1489 (1985).

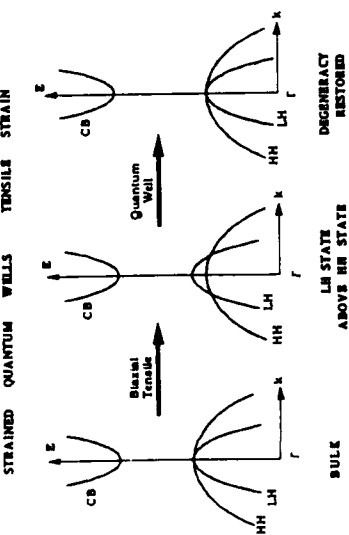


Figure 1.: Schematics of the conduction and the valence bands of a III-V semiconductor at the Brillouin Zone center for tensile stress in a quantum well

| | | |
|---------|-------------------|---|
| Undoped | 0.1 μm | $\text{Al}_{0.3}\text{Ga}_{0.7}\text{As}$ |
| Undoped | 80 \AA | $\text{GaAs}_{0.91}\text{P}_{0.09}$ |
| Undoped | 0.1 μm | $\text{Al}_{0.3}\text{Ga}_{0.7}\text{As}$ |
| Undoped | 110 \AA | $\text{GaAs}_{0.91}\text{P}_{0.09}$ |
| Undoped | 0.1 μm | $\text{Al}_{0.3}\text{Ga}_{0.7}\text{As}$ |
| Undoped | 140 \AA | $\text{GaAs}_{0.91}\text{P}_{0.09}$ |
| Undoped | 0.1 μm | $\text{Al}_{0.3}\text{Ga}_{0.7}\text{As}$ |

Undoped GaAs substrate

Figure 2.: Schematic structure of the quantum well layers used for F implantation and anneal.

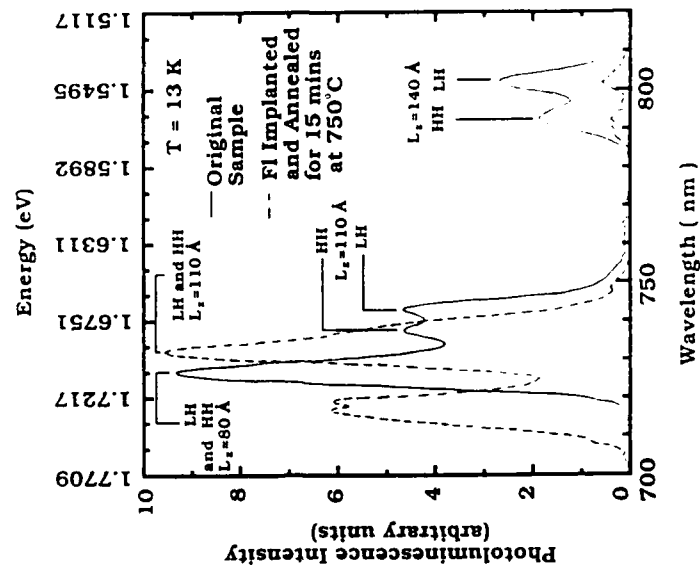


Figure 3 : Low temperature Photoluminescence spectrum of 80, 110, and 140 \AA $\text{GaAs}_{0.91}\text{P}_{0.09}/\text{Al}_{0.3}\text{Ga}_{0.7}\text{As}$ single quantum wells for light polarized parallel to the layers. The broken curves were obtained after Fluorine implantation and anneal. After 15 minutes anneal the HH and LH transitions of the 110 \AA well overlap to give a single peak of double the intensity as that of the original intensity

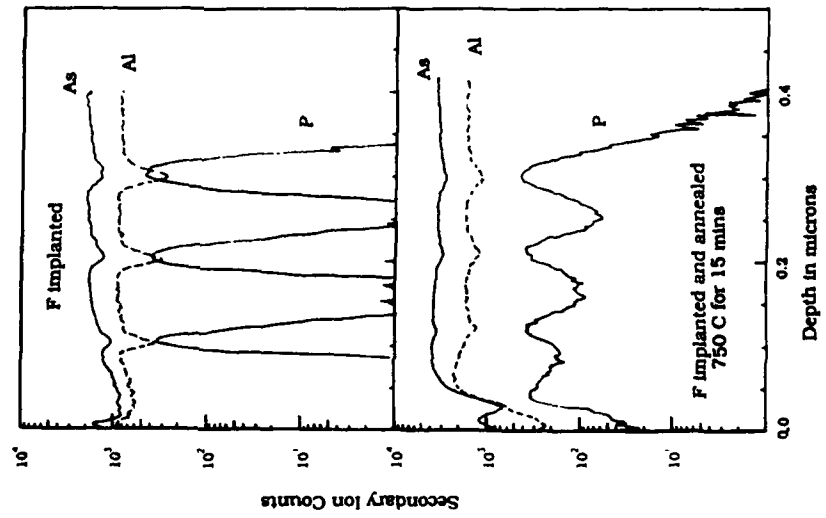


Figure 4 : SIMS measurement of the P, As, and Al profile of as implanted and implanted & annealed 80, 110, and 140 Å GaAsP/AlGaAs single QWs

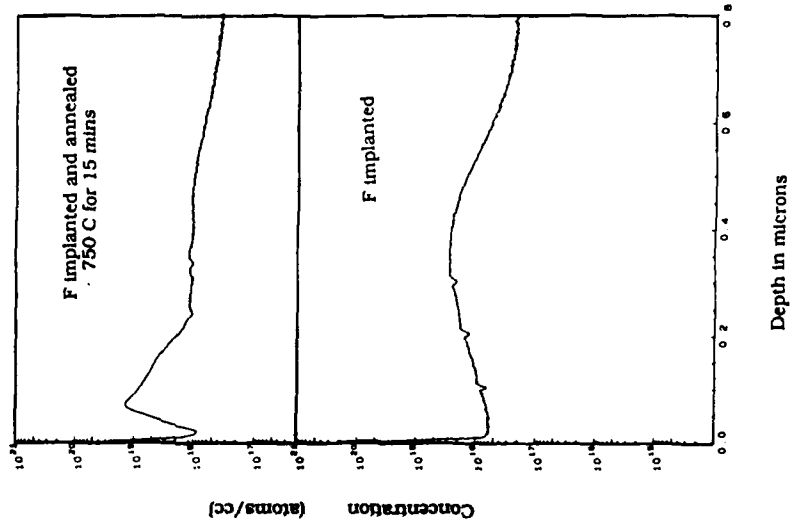


Figure 5 : SIMS measurement of the F dopant in GaAsP/AlGaAs SQWs concentration after implantation and after implantation and 15 min. anneal.

SEMICONDUCTOR WAVEGUIDE SWITCHES AND MODULATORS

KUNIO TADA

DEPARTMENT OF ELECTRONIC ENGINEERING, UNIVERSITY OF TOKYO
HONGO 7-3-1, BUNKYO-KU, TOKYO, 113, JAPAN

1. Introduction

Many people think that the electrooptic properties of GaAs and InP are inferior to those in LiNbO₃. This is not the case. It is true that the linear electrooptic coefficient r is much smaller in these semiconductors than in LiNbO₃. However, the refractive index n is much larger, and the relative permittivity ϵ_r is much smaller. As a result, the most important figure of merit $P/\Delta f$ (modulating power/bandwidth), which is proportional to ϵ_r/n^3r^2 in waveguide modulators, in GaAs or InP is comparable to that in LiNbO₃ in the wavelength region 1–1.6 $\mu\text{m}^{1,2}$. Besides the linear electrooptic (Pockels) effect, a variety of physical phenomena in these materials resulting in changes of the refractive index and the absorption coefficient can be utilized to build fast and compact modulators/switches. These phenomena include the Franz-Keldysh effect (electroabsorption), quantum-confined Stark effect, free carrier plasma effect and band-filling effect. Moreover, because these compound semiconductors offer the obvious advantage of monolithic integration of almost all kinds of useful photonic and electronic devices to form integrated optical circuits (IOC) and optoelectronic integrated circuits (OEIC), waveguide switches and modulators based on semiconductors seem to be very promising in the long run. This paper reviews some of the recent works and tries to indicate some future directions.

2. Devices Based on Field-Induced Effects

The length l of electrooptic semiconductor waveguide modulators/switches is typically a few millimeters. If they are lumped-constant devices, the 3dB cutoff frequency (bandwidth) of modulation Δf is ultimately limited by the light propagation time and is about $[4/l(\text{in cm})]\text{GHz}$. The actual Δf is usually below several GHz and is limited by the parasitic elements such as depletion layer capacitance, electrode layer resistance, and bonding wire inductance³. Traveling-wave configuration is employed for a very high Δf , which is limited by the amount of mismatch between the propagation times of the guided optical and electromagnetic waves. The switching voltage, which is inversely proportional to l , can be much reduced by increasing l in this configuration. GaAs/AlGaAs traveling-wave single-waveguide⁴ and Mach-Zehnder⁵ modulators were developed. The first GaAs/AlGaAs traveling-wave directional coupler switch has recently been reported⁶. By employing a semi-insulating GaAs substrate and a thin (2 μm) conductive layer sandwiched between the substrate and the waveguide layer, as shown in Fig.1, dielectric loss and excessive slow-wave properties can be relaxed in the microwave guide structure. Switch-

ing voltage of 10.4V and Δf of 9.1 GHz have been obtained at 1.06 μ m wavelength.

A monolithic 4 \times 4 optical matrix switch composed of conventional GaAs/AlGaAs electrooptic directional couplers has been demonstrated⁷. However, such devices built on (100) substrate are operative only for TE-polarized light, and polarization-independent directional coupler switches are required for photonic switching applications. It has been depicted that these devices can be built on (111) substrate, and some theoretical analyses and design examples are shown⁸. Actual devices have been fabricated very recently⁹.

The Franz-Keldysh effect is a slight decrease of effective bandgap energy in bulk semiconductor under an applied high electric field. Miniature and high-speed electroabsorption modulators monolithically integrated with DFB laser diodes are widely known.

Multiple-quantum-well (MQW) modulators are based on the quantum-confined Stark effect (QCSE) in MQWs embedded in a waveguide. This effect is a remarkable decrease in the effective bandgap under an electric field applied perpendicular to the QW layers. This shift of the absorption edge, being associated with similar shift of sharp absorption peaks due to excitations, causes large changes in optical constants near the bandgap. A large number of single-waveguide electroabsorptive modulators and a few of directional coupler switches as well as intersecting waveguide switches have been reported so far. Almost all of them employ QWs with rectangular potential profile. Use of modified potential profiles such as graded, coupled, and parabolic potential profiles will give us a new horizon in semiconductor modulators/switches. Polarization-independent waveguide switches based on the QCSE in parabolic QWs have been proposed¹⁰ and implemented very recently¹¹. Structure of a unit QW with equivalent parabolic potential profile and a preliminary result are shown in Fig.2. Improvement of this device is under way.

3. Devices Based on Carrier-Injected Effects

Large changes in the optical constants can also be caused by injecting free carriers into a waveguide layer. A compact (8mm-long) non-blocking 4 \times 4 matrix switch was developed¹², which was composed of 32 Y-shaped total-internal-reflection type switches. A new device structure for improving the relatively low speed of these forward-biased devices has been proposed¹³, and demonstrated recently¹⁴. A schematic diagram of the simplest type among the proposed bipolar transistor carrier-injected waveguide modulator/switches is illustrated in Fig.3. This shows a cross section of a heterojunction bipolar transistor (HBT) whose p-GaAs base layer works also as waveguide layer of an absorption modulator. Carriers are injected and stored only in this layer. In comparison with conventional diode-structured devices where the switching times are most often limited by the lifetime of injected carriers, the triode-structured devices can be much faster if high speed carrier injection and removal are performed through the base terminal. The amplification nature

of transistors also means that large emitter or collector switching currents can be controlled by small base currents. The actual sample has MBE-grown ten epilayers including two composition-grading layers which prevent the decrease of current amplification factor. An output on/off ratio of 2.1 and a switching time of 1.6ns has been obtained with a turn-on base current of 3mA.

Devices based on quantum well electron transfer have been proposed and demonstrated¹⁵⁾.

4. Comment

One of important issues in semiconductor waveguide switches and modulators is the large optical insertion loss mainly caused by a large coupling loss. Reducing the coupling loss to fiber is the most urgent issue. Because there exists a trade-off between the coupling efficiency and switching voltage or current, new simple structures near the end facet such as a large optical window should be devised for better coupling efficiency. Monolithic integration of the device with other components such as laser diode is another way to cope with this problem. More positive way would be incorporation of traveling-wave optical amplifiers into switches and modulators. In order to solve all the problems mentioned above, the role of semiconductor optoelectronic devices fabrication technologies will become more and more important.

References

- 1) N.Suzuki and K.Tada : Jpn. J. Appl. Phys., **23**, 291 (1984.3)
- 2) N.Suzuki and K.Tada : Jpn. J. Appl. Phys., **23**, 1011 (1984.8)
- 3) K.Tada, S.Kawanishi and H.Hayashi : Trans. IEICE, **J71-C**, 709 (1988.5)
- 4) S.Y.Wang and S.H.Lin : J. Lightwave Technology, **6**, 758 (1988.6)
- 5) R.G.Walker, I.Bennion and A.C. Carter : IOOC'89, **19C2-5**(PD) (1989.7.19, Kobe)
- 6) H.Hayashi and K.Tada : Appl. Phys. Lett., **57**, 227 (1990.7.16)
- 7) K.Komatsu et al. : Photonic Switching II (Editors: K.Tada and H.S.Hinton, Springer-Verlag Berlin, Heidelberg 1990), pp.67-71
- 8) K.Tada and H.Noguchi : Trans. IEICE, **E73**, 88 (1990.1)
- 9) K.Komatsu et al. : Photonic Switching '91, **FA2** (1991.3.8, Salt Lake City)
- 10) T.Ishikawa, S.Nishimura and K.Tada : Jpn. J. Appl. Phys., **29**, 1466 (1990.8)
- 11) K.Tada et al. : Photonic Switching '91, **FB3** (1991.3.8, Salt Lake City)
- 12) H.Inoue et al. : IEEE J. Selected Areas in Communications, **6**, 1262 (1988.8)
- 13) K.Tada and Y.Okada : IEEE Electron Device Lett., **EDL-7**, 605 (1986.11)
- 14) Y.Okada, T.Ishikawa and K.Tada : Appl. Phys. Lett., **55**, 2591 (1989.12.18)
- 15) J.E.Zucker : IEEE Photonic Technology Lett., **2**, 804 (1990.11)

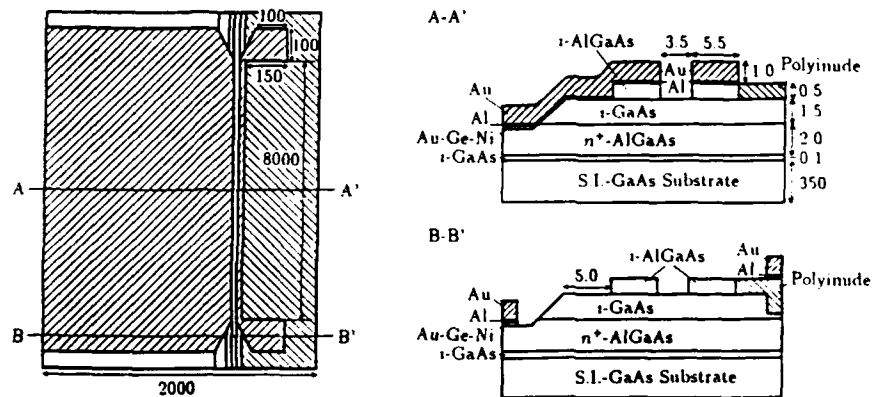


Fig. 1. Top view (left) and cross-sectional view (right) of the traveling-wave directional coupler switch⁶. Lengths are in μm .

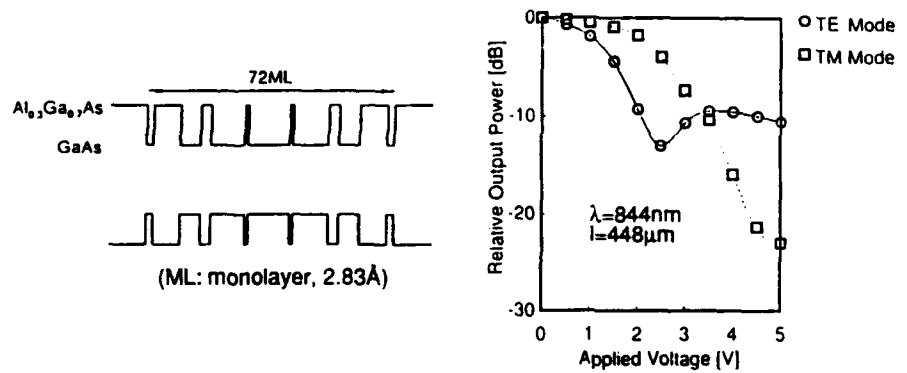


Fig. 2. Structure of a quantum well (left) and measured characteristics (right) of the polarization-independent waveguide switch with equivalent parabolic QWs¹¹.

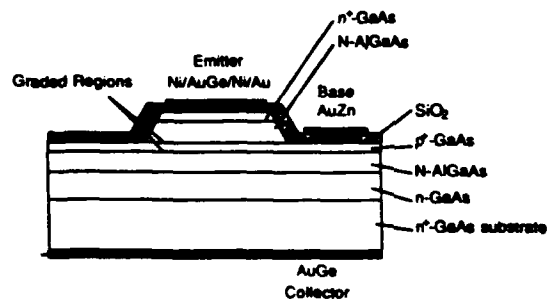


Fig. 3. Cross-sectional diagram of the HBT carrier-injected waveguide modulator¹⁴.

Properties of Waveguides, Routing Structures and Switches
Fabricated by Impurity Induced Layer Disordering

T. A. DeTemple
Department of Electrical and Computer Engineering
University of Illinois
Urbana, IL 61801

Since its discovery in 1981, the phenomena of impurity induced layer disordering (IILD), or intermixing, has received some attention because of its promise as a planar optically self aligned fabrication method for buried channel optical waveguide structures such as PIC or OEIC¹. The process is such that the intermixed region has a higher bandgap and hence lower index of refraction than the original structure permitting lateral index of refraction control via masks. Originally seen in AlGaAs, the effect is now known to exist in three other laser related alloys, all of which contain graded Al-Ga layers and which preserve lattice matching after intermixing²⁻⁴.

Since low threshold current, index guided lasers have been fabricated by IILD⁵, the primary questions one may ask regarding IILD fabrication deal with the quality of the waveguides as routing structures and what else can be made from the same heterostructure. The long range issue focuses on the possible existence of a universal heterostructure which can be processed for multiple device applications.

This talk will concentrate first on the non-laser aspects of single AlGaAs structures fabricated by IILD. In particular, fabrication methods will be outlined and data on the optical properties of simple routing structures, such as s-bends, will be presented⁶. Electro-absorption⁷ and electro-refraction⁸ modulators have been fabricated by IILD and their properties and device implications will be discussed.

Next, the issues associated with the integration of multiple devices, passive and active, will be discussed. Of special importance is device isolation, both electrical and optical, and the means to achieve these by oxygen incorporation via IILD⁵. Integrated band edge devices such as amplifiers would require transparent guide sections. Impurity⁹, via IILD, and impurity free modifications of the band gap via vacancy incorporation (VILD) have been demonstrated¹⁰ and data on the properties of such structures show that both IILD and VILD can be used for lateral and axial intermixing applications without compromising routing ability¹¹.

Selected integrated PIC's (integrated extended cavity lasers and time slot interchange switches) will be discussed which aid in formulating unresolved aspects of IILD and VILD. These also identify bottleneck issues associated with the presently studied heterostructures and with the integration of lasers into the guided structure.

Research supported by the National Science Foundation sponsored Engineering Research Center for Compound Semiconductor Microelectronics.

References

1. D.G. Deppe and N. Holonyak, Jr., "Atom diffusion and impurity-induced layer disordering in quantum well III-V semiconductor heterostructures" J. Appl. Phys., **64**, R93-R113 (1988).
2. Y. Kawamura, H. Asahi, A. Kohzen and K. Wakita, "Disordering by Zn-diffusion of InGaAs/InAlAs MQW Superlattice Structure Grown by MBE", Elec. Lett., **21**, 218-219 (1985)
3. D.G. Deppe, D.W. Nam, N. Holonyak, Jr., K.C. Hsieh, J.E. Baker, C.P. Kuo, R.M. Fletcher, T.D. Osentowski, and M.G. Craford, "Impurity induced layer disordering of high gap In (Al Ga) P heterostructures", Appl. Phys. Lett., **52**, 1413-1415 (1988).

4. J.S. Major, Jr., D.C. Hall, L.J. Guido, N. Holonyak, Jr., P. Gavrilovic, K. Meehan, J.E. Williams, and W. Stutius, "High-power disorder-defined coupled stripe AlGaAs-GaAs-InGaAs quantum well heterostructure lasers", Appl. Phys. Lett., 55, 271-276 (1989).
5. L.J. Guido, J.S. Major, Jr., J.E. Baker, N. Holonyak, Jr. and R.D. Burnham, "Disorder-defined buried-heterostructure AlGaAs-GaAs quantum well lasers by diffusion of silicon and oxygen from Al-reduced SiO₂", Appl. Phys. Lett., 54, 1265-1267 (1989).
6. T.K. Tang, P.D. Swanson, M.E. Givens, T.A. DeTemple, J.J. Coleman and I.A. White, "Losses in Semiconductor Waveguide S-Bends Fabricated by Impurity Induced Layer Disordering", Optics Lett., 13, 1138-1140 (1988).
7. P.D. Swanson, T.K. Tang, M. E. Givens, L.M. Miller, T.A. DeTemple and J.J. Coleman, "Electroabsorption in Single Quantum Well GaAs Laser Structures", Appl. Phys. Lett., 54, 1716-1718 (1989).
8. T. Hausken, T.C. Huang, K.W. Lee, R.J. Simes, N. Dagli, and L.A. Coldren, "Impurity-induced-disordered phase modulators in AlGaAs/GaAs quantum well and double-heterostructure waveguides", Appl. Phys. Lett., 53, 728-730 (1988).
9. R.L. Thornton, J.E. Eppler, and T.L. Paoli, "Monolithic Integration of a transparent dielectric waveguide into an active laser cavity by impurity-induced disordering", Appl. Phys. Lett., 51, 1983-1985 (1987).
10. J.D. Ralston, S. O'Brien, G.W. Wicks and L.F. Eastman, "Room-temperature exciton effects in partially intermixed GaAs/AlGaAs superlattices" Appl. Phys. Lett., 52, 1511-1513 (1988).
11. T. Tang, P. Swanson, C. Herzinger, L. M. Miller, T. M. Cockerill, R. P. Bryan, T. A. DeTemple, and J. J. Coleman, "S-bend Loss in Disorder-Delineated GaAs Heterostructure Laser Waveguides with Native and Blue Shifted Active Regions", Appl. Phys. Lett., 57, 741-743 (1990).

Room Temperature Stark-ladder Transitions and Electro-optic Bistability in GaAs/AlAs Superlattices with Different Miniband Widths

K. Kawashima, K. Fujiwara, T. Yamamoto, M. Sigeta, and K. Kobayashi

ATR Optical and Radio Communications Research Laboratories,

Seika-cho, Soraku-gun, Kyoto 619-02, Japan

Recently, there has been an increasing interest in Wannier-Stark localization in superlattices [1-3] for various advantages to photonic device applications such as optical modulators or bistable switching devices [4,5]. To achieve a high on/off ratio bistable operation, which is based on a self-electro-optic-effect device (SEED) [6], device improvement using a Fabry-Perot resonator and/or a reflective structure has been reported [7]. However, for application to vertical transmission devices, it is important to enhance the oscillator strength of optical absorption in superlattice layers, which is associated with both electric field-induced blue shift of the absorption edge and additional absorption peak shifts by Stark-ladder transitions [1-3].

In this paper, we report on a systematic study of room temperature Stark-ladder transitions in GaAs/AlAs superlattices with different miniband widths. We observed the highest quantum coherence of 11 periods in the wide-miniband superlattice. Furthermore, we show the dependence of electro-optic bistable properties on the oscillator strength of the Stark-ladder transitions.

We prepared 6 samples which consist of the same structure except for a superlattice layer. The growth sequence was as follows: (a) n-GaAs buffer, (b) n-Al_{0.4}Ga_{0.6}As cladding, (c) a nominally undoped 100-period of GaAs/AlAs superlattice which was embedded in undoped Al_{0.4}Ga_{0.6}As cladding, (d) p-Al_{0.4}Ga_{0.6}As cladding, and (e) p-capping layers. The barrier thickness of the superlattices in samples #1, #2, #3, and #4 were 5.7Å, 8.6Å, 11.4Å and 17.3Å, respectively. The well thickness of these samples was the same: 31.3Å. Samples #5 and #6 have wells of 26.1Å and 39.2Å, respectively, and consisted of the same barrier as sample #2. Conventional lithographic techniques and wet etching were used to fabricate p-i-n diodes which have a windowed Au electrode. These sample structure is schematically shown in Fig. 1. Room temperature photocurrent (PC) spectra were measured at various voltages using monochromatic light from a halogen lamp. PC-voltage characteristics of the diodes and electro-optic bistable properties of SEED-type devices were measured using an Ar⁺ laser pumped titanium-sapphire laser. —

Figure 2 represents PC spectra for samples #1, #2, #3 and #4 under a high reverse bias voltage ($V_b = 14V$). Top bars in Fig. 2 indicate the calculated miniband widths (140~17meV) for each sample. Under high electric field regimes the electron

wavefunction tends to localize in each well. As a result, a heavy-hole(HH) exciton absorption peak (namely, 0-th Stark ladder transition) is observed around 730nm in each sample. In wider-miniband samples, because of large probability of electron tunneling , an additional peak due to the $n=-1$ Stark ladder transition is observed more clearly in the lower energy.

Figure 3 shows a PC-voltage curve of sample #1 which consists of the thinnest barrier. Stark-ladder transitions down to $n=-5$ are resolved. Such a high quantum coherence [8,9] of over 11 periods shows that this thin barrier structure was grown with high homogeneity. Under lower electric field regimes than that shown in fig. 2, absorption peaks due to $n \neq 0$ Stark-ladder transitions were observed in PC spectra in every sample except sample #4. In Fig. 4, measured slopes of the field-induced energy shifts of Stark-ladder transitions were plotted as a function of a period D . The dashed lines represent the calculated slopes neD [1,2]. This agreement gives clear evidence that Wannier-Stark localization occurs over a wide range of miniband widths.

We have studied the dependence of SEED characteristics on both the HH exciton absorption line shape and the oscillator strength of $n \leq -1$ Stark-ladder transitions. To observe the SEED operation, we have connected a load resistor and a constant bias in series to the each sample. In fig. 5 we present typical PC versus input light power characteristics of several wavelengths of samples #1, #2, #3, and #4. Fig. 5 shows that bistabilities clearly depend on the miniband width of superlattice. In sample #1, because the HH exciton peak is broad (which was shown in fig. 2), and the oscillator strength of higher index Stark-ladder transitions is large, it is difficult to get a clear bistable hysteresis loop. In sample #2, two bistable loops are observed: one that in the lower power region arises from the $n=-1$ Stark ladder transition and the other refers to the $n < -2$ Stark-ladders. In sample #3, a large on/off ratio (> 2) bistability is demonstrated at the operation wavelength of 750nm. At wavelengths longer than 755nm, only one hysteresis loop due to the $n=-1$ Stark-ladder is observed. These features are associated with the sharpness of localized HH exciton peaks, and weakness of oscillator strength due to the $n < -2$ Stark ladder transitions. In sample #4, the localized HH exciton line shape is sharp as shown in Fig. 2. However, its miniband width is too narrow, and the field-induced blue-shift of the absorption edge is hidden in the HH exciton peak. Therefore, the operation wavelength to obtain the bistabilities is restricted within a narrow range.

In conclusion, we have systematically studied room temperature Stark-ladder transitions in GaAs/AlAs superlattices with different miniband widths. We have observed the highest quantum coherency of 11 periods in wide-miniband superlattice. A wide bistable loop was obtained in the superlattice whose miniband width is of the order of 50meV.

REFERENCES

- [1] E. E. Mendez, F. Agullo-Rueda, and J. M. Hong, Phys. Rev. Lett. 60, 2426 (1988)
- [2] K. Fujiwara, H. Schneider, R. Cingolani, and K. Ploog, Solid. State. Commun., 72, 935 (1989)
- [3] K. Fujiwara, Optical and Quantum Electronics, 22, S99 (1990)

- [4] I. Bar-Joseph, K. W. Goossen, J. M. Kuo, R. F. Kopf, D. A. B. Miller, and D. S. Chemla, *Appl. Phys. Lett.* **55**, 340 (1990)
 [5] H. Schneider, K. Fujiwara, H. T. Grahn, K. v. Klitzing, and K. Ploog, *Appl. Phys. Lett.* **56**, 12 (1990)
 [6] D. A. B. Miller, D. S. Chemla, T. C. Damen, T. H. Wood, C. A. Burrus, Jr., A. C. Gossard, W. Wiegmann, *IEEE J. Quantum Electron.*, QE-21, 1462 (1985)
 [7] K-K. Law, R. H. Yan, L. A. Coldren, and J. L. Merz, *Appl. Phys. Lett.* **57**, 13 (1990)
 [8] E. E. Mendez, F. Agullo-Rueda, and J. M. Hong, *Appl. Phys. Lett.* **56**, 25 (1990)
 [9] F. Agullo-Rueda, E. E. Mendez, and J. M. Hong, *Phys. Rev. B* **40**, 2, 1357 (1988)

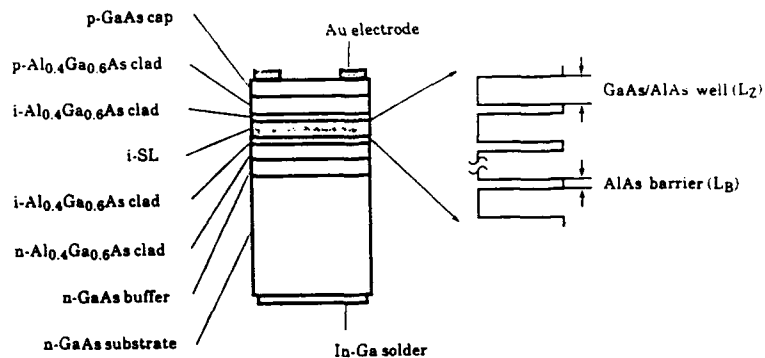


Figure 1
Schematic diagram of the sample structure.

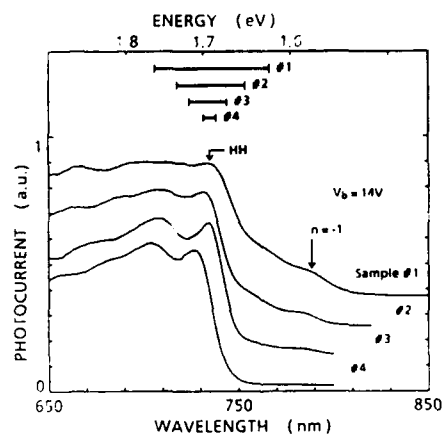


Figure 2
Photocurrent spectra under high field regime of superlattice samples #1, #2, #3, and #4. The peak labels give the Stark-ladder index. Top bars indicate the calculated miniband widths for each sample.

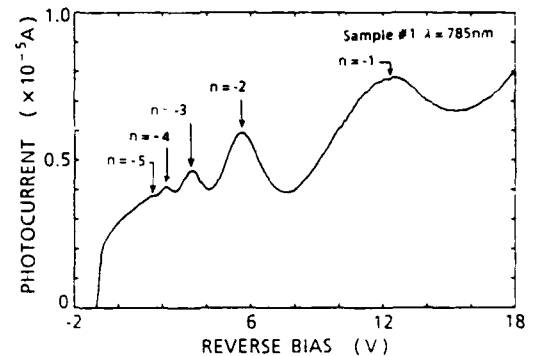


Figure 3
Photocurrent-bias voltage characteristics of sample #1 at room temperature. The peak labels give the Stark-ladder index.

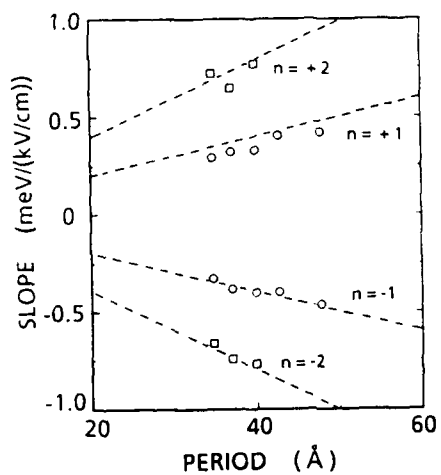


Figure 4
The slope of n -th ($n = \pm 1, \pm 2$) Stark-ladder transitions as a function of the superlattice period. The dashed line represents the calculated slope.

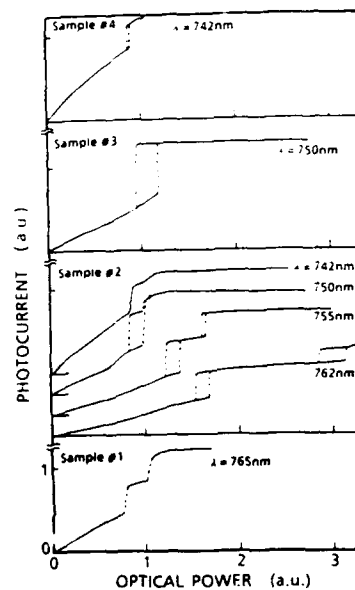


Figure 5
Photocurrent versus illumination power for samples #1, #2, #3, and #4.

**Very Low-Voltage MBE-grown Asymmetric Fabry-Perot Reflection Modulator based on
Superlattice Wannier-Stark Localization**

K-K. Law, J. L. Merz, and L. A. Coldren

Department of Electrical and Computer Engineering,
University of California, Santa Barbara
Santa Barbara, CA 93106

Surface-normal optical modulators based on III-V semiconductor quantum wells (QWs) and superlattices (SLs) are important for potential applications such as two-dimensional arrays for optical interconnection and optical processing. Asymmetric Fabry-Perot (ASFP) structures[1-4] utilizing electroabsorption effects of either QWs or SLs inside the cavities sandwiched by a pair of asymmetric mirrors (with bottom mirror more reflective) have been implemented with high contrast ratios. Depending on the active medium and the ASFP configuration, the ASFP can be either normally-on or normally-off. The general operating principle of a normally-on multiple-QW ASFP is to red-shift the heavy hole exciton of the QWs by the quantum confined Stark effect (QCSE) towards the Fabry-Perot (FP) resonance to balance the initially asymmetric FP cavity. For a normally-off SL ASFP (SL-ASFP), however, the off level in the low-field case is attained by aligning the FP mode at the appropriate photon energy relative to the SL absorption edge to match the top and effective bottom mirror reflectivities. Upon application of fields, such an ASFP will be turned on by reducing the cavity loss at resonance through the pseudo-blue-shift[5] of the absorption edge caused by Wannier-Stark localization in the SL[6]. In contrast to the normally-on ASFP, the normally-off modulator is also particularly suited for the implementation of high-contrast self-electro-optic effect devices (SEEDs)[7] due to the SL-ASFP's negative differential photoconductivity when illuminated in the spectral range around the FP resonance.

Among other design criteria, one of the most important considerations for a surface-normal modulator is its operating voltage swing. Low drive voltages are important because of compatibility with that in the modern electronic circuits and low drive powers for high-speed operations. A high-contrast normally-off SL-ASFP reported previously requires an operating voltage swing of 8V[4]. In order to further reduce the operating voltage, while using the same SL structure, we can decrease the number of periods of SL in the cavity by appropriately increasing the top mirror reflectivity[2] because the required critical amount of absorption and active layer thickness product for the zero-reflectivity off-state decreases (Fig. 1). The front mirror reflectivity was increased from -0.32 in the previous SL-ASFP[4] to -0.6 in the current one, and the number of periods of SL needed could be reduced by $\sim 1/2$. In this paper, we report a MBE-grown monolithic normally-off transverse asymmetric Fabry-Perot reflection modulator using Wannier-Stark localization in a superlattice with an operating voltage swing of less than 3V. A contrast ratio of $>26:1$ at the FP resonance and a reflection change of 33% at a wavelength $\sim 20\text{\AA}$ away from the FP mode has been achieved. Also the pragmatic limitations that are imposed on the device performance and integration of such modulators and optical logic switches by the MBE growth will be discussed.

The device structure, as shown in Fig. 2, was grown by MBE on a two-in wafer in a modular Varian Gen II MBE system. The successful operation of the SL-ASFP relies on the meticulous alignment of the FP resonance at a relevant wavelength relative to the SL absorption edge. The FP mode wavelength is determined by both the thickness and refractive index of the medium embedded inside the cavity and the grating mirror thicknesses. Also the SL absorption edge and the magnitude of the absorption change are quite sensitive to well and barrier widths. Therefore the growth rate calibration by RHEED oscillations is crucial to grow device structures close to the design parameters. All the layers except the active undoped SL medium were grown at $\sim 570^\circ\text{C}$ to avoid Ga reevaporation and minimize dopant diffusion. The mirror layers and the SL medium (618\AA AlAs/ 535\AA $\text{Al}_{0.3}\text{Ga}_{0.7}\text{As}$) were grown with substrate rotation to control their uniformity across the wafer to $\sim 3\%$. The SL was grown at $\sim 690^\circ\text{C}$ to optimize its optical properties. The device contains a 20.5-period bottom mirror (Si-doped) and a 3-period top mirror (Be-doped) stack separated by an undoped SL structure (52.5 pairs of 30\AA GaAs/ 30\AA $\text{Al}_{0.3}\text{Ga}_{0.7}\text{As}$) and a $0.64\mu\text{m}$ Be-doped $\text{Al}_{0.3}\text{Ga}_{0.7}\text{As}$ layer (Fig. 2).

Fig. 3 shows the narrow-band modulation spectra for one of our device at various biasing voltages. The positions of the FP modes at different voltages are indicated by the dashed line. Because of the relatively large built-in field, a slight forward bias of $+0.18\text{V}$ is needed to offset the partial Stark-localization of the carriers in the SL to bring the FP mode at $\lambda \sim 7670\text{\AA}$ to its minimum. The FP mode reflectivity increases monotonically as the electric field across the SL increases and also the full-width-half-maximum of the FP mode reduces with increasing field. This is caused by the decrease in absorption in the spectral range around the FP mode due to the Wannier-Stark localization effect. Recovery of the QW exciton can be readily observed as reflectivity dip at $\lambda \sim 7540\text{\AA}$, as both electron and hole wavefunctions begin to be strongly localized with biases $> -0.5\text{V}$. In Fig. 4(a) and (b), both the contrast ratio $(=R(-2.75\text{V}) / R(+0.18\text{V}))$ and the change $[\Delta R(V)=R(V) - R(+0.18\text{V})]$ in reflectivities of the SL-ASFP as a function of wavelength are shown. A contrast ratio of more than 26 was attained at $\lambda \sim 7670\text{\AA}$. The contrast ratio decreases rapidly from its peak around the FP mode. A contrast ratio of >10 can be attained over a spectral width of $>10\text{\AA}$. The $\Delta R(-2.75\text{V})$ is at its peak value of $\sim 33\%$ at $\lambda \sim 7690\text{\AA}$. The $\Delta R(-2.75\text{V})$ at $\sim 7670\text{\AA}$ is $\sim 24\%$ ($\sim 72\%$ of the peak ΔR). A change of at least 24% can be observed over a larger optical bandwidth of $>70\text{\AA}$. Because of the complex change of the SL's absorption spectrum with applied field and the FP reflectivity's nonlinear dependence on cavity loss, ΔR is highly nonlinear with applied voltage. The reflectivity increases rapidly upon changing the bias from $+0.18\text{V}$ to -0.5V , and as a result, ΔR per unit drive voltage (from $+0.18\text{V}$ to -0.5V) are as high as $\sim 32\%/V$ and $\sim 28\%/V$ at $\sim 7685\text{\AA}$ and $\sim 7635\text{\AA}$ respectively. However, the ΔR increases more gradually with bias beyond -1V . Devices within an area of $> 1.6\text{cm} \times 0.3\text{mm}$ of the wafer with about the same ΔR (within $\sim 5\%$) at the FP mode wavelength with $< \sim 0.2\%$ variation from the one shown in Fig. 3 were also attained.

Due to the residual absorption below the high-field absorption edge, the insertion loss at the wavelength of peak contrast is about 6dB. For such an ASFP structure relying on pseudo-blue-shift mechanism inside the cavity to achieve normally-off type operation, albeit there is large enough

absorption at low field in the active region to yield a "zero" off-level, the loss at high field is still significant enough to contribute a relatively high insertion loss even with >99% bottom mirror reflectivity. This can be attributed to the relatively low contrast ratio (<3) of the SL absorption coefficient. Other more complex quantum wells such as symmetric coupled QWs[8] and asymmetric triangular QWs[9,10] that rely on significantly reducing the oscillator strength of the optical absorption of the zero-field exciton using field by separating the electron and hole distributions in the wells can also be adapted in the normally-off ASFP structure. In particular, by operating the photon energy at the zero-field ground state heavy hole exciton transition of an asymmetric triangular QW, large absorption contrast has been theoretically proposed[9] at a relatively small field change. Thence, ASFP incorporating such type of quantum well will potentially provide normally-off operation with high-contrast, low insertion loss and low operating voltage. Such kind of ASFPs also have the potential application as high-performance SEED with very low or even no bias.

In conclusion, we have utilized the precise layer thickness and composition control offered by MBE to implement a normally-off surface normal superlattice asymmetric Fabry-Perot modulator with a contrast ratio of more than 26:1 at a voltage swing of less than 3V. The modulation is attained by reducing the cavity loss at the FP resonance through the SL Wannier-Stark localization. Such type of monolithic modulators with uniform characteristics provided by meticulous control of MBE growth can be integrated into two-dimensional arrays for optical interconnection and optical computation.

The authors would like to acknowledge C. P. Chao for his technical assistance. We would also like to thank R. H. Yan for discussions.

REFERENCES:

- [1] R. H. Yan, R. J. Simes and L. A. Coldren, *IEEE Photon Tech. Lett.*, vol. 1, pp. 273-275, 1989.
- [2] R. H. Yan, R. J. Simes and L. A. Coldren, *IEEE Photon Tech. Lett.*, vol. 2, pp. 118-119, 1990.
- [3] M. Whitehead, A. Rivers, G. Parry, J. S. Roberts and C. Button, *Electron. Lett.*, vol. 25, pp. 984-985, 1989.
- [4] K-K. Law, R. H. Yan, J. L. Merz and L. A. Coldren, *Appl. Phys. Lett.*, vol. 56, pp. 1886-1888, 1990.
- [5] For a discussion on the distinction between pseudo-blue-shift and true blue-shift, see D. A. B. Miller, *Optical and Quantum Electron.*, vol. 22, pp. 561-598, 1990.
- [6] J. Blase, P. Voisin, M. Allovon and M. Quillec, *Appl. Phys. Lett.*, vol. 53, pp. 2632-2634, 1988; E. E. Mendez, F. Agullo-Rueda and J. M. Hong, *Phys. Rev. Lett.*, vol. 60, pp. 2426-2429, 1988; K.W. Gossen, I. Bar-Joseph, J. E. Zucker, J. M. Kuo, R. F. Kopf, D. A. B. Miller and D. S. Chemla, in *Conference Digest IEEE LEOS Annual Meeting*, Orlando, Florida, 1989, paper OE3.3.
- [7] K-K. Law, R. H. Yan, L. A. Coldren and J. L. Merz, *Appl. Phys. Lett.*, vol. 57, pp. 1345-1347, 1990.
- [8] M. N. Islam, R. L. Hillman, D. A. B. Miller, D. S. Chemla, A. C. Gossard and J. H. English, *Appl. Phys. Lett.*, vol. 50, pp. 1098-1100, 1987.
- [9] G. D. Sanders and K. K. Bajaj, *Appl. Phys. Lett.*, vol. 55, pp. 930-932, 1989.
- [10] K-K. Law, R. H. Yan, A. C. Gossard and J. L. Merz, *J. Appl. Phys.*, vol. 67, pp. 6461-6465, 1990.

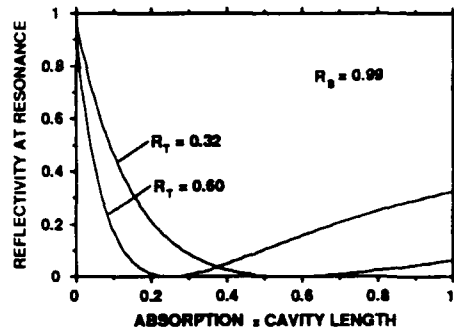


Fig. 1 ASFP reflectivity at resonance as a function of the cavity absorption and cavity length product for bottom reflectivity of 0.99 and top mirror reflectivities of 0.32 and 0.60.

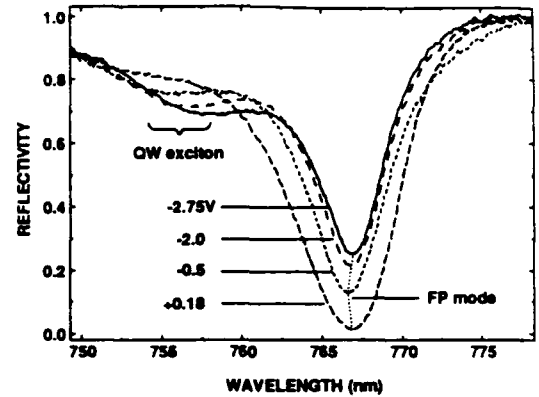


Fig. 3 Modulation spectra of the SL-ASFP for various bias voltages.

Fig. 2 Schematic diagram of the SL-ASFP layer structure. The top and bottom mirror reflectivities are 60% and 69% respectively. The active region has 52.5 periods of undoped 30Å GaAs / 30Å $\text{Al}_{0.3}\text{Ga}_{0.7}\text{As}$ superlattice.

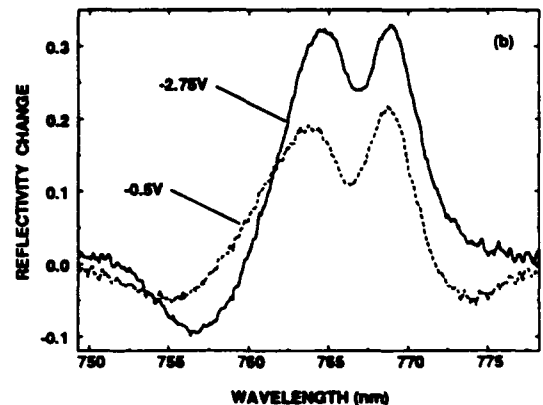
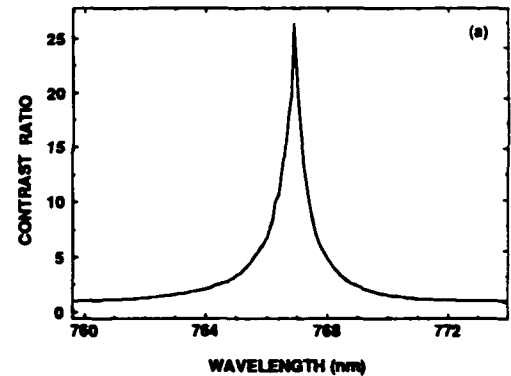
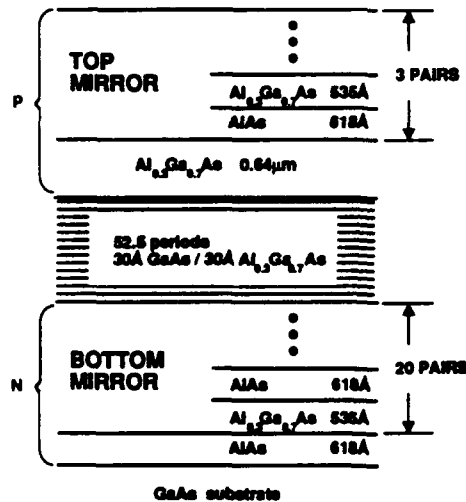


Fig. 4(a) Contrast ratio in reflectivity between -0.18V and -2.75V and (b) reflectivity change at -2.75V and -0.5V as a function of wavelength.

Room Temperature Excitonic Transitions and Electro-Optical Bistability in Strained $\text{In}_x\text{Ga}_{1-x}\text{As}/\text{Al}_{0.15}\text{Ga}_{0.85}\text{As}$ Multiple Quantum Wells

K. Kawashima, K. Fujiwara, and K. Kobayashi
ATR Optical and Radio Communications Research Laboratories,
Seika-cho, Soraku-gun, Kyoto 619-02, Japan
and

N. Sano
Department of Physics, School of Science, Kwansei Gakuin University,
Nishinomiya 662, Japan

Recently, there have been a great deal of attention in strained $\text{In}_x\text{Ga}_{1-x}\text{As}$ heterostructures grown on the GaAs substrate [1]. This is because the strained systems can provide additional freedom for the material design and various advantages to optoelectronic device applications. For applications to vertical-beam optical devices which are very useful for parallel optical beam processing, however, the advantage offered by the $\text{In}_x\text{Ga}_{1-x}\text{As}$ material system is crucial [2-6]. This is because the exciton resonance absorption can occur at energy below the bandgap of the GaAs substrate. This means that there is no need to remove the substrate to transmit the radiation at wavelength of interest. This is in fact the great advantage of the $\text{In}_x\text{Ga}_{1-x}\text{As}$ material system especially for an integrated-type device. Although recent advancement of the crystal growth techniques enables us to prepare high quality strained epitaxial layers, basic understanding of the band lineup problem is still controversial [7-10]. Investigations of the pseudomorphic strained heterostructures are therefore important in tailoring the device characteristics.

In this paper, we report on optical absorption properties of strained $\text{In}_x\text{Ga}_{1-x}\text{As}/\text{Al}_{0.15}\text{Ga}_{0.85}\text{As}$ multiple quantum wells (MQW) with nominal x values of 0.05, 0.10 and 0.15 by photocurrent (PC) spectroscopy. By virtue of the stronger quantum confinement by $\text{Al}_{0.15}\text{Ga}_{0.85}\text{As}$ barriers, distinct exciton resonances are observed up to 2nd order even at room temperature. A theoretical model analysis is given which explains all the energies of both parity allowed and forbidden transitions, fully taking account of the strain-induced energy-shifts due to the conduction and valence band deformation. Using the merit of the substrate transparency at the exciton resonance, a novel electro-optic bistable device is proposed and demonstrated without removal of the GaAs substrate.

The $\text{In}_x\text{Ga}_{1-x}\text{As}/\text{Al}_{0.15}\text{Ga}_{0.85}\text{As}$ MQW structures were grown on n^+ -type GaAs (100) substrates by molecular beam epitaxy [5]. Five periods of nominally undoped $\text{In}_x\text{Ga}_{1-x}\text{As}$ quantum wells with a width of $L_z = 100 \text{ \AA}$ and $L_B = 250 \text{ \AA}$ thick $\text{Al}_{0.15}\text{Ga}_{0.85}\text{As}$ barriers in between were grown at 470°C . They are confined by undoped 500 \AA $\text{Al}_{0.15}\text{Ga}_{0.85}\text{As}$ and $0.1 \mu\text{m}$ $\text{Al}_{0.3}\text{Ga}_{0.7}\text{As}$ layers. These layers are further clad by n - and p -type $\text{Al}_{0.3}\text{Ga}_{0.7}\text{As}$ layers to form p - i - n structures. The p - i - n diode were processed in about $400 \mu\text{m}$ mesas and gold-ring electrodes as contact on the p -material

were formed by standard photolithography. Back-side ohmic contact was formed on a corner part with In-Ga alloy solders. The sample structure is illustrated in Fig. 1. PC spectra were measured at room temperature in a dc mode using a lamp-monochromator system as a light source. Optical switching experiments were performed using a titanium-sapphire laser, pumped by a 6W argon laser, which can cover the wavelength range between 850 and 1000 nm.

Figure 2 shows room temperature PC spectra of the $\text{In}_x\text{Ga}_{1-x}\text{As}/\text{Al}_{0.15}\text{Ga}_{0.85}\text{As}$ MQW p-i-n diodes. The spectra were taken under illumination from top of the epitaxial layers with the bias voltage $V_b=0$ (nearly equivalent to the flat band conditions). Assignment of the transitions is also indicated in Fig. 2 (discussed later). Here we use in the following the notation $ij\text{H}$ ($ij\text{L}$) for heavy-hole (light-hole) exciton transition between the i -th electron and j -th heavy-hole (light-hole) subband. Sharp exciton resonances are clearly seen up to the 2nd order. Linewidth of the 11H transition in Fig. 2 is as low as 14 meV at room temperature. This demonstrates excellent quality of our strained epitaxial layers and homogeneous layer thickness and In distribution in the well layers. In Fig. 2, we note that the 11L exciton transition is clearly seen. This results from the fact that the lowest light-hole subband is certainly bounded in the well because of the use of $\text{Al}_{0.15}\text{Ga}_{0.85}\text{As}$ barrier. The energy separation, ΔE_{LH} , of the 11L and 11H transitions is found to be 27, 47, and 72 meV, increasing with the In content in the well. This gives direct evidence for the strain-induced effect on the valence band splitting.

In order to quantitatively explain the experimental results, we have calculated subband structures, fully taking the strain effect into account. For that, we assume that the lattice-mismatch is accommodated by the elastic strain given by the tensor ϵ_{ij} ($\epsilon_{xx}=\epsilon_{yy}=\epsilon=(a_L-a_S)/a_L$, $\epsilon_{zz}=-2C_{12}/C_{11}\epsilon$) with the lattice constants a_L and a_S of the unstrained ternary $\text{In}_x\text{Ga}_{1-x}\text{As}$ layer and of the substrate, respectively. We further assume that valence-band offsets between unstrained $\text{In}_x\text{Ga}_{1-x}\text{As}$ and $\text{Al}_{0.15}\text{Ga}_{0.85}\text{As}$ are calculated by a simple summation of the offset values for the $\text{In}_x\text{Ga}_{1-x}\text{As}/\text{GaAs}$ and $\text{GaAs}/\text{Al}_{0.15}\text{Ga}_{0.85}\text{As}$ heterointerfaces using a linear interpolation scheme [9]. For the latter offset value, we use a widely accepted 64/36 rule. Thus, our present model is naturally connected to the model by Gershoni et al [9]. (the limit of $y=0$ in the $\text{In}_x\text{Ga}_{1-x}\text{As}/\text{Al}_y\text{Ga}_{1-y}\text{As}$ system). Our calculation shows that the transition energy changes from that of bulk unstrained $\text{In}_x\text{Ga}_{1-x}\text{As}$ by two effects of strain and quantum confinement. We find that the ΔE_{LH} is mostly determined by the valence-band axial deformation potential and indirectly through the hole confinement energy variations by the hydrostatic deformation potential. This is because the hydrostatic strain component moves the valence band edges by the same amount. Therefore, the measured ΔE_{LH} allows us to determine the x value in the well accurately and self-consistently, as indicated in Fig. 2. We should point out that the precise determination of the x value is particularly important because of its sensitivity to the transition energy. In Fig. 2, the calculated results are also indicated by vertical bars, assuming a exciton binding energy of 7 meV [7]. Excellent agreement between theory and experiment is obtained.

When the reverse bias voltage was increased, both parity allowed and forbidden exciton transitions are observed. Variations of the transition energies are plotted in

Fig. 3 for the sample with $x=0.143$. Agreement with the theory is again obtained for the parity forbidden transitions under the flat-band conditions. When we increase the reverse bias voltage, the 11H resonance peak is red-shifted and the oscillator-strength decreases, accompanied by a linewidth broadening. Parity forbidden transitions (12H and 21H) increase their intensity with increasing reverse bias. These features are attributed to the quantum confined Stark effect [11]. As shown in the inset of Fig. 3, negative differential PC regions are observed at the energy below the bandgap of the GaAs substrate. Therefore, we obtain a bistable self-electro-optic effect device (SEED) by connecting a load resistor (R) and a constant bias (V_0) in series to the sample [5]. It should be stressed that the bistable operation is achievable without removing the substrate at the wavelength where the substrate is transparent. As demonstrated in Fig. 4, all optical bistability is also obtained by connecting a LED in series. That is, optical switching and hysteresis loop of the optical output power versus the input power are demonstrated at two different wavelengths λ_1 and λ_2 . This result suggests an important implication for a vertically integrated-type asymmetric SEED device that uses two wavelengths and one pixel instead of using one wavelength and two pixels like a symmetric SEED [12]. This type of integration is possible when at least one of the wavelengths is transparent to the substrate with the use of strained $\text{In}_x\text{Ga}_{1-x}\text{As}$ system.

REFERENCES

- [1] R. G. Waters and J. J. Colemann, Conference on Laser and Electro-optics 1990 Technical Digest Series, Vol.7 (Optical Society of America, Washington, DC 1990) pp.32-33.
- [2] T. E. Van Eck, P. Chu, W. S. C. Chang, and H. H. Wieder, Appl. Phys. Lett. 49, 135 (1986).
- [3] W. Dobbelaere, S. Kalem, D. Huang, M. S. Unl , and H. Morkoc, Electron. Lett. 24, 294 (1988).
- [4] T. K. Woodward, T. Sizer, II, D. L. Sivco, and A. Y. Cho, Appl. Phys. Lett. 57, 548 (1990)
- [5] K. Fujiwara, K. Kawashima, K. Kobayashi, and N. Sano, Appl. Phys. Lett. 57, 2234 (1990)
- [6] S. Niki, A. Cheng, J. C. P. Chang, W. S. C. Chang, and H. H. Wieder, Jpn. J. Appl. Phys. 29, L1833 (1990)
- [7] J. -P. Reithmaier, R. H ger, H. Riechert, A. Heberle, G. Abstreiter, and G. Weimann, Appl. Phys. Lett. 56, 536 (1990)
- [8] K. Shiraishi and T. Ohno, Jpn. J. Appl. Phys. 29, L556 (1990)
- [9] D. Gershoni, J. M. Vandenberg, S. N. G. Chu, H. Temkin, T. Tanbun-Ek, and R. A. Logan, Phys. Rev. B40, 10017 (1990)
- [10] D. J. Arent, Phys. Rev. B41, 9843 (1990)
- [11] D. A. B. Miller, D. S. Chemla, T. C. Damen, T. H. Wood, C. A. Burrus, Jr., A. C. Gossard, and W. Wiegmann, IEEE J. Quantum Electron., QE-21, 1462 (1985)
- [12] A. L. Lenitine, H. S. Hinton, D. A. B. Miller, J. H. Henry, J. E. Cunningham, and L. M. F. Chirovsky, Appl. Phys. Lett. 52, 1419 (1988)

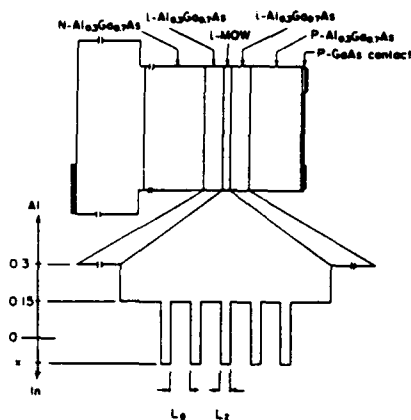


Figure 1
Schematic diagram of the sample structure.

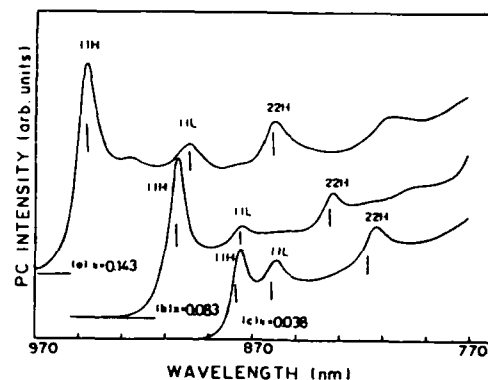


Figure 2
Photocurrent spectra of the MQW samples ($L_2=100$ Å) with $V_b=0$. Calculated wavelengths for the $11H(L)$ exciton transitions are indicated by vertical bars.

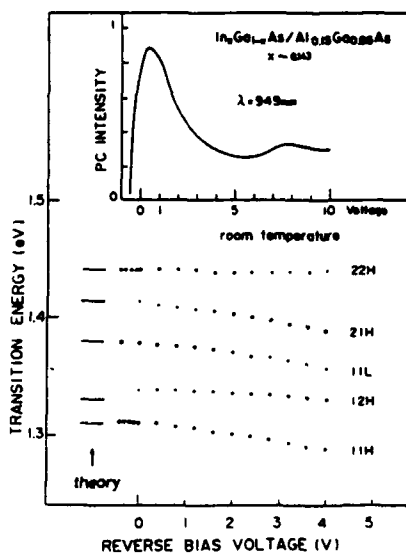


Figure 3
Exciton transition energy versus reverse bias voltage V_b . The inset shows photocurrent intensity versus V_b under illumination at $\lambda_1=949$ nm.

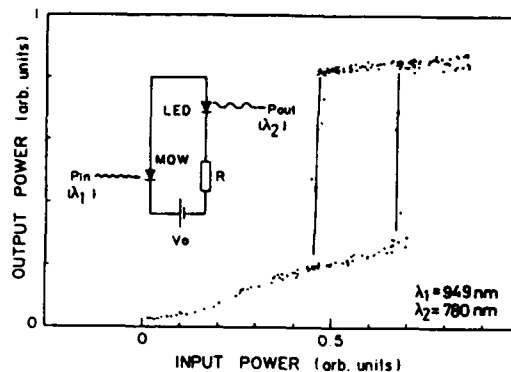


Figure 4
Optical output versus input power for a LED biased SEED device at wavelength $\lambda_1=949$ nm and $\lambda_2=780$ nm. The arrows refer to the direction of the increase and decrease of the optical power. The inset shows the configuration of the device circuit ($R=1$ M Ω , $V_0=12$ V).

Ultrafast Measurements of Tunneling Dynamics
in a GaAs/AlGaAs MQW Pin Optical Modulator

C. B. Park, A. Miller, D. C. Hutchings, P. LiKamWa

Center for Research in Electro-Optics and Lasers,

University of Central Florida,

Orlando, FL 32826

Tel: (407) 658 6800

It has attracted much attention to investigate the mechanisms responsible for the vertical transport of photogenerated carriers in semiconductor multiple quantum wells since all photoconductive devices depend on it for their properties. The photoconductive rise time which is directly related to the carrier sweep-out time gives important characteristics such as switching time and risetime to SEED (Self Electro-optic Effect Device) - type logic devices and photodetectors. The ultrafast response depends on the detailed nature of the cross well carrier transport mechanisms. Previous measurements have employed the excite-probe technique with electrically biased MQWs to monitor thermionic emission and tunneling via transmission changes caused by the relaxation of the quantum confined Stark effect as carriers leaving the wells¹⁻³. In the present work, we have extended these measurements to longer time delays and investigated the effects of higher carrier densities appropriate to nonlinear optical switching devices. In this case, the response is significantly altered because of the space-charge field dynamically changing the absorption coefficient and tunneling rates. Measurements have been carried out as a function of laser intensity over a range of applied fields including conditions of resonant tunneling. The results are being numerically modeled to determine the effects of local field changes. We have employed 1 psec pulses from

C B Park et al "Ultrafast Measurements of Tunneling Dynamics..."

a cavity dumped and synchronously mode-locked Styryl 9 dye laser. The MQW device was grown by MOVPE⁴ and has 60 GaAs wells of width 87Å and $\text{Al}_x\text{Ga}_{1-x}\text{As}$ ($x=0.3$) 60Å thick barriers. Excite-probe measurements at photon energies just below the exciton resonance determined the photoconductive risetime via changes in transmission caused by a blue shift of the exciton peak resulting from screening of the field by the carriers leaving the wells and moving towards the contacts. The signal consisted of a rise due to charge separation screening the field and a subsequent fall due to transverse diffusion of the carriers in the doped regions⁵. At low excitation levels, the field dependent risetime varied from over 300 psec to 10psec as a function of applied voltage. These process occur on timescales faster than the external bias circuitry can respond. A minimum of 20ps risetime was measured at 5V corresponding to conditions of resonant tunneling between the $n=1$ level in one well and the $n=2$ level in the adjacent well. The temporal response at higher excitation levels is shown in figure 1. The measurements shown were made under initial conditions of resonant tunneling. As the carrier density is increased, the response time lengthens. The transmission response will depend on the form of the absorption feature, the locally induced space charge fields and the way the functional form of these parameters vary with applied electric field. We ascribe the observed temporal response to a slowing of carrier tunneling from the wells due to the larger space charge fields (and therefore lower net field) induced at higher carrier densities.

We have modeled the temporal response of the pin modulator numerically. This self-consistent model computes the spatial distribution of electrons within each well as a function of time after carrier generation by the excitation pulse. The evolution of the local field within each well is used to derive inter-well scattering rates, tunneling rates from the confined states within the wells to the continuum, and transit rates across the device. We also allow for the transverse diffusion of electrons in the contact region.

C B Park et al "Ultrafast Measurements of Tunneling Dynamics..."**References**

1. G Livescu, A M Fox, D A B Miller, T Sizer, W H Knox, A C Gossard, J H English Phys. Rev. Lett. 63 438 (1989)
2. R J Manning, P J Bradley, A Miller, J S Roberts, P Mistry, M Pate Electron. Lett. 24 854 (1988)
3. R J Manning, P J Bradley, A Miller, J S Roberts, P Mistry, M Pate Electron. Lett. 25 269 (1989)
4. M Whitehead, G Parry, J S Roberts, P Mistry, P Li Kam Wa, J P R David Electron. Lett. 23 854 (1987)
5. G Livescu, A M Fox, D A B Miller, T Sizer, W H Knox, J E Cunningham, A C Gossard, J H English, Semicond Sci. Technol. 5 549 (1990)

C B Park et al "Ultrafast Measurements of Tunneling Dynamics..."

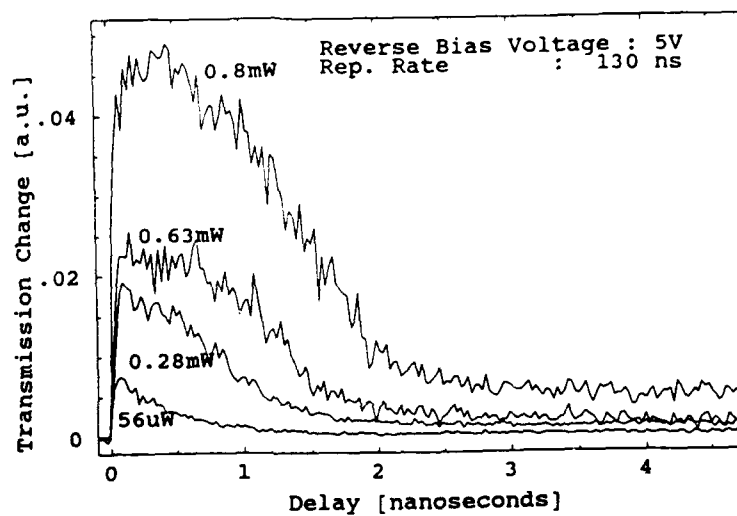


Figure1: Low power probe pulse transmission of a biased GaAs/AlGaAs pin structure as a function of delay after excitation by pump pulses at four different average powers.

Author Index

A

Aiga, M., 172
 Albrechtsen, O., 60
 Alvarado, S.F., 60
 Arai, S., 180
 Arakawa, Y., 84
 Asahi, H., 42, 76
 Asakawa, K., 122

B

Benedict, M.K., 146
 Bimberg, D., 68
 Bishop, K.P., 54
 Bona, G.L., 146
 Bose, S.S., 34
 Bour, D.P., 150
 Brillson, L.J., 130
 Buchmann, P., 146
 Butler, J.K., 150
 Bugajski, M., 38

C

Cahoon, M., 146
 Cao, H.L., 168
 Carlson, N.W., 150
 Chan, W.K., 154
 Chao, C.P., 164
 Chirovsky, L.M.F., 192
 Choi, H.K., 150
 Christen, J., 68
 Clauws, P., 104
 Coldren, L.A., 210
 Cooper, D.M., 176
 Coutts, T.J., 126
 Curtis, A.P., 34

D

Das, U., 195
 D'Asaro, L.A., 192
 Datwyler, K., 146
 Davis, S., 195
 DeFreez, R.K., 92, 150
 Demeester, P., 104
 Deneuve, A., 46
 DeTemple, T.A., 203
 Dietrich, H.P., 146
 Dobashi, M., 168

E

Evans, G.A., 150

F

Feygenson, A., 21
 Fischer, A., 88
 Fletcher, N.C., 176
 Floyd, P., 164
 Fujiwara, K., 206, 214
 Fukatsu, S., 96

G

Gaspar, S.M., 54
 Gautam, D.K., 142
 Gessert, T.A., 126
 Gonda, S., 42
 Gossard, A.C., 164
 Gottscho, R.A., 54
 Grundmann, M., 68

H

Hamada, M., 188
 Hamm, R.A., 21
 Hammer, J.M., 150
 Hasegawa, S., 76
 Hickman, K.C., 54
 Hirata, S., 160
 Hiratani, Y., 25
 Holloway, P.H., 46, 118, 134
 Hori, Y., 108
 Horikoshi, Y., 29
 Hosomatsu, H., 168
 Hsu, J-T., 195
 Hu, S.Y., 164
 Hutchins, D.C., 218

I

Iga, K., 112
 Ino, S., 56
 Inoue, K., 76
 Itaya, Y., 184
 Ito, R., 96
 Iwamura, H., 50
 Iwata, H., 122

K

Kato, M., 108
Kato, T., 64
Kawashima, K., 206, 214
Kim, S., 42
Kimura, K., 76
Kirk, J.B., 150
Kobayashi, K., 206, 214
Kobayashi, N., 29
Kokubo, Y., 172
Kopf, R.F., 192
Koyama, F., 112
Kornblit, A., 54

L

Law, K-K., 164, 210
Lee, H., 150
Lehmann, H., 80
Li, X., 126
Liew, S.K., 150
LiKamWa, P., 218
Lootens, D., 104
Luo, Y., 168

M

Maehashi, K., 76
Marari, K., 184
Marti, U., 80
Martin, D., 80
Matsutani, A., 112
McNeil, J.R., 54
Meier, H.P., 60
Merz, J.L., 164, 210
Miller, A., 218
Monnard, R., 80
Mori, Y., 160
Moser, A., 146

N

Naganuma, M., 50
Nakano, Y., 142, 168
Nakashima, H., 76
Nannichi, Y., 116
Naqvi, S.S., 54
Narui, H., 160
Nishida, T., 50
Nogiwa, S., 188
Nojima, S., 50
Notomi, M., 50

O

Ohashi, M., 96
Ohki, Y., 25
Ohkouchi, S., 64
Okamoto, K., 17
Okamoto, M., 50, 184
Oki, T., 188
Ornoch, J., 38
Osaka, F., 64

P

Panish, M., 21
Park, C.B., 218
Pearton, S.J., 100, 192
Ploog, K., 88
Proctor, M., 80

Q

Quinn, W.E., 13

R

Ramaswamy, R.V., 195
Ramesh, R.S., 29
Reichert, W., 150
Reinhard, F.K., 80
Renaud, Ph., 60
Ritter, D., 21

S

Sakakibara, K., 9, 138
Salemink, H.W.M., 60
Sano, N., 214
Sasso, G., 146
Sato, M., 76
Seitz, H.K., 146
Sekiguchi, Y., 9, 138
Schubert, E.F., 5
Shima, A., 172
Shiraki, Y., 96
Sigeta, M., 206
Sogawa, F., 108
Stevie, F.A., 195
Stillman, G.E., 34
Strausser, Y.E., 54
Suda, K., 188
Sudersena, T., 29
Suematsu, Y., 180

T

Tada, K., 142, 168, 199
 Takahashi, S., 96
 Takizawa, J., 42
 Tamamura, T., 50
 Tanaka, I., 64
 Tanner, D., 46
 Tatham, M.C., 176
 Temkin, H., 21
 Tsang, W.T., 2

V

Van Daele, P., 104
 Vettiger, P., 146
 Voegeli, O., 146

W

Wada, M., 9, 138
 Walpole, J.N., 150
 Wang, C.A., 150
 Wang, Y., 134
 Wang, Y.L., 21
 Wang, Y.X., 118
 Webb, D.J., 146
 Weiner, J.S., 21
 Westbrook, L.D., 176
 Widmer, R., 80
 Wieck, A.D., 88
 Wilson, S., 54
 Wolf, P., 146

Y

Yablonovitch, E., 154
 Yamaguchi, K-I., 17
 Yamaguchi, H., 29
 Yamamoto, E., 188
 Yamamoto, T., 206
 Yi-Yan, A., 154
 Yu, S.J., 42

Z

Zelezny, V., 46